

UNIVERSITY OF CALIFORNIA

Los Angeles

**Particle-In-Cell Simulations of Stimulated
Raman Scattering for Parameters Relevant to
Inertial Fusion Energy**

A dissertation submitted in partial satisfaction

of the requirements for the degree

Doctor of Philosophy in Physics

by

Benjamin John Winjum

2010

© Copyright by
Benjamin John Winjum
2010

The dissertation of Benjamin John Winjum is approved.

Christoph Niemann

Troy Carter

Chandrasekhar Joshi

Warren Mori, Committee Chair

University of California, Los Angeles

2010

*To my parents,
for their eternal and gracious support.*

TABLE OF CONTENTS

1	Introduction	1
1.1	Laser-Plasma Interactions (LPI)	3
1.2	Previous Work	4
1.2.1	Experimental	6
1.2.2	Simulation	8
1.3	Dissertation Outline	11
2	Theory and Methods	13
2.1	SRS Theory	13
2.2	Plasma Wave Theory	19
2.3	Methods	25
2.3.1	OSIRIS	25
2.3.2	Parameter Space	28
2.3.3	Diagnostics	29
2.3.4	Resonance	30
3	1D fixed ion simulations of SRS	34
3.1	Introduction	34
3.2	Parameters	37
3.3	Case I	39
3.4	Cases 1-30 vs. 3-30	67
3.5	Case IV	80

3.6	Conclusions	94
4	Trends in 1D SRS	97
4.1	Parameters	98
4.2	SRS threshold and growth	99
4.3	First Burst of SRS	106
4.4	Recurrence	114
4.5	Reflectivity	126
4.6	Conclusions	142
5	Mobile Ions and Multi-dimensional Behavior of SRS	144
5.1	Parameters	144
5.2	Mobile Ions	146
5.3	2D	151
6	Conclusions and Directions for Future Work	165
6.1	Summary	165
6.2	Extending Simulations to Density Gradients and Higher Temperatures and Laser Intensities	168
6.2.1	Density Gradients	168
6.2.2	Forward SRS and Rescatter	171
6.2.3	Stationary Structures	175
6.2.4	Exciting Nonresonant Modes	176
6.3	Seeding SRS	178
6.4	Concluding Remarks	179

A The Fluid Frequency Shift of an Electron Plasma Wave	180
A.1 Derivation of the Fluid Frequency Shift	180
A.2 Comparison of the Fluid and Kinetic Frequency Shifts	184
A.3 Summary	187
B Number of Particles Per Cell	188
References	193

LIST OF FIGURES

1.1	Schematic for indirectly driven fusion on NIF using a hohlraum. Reprinted with permission from D. E. Hinkel, D. A. Callahan, A. B. Langdon, S. H. Langer, C. H. Still, and E. A. Williams. Phys. Plasmas 15 , 56314 (2008). Copyright 2008, American Institute of Physics.	2
2.1	Absolute threshold of SRS as a function of density and temperature. Contours show where the intensity of 3ω laser light (in W/cm^2) satisfies the threshold condition.	18
2.2	$k\lambda_D$ of the daughter plasma wave in backward SRS.	20
2.3	Electron momentum (black) and plasma wave potential (red) versus space in wavelengths. Electrons move along the black curves, with the closed curves representing possible trapped particle orbits as they bounce in the periodic potential.	21
2.4	Conceptual picture of SRS waves and drivers. The relative amplitudes are arbitrary.	33
3.1	Spatial profile of the E1-Field during SRS growth for Case I.	40
3.2	Plasma wave growth during the initial burst of SRS for Case I. The enveloped E1-field is plotted at a sequence of times over the length of the simulation (left) and a sequence of spatial points over $\omega_0 t = 5000 - 10000$ (right).	41
3.3	Electron phasespace during initial SRS growth for Case I.	43

3.4	Frequency-wavenumber space of the E1-field for Case I. Top and middle plots have logarithmic scales for the magnitude as opposed to the bottom plot which has a linear scale. The ω and k scales are magnified in going from top to bottom.	45
3.5	The Bohm-Gross plasma wave dispersion curve (3), the light wave dispersion curve (1), and the potential plasma modes that satisfy ω and k matching (2) are shown, color-matched where the matched modes lie.	47
3.6	Spatial profile of the frequency (bottom) and wavenumber (top) content of the E1-field for Case I.	48
3.7	Wavenumber vs. time for the E1-field of Case I.	49
3.8	Temporal evolution of the frequency content of the E1-field for Case I.	50
3.9	High/low-pass filtered E1 and E3 fields during SRS growth for Case I. The incident (red) and backscattered (black) light waves are shown on left; the SRS plasma wave (red) and lower wavenumber sidebands (black) are on the right. The E1-field is filtered at $kc/\omega_0 = 1.4$, while the E3-field is filtered at $kc/\omega_0 = 0.8$	51
3.10	SRS resonance diagnostic for the first SRS burst of Case I.	54
3.11	Spatial profile of the E1-Field during SRS growth for Case I.	56
3.12	Effect of sidebands on the electron phasespace and the E1-field for Case I.	57
3.13	The phase velocity (v_2) and velocity at the top of the trapped particle buckets (v_1) are shown on the distribution function, phas-espace, and ω versus k plots.	58

3.14 Electron phasespace and the corresponding distribution function (spatially averaged over the same region as the plotted phasespace) for Case I.	60
3.15 Reflectivity versus time for Case I.	62
3.16 Electron phasespace at edge of packet for Case I.	63
3.17 Temporal evolution of the E1-field at several positions in space for Cases 1-30 (left) and 3-30 (right).	67
3.18 Spatio-temporal evolution of the E1-field for Cases 1-30 (left) and 3-30 (right).	68
3.19 Temporal evolution of the E1-field at $x\omega_0/c = 129$ for Cases 1-30 (left) and 3-30 (right).	70
3.20 Frequency vs. Wavenumber for Cases 1-30 (top) and 3-30 (bot- tom). The right column is zoomed-in plots.	71
3.21 Wavenumber evolution for Cases 1-30 (top) and 3-30 (bottom). . .	72
3.22 Filtered E1 (bottom) and E3 (top) Fields for Case 1-30 at the time of saturation of the first SRS burst.	74
3.23 Filtered E1 (bottom) and E3 (top) Fields for Case 3-30 at the time of saturation of the first SRS burst.	74
3.24 Saturation time for Cases 1-30 (top) and 3-30 (bottom).	75
3.25 Frequency vs. Position of the E1 (left) and E3 (right) Fields for Case 1-30.	76
3.26 Frequency vs. Position of the E1 (left) and E3 (right) Fields for Case 3-30.	76

3.27 Filtered E1 and E3 Fields for Case 1-30 (bottom) and 3-30 (top) showing SRS growth in a convecting plasma packet.	77
3.28 Frequency vs. Position of the E1 and E3 Fields for Case 1-30. . .	78
3.29 Frequency vs. Position of the E1 and E3 Fields for Case 3-30. . .	78
3.30 Spatio-temporal evolution of the enveloped E1-field for Case IV. .	81
3.31 Frequency vs. wavenumber of the E1-field for Case IV.	83
3.32 Wavenumber vs. time for the E1-field for Case IV.	85
3.33 Frequency vs. time of the plasma waves (Wigner transform of the E1-field) at $x\omega_0/c = 200$ and 400 for Case IV. Top two plots show first half of simulation from $\omega_0 t = 0 - 10000$, while the bottom plot shows the second half (only for $x\omega_0/c = 400$) from $\omega_0 t = 10000 - 20000$	86
3.34 Envelopes of filtered E-fields for Case IV. Left: incident (top 3 lines) and backscattered (bottom 3 lines) light waves; right: SRS plasma wave (red) and sidebands (black).	87
3.35 Spatially averaged distribution function (left) and electron phaspace plots (right) for Case IV at $\omega_0 t = 2800, 3000$, and 3200. . .	88
3.36 Envelopes of filtered E-fields for Case IV. Left: incident (top 3 lines) and backscattered (bottom 3 lines) light waves; right: SRS plasma wave (red) and sidebands (black).	89
3.37 Spatially averaged distribution function for Case IV at $\omega_0 t = 0, 2500$, and 5000.	91
3.38 Frequency vs. space of the plasma waves (E1-field, left) and scattered light waves (E3-field, right) for Case IV.	92

3.39 Frequency vs. space of the plasma waves (E1-field, left) and scattered light waves (E3-field, right) for Case IV.	93
4.1 The number of convective gain lengths in the simulation box at the onset of SRS.	100
4.2 Measured simulation growth rates. Theory curves show the absolute growth rate.	101
4.3 Ratio of measured growth rate to the undamped ($\gamma_p = 0$) absolute growth rate.	102
4.4 Trapped particles in simulation 30-3-100, with $v_{osc}/c = 0.008$. . .	104
4.5 Maximum E1-field amplitude during the first burst of SRS.	107
4.6 Frequency shift versus maximum E1-field amplitude of the first burst of SRS.	109
4.7 Saturation of the first SRS burst due to pump depletion for Case 26-3-100, $v_{osc}/c = 0.0052$. Space versus time of the longitudinal E1-field (top-left) and backscattered light (top-right), resonance diagnostic (bottom-left), and Manley-Rowe (bottom-right).	111
4.8 Ratio of the measured growth rate to the detuning rate as given by $\Delta\omega/\pi$ from the frequency shift of the first burst.	113
4.9 Time vs. reflectivity (left) and time vs. space of the backward-propagating light (middle) and E_x -field (right). The simulation parameters are equivalent with the exception of driving laser intensity I_0 as noted.	116
4.10 Spatial-temporal content of the longitudinal E-field with laser of half-intensity launched from the left.	118

4.11 Reflectivity (left) and spatial-temporal content of the longitudinal E-field (right) when the initial laser stops at $\omega_0 t = 7000$ and a second laser is sent in at $\omega_0 t = 9000$ (bottom) or not at all (top).	119
4.12 Packet velocity versus $k\lambda_D$	121
4.13 (a) Reflectivity vs. time (left), transmittivity vs. time (right), and time versus space of the E_x -field (middle) for $L = 60 \mu\text{m}$ and $I_0 = 1.9 \times 10^{15} \text{ W/cm}^2$. (b) Spatio-temporal evolution of backward (left) and forward (right) propagating light for the same simulation. (c) Spatial-frequency content of the transverse (left) and longitudinal (right) E-fields at two times during packet convection, obtained by a windowed FFT.	123
4.14 Evolution of the plasma wave for Case 26-3, with v_{osc}/c of (a) 0.0052, (b) 0.0067, (c) 0.0079, (d) 0.0095, (e) 0.021, and (f) 0.030.	127
4.15 Reflectivities vs. time for Case 26-3.	128
4.16 Evolution of the plasma wave for Case 26-700, with v_{osc}/c of (a) 0.0052, (b) 0.0067, (c) 0.0079, (d) 0.0095, (e) 0.021, and (f) 0.030.	129
4.17 Reflectivities vs. time for Case 26-700.	130
4.18 Evolution of the plasma wave for Case 30-3, with v_{osc}/c of (a) 0.011, (b) 0.013, (c) 0.016, (d) 0.019, (e) 0.021, and (f) 0.030.	131
4.19 Reflectivities vs. time for Case 30-3.	132
4.20 Evolution of the plasma wave for Case 30-700, with v_{osc}/c of (a) 0.011, (b) 0.013, (c) 0.016, (d) 0.019, (e) 0.021, and (f) 0.030.	133
4.21 Reflectivities vs. time for Case 30-700.	134
4.22 Evolution of the plasma wave for Case 34-3, with v_{osc}/c of (a) 0.011, (b) 0.016, (c) 0.019, (d) 0.021, and (e) 0.030.	135

4.23 Reflectivities vs. time for Case 34-3	136
4.24 Evolution of the plasma wave for Case 34-700, with v_{osc}/c of (a) 0.011, (b) 0.016, (c) 0.019, (d) 0.021, and (e) 0.030.	137
4.25 Reflectivities vs. time for Case 34-700.	138
4.26 Reflectivity versus the number of convective gain lengths in the simulation box (top) and incident laser intensity for 3ω light (bot- tom).	140
5.1 Transverse Field (E2-field) showing the incident laser profile.	145
5.2 For $k\lambda_D = 0.30$, time vs. space plots of the longitudinal E-field for $T_e = 1$ (left) and 3 keV (right), with $ZT_e/T_i = 3$ (top), 5 (middle), and 10 (bottom).	147
5.3 For $k\lambda_D = 0.30$, reflectivity vs. time for $T_e = 1$ (left) and 3 keV (right), with $ZT_e/T_i = 3$ (top), 5 (middle), and 10 (bottom).	147
5.4 For $k\lambda_D = 0.26$, time vs. space plots of the longitudinal E-field for $T_e = 700$ eV (left) and 3 keV (right), with $ZT_e/T_i = 3$ (top), 5 (middle), and 10 (bottom).	149
5.5 For $k\lambda_D = 0.26$, reflectivity vs. time for $T_e = 700$ eV (left) and 3 keV (right), with $ZT_e/T_i = 3$ (top), 5 (middle), and 10 (bottom).	149
5.6 Reflectivities for Cases 1-30-2D (top) and 3-30-2D (bottom). Re- flected light shown as time vs. x2 (left) and the temporal evolution of the total reflected intensity divided by incident intensity (right).	152
5.7 E1-field during saturation of the first burst of SRS.	154
5.8 Incident and backscattered laser light at three times during satu- ration of the first burst of SRS.	155

5.9	Maximum E1-field amplitude versus time for 1D (left) and 2D (right). The 2D plot represents the E1-field maximum on a lineout through the center of the simulation domain.	156
5.10	Frequency versus wavenumber of the E1-field for 1D (top) and 2D (bottom), where the 2D E1-field is taken along the central axis. .	157
5.11	Incident and backscattered laser light at three times during saturation of the second burst of SRS.	158
5.12	Reflectivity vs. Time (left) and Time vs. Space plots of the E1-field (right). The 2D plot represents the E1-field on a lineout through the center of the simulation domain.	160
5.13	Top: E1-field in space at two neighboring times for 2D case. Bottom: Frequency versus Perpendicular Wavenumber for the backscattered light is shown for early (left) and late (right) times.	161
5.14	E1-field during and after the second burst of SRS.	162
5.15	E1-field during continued convection of the central filament and subsequent regrowth of a third burst of SRS.	163
6.1	Temporal evolution of reflectivity (top), longitudinal E1-fields (2nd from top), and wavenumbers (3rd from top), and frequency versus wavenumber of the E1-fields (bottom) for Cases I-grad (left) and 3-30-grad (right).	169
6.2	Wavenumber evolution of plasma waves (left) and light waves (right), and frequency versus wavenumber for the plasma waves (bottom), for $T_e = 5.0$ keV, $n/n_{cr} = 0.09$, and $I_0 = 1 \times 10^{16}$ W/cm ² for 3ω light.	173

6.3	Space versus time of the E1-field with log (top-left) and non-log (top-right) scales; electron phasespace (2nd down) and spatially averaged distribution function (3rd down) at $\omega_0 t = 18800$; and transmittivity versus time (bottom). $T_e = 5.0$ keV, $n/n_{cr} = 0.09$, and $I_0 = 1 \times 10^{16}$ W/cm ² for 3ω light.	174
6.4	Electron phasespace for Case IV with $v_{osc}/c = 0.045$	175
6.5	Frequency versus wavenumber for $T_e = 3.0$ keV, $n/n_{cr} = 0.129$, and $I_0 = 1 \times 10^{16}$ (top) and 10^{17} (bottom) W/cm ² for 3ω light. . . .	177
A.1	Frequency shifts. Solid lines represent the sum of fluid plus kinetic shifts for three amplitudes, $eE/m\omega_p v_{the} = 0.2, 0.5, 0.8$. The dashed lines are the fluid or kinetic shift only for $eE/m\omega_p v_{the} = 0.5$	185
A.2	Fluid plus kinetic frequency shift as a function of amplitude relative to the Coffey wavebreaking limit, E_{max}	186
B.1	Reflectivity for simulations with varying numbers of particles per cell. $T_e = 3$ keV, $n/n_{cr} = 0.128$, $L = 100$ μm.	189
B.2	Reflectivity and enveloped longitudinal E-field for simulations with 8192 (bottom) versus 512 (top) particles per cell. $T_e = 3$ keV, $n/n_{cr} = 0.128$, $L = 100$ μm.	190
B.3	Reflectivity and enveloped longitudinal E-field for simulations with 8192 (bottom) versus 512 (top) particles per cell. $T_e = 1$ keV, $n/n_{cr} = 0.059$, $L = 100$ μm.	191

LIST OF TABLES

2.1	Common parameters for studying SRS.	26
2.2	Normalized simulation parameters.	27
3.1	Simulation Parameters for Chapter 3. The conversion to physical units uses $\lambda_0 = 0.351 \mu\text{m}$	38
4.1	Normalized simulation parameters for studying SRS trends.	99

ACKNOWLEDGMENTS

I would not have been able to complete my doctoral research without the patience, support, guidance, and camaraderie of many individuals who have accompanied me along my path.

I would first like to acknowledge all of the graduate students and postdocs who have provided me with a stimulating research group during my scientific development: Joe Ralph, Miaomiao Zhou, Mikhail Tzoufras, Chengkun Huang, Wei Lu, Weiming An, Art Pak, Frederico Fiuzza, Sam Martins, Thomas Grismayer, Josh May, Tyan-Lin Wang, and Ian Ellis. I would also like to thank all of the senior researchers who have provided me with assistance and guidance in my computational research of SRS: John Tonge, Viktor Decyk, and Jean-Noel Leboeuf at UCLA, and Bruce Langdon, Denise Hinkel, and David Strozzi at LLNL.

I owe a special debt of gratitude to Frank Tsung for all of the hours he has spent helping me with OSIRIS, IDL, and scientific research in general. I am especially indebted to Jay Fahlen, a friend and scientific foil who has toiled together with me on the study of SRS and nonlinear plasma waves.

I would like to thank George Morales and Steve Cowley for teaching me plasma physics with their lectures and seminars, and I would like to thank all of the members of my committee, Chris Niemann, Troy Carter, Chan Joshi, and Warren Mori for overseeing my doctoral studies to completion. I would particularly like to thank Chan Joshi, a continual scientific guide who I have known since the beginning of my research and who has helped to provide me with a stimulating research environment. Finally, I am indebted to Warren Mori, my scientific mentor and a wonderful plasma physicist who has guided my research, analyzed my work, and been very patient with my years of seeking out and

explaining the intricacies of a very difficult subject.

My life outside of research has required a support of its own, and I am deeply grateful to have had the support of Jenny Cho, Francine Redada, Connie Steel, my aunt Susan Ellis, my late grandfather Wendell Pauling, and my parents and brother, Jim, Joan, and David Winjum, all of whom serve as a reminder that I am surrounded by a loving circle of family and friends.

VITA

1978	Born, Valley City, North Dakota, USA.
2001	B.S. Physics The Pennsylvania State University
2003	M.S. Physics University of California, Los Angeles
2001–2004	Teaching Assistant Physics & Astronomy Department University of California, Los Angeles
summer, 2006	Student Intern Lawrence Livermore National Laboratory Livermore, CA
2003–present	Graduate Student Researcher Physics & Astronomy and Electrical Engineering Departments University of California, Los Angeles

PUBLICATIONS

B. J. Winjum, J. E. Fahlen, F. S. Tsung, W. B. Mori, “The effects of plasma wave packets and local pump depletion in stimulated Raman scattering.” in preparation.

B. J. Winjum, J. E. Fahlen, F. S. Tsung, W. B. Mori, “The growth, saturation, and recurrence of stimulated Raman scattering for moderate $k\lambda_D$.” in preparation.

B. J. Winjum, J. E. Fahlen, F. S. Tsung, W. B. Mori, “A transition from convective to absolute instability in stimulated Raman scattering.” in preparation.

J. E. Fahlen, B. J. Winjum, T. Grismayer, W. B. Mori, “Transverse plasma wave localization in multiple dimensions.” in preparation.

J. E. Fahlen, B. J. Winjum, T. Grismayer, W. B. Mori, “Propagation and damping of nonlinear plasma wave packets.” Phys. Rev. Lett. 102, 245002 (2009).

- B. J. Winjum, J. Fahlen, and W. B. Mori, “The relative importance of fluid and kinetic frequency shifts of an electron plasma wave.” *Phys. Plasmas* 14, 102104 (2007).
- B. Abbott et al. (LIGO Scientific Collaboration), “Joint LIGO and TAMA300 search for gravitational waves from inspiralling neutron star binaries.” *Phys. Rev. D* 73, 102002 (2006).
- B. Abbott et al. (LIGO Scientific Collaboration), “Search for gravitational waves from binary black hole inspirals in LIGO data.” *Phys. Rev. D* 73, 062001 (2006).
- B. Abbott et al. (LIGO Scientific Collaboration), “Upper limits from the LIGO and TAMA detectors on the rate of gravitational-wave bursts.” *Phys. Rev. D* 72, 122004 (2005).
- B. Abbott et al. (LIGO Scientific Collaboration), “First all-sky upper limits from LIGO on the strength of periodic gravitational waves using the Hough transform.” *Phys. Rev. D* 72, 102004 (2005).
- B. Abbott et al. (LIGO Scientific Collaboration), “Search for gravitational waves from primordial black hole binary coalescences in the galactic halo.” *Phys. Rev. D* 72, 082002 (2005).
- B. Abbott et al. (LIGO Scientific Collaboration), “Search for gravitational waves from galactic and extra-galactic binary neutron stars.” *Phys. Rev. D* 72, 082001 (2005).
- B. Abbott et al. (LIGO Scientific Collaboration), “Upper limits on gravitational wave bursts in LIGO’s second science run.” *Phys. Rev. D* 72, 062001 (2005).
- B. Abbott et al. (LIGO Scientific Collaboration), “Search for gravitational waves associated with the gamma ray burst GRB030329 using the LIGO detectors.” *Phys. Rev. D* 72, 042002 (2005).
- B. Abbott et al. (LIGO Scientific Collaboration), “Limits on Gravitational-Wave Emission from Selected Pulsars Using LIGO Data.” *Phys. Rev. Lett.* 94, 181103 (2005).
- B. Abbott et al. (LIGO Scientific Collaboration), “Detector description and performance for the first observations between LIGO and GEO.” *Nucl. Instrum. Methods Phys. Res., Sect. A* 517, 154 (2004).
- B. Abbott et al. (LIGO Scientific Collaboration), “Analysis of first LIGO science

- data for stochastic gravitational waves.” Phys. Rev. D 69, 122004 (2004).
- B. Abbott et al. (LIGO Scientific Collaboration), “Analysis of LIGO data for gravitational waves from binary neutron stars.” Phys. Rev. D 69, 122001 (2004).
- B. Abbott et al. (LIGO Scientific Collaboration), “First upper limits from LIGO on gravitational wave bursts.” Phys. Rev. D 69, 102001 (2004).
- B. Abbott et al. (LIGO Scientific Collaboration), “Setting upper limits on the strength of periodic gravitational waves from PSR J1939+2134 using the first science data from the GEO 600 and LIGO detectors.” Phys. Rev. D 69, 082004 (2004).

ABSTRACT OF THE DISSERTATION

**Particle-In-Cell Simulations of Stimulated
Raman Scattering for Parameters Relevant to
Inertial Fusion Energy**

by

Benjamin John Winjum

Doctor of Philosophy in Physics

University of California, Los Angeles, 2010

Professor Warren Mori, Chair

Using the electromagnetic Particle-In-Cell (PIC) code OSIRIS, stimulated Raman scattering (SRS) is simulated in 1 and 2D under conditions relevant to Inertial Fusion Energy (IFE) and the National Ignition Facility (NIF). In this regime, the plasma wave has a $k\lambda_D \gtrsim 0.3$ (k is the plasma wave wavenumber and λ_D is the plasma Debye length) and kinetic effects are important even for small amounts of growth. OSIRIS simulations show that inflation, frequency shifts, sideband instabilities, beam modes, pump depletion, plasma wave convection, plasma length, and ion motion all play a role in SRS dynamics. While each nonlinearity is a subject in its own right, an array of simulations are used to study the dynamics of SRS behavior as a whole.

A comprehensive picture of the onset, saturation, and recurrence of SRS is presented. The onset is shown to depend on the convective gain length in the strongly damped regime. Even though SRS is below the absolute threshold, it is shown to grow at the undamped absolute growth rate due to the effect of trapped particles. Saturation is shown to depend on both the plasma wave's nonlinear frequency shift and pump depletion, with sidebands and beam modes growing significantly only after saturation. Following saturation, plasma waves are shown to convect as a packet which Raman scatters at a shifted frequency,

with recurrence depending on the nonlinear packet speed, shifted frequencies, and pump depletion.

The 1D simulations indicate that total time-averaged reflectivities less than 1% require the ratio of the speckle length to the convective gain length to be $\lesssim O(1)$. The total time-averaged reflectivity is shown to be lower when the ratio of the growth rate to the detuning rate due to the nonlinear frequency shift is lower ($\lesssim O(1)$) and lower for shorter simulated speckle lengths. Instantaneous reflectivity levels are shown to increase in time when multiple plasma packets exist simultaneously within the simulated space. 2D reflectivity is shown to be lower in comparison with 1D due to transverse localization of the plasma wave, but the same dependence of the instantaneous reflectivity on the nonlinear frequency shift and plasma packet effects is shown. The results indicate that mesoscale models that incorporate kinetic effects must include the effects of plasma packets and a nonlinear frequency shift, albeit the frequency shift is shown to be larger than theoretically expected.

CHAPTER 1

Introduction

The National Ignition Facility (NIF), recently commissioned at the Lawrence Livermore National Laboratory (LLNL), seeks to produce for the first time a controlled thermonuclear burn of fusion fuel [1]. The NIF laser bays cover an area the size of two football fields with the ultimate goal of achieving fusion burn in a pellet approximately one millimeter in size. 192 laser beams, with a total peak energy of 1.8 MJ and a peak power of 700 TW (in total sum the largest laser in the world), will be precisely smoothed, shaped, targeted, and timed to compress the pellet to temperatures nearly a million times room temperature and densities that are thousands of times liquid densities over a couple billionths of a second.

Fifty years after the invention of the laser in 1960, NIF is poised to attempt to achieve ignition in 2010. Soon after the laser was invented, research began on using laser energy to compress and drive fusion reactions in a small pellet of fuel [2, 3, 4]. A typical fuel pellet for NIF consists of a sphere of deuterium-tritium ice, cryogenically cooled and surrounded by a layer of low-Z ablator material such as Be. The ablator is heated either by directly shining the lasers at the pellet (direct drive) or by converting the laser energy into a bath of hot x-rays which then drive the ablation (indirect drive). As the ablator material is heated and expands, the interior deuterium-tritium mixture is compressed by conservation of momentum. Once the central part of the fuel is compressed to sufficiently

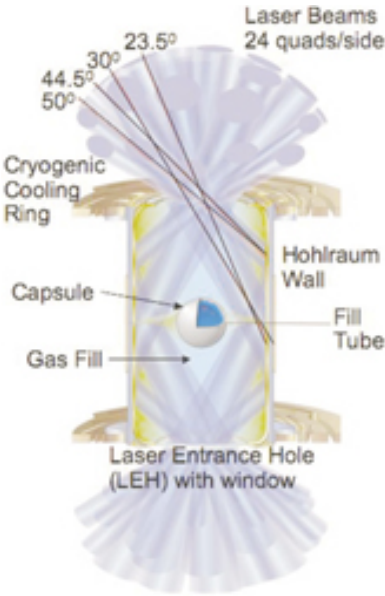


Figure 1.1: Schematic for indirectly driven fusion on NIF using a hohlraum. Reprinted with permission from D. E. Hinkel, D. A. Callahan, A. B. Langdon, S. H. Langer, C. H. Still, and E. A. Williams. Phys. Plasmas **15**, 56314 (2008). Copyright 2008, American Institute of Physics.

high densities and temperatures, fusion reactions begin and a burn propagates throughout the rest of the fuel before it can cool. Since the fusion reactions occur more quickly than the hot fuel can expand, the fuel is said to be confined by its inertia and this type of fusion is called inertial confinement fusion (ICF).

For indirect drive, the pellet is surrounded by a hohlraum, a small cylinder of high-Z material (mixture of Au and U); the lasers are converted into x-rays by focusing them onto the interior of the hohlraum walls. A schematic of the set-up for indirect drive is shown in Figure 1.1. There are efficiency trade-offs between direct and indirect drive. Direct drive couples the laser energy more efficiently to the ablator. However, it requires stricter tolerances on laser profile and pointing accuracy to achieve the highly symmetric implosion, as well as on the smoothness

of the pellet surface to limit the detrimental effects of hydrodynamic instabilities such as the Rayleigh-Taylor instability. Indirect drive couples the energy less efficiently, but it has the advantage of relaxing the aforementioned tolerances and has therefore been chosen for the initial stage of ICF on NIF.

As the laser propagates into the hohlraum for indirect drive, it will pass through several millimeters of plasma and be subject to instabilities such as stimulated Raman scattering (SRS) and stimulated Brillouin scattering (SBS), where SRS (SBS) is the resonant decay of the laser into an electron plasma (ion acoustic) wave and another light wave. One of these laser-plasma instabilities, stimulated Raman scattering, forms the subject of this dissertation.

1.1 Laser-Plasma Interactions (LPI)

The laser pulse on NIF will be approximately 10 ns in length, carefully tailored to produce several successive shocks that will maximize the spherical compression of the fuel pellet. As the laser beams enter the hohlraum, they will first pass through a low-Z gas fill before irradiating the hohlraum walls. This low-Z gas is necessary to prevent the interior walls from expanding during the first, relatively long part of the laser drive. The low-Z gas will be ionized, creating a plasma which can then interact with the remaining part of the pulse. At peak laser power, the laser energy must propagate through several millimeters of hot, underdense plasma in which the electron temperature is 2-6 keV and the electron density is approximately 10% of the critical density, where the critical density $n_c \simeq 10^{21}/\lambda_0^2$ cm⁻³ with λ_0 the laser wavelength in microns.

Several nonlinear laser-plasma instabilities (LPI) may interfere with the lasers' propagation. The laser beams may dig into the density and alter the refractive

index, resulting in filamentation and beam spray. If the plasma has a bulk flow, the beams may bend and disrupt the drive uniformity. In addition, there may be a transfer of energy between laser beams as they cross paths while entering the hohlraum at the laser entrance hole (LEH). The laser energy may be directly lost through parametric decay instabilities which reflect the light (SRS and SBS), and if these instabilities vary between beams, this might further disrupt the symmetry. Finally, the plasma waves generated in SRS can produce energetic electrons that threaten to preheat the target before compression is achieved.

Specifically, in SRS, the laser resonantly decays into an electron plasma wave and another scattered light wave. Should the light scatter backwards, this will be a direct loss of energy driving the implosion. If the light scatters sideways, the precise symmetry will be affected. Finally, the electron plasma wave may produce hot electrons, and should these reach the pellet before it is fully compressed, the pellet could heat and expand before ignition occurs. A thorough understanding of SRS is needed to accurately predict how it will affect NIF’s operation, as well as to guide the way to an operable parameter regime. There is also hope that this knowledge can be used in the future to relax some of the safety margin that has been built into the initial stage of operation. Just as importantly, understanding SRS is critical to developing a plan forward for IFE.

1.2 Previous Work

Extensive research on LPI has been conducted in coordination with the development of ICF (for a general history, see [5], Sec. II). Early on, LPI in general, and SRS in particular, were recognized as constraints on the intensity of the laser drive. A fundamental theoretical basis for two laser-plasma parametric instabilities, SRS and SBS, was formulated in the 1970’s by Forslund *et al.* [6, 7]

and Drake *et al.* [8] who studied the thresholds and growth rates. In addition, Forslund *et al.* [6, 7] provided an extensive exploration of growth rates, gain lengths, differences between convective and absolute behavior, and possible nonlinearities involved, as well as provided simulation results.

Experimental research on SRS also began in the 1970's with neodymium glass [9] and carbon dioxide [10] lasers, with wavelengths of 1.06 and 10.6 μm , respectively, where SRS was found to have detrimental consequences to the efficient operation of laser-driven fusion. Both backscattering and forward scattering [11] were subjects of investigation and the generation of hot electrons was a concern. With the Shiva laser at LLNL, high-intensity 1.064- μm light produced very high-energy electrons through the $2\omega_p$ and SRS instabilities [12, 13].

Since SRS growth is dependent on $I_0\lambda_0^2$ [6], where I_0 is the laser intensity, the effects of SRS could be reduced for a given laser intensity by shortening the laser wavelength. By frequency doubling or tripling the Nd:glass laser light (2ω or 3ω light, respectively) the laser wavelength was reduced and the intensity threshold for SRS was increased. SRS was studied in a range of plasmas with the Argus laser at 0.532- μm [14], the Novette laser at 0.532- μm [15] and 0.27- μm [16], and the U. of Rochester's Omega laser at 0.35- μm [17]. SRS experiments with the Nova laser, NIF's predecessor, began in the late 1980's (for example, [18, 19, 20]). Nova used 0.351- μm light, and this is the wavelength that will be used on NIF. The actual parameter regimes of NIF will not be available until NIF is operational, but the experiments on Nova attempted to study SRS in regimes that were as close as possible to those expected at NIF.

Several recent experiments and a range of past simulation works will be summarized here. A more comprehensive description of the early history of ICF research can be found in papers by Lindl *et al.* [1, 5] and references therein.

1.2.1 Experimental

Experiments performed on the Nova laser at LLNL, the Trident laser at Los Alamos National Laboratory (LANL), and the Omega laser at the Laboratory for Laser Energetics (LLE) explored SRS in regimes of relevance to NIF with plasmas of varying densities and compositions and lasers of varying intensities. Since LPI are intensity-dependent and sensitive to laser beam intensity nonuniformities such as regions of high-intensity fluctuations (hot-spots, or speckles), the effects of several laser-beam smoothing techniques were tested as well. These techniques included random phase plates [21], kinoform phase plates [22], smoothing by spectral dispersion [23], and polarization smoothing [24, 25], and they were found to decrease the reflectivities of SRS and SBS (e.g., [26]). Our focus here, however, is on the new nonlinear effects that were seen in SRS behavior that could affect individual speckles as well as how speckles interact between each other.

First, there appeared to be an anti-correlation between SRS and SBS in experiments on Nova [27] and Trident [28] and at the Laboratoire pour l’Utilisation des Lasers Intenses [29]. The instabilities did not strongly occur simultaneously, but rather one or the other instability appeared to dominate at any given time. Although this is still an open subject, later Trident experiments showed that SRS and SBS were not systematically anti-correlated and concluded that mechanisms other than mode competition were at play [30].

Second, experiments in Nova gasbags [31] and toroidal hohlraums [32, 33] found that the SRS reflectivity increased with an increase in the damping rate of ion acoustic waves. This was interpreted as evidence that the Langmuir decay instability (LDI) saturated SRS, where LDI is the decay of the SRS plasma wave into an ion acoustic wave and another plasma wave, first studied by Goldman and Dubois [34, 35]. The increase in ion wave damping would increase the LDI

threshold and SRS could thereby be driven to higher amplitudes. However, these experiments did not see much of an effect until the plasma heater turned off, with SRS convectively saturating until the plasma cooled to the point at which the LDI threshold was crossed. These experiments used a range of hydrocarbon gas fills with moderate ion charge Z . Later experiments with more NIF-relevant gas fills of H, He, and Ne and different multiple-species ion modes saw little change in SRS reflectivity as the ion damping increased [36].

Finally, toroidal hohlraum experiments by Fernandez *et al.* [37] showed several unexpected features in SRS behavior as the laser intensity and electron density were varied. The SRS reflectivity was shown to only weakly vary across separate electron densities, it had a sudden and dramatic onset, and the reflectivity settled at a relatively constant level as the laser intensity was increased past the onset value. The onset was found to occur at an intensity for which the speckle length was approximately equal to the length for one e-folding of convective SRS growth. This onset had been suggested in earlier theoretical work that studied the response of a statistical ensemble of hot spots in a beam smoothed with a random phase plate [38]. The apparent independence from density and the plateau in reflectivity level were both taken to suggest that SRS was nonlinearly saturated.

Several experiments were then performed by Montgomery *et al.* [28, 39, 40] on the Trident laser in an attempt to model a single laser hot spot interacting with plasma. These showed the dramatic onset of SRS reflectivities at lower intensities than expected from linear theory. They also showed direct evidence of LDI cascades from the decay of SRS plasma waves. Kline *et al.* [41, 42] extended these results to show a transition between fluid and kinetic nonlinearities. Multiple cascades of LDI were seen for low $k\lambda_D$ (where k is the wavenumber of

the electron plasma wave and λ_D is the electron Debye length), whereas a single plasma wave, broadened in frequency, was seen for higher $k\lambda_D$.

The experiments of Montgomery *et al.* and Kline *et al.* were performed with 2ω light. A number of other authors have explored the prospects of using 2ω light as well [43, 44, 45], since more laser power would be available without the losses from frequency-tripling. It is likely that 2ω light will be investigated after the current operation of NIF with 3ω light. The operation at 2ω light will likely be limited by keeping SRS at acceptable levels.

Including the experiments of Montgomery *et al.* and Kline *et al.*, experimental work has been limited to diagnostics that do not have the temporal resolution to capture the kinetic effects of wave-particle interactions. SRS can develop on the picosecond time scale, with highly nonlinear wave-particle interactions that develop on the sub-picosecond time scale. While Fernandez *et al.* [46] recently showed that SRS was suppressed for most of the underdense plasma in a NIF hohlraum where $k\lambda_D > 0.45$, there will still be regions of the plasma where $k\lambda_D$ is lower. In these regions of plasma where $k\lambda_D \lesssim 0.35$, there can still be strong SRS growth on time and length scales on the order of a speckle length and duration. Within a single speckle, there can be significant nonlinear wave-particle interactions, and this has motivated recent work on computer simulations of SRS.

1.2.2 Simulation

Particle-in-cell (PIC) simulations have been a useful tool in studying the nonlinear kinetic effects involved with SRS. The work of Forslund *et al.* mentioned previously used PIC simulations to support and validate their theoretical work on SRS and SBS [6, 7], although the simulations were limited in size to only a couple laser wavelengths and the laser amplitude ($I_0\lambda_0^2 \geq 10^{15}$ W $\mu\text{m}^2/\text{cm}^2$) was fairly

high when compared against the current intensities on NIF, even when accounting for laser hot spots. Cohen and Kaufman studied the nonlinear effects of a frequency shift on SRS in ponderomotively-driven electrostatic PIC simulations, but they were single wavelength simulations [47, 48]. Estabrook *et al.* simulated the nonlinear behavior of SBS and of both forward and backward SRS with PIC, focusing in particular on the generation of hot electrons [49, 50, 51]. While these simulations were for lengths of $\approx 100\lambda_0$, the laser amplitude was high with $I_0\lambda_0^2 \geq 10^{16} \text{ W } \mu\text{m}^2/\text{cm}^2$. In addition to having ordinary SBS and SRS, the possibility of having multiple different scatterings and rescatterings in NIF-relevant plasmas has been shown in PIC simulations by Langdon and Hinkel [52] and Hinkel *et al.* [53], but they studied the temporal evolution of the wavenumber modes and the total electron distribution function without studying in detail the spatial dynamics or kinetic effects.

Computing power has grown exponentially with each new decade, and with its growth have come progressively larger PIC simulations. The recent experimental work mentioned above, with its suggestion that novel kinetic physics plays a vital role in the nonlinear behavior of SRS, has motivated a slew of authors to focus on the nonlinearities of SRS that are observed in simulations and the nonlinear wave-particle interactions between the SRS plasma wave and the particles trapped in the wave. Vu *et al.* [54, 55] utilized the nonlinear change in a plasma wave's damping rate and frequency due to trapped particles (from O'Neil [56] and Morales and O'Neil [57]) to explain SRS behavior observed in reduced particle-in-cell simulations. They argued that the nonlinear frequency shift due to trapped particles saturates SRS by detuning the necessary resonance for instability growth. Furthermore, they have used the reduced damping caused by trapping to provide an explanation (called inflation) for the observation of SRS for parameters in which linear theory predicts insignificant growth [58]. Additional modes

may grow in the plasma due to nonlinear wave-particle interactions, particularly sidebands and beam modes. Brunner and Valeo [59], using the trapped-particle-instability (TPI) model of sideband growth from Kruer *et al.* [60], have proposed that these sidebands may affect SRS. Yin *et al.* [61, 62] used the non-Maxwellian electron distribution function from simulations to numerically solve for electrostatic modes in the plasma, finding beam acoustic modes (BAM) that matched simulation results. As the authors also pointed out, these beam acoustic modes intersected with a spectral streak of the primary plasma wave. As the frequency of the plasma wave shifted down, these intersecting points resulted in subsequent bursts of frequency-down-shifted SRS that could frequency match with normal light waves provided that its wavenumber shifted slightly higher too, and this was seen. Albrecht-Marc *et al.* [63] have used this spectral streak to argue that a frequency shift of the SRS plasma wave does not saturate the instability, provided that resonance is maintained along the streak. Instead, they proposed that the coalescence of neighboring potential wells of the plasma wave (as evidenced in the merging of trapped particle vortices) results in a turbulent state that gives rise to lower wavenumber electrostatic modes and ultimately disrupts SRS. Finally, Strozzi *et al.* [64] have pointed out that the primary SRS plasma wave and the sideband/BAM modes can parametrically couple, resulting in a mode with very low frequency and wavenumber.

The field has become rather “saturated with nonlinearities,” but there remains no clear evidence as to which nonlinearity, if any (or all), is the controlling saturation mechanism. This is complicated by the fact that the relative importance of a nonlinearity depends on the laser and plasma parameters, i.e., there is no universal answer. Furthermore, none of the authors above have studied the spatial dynamics of SRS, choosing instead to focus on the growth and saturation of the instability with little regard for how the instability subsequently

evolves. The goal of the work shown in these pages is to redress these issues by showing how all of the nonlinearities evolve, which ones are most relevant to the saturation, how the instability evolves after saturation, and how the instability is affected by the fact that it is spatially localized.

1.3 Dissertation Outline

Using the fully electromagnetic particle-in-cell (PIC) code OSIRIS [65, 66, 67], a wide range of computer simulations have been performed in the hope of providing a comprehensive picture of one and two-dimensional SRS in laser speckles. The exponential growth of computer power and memory have allowed for significantly longer simulations and simulations with more particles. For example, in the classic paper of Forlund *et al.* [7] from 1975 on Raman and Brillouin scattering, approximately 20,000 particles were simulated over a length of $15 c/\omega_p$ for 3000 ω_p^{-1} . By contrast, the smallest run in this dissertation simulates 2,000,000 particles over a length of $537 c/\omega_p$ for 6300 ω_p^{-1} , while the largest simulations follow $\approx 10^9$ particles for $10^5 \omega_p^{-1}$. The number of particles and the simulation length are particularly important for studying SRS in NIF-relevant parameters, as will be evidenced in later chapters.

The dissertation is organized as follows. Chapter 2 presents a theoretical framework for studying SRS and the relevant nonlinear effects, followed by an explanation of the simulation and diagnostic techniques that have been used. Chapter 3 focuses closely on a qualitative exploration of a few particular simulations to illustrate the important physics. Chapter 4 extends the simulations to a range of parameters and illustrates the commonalities and transitions in behavior as each parameter is varied. Chapter 5 studies additional nonlinearities that arise with mobile ions in 1D, as well as multi-dimensional effects that occur in

2D simulations. Chapter 6 draws the dissertation to a close with conclusions and final remarks, along with presenting results which have been seen in simulations but have not yet been thoroughly studied and may provide the impetus for future work.

CHAPTER 2

Theory and Methods

This chapter summarizes several results from the fundamental theory of SRS and nonlinear plasma waves. These theoretical results will be used later when analyzing simulation results. Following this, the simulation methods and diagnostic tools that were used to simulate SRS are described.

2.1 SRS Theory

The basic theory for SRS was studied extensively by Forslund *et al.* [6]. Only a brief summary of the results that are required for this dissertation is presented here, and the reader is referred to Forslund for a more extensive treatment.

Beginning with the standard fluid and Maxwell equations, one can derive the differential equations that describe the coupling between light waves and the plasma,

$$\left(\frac{\partial^2}{\partial t^2} + \gamma_A \frac{\partial}{\partial t} + \omega_p^2 - c^2 \nabla^2 \right) \mathbf{A} = -\frac{\omega_p^2}{N_0} n_e \mathbf{A}, \quad (2.1)$$

$$\left(\frac{\partial^2}{\partial t^2} + \gamma_p \frac{\partial}{\partial t} + \omega_p^2 - 3v_{the}^2 \nabla^2 \right) n_e = \frac{e^2 N_0}{2m_e^2 c^2} \nabla^2 (\mathbf{A} \cdot \mathbf{A}). \quad (2.2)$$

The electron density has been separated into the homogenous and inhomogenous part ($N = N_0 + n_e$), \mathbf{A} is the vector potential, ω_p is the plasma frequency ($\omega_p^2 = 4\pi N_0 e^2 / m_e$), v_{the} is the electron thermal velocity ($v_{the} = \sqrt{T_e / m_e}$), $\gamma_{A,p}$ are the light and plasma wave's phenomenological damping rates, e and m_e are the

electron's charge and mass, and c is the speed of light. As this dissertation is primarily a study of SRS, the ions are neglected here.

By treating waves as having the form $\exp[i(\omega + m\omega_0)t - i(k + mk_0)x]$, with m an integer and ω_0 and k_0 the frequency and wavenumber of the incident (pump) light wave, respectively, the previous equations are resonant when frequency and wavenumber matching conditions are met. The $m = 0$ density perturbation requires $m = \pm 1$ for the most dominant light waves, with

$$\omega_0 = \omega_1 \pm \omega_2, \quad (2.3)$$

$$k_0 = k_1 \pm k_2, \quad (2.4)$$

where the subscript 1 (2) is used for the backscattered light (plasma) wave. The plus and minus sign give two waves, the Stokes and Anti-Stokes waves, respectively. For linearly polarized light, the linear perturbations give,

$$\left(\frac{\partial^2}{\partial t^2} + \gamma_{A_0} \frac{\partial}{\partial t} + \omega_p^2 - c^2 \nabla^2 \right) \mathbf{A}_0 = -\frac{\omega_p^2}{N_0} n_e \mathbf{A}_1, \quad (2.5)$$

$$\left(\frac{\partial^2}{\partial t^2} + \gamma_{A_1} \frac{\partial}{\partial t} + \omega_p^2 - c^2 \nabla^2 \right) \mathbf{A}_1 = -\frac{\omega_p^2}{N_0} n_e \mathbf{A}_0, \quad (2.6)$$

$$\left(\frac{\partial^2}{\partial t^2} + \gamma_p \frac{\partial}{\partial t} + \omega_p^2 - 3v_{the}^2 \nabla^2 \right) n_e = \frac{e^2 N_0}{2m_e^2 c^2} \nabla^2 (\mathbf{A}_0 \cdot \mathbf{A}_1). \quad (2.7)$$

These equations can be Fourier analyzed. Solving Eqn. (2.6) for \mathbf{A}_1 and substituting the result into Eqn. (2.7), the Raman dispersion relation is found:

$$1 + \chi_e = -\frac{\chi_e k_2^2 v_{osc}^2}{4} \left[\frac{1}{\omega_+^2 - \omega_p^2 - c^2 k_+^2} + \frac{1}{\omega_-^2 - \omega_p^2 - c^2 k_-^2} \right], \quad (2.8)$$

where $\omega_{+/-}$ are for the Stokes/Anti-Stokes wave, v_{osc} is the quiver velocity of an electron due to \mathbf{A} ($v_{osc} = eA_\perp/m_e c$), and χ_e is the fluid susceptibility for electrons,

$$\chi_e = \frac{-\omega_p^2}{(\omega - i\gamma_p)^2 - 3k^2 v_{the}^2}. \quad (2.9)$$

This analysis can be straightforwardly extended into the kinetic regime [6, 8], where the kinetic susceptibility,

$$\chi_e = -\frac{1}{2(k\lambda_D)^2} Z' \left(\frac{\omega}{\sqrt{2}v_{the}k} \right), \quad (2.10)$$

takes the place of the fluid susceptibility in the dispersion relation, where Z' is the derivative of the plasma dispersion function. The dispersion relation (Eqn 2.8) with the kinetic susceptibility will be used for numerical calculations.

The Raman dispersion relation can be used to find the SRS temporal growth rate, γ_{SRS} , where $\omega = \omega_2 + i\gamma_{SRS}$ is a solution of Eqn. (2.8) for real k . By using the fluid susceptibility when the damping rates are negligible (but still in keeping with $\text{Im}[\omega] \ll \omega_p$), a relatively simple expression for the temporal growth rate may be found,

$$\gamma_0 = \frac{kv_{osc}}{4} \frac{\omega_p}{\sqrt{\omega_1\omega_2}}. \quad (2.11)$$

This will be referred to as the undamped temporal growth rate and reserved for the symbol γ_0 . The threshold condition for instability growth can be given by

$$\gamma_{SRS} > \sqrt{\gamma_p \gamma_{A1}}. \quad (2.12)$$

This expression depends on the damping rates of both daughter waves.

The damping rates are determined primarily through non-collisional Landau damping for the plasma waves and collisional damping for the light waves. The collision rate for parameters relevant to this dissertation are small. The standard Plasma Formulary expression for electron-ion collision rates [68],

$$\nu_{ei} = 2.9 \times 10^{-6} \lambda_{ei} n_e T_e^{-3/2} \text{sec}^{-1}, \quad (2.13)$$

$$\lambda_{ei} = 24 - \ln(n_e^{1/2} T_e^{-1}), \quad (2.14)$$

gives a collision rate of $6 \times 10^{11} \text{ sec}^{-1}$ for $T_e = 1 \text{ keV}$ and $n_e = 9 \times 10^{20} \text{ cm}^{-3}$. The inverse gives $\approx 2 \text{ ps}$. Given that the simulations here are run for typically 4

ps, during which time several growths and saturations of SRS can occur, the effect of electron-ion collisions will be neglected (electron-ion and electron-electron collisions could affect the kinetic damping described next by modifying the shape of the distribution function [69] or by decorrelating a particle before a bounce time, to be defined shortly). The kinetic damping rate of the plasma waves, on the other hand, can be significant. The calculated value that will be used is the solution for $\text{Im}[\omega]$ found from:

$$\epsilon = 1 + \chi_e = 0. \quad (2.15)$$

Given that γ_{A_1} will be neglected, there is no threshold value for instability growth. Nevertheless, there are different temporal growth rates depending on the ratio of γ_p/γ_0 and there are classifications of spatial-temporal growth depending on the noise source. The temporal growth rate mentioned above (γ_0) is for the homogenous (infinite) plasma where the waves grow everywhere from a noise source existing in all space for a chosen k , as opposed to growth in space from a localized seed. By choosing a real k , one finds the growth rate from the most unstable solution for $\text{Im}[\omega]$ in the Raman dispersion relation. If in addition to complex ω one allows for complex k , the instability analysis involves following k roots in the complex k -plane. The analysis is not presented here, except to mention that $\text{Im}[\omega]$ is no longer the temporal growth rate at each location in space (see Forslund *et al.* [6]).

In the spatial-temporal problem, a seed perturbation localized in space and time can grow, but as the backscattered light wave and the plasma wave in backward SRS travel in opposite directions, growth at one point in space may be outstripped by the plasma wave's damping rate or the velocity of the two waves away from each other. As the light wave is negligibly damped, the instability will appear to grow along with it (in the backwards direction) as the light wave

continues to grow and interact with plasma. SRS will grow convectively in a pulse that travels at a speed that can be determined by calculating $\partial\omega/\partial k$ from Eq. (2.8).

As the growth rate increases and/or the plasma wave's damping rate decreases, there will be a greater likelihood that an observer at a fixed point in space will not see the waves out-strip each other before dying away. Above a threshold value, SRS will grow in the absolute sense, where SRS will continue to grow at each point in space, as opposed to growing for only as long as the pulse travels past the fixed point. The threshold condition for absolute instability is:

$$\beta \equiv \frac{\gamma_p}{\gamma_0} \sqrt{\frac{v_-}{v_g}} < 2. \quad (2.16)$$

Here, v_- and v_g are the group velocities of the backscattered light and plasma waves, respectively. Figure 2.1 shows the absolute thresholds in terms of v_{osc}/c , although several contours are labelled for a 3ω laser intensity in W/cm^2 . All simulations in this dissertation are driven between $10^{14} - 10^{16} \text{ W/cm}^2$ for 3ω light with plasma parameters that lie primarily to the left of the shown contours, meaning that they are mostly below the absolute threshold.

The asymptotic temporal and spatial gains for absolute growth can be shown to be [6]:

$$\text{Im}[\omega] = -2\gamma_0 \sqrt{\frac{v_g}{v_-}} + \gamma_p, \quad (2.17)$$

$$\text{Im}[k] = \frac{\gamma_0}{\sqrt{v_- v_g}}. \quad (2.18)$$

For strong damping ($\beta \gg 2$) there is only convective gain. Under these conditions, if the noise source remains on for all time at a localized point in space, then there will be spatial gain given by

$$\text{Im}[k] = \frac{\gamma_0^2}{\gamma_p v_-}. \quad (2.19)$$

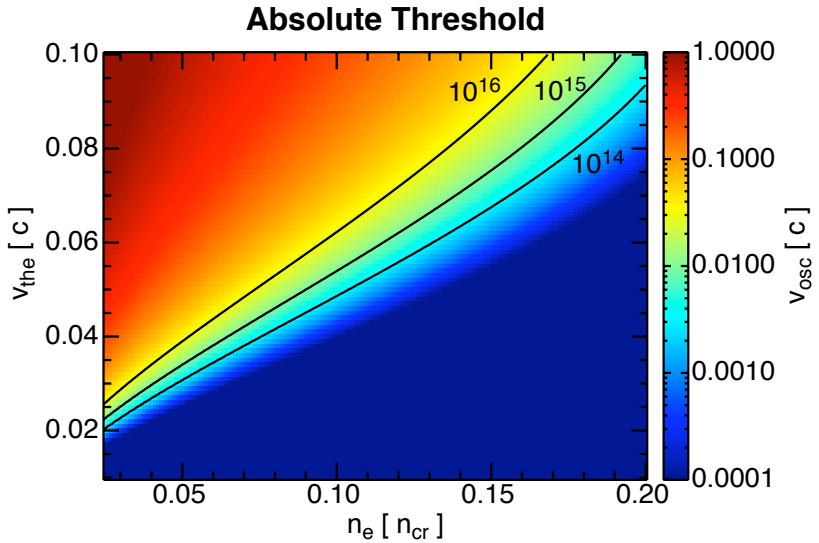


Figure 2.1: Absolute threshold of SRS as a function of density and temperature. Contours show where the intensity of 3ω laser light (in W/cm^2) satisfies the threshold condition.

This is also the rate at which a packet will get amplified as it convects backward with the scattered light near the speed of light. This will be useful later, where the effect of plasma length will be studied in terms of the convective gain length, the length required for the instability to grow by one e-folding in amplitude. The convective gain length is here defined as,

$$L_{conv} \equiv \frac{1}{\text{Im}[k]} = \frac{\gamma_p v_-}{\gamma_0^2}. \quad (2.20)$$

Most of the simulations that are studied in this dissertation are in the strongly damped regime, that is, $\gamma_p > \gamma_0$. Equivalently, most of the simulations here are below the absolute threshold.

2.2 Plasma Wave Theory

While the theory above is important to the onset and growth of SRS, the evolution of SRS is dependent on the nonlinear behavior of the plasma wave, specifically with regard to its amplitude, frequency, and damping rate. The nonlinear behavior of an electron plasma wave is a subject of fundamental interest to plasma physics. In the late 1950s and early 1960s, the maximum amplitude and frequency shift of nonlinear plasma oscillations in cold plasmas was investigated [70, 71, 72]. It was found that the oscillation amplitude was limited to the phase velocity of the wave. It was also found that even though all nonlinear oscillations contain harmonics, only relativistic mass effects lead to a (negative) frequency shift. In cold plasmas, therefore, there is no frequency shift for waves with phase velocities much less than the speed of light.

In the 1960s, nonlinear plasma waves in warm plasmas were investigated. Several authors considered the frequency shift predicted in the fluid limit using an adiabatic pressure [73, 74, 75, 76, 77, 78]. These equations also follow from the use of a waterbag distribution function and are valid when $k\lambda_D \lesssim 0.2$. The fluid frequency shift is positive and proportional to the amplitude of the wave squared. While these papers provide different expressions for the frequency shift, these differences were resolved in Ref. [76]. Furthermore, Coffey used these equations to show that the oscillation amplitude was limited to a wave amplitude where particles at the edge of the waterbag become trapped [78]. This wavebreaking limit is given by

$$\frac{eE_{coff}}{mv_\phi\omega_p} = (1 - \frac{1}{3}\beta - \frac{8}{3}\beta^{1/4} + 2\beta^{1/2})^{1/2},$$

where $\beta = 3v_{the}^2/v_\phi^2$ and v_ϕ is the wave's phase velocity.

In the fluid limit, $v_\phi \gg v_{the}$ so that there are very few particles that are

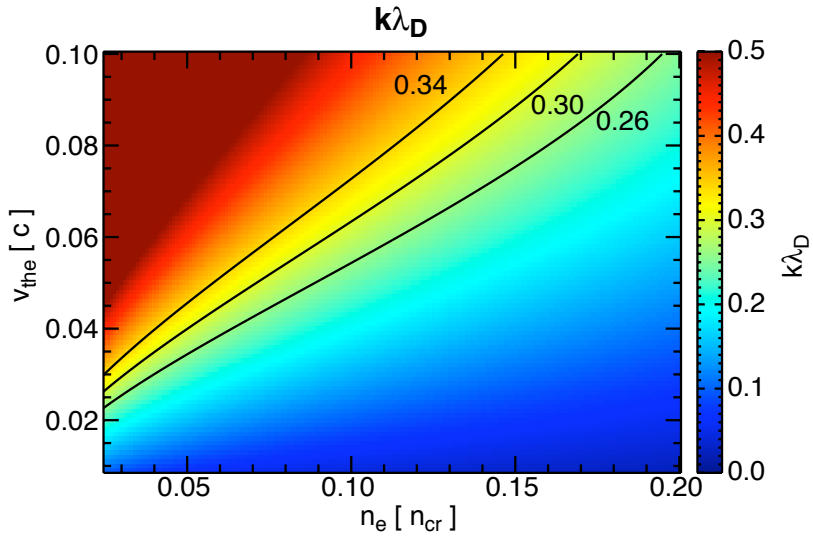


Figure 2.2: $k\lambda_D$ of the daughter plasma wave in backward SRS.

“resonant” with the wave. However, as the phase velocity decreases and v_{the}/v_ϕ increases, kinetic effects begin to play a large role in the evolution of the plasma wave. This ratio is commonly expressed as $k\lambda_D$ ($\approx v_{the}/v_\phi$), where k is the wavenumber of the plasma wave. The range of $k\lambda_D$ for the densities and temperatures shown for the absolute threshold (Figure 2.1) are shown in Figure 2.2. While the growth of SRS is dependent on the relative magnitude of γ_0 to γ_p , the behavior of the plasma wave in SRS is dependent on the relative magnitude of v_ϕ to v_{the} . All of the simulations in this dissertation lie between the contours shown ($k\lambda_D = 0.26 - 0.34$).

Particles that are travelling near the phase velocity of the plasma wave see a nearly stationary wave structure and can oscillate (bounce) in the wave’s periodic potential wells. As will be shown in the simulations here, these trapped particles play an important part in the evolution of SRS. Figure 2.3 shows a schematic picture of the orbits of trapped particles in phasespace. If the wave has a simple sinusoidal form, $E \sin kx$, deeply trapped particles oscillate in the wave with a

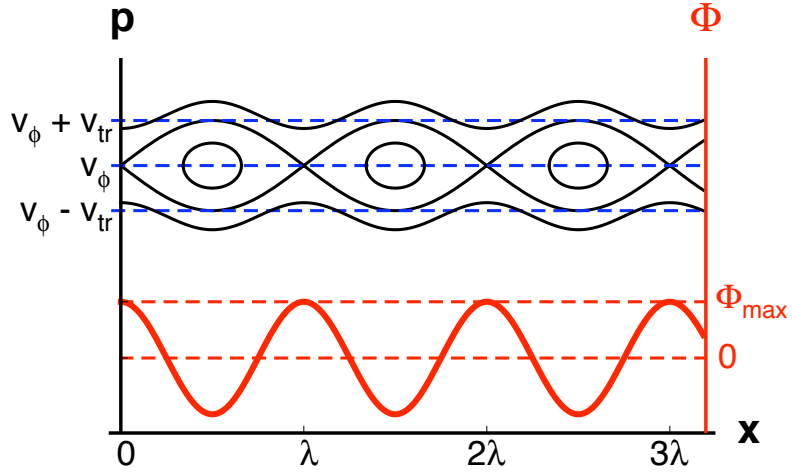


Figure 2.3: Electron momentum (black) and plasma wave potential (red) versus space in wavelengths. Electrons move along the black curves, with the closed curves representing possible trapped particle orbits as they bounce in the periodic potential.

frequency (the bounce frequency ω_B) given by the linearized force equation in the frame of the wave,

$$m\ddot{x} = -eE \sin kx \approx -eEkx, \quad (2.21)$$

$$\omega_B = \sqrt{\frac{eEk}{m}}. \quad (2.22)$$

Therefore, the time it takes for a deeply trapped particle to execute one bounce (the bounce time) is $\tau_B = 2\pi/\omega_B = 2\pi\sqrt{m/eEk}$. These potential wells will be called trapped particle buckets, or simply buckets. The range of velocities that lie within the trapped particle separatrix is the trapping width. Using conservation of energy for particles,

$$\frac{eE}{k} \cos kx + \frac{1}{2}mv^2 = \text{constant}, \quad (2.23)$$

a particle traveling along the separatrix from $(x, v) = (0, 0)$ to $(\lambda/2, v_{tr})$ gives the

trapping width,

$$v_{tr} = 2\sqrt{\frac{eE}{mk}}. \quad (2.24)$$

The use of the warm fluid equations neglects the role of trapped particles. In the pioneering work of Bernstein, Green, and Kruskal [79] it was shown that for a given traveling wave form, it is possible to find a self-consistent distribution function that includes trapped and untrapped particles. These nonlinear traveling wave solutions to the Vlasov equation are now referred to as BGK modes. In the early 1970s, the frequency and wavenumber shifts due to trapped particles were calculated by Morales and O’Neil [57]. In their work, they assumed that the wave did not contain harmonics. They found that after several bounce times for a trapped particle, the damping tends toward zero and the frequency shift reaches a steady state, negative value. Thus, they found a BGK solution for a wave without harmonics and a frequency near its linear value. Assuming the initial value problem, and assuming that the wave amplitude is constant in space (it can change in time), the frequency decreases from its linear value ω_0 , oscillating at approximately twice the bounce frequency as it asymptotically approaches,

$$\frac{\delta\omega}{\omega_0} = -1.63\sqrt{\frac{eE}{mk}} \left(\frac{\omega_p}{k}\right)^2 \left(\frac{\partial^2 f_0}{\partial v^2}\right)_{v_\phi} \left(\frac{\partial\epsilon}{\partial\omega}\right)_{\omega_0}^{-1}, \quad (2.25)$$

with the amplitude restricted to be $(eE/mk)^{1/2} \ll v_{the}^2/v_\phi$, or equivalently, $v_{osc}/v_{the} \ll (v_{the}/v_\phi)^3$. The kinetic frequency shift is proportional to the square root of the wave amplitude because the number of trapped particles depends similarly on the square root of the wave amplitude. In the early 1990s, Holloway and Dorning examined BGK-like solutions to the Vlasov equation in which the modifications to the initial distribution function are small [80].

As mentioned in Chapter 1, the nonlinear changes in the frequency and damping rate of nonlinear plasma waves have recently received renewed interest because

of their potential role in determining the saturation and threshold of SRS for laser drivers in ICF [54, 55, 42, 62, 81]. In this recent work, only the role of trapped particles and flattening of the distribution function have been considered, while the nonlinear fluid contribution from harmonics has largely been ignored. Several authors have considered the contribution of both fluid and kinetic effects, but the focus was on ion-acoustic waves ([82] and references therein). Rose and Russell looked at harmonics in the context of driven, steady state solutions to the Vlasov equation (small amplitude BGK modes) after initially assuming that the response was harmonic [81]. They found a frequency shift that was very close to that of Morales and O’Neil and is similarly valid for strictly small amplitude waves, but they found the higher harmonics to be small and did not calculate any corresponding correction to the frequency shift from them. Harmonics and their effects can become important in driven waves. The fluid (harmonic) and kinetic (trapped particle) shifts have different wave amplitude dependencies, and furthermore different signs, so to determine the relative importance of each, it is important to know the proportionality coefficients. The present author calculated the fluid frequency shift of a nonlinear plasma wave [83]; details are given in Appendix A. For the initial value problem in which the wavenumber, k , is fixed, the nonlinear modification to the dispersion relation is,

$$\omega^2 = \omega_p^2 + 3v_{the}^2k^2 \left(1 + \frac{5}{2} \frac{v_{osc}^2/v_\phi^2}{(1 - 3v_{the}^2/v_\phi^2)^2} \right), \quad (2.26)$$

where v_{osc} here is related to the first-order amplitude of the plasma wave.

All of the simulations for this dissertation are sufficiently kinetic that there is a negligible positive frequency shift from the contribution from harmonics. As will be shown later, all of the frequency shifts are actually more negative than the theoretical shift predicted from Morales and O’Neil and they do not scale with the square root of the wave amplitude times a fixed coefficient. For the purposes

of this dissertation, therefore, we will use Eq. 2.25 only as a reference point from which to make comparisons with a theoretical value of the frequency shift, with ϵ as the kinetic dielectric mentioned previously and f_0 taken to be a Maxwellian distribution function. Strictly speaking, the plasma wave amplitudes here are larger than the amplitude restriction in the theory of Morales and O’Neil, the distribution function is no longer Maxwellian by the time SRS saturates, and $k\lambda_D > 0.25$ ($v_\phi \lesssim 4v_{the}$). A more thorough theoretical treatment of nonlinear frequency shifts is left for future work.

In addition to altering the plasma wave damping rate and frequency, trapped particles can also interact with the plasma wave to produce sidebands. These plasma modes were first noticed in experiments by Wharton *et al.* [84], where the sidebands were separated in frequency from the primary plasma wave by the bounce frequency of the trapped particles. Kruer *et al.* [60] formulated a basic theory of sideband growth by treating the trapped particles as a single particle that oscillated in the wave’s potential well (a coherent bunched oscillator that interacted with the plasma wave), deriving a growth rate and dispersion relation for the sidebands. Tsunoda and Malmberg [85] presented a conceptual picture of how the trapped particles could cause sideband growth by spending more of their bounce time giving energy to, as opposed to taking energy from, sideband modes of the proper wavenumber and frequency. DeNeef [86] showed experimentally that a small test wave launched with a large-amplitude plasma wave behaved in agreement with theoretical calculations that treated the test wave as a modulation of the large wave’s amplitude and phase.

As no quantitative comparisons will be made with regard to the sidebands that are seen here, the reader is referred to the literature for further exploration. However, the modulation of the SRS plasma wave’s amplitude due to sidebands

will be evidenced in the simulations shown later. For an SRS plasma wave of frequency ω_1 and wavenumber k_1 and a sideband of frequency ω_2 and wavenumber k_2 , the modulation of the SRS plasma wave will be evidenced in a beat pattern with wavelength $2\pi/(k_1 - k_2)$ that moves at a velocity $v_{beat} = (\omega_1 - \omega_2)/(k_1 - k_2)$, a velocity that will be close to the plasma wave's group velocity. Furthermore, the amplitude of the sidebands relative to the SRS plasma wave can be inferred from the modulation. As the sidebands grow in amplitude, the modulation will become more pronounced; when the sidebands have an amplitude comparable to the SRS plasma wave, the modulation will be nearly 100%. This is of particular importance to the behavior of the trapped particles, for the beat pattern disrupts the periodicity of the SRS plasma wave's potential wells and large numbers of trapped particles can therefore move from one bucket into a neighboring bucket.

2.3 Methods

All comparisons with the theory mentioned in the previous sections utilize the equations given in Table 2.1 (in cgs units).

2.3.1 OSIRIS

SRS was simulated with the relativistic, electromagnetic particle-in-cell (PIC) code OSIRIS [65, 66, 67] in 1 and 2D, with the 1D simulations being 2D with two cells in the transverse direction. The simulation box was almost always filled everywhere with a plasma of constant density and temperature. The spatial resolution was chosen so that the cell size was on the order of an electron Debye length, and the number of particles per cell was kept at approximately 512. Both the cell size and the number of particles were varied to test for convergence in the

Table 2.1: Common parameters for studying SRS.

Theoretical Parameters		
Name	Parameter	Expression
plasma frequency	ω_p	$\sqrt{4\pi n_e e^2/m_e}$
vosc	v_{osc}	eA_\perp/mc
phase velocity	v_ϕ	ω/k
group velocity	v_g	$\begin{aligned} \partial\omega/\partial k &= -\text{Re}((\partial\epsilon/\partial k)/(\partial\epsilon/\partial\omega)) \\ &= v_\phi + 2\sqrt{2}v_{the}\text{Re}[Z'(s)/Z''(s)] \end{aligned}$
plasma wave	v_g	$\approx 3v_{the}^2/v_\phi$
light wave	v_-	c^2/v_ϕ
susceptibility	χ_e	$-(1/2k^2\lambda_D^2)Z'(\omega/\sqrt{2}kv_{the})$
temporal growth rate	γ_{SRS}	$1 + \chi_e = -(\chi_e k_2^2 v_{osc}^2/4)(\omega_-^2 - \omega_p^2 - c^2 k_-^2)^{-1}$
	γ_0	$\frac{kv_{osc}}{4} \frac{\omega_p}{\sqrt{\omega_1\omega_2}}$
absolute threshold		$\frac{\gamma_p}{\gamma_0} \sqrt{\frac{v_-}{v_g}} < 2$
absolute growth rate	γ_{abs}	$2\gamma_0 \sqrt{v_g/v_-} - \gamma_p$
convective gain length	L_g	$v_g \gamma_p / \gamma_0^2$
bounce frequency	ω_B	$\sqrt{eEk/m}$
bounce time	τ_B	$2\pi/\omega_B$
trapping width	v_{tr}	$2\sqrt{eE/mk}$
Coffey limit	E_{coff}	$\begin{aligned} \frac{eE_{coff}}{mv_\phi\omega_p} &= (1 - \frac{1}{3}\beta - \frac{8}{3}\beta^{1/4} + 2\beta^{1/2})^{1/2} \\ \beta &= 3v_{the}^2/v_\phi^2 \end{aligned}$
Landau damping rate	γ_p	$\text{Im}[\omega] : 1 + \chi_e = 0$

Table 2.2: Normalized simulation parameters.

Normalizations					
time	$\omega_0 t$	frequency	ω/ω_0	momentum	$p/m_e c$
space	$x\omega_0/c$	wavenumber	kc/ω_0	electric field	$eE/m_e c\omega_0$

study of SRS; the number of particles per cell is discussed in Appendix B. The boundary conditions were a thermal bath boundary for particles and a Lindman, open boundary [87] for the electromagnetic fields; in 2D, the transverse boundary was periodic for the electromagnetic fields.

The incident light was sent into the box via an antenna at the simulation edge, with a brief rise time of $300 1/\omega_0$ but an otherwise constant amplitude for the duration of each simulation. The length of the box is always denoted as either the “x” direction or the “1” direction. The polarization of the incident light for the 1D simulations is in the “3” (z) direction. For the 2D simulations, the plane of the box is in the x-y plane, or equivalently the 1-2 plane, with the antenna polarized in the “2” (y) direction, that is, in the plane of the simulation box. The 2D antenna produces a Gaussian pulse with focal spot-size of width W_0 , that is, $E(y) = E_{max}e^{-(y-y_c)^2/2W_0^2}$ at focus (chosen to be at the center of the box), with the transverse center of the pulse, y_c , always equidistant between 0 and the maximum y-value for the simulation.

The laser frequency ω_0 , the speed of light c , and the electron’s charge e and mass m_e are all set equal to 1, with normalizations of other variables expressed in these units. Several common quantities are shown in their normalized form in Table 2.2. When the normalized simulation units are converted to physical units, all simulations here are considered to be simulations of a laser beam with wavelength $\lambda_0 = 0.351 \mu\text{m}$. However, we emphasize that PIC simulations do

not have any assumptions regarding the absolute choice of density and laser frequency. Rather, they provide a self-similar set of results for a ratio of ω_0/ω_p . Recently, collisions have been added into the models and in this case, the value of the density and temperature does matter.

2.3.2 Parameter Space

The plasma and laser parameters that were chosen for this study were motivated by relevance to NIF and ICF, as well as being motivated by the recent simulation work mentioned in Chapter 1. The plasma parameters are chosen to have a moderate $k\lambda_D$ (≈ 0.30) in accord with those parts of the hohlraum plasma that will have the largest amount of SRS growth. The single hot spot experiments of Montgomery *et al.* [40] had an electron temperature of 700 eV, while the moderate $k\lambda_D$ region of a NIF hohlraum will have an electron temperature of approximately 3 keV [1, 88]. These set the bounds on the electron temperature in the simulations, and when considered together with $k\lambda_D = 0.26 - 0.34$, the electron densities as well.

The average laser intensity on NIF at peak power (several 10^{14} W/cm²) is expected to be below the SRS threshold, but a certain fraction of the laser beam will consist of high intensity speckles. The distribution of speckles with intensity I , given an average laser intensity of I_0 , is given by $P(I) = I_0^{-1}e^{-I/I_0}$, or for a beam that has polarization smoothing, $P(I) = 4I/I_0^2e^{-2I/I_0}$ (see Section 3.B.4 of [1]). This implies that several percent of the laser beam power will therefore be at intensities greater than $5I_0$. The laser intensity simulated here covers a range of intensities from $10^{14} - 10^{16}$ W/cm², that is, intensities ranging from the average NIF laser intensity to many times the average.

Finally, the spatial scale of the speckles is determined by the beam f /number

and laser wavelength (λ_0), with a length of $8f^2\lambda_0$ (the Rayleigh range of the lens) and a transverse size of $f\lambda_0$ for full width at half-maximum (the diffraction limited spot width for the lens) ([1], p. 370). For the $f/8$ beams on NIF with $\lambda_0 = 0.351$ nm, this gives a speckle size of $180 \mu\text{m} \times 2.8 \mu\text{m}$. A range of interaction lengths will be shown that range from $30 - 100 \mu\text{m}$.

2.3.3 Diagnostics

Many new diagnostics were written to study the behavior of SRS in these simulations. The OSIRIS code was modified to output the electric fields at every instant of time and space, with a possible interval between instants if desired. This allows for detailed plots of the temporal and spatial behavior of the plasma waves, as well as the frequencies and wavenumbers after applying an FFT to the field data. The space and time plots will primarily be shown for enveloped fields which are a linear interpolation between every local maximum of the particular field.

An important diagnostic for SRS is the instantaneous reflectivity. The reflectivity is measured at the incident edge. To eliminate the antenna signal from the transverse field, all frequencies larger than $0.8\omega_0$ were zeroed. The result was then spatially averaged over approximately one wavelength of backscattered light near the boundary, squared, and divided by the expected squared intensity of the antenna to give a percentage energy reflectivity. The reflectivity in 2D was instead measured by subtracting the known antenna signal off of the electric field. The result was squared, summed over the transverse direction, and then divided by the expected, squared, summed intensity of the antenna. Although these methods would not eliminate forward SRS light or rescatter of backward SRS (at the cells adjacent to the boundary), these other instabilities would typi-

cally grow, if at all, at locations away from the incident edge (for forward scatter, on the far edge of the simulation box) and travel away from the incident edge. Regardless, each simulation was checked for such signals for verification. This method was tested with test signals and found to be accurate to within a few percent.

Frequent use will be made of the FFT to obtain the frequency and wavenumber content of the electric fields. When looking at the frequency content as a function of time, however, or the wavenumber as a function of space, there is a fundamental limit on the resolution that may be obtained. For these two types of plots (ω vs. t and k vs. x), the Wigner transform with a Choi filter was used [89].

2.3.4 Resonance

One diagnostic is given special attention here. It was used to determine the extent to which frequency and/or wavenumber shifts detuned the SRS resonance.

The product of the pump and scattered light waves drive the electron plasma wave, as evidenced in the plasma wave equation,

$$\left(\frac{\partial^2}{\partial t^2} + \gamma_p \frac{\partial}{\partial t} + \omega_p^2 - 3v_{the}^2 \nabla^2 \right) n_e = \frac{e^2 N_0}{2m_e^2 c^2} \nabla^2 (\mathbf{A}_0 \cdot \mathbf{A}_1). \quad (2.27)$$

If the instantaneous frequencies of the three waves do not match, then the frequency of the drive on the right-hand side of the equation will not match the frequency on the left-hand side. Let us take a simple case with three waves that satisfy the frequency-matching condition. Say that the two light waves, traveling in opposite directions and driving backward SRS, are of the form,

$$\mathbf{A}_0 = a_0 \cos(\omega_0 t - k_0 x) \hat{\mathbf{z}}, \quad (2.28)$$

$$\mathbf{A}_1 = a_1 \cos(\omega_1 t + k_1 x) \hat{\mathbf{z}}. \quad (2.29)$$

Given that we are looking for variations in the longitudinal direction ($\nabla = \hat{\mathbf{x}} \partial_x$),

the driving term then has the functional form,

$$\begin{aligned}\nabla^2(\mathbf{A}_0 \cdot \mathbf{A}_1) = -\frac{a_0 a_1}{2} & ((k_0 + k_1)^2 \cos((\omega_0 - \omega_1)t - (k_0 + k_1)x) + \\ & (k_0 - k_1)^2 \cos((\omega_0 + \omega_1)t - (k_0 - k_1)x))\end{aligned}\quad (2.30)$$

Since we are looking for what resonates with the density fluctuations, $n_e = c \sin(\omega_2 t - k_2 x)$, we keep only that term in the drive that resonantly drives the plasma wave at $\omega_2 = \omega_0 - \omega_1$ and $k_2 = k_0 + k_1$, namely,

$$\nabla^2(\mathbf{A}_0 \cdot \mathbf{A}_1) = -\frac{a_0 a_1 (k_0 + k_1)^2}{2} (\cos((\omega_0 - \omega_1)t - (k_0 + k_1)x)) \quad (2.31)$$

For a driven wave at resonance, the oscillator lags the driver by 90 degrees. The plasma wave therefore has the functional form,

$$n_e \propto -\sin((\omega_0 - \omega_1)t - (k_0 + k_1)x).$$

Another way of looking at this is via the ponderomotive force that drives the density fluctuation, that is,

$$\mathbf{F}_p \propto -\nabla(\mathbf{A}_0 \cdot \mathbf{A}_1) \quad (2.32)$$

$$\propto -\hat{\mathbf{x}} \partial_x (a_0 a_1 (\cos(\omega_0 t - k_0 x) \cos(\omega_1 t + k_1 x))). \quad (2.33)$$

By again only considering the resonant term (or by averaging out the fast frequency component at $\omega_0 + \omega_1$),

$$F_p \propto -\frac{a_0 a_1 (k_0 + k_1)}{2} (\sin((\omega_0 - \omega_1)t - (k_0 + k_1)x)).$$

This force pushes electrons from low density regions to high density regions. It may also be noted that it is in phase with the density fluctuation, meaning that $F_p \propto -\sin$ reinforces a density perturbation of the form $n_e \propto -\sin$. We note that when damping, exponential growth, and frequency shifts arise, it is more complicated.

The E-field is what is readily available from the simulations. If we look instead at the E-field of the waves,

$$\mathbf{E}_0 = -\frac{1}{c} \partial_t \mathbf{A}_0 = \frac{a_0 \omega_0}{c} \sin(\omega_0 t - k_0 x) \hat{\mathbf{z}} \quad (2.34)$$

$$\mathbf{E}_1 = -\frac{1}{c} \partial_t \mathbf{A}_1 = \frac{a_1 \omega_1}{c} \sin(\omega_1 t + k_1 x) \hat{\mathbf{z}} \quad (2.35)$$

By taking the derivative of the product and averaging out the high frequency component, the functional form of the ponderomotive driver is recovered, that is,

$$\partial_x (\mathbf{E}_0 \cdot \mathbf{E}_1) = \frac{a_0 a_1 \omega_0 \omega_1 (k_0 + k_1)}{2c^2} \sin((\omega_0 - \omega_1)t - (k_0 + k_1)x) \quad (2.36)$$

$$\propto -F_p \quad (2.37)$$

$$\propto -n_e \quad (2.38)$$

$$\propto \partial_x E_2, \quad (2.39)$$

where E_2 is the longitudinal E-field of the density fluctuation through the use of Gauss' Law,

$$\nabla \cdot \mathbf{E}_2 = -4\pi e n_e,$$

where the background ion and electron densities cancel and just the density fluctuation of the electron plasma wave remains. The relative phases for several of the afore-mentioned terms are shown schematically in Figure 2.4 for densities, fields, and vector potentials of arbitrary amplitude.

When a harmonic oscillator is driven off-resonance or a nonlinear frequency shift is included, then the drive and the response develop an additional phase shift. When the phase shift is $\pi/2$, growth ceases. For larger phase shifts, the response decreases in amplitude and energy is transferred back to the drive from the response.

The key result is that to lowest order we may ascertain whether SRS is being resonantly driven by multiplying $\partial_x (\mathbf{E}_0 \cdot \mathbf{E}_1)$ by $\partial_x E_2$. The product should be

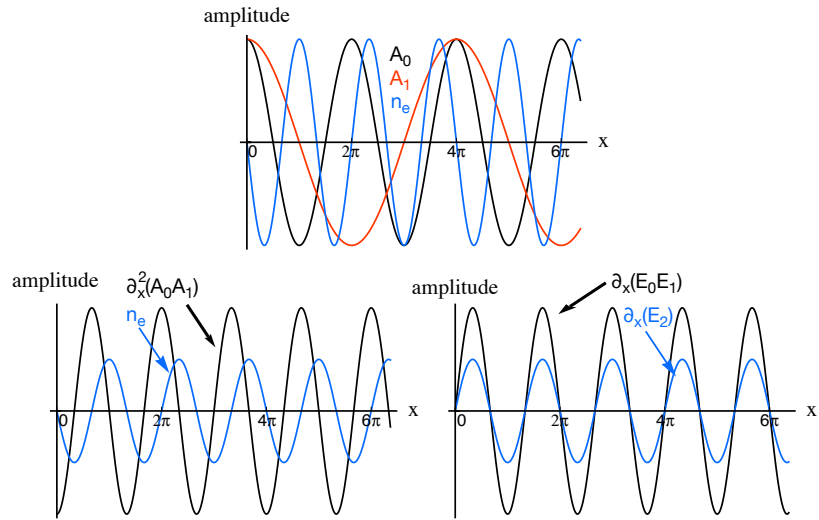


Figure 2.4: Conceptual picture of SRS waves and drivers. The relative amplitudes are arbitrary.

positive, provided that the waves are in phase. If it is negative, that will reveal that the instability is no longer undergoing “resonant” growth, but rather is being stabilized. A frequency shift, for example, will cause this product to swing from positive to negative (and back again at a rate dependent on the shift). This diagnostic will be used in Chapters 3 and 4 when various saturation mechanisms are compared.

CHAPTER 3

1D fixed ion simulations of SRS

3.1 Introduction

A complete model of the nonlinear behavior of SRS for NIF-relevant parameters must account for the simultaneous presence and interaction of a range of nonlinearities. As pointed out in the first chapter, previous authors have each focused on primarily one nonlinearity in their analyses of SRS simulations. The intricate, highly nonlinear behavior of SRS makes it difficult to conclusively establish whether a nonlinear effect is the cause of SRS saturation or whether it is merely present while another nonlinearity saturates SRS. The effectiveness of one nonlinearity over another in the saturation and evolution of SRS should be established, and any causal relationships between the various nonlinearities should be understood.

This chapter examines four particular simulations. Given the complex behavior of SRS, the quantitative exploration of SRS across a range of parameters is delayed until the next chapter. A more complete comparison of the onset thresholds, growth rates, wave magnitudes, frequency shifts, packet effects, recurrence rates, and reflectivities will be presented there. The aim of this chapter is to introduce and examine each nonlinearity that arises in the simulations of SRS in the context of examining the evolution of SRS in particular simulations considered individually. In so doing, various types of plots that will be used in

Chapter 4 are also introduced. These simulations will be examined in depth to present a qualitative picture of SRS before the quantitative results across a range of parameters are presented in the following chapter.

A coherent presentation of SRS behavior for these simulations is complicated by the simultaneous presence of several nonlinearities. Each simulation will be presented in roughly the same manner. First, the growth of SRS will be presented, with a focus on the spatial and temporal growth of the plasma waves. Secondly, the frequencies and wavenumbers of the plasma modes will be presented. The total frequency and wavenumber spectrum will be shown first, after which the temporal and spatial behavior of the frequencies and wavenumbers will be shown. The amplitudes of the plasma waves, sidebands, backscattered light, and incident light will then be shown during the first burst of SRS. In comparison with the timing of the frequency and wavenumber shifts, the sideband amplitudes, and the amplitudes of the light waves, conclusions will be drawn about the saturation of the first burst. Following this, the electron phasespace evolution before and after saturation will be shown. Finally, the convection of plasma waves and SRS recurrence will be studied as the system evolves after the first burst of SRS.

The first simulation that will be examined, Case I, was chosen in correspondence with the simulation parameters of Vu *et al.* [54] and Brunner and Valeo [59]. They argued, respectively, that the nonlinear frequency shift of the plasma wave detunes the instability and that sidebands play a potentially energetically significant role in SRS. The last simulation of this chapter, Case IV, is relevant to the simulation parameters of Yin *et al.* [61, 62] and Strozzi *et al.* [64] (as well as the single laser hot-spot experimental parameters of Montgomery *et al.* [40]). Yin *et al.* suggested that beam acoustic modes (BAMs) were important for recurrences of the SRS bursts, while Strozzi pointed out that the BAMs could

themselves decay via electron Thompson scattering.

Intermediate between these two Cases will be the second and third simulations of the chapter, Cases 1-30 and 3-30. The parameters of these two simulations were chosen to probe an intermediate range between Cases I and IV in terms of laser intensity and $k\lambda_D$. Compared to each other, the simulations are identical save for their electron temperature and density (while keeping $k\lambda_D$ fixed). The parameters are presented shortly, but these simulations have $k\lambda_D = 0.30$ with temperatures of 1 and 3 keV, so they are labelled as Cases 1-30 and 3-30, respectively. Cases 1-30 and 3-30, in addition to being intermediate between Cases I and IV, also serve as a first illustration of the difference between the NIF-relevant electron temperature of 3 keV and the slightly lower temperature of 1 keV, a difference which will be emphasized in the following chapter. Cases I and IV both have an electron temperature that is lower than the expected electron temperature for ICF on NIF.

While Cases I and IV provide for a comparison against previously published simulations, Cases 1-30 and 3-30 form the primary basis for this work's comprehensive picture of SRS. Case I will be shown to have small frequency and wavenumber shifts, with only one burst of SRS and pump depletion playing a significant role in SRS saturation. Case IV will be shown to have very large frequency and wavenumber shifts, with multiple bursts of SRS and frequency shifts as the saturation mechanism. Cases 1-30 and 3-30 will be shown to saturate via both of these two saturation mechanisms, frequency shift detuning and pump depletion respectively. In all Cases, sidebands only grow significantly after saturation. The SRS plasma waves convect as a packet after saturation, moving with an apparent speed that is faster than the group velocity due to an etching of the rear edge of the packet [90]. Recurrence will be shown to be due to two effects.

First, SRS continues to occur in convecting plasma packets. This backscattered light beats with the pump between the rear of the packet and where the laser enters the plasma. This results in driven plasma wave growth, saturation, and decay with a periodicity dependent on the nonlinear frequency shift. Secondly, SRS can grow anew in the region left behind by the convecting packets after the packets have convected a sufficient distance for convective growth to recur.

3.2 Parameters

All of the simulations are normalized against the NIF-relevant 3ω light frequency with the laser wavelength $\lambda_0 = 351$ nm. They all had fixed ions to focus solely on SRS without the additional complication of ion waves, and they were run to a maximum time of $\omega_0 t = 20,000$, or equivalently 4 ps for 3ω light. The specific parameters are shown in Table 3.1 and listed below.

For Case I, the electron temperature is $T_e = 1.5$ keV ($v_{the}/c = 0.054$), the electron density is $n/n_{cr} = 0.10$, and the simulation length is $100 \mu\text{m}$ (normalized length = $1790 c/\omega_0$). The laser intensity is $I_0 = 5.4 \times 10^{14} \text{ W/cm}^2$ ($v_{osc}/c = 0.007$). 32768 cells were used, with 4096 particles per cell (the large number of cells and particles in this particular Case is used to clearly show the evolution of electron phasespace). For backward SRS, the plasma wave has a wavenumber $k_2 c/\omega_0 = 1.52$ and frequency $\omega_2/\omega_0 = 0.35$, with a phase velocity $v_\phi/c = 0.23$, group velocity $v_g/c = 0.05$, and $k_2 \lambda_D = 0.26$.

For Cases 1-30 and 3-30, the simulation length is $100 \mu\text{m}$ (normalized length = $1790 c/\omega_0$). The laser intensity is $I_0 = 1.5 \times 10^{15} \text{ W/cm}^2$ ($v_{osc}/c = 0.0116$). 8192 cells were used, with 512 particles per cell. For Case 1-30 (3-30), the electron temperature is $T_e = 1 \text{ keV}$ (3 keV) with a corresponding $v_{the}/c = 0.0442$ (0.0766).

Table 3.1: Simulation Parameters for Chapter 3. The conversion to physical units uses $\lambda_0 = 0.351 \mu\text{m}$.

Parameter	Case I	Case 1-30	Case 3-30	Case IV
$k\lambda_D$ (backward SRS)	0.26	0.30	0.30	0.34
I_0 (W/cm ²)	5.4×10^{14}	1.5×10^{15}	1.5×10^{15}	1.0×10^{16}
length (μm)	100	100	100	60
T_e (keV)	1.5	1.0	3.0	0.7
v_{the}/c	0.054	0.0442	0.0766	0.037
n/n_{cr}	0.10	0.059	0.128	0.036
v_{osc}/c	0.007	0.0116	0.0116	0.030
length (c/ω_0)	1790	1790	1790	1074
ω_2/ω_0	0.35	0.28	0.41	0.23
$k_2 c/\omega_0$	1.52	1.65	1.40	1.73
v_ϕ/c	0.23	0.17	0.29	0.13
v_g/c	0.05	0.051	0.088	0.04
no. of cells	32768	8192	8192	4915
particles per cell	4096	512	512	512
β	2.6	5.8	4.9	4.8

The electron density was then chosen to give $k\lambda_D = 0.30$. Thus, for Case 1-30 (3-30) the electron density was $n/n_{cr} = 0.059$ (0.128). For backward SRS, the plasma wave has a wavenumber $k_2c/\omega_0 = 1.65$ (1.40) and frequency $\omega/\omega_0 = 0.28$ (0.41), with a phase velocity $v_\phi/c = 0.17$ (0.29) and group velocity $v_g/c = 0.051$ (0.088).

For comparison with v_{the} and ω_p as the normalizing parameters instead of c and ω_0 , the parameters would be as follows. Case 1-30 (3-30) had a simulation length of $L = 8360(9840)v_{the}/\omega_p$, $kv_{the}/\omega_p = 0.30$ (0.30), $\omega/\omega_p = 1.15$ (1.15), $v_\phi/v_{the} = 3.8$ (3.8), and $v_g/v_{the} = 1.15$ (1.15). In addition, the normalized laser intensity was $v_{osc}/v_{the} = 0.26$ (0.15). From these, it can be seen that while the normalized frequencies, wavenumbers, and velocities are similar between the two cases, Case 1-30 has a slightly shorter length in terms of Debye lengths and is also more strongly driven relative to v_{the} .

Finally, SRS is most strongly driven in Case IV, as well as being more kinetic with $k\lambda_D = 0.34$. The electron temperature is $T_e = 0.7$ keV ($v_{the}/c = 0.037$), the electron density is $n/n_{cr} = 0.036$, and the simulation length is 60 μm (90 μm for 2ω laser light, normalized length = 1074 c/ω_0). The laser intensity is $I_0 = 4.4 \times 10^{15}$ (1×10^{16}) W/cm² for $2\omega_0$ ($3\omega_0$) light ($v_{osc}/c = 0.030$). 4915 cells were used, with 512 particles per cell. For backward SRS, the plasma wave has a wavenumber $k_2c/\omega_0 = 1.73$ and frequency $\omega_2/\omega_0 = 0.23$, with a phase velocity $v_\phi/c = 0.13$, group velocity $v_g/c = 0.04$, and $k_2\lambda_D = 0.34$.

3.3 Case I

The parameters of Case I have been simulated by Vu *et al.* and Brunner and Valeo, as mentioned previously. Their work focused on frequency detuning and

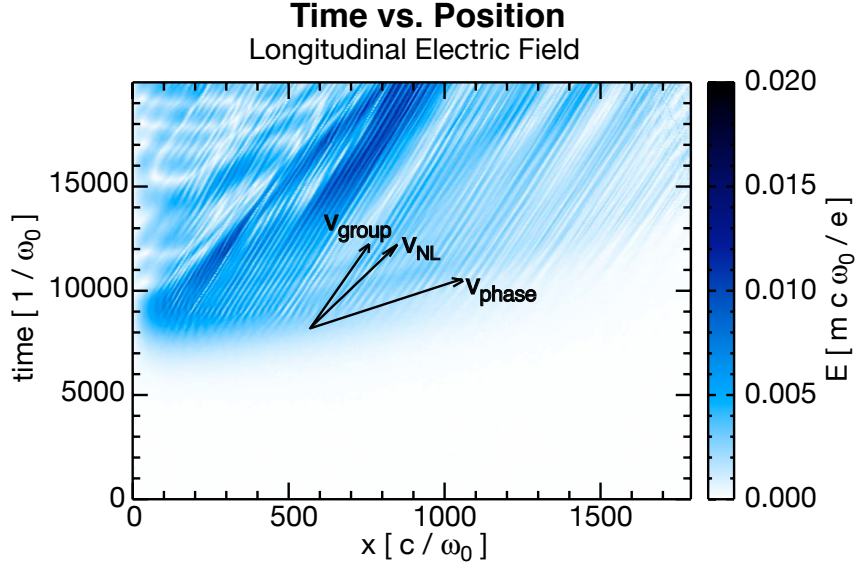


Figure 3.1: Spatial profile of the E1-Field during SRS growth for Case I.

sidebands. This section will conclude that (for this particular case) pump depletion plays a significant role in the saturation with phase detuning eventually causing the amplitude of the reflected light (and the plasma wave) to decrease. Sidebands do not saturate the instability. The sidebands and the shifts in frequency and wavenumber affect the evolution of the instability after saturation. In particular, the periodicity of reflected light will be correlated with the frequency shift and the evolution of electron phasespace will be correlated with the sidebands.

Figure 3.1 shows the spatio-temporal evolution of the plasma waves over the entire simulation. Plotted here is the enveloped longitudinal E-field (E1-field). The laser enters from the left edge of the simulation box ($x\omega_0/c = 0$) and, after a rise time of $\omega_0 t = 300$, continuously drives the system. At approximately $\omega_0 t = 5000$, SRS starts growing from noise (of RMS amplitude $eE/mc\omega_0 \approx 6 \times 10^{-5}$), and by approximately $\omega_0 t = 9000$, SRS has saturated. The point of maximum

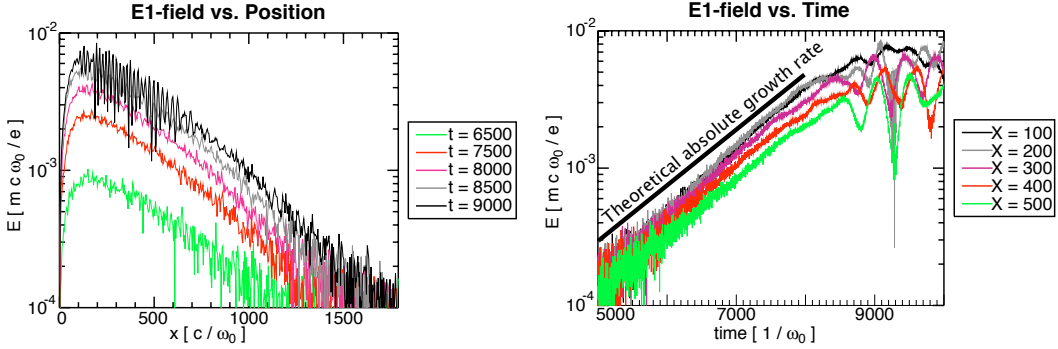


Figure 3.2: Plasma wave growth during the initial burst of SRS for Case I. The enveloped E1-field is plotted at a sequence of times over the length of the simulation (left) and a sequence of spatial points over $\omega_0 t = 5000 - 10000$ (right).

instability growth is localized in space and the plasma waves form a plasma wave packet. After the instability saturates and the plasma waves stop growing, they convect as a packet through the box. The plasma waves' wavefronts travel at the phase velocity. The plasma packet convects through the system at a packet velocity (marked as v_{NL}) intermediate between the plasma wave's group and phase velocities. The packet appears to move faster than the group velocity because the rear edge of the packet is etched away as new particles continually become trapped at the packet edge [90]. This velocity will be expanded upon in the next chapter. Finally, there is also a periodic spatial modulation that moves at a velocity close to the group velocity. As will be shown later, this modulation is due to sidebands that modulate the E1-field of the SRS plasma wave.

The theory of Forslund *et al.* [6] predicts that SRS is below the absolute threshold for Case I, albeit only slightly ($\beta \approx 3$, where the linear Landau damping rate is used). Figure 3.2 shows the spatial and temporal growth of the first burst of SRS. The left plot shows the enveloped E1-field in space at a sequence of times during growth, while the right plot shows the temporal growth at a sequence

of spatial points. For comparison, the theoretical absolute growth rate is also plotted as a solid black line in the temporal plot, where the temporal absolute growth is taken to be $2\gamma_0\sqrt{v_g/v_-}$ and the damping rate contribution has been neglected (γ_0 is the temporal growth rate and $v_g(v_-)$ is the plasma (backscattered light) wave's group velocity, see Chapter 2). There is good agreement between the temporal growth of the plasma waves and the theoretical line (we will discuss why shortly). The spatial plot shows growth in time at each spatial point, that is, SRS is growing like an absolute instability as opposed to a convective instability. The location of the peak amplitude of SRS remains fixed in space. Furthermore, each spatial point in the plot is growing at approximately the same temporal growth rate, in close correspondence with the absolute growth rate. Strictly speaking, this is true for the points that are spatially close to the peak, with the growth rate decreasing slightly as the distance from the peak growth point increases.

The instability can approach absolute-like behavior, even though it is below the absolute threshold, because the plasma wave damping rate can be altered by trapped particles. In the inflation theory of Vu *et al.* [58], the Landau damping rate can be suppressed enough for SRS to transition from the strongly damped to weakly damped convective regimes. Although it was not addressed in their work, it is also possible to transition to the absolute regime. The trapped particle behavior during SRS growth is shown in Figure 3.3, the electron phasespace during the first burst of SRS. The spatial window ($x\omega_0/c = 300 - 400$) is near the region of peak growth and has been reduced from the whole plasma length in order to show the wavelength scale. The circular structures correspond to particles that have been trapped in the plasma wave's potential, and they will be referred to as the trapped particle buckets, or more simply as buckets. At $\omega_0 t = 6000$, the plasma wave amplitude is $eE/mc\omega_0 \approx 0.0005$ with a corresponding bounce time $\tau_b \approx 230\omega_0^{-1}$ and trapping width of $v_{tr} \approx 0.04c$. This trapping width corresponds

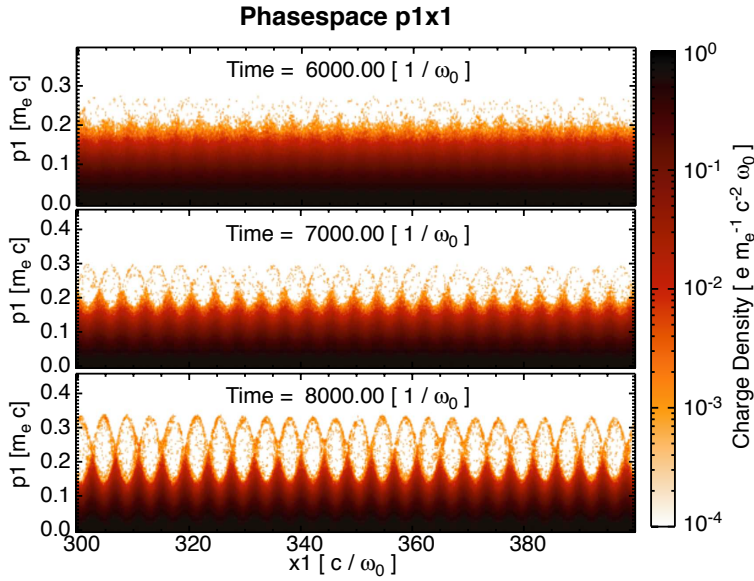


Figure 3.3: Electron phasespace during initial SRS growth for Case I.

precisely to the height of the buckets above the phase velocity, $v = 0.27c$ (here $v_\phi = 0.23c$). By $\omega_0 t = 8000$, the amplitude of the plasma wave has increased to $eE/mc\omega_0 \approx 0.004$, with $\tau_b \approx 80\omega_0^{-1}$ and $v_{tr} \approx 0.1c$. This trapping width also corresponds with the trapping width seen in phasespace. As a side note, a particle traveling at v_ϕ will travel $x\omega_0/c = 230$, or twice the window size, in a time of $\omega_0 t = 1000$. Within the elapsed time of $\omega_0 t = 2000$ between the three frames shown in the figure, the trapped particles will have bounced at least 8 times (conservatively taking the longest bounce time at $\omega_0 t = 6000$). The damping rate of a plasma wave will change dramatically over the first couple bounce periods of the trapped particles. Since the plasma wave is continually being driven to larger amplitudes, the asymptotic decrease to zero damping may not apply, but these plots, and the corresponding number of bounce periods, indicate that the damping rate of the plasma wave is different from the linear Landau value as the SRS instability is undergoing growth.

The electrostatic modes that are present during SRS growth and saturation are plotted in Figure 3.4, where the Fourier transform of the E1-field in both space and time is shown (the transform is taken over the entire spatial length of the simulation and over a time window of $\omega_0 t = 7000\text{-}9500$, that is, surrounding the time of saturation). The linear dispersion of plasma modes, $\omega^2 \approx \omega_p^2 + 3k^2 v_{the}^2$, appears at low levels. The SRS plasma wave is present at $(\omega/\omega_0, kc/\omega_0)$ of $(0.35, 1.5)$, and it is surrounded by sidebands over a range of close frequencies and wavenumbers. The lower-wavenumber sidebands are stronger than those at higher wavenumbers, with the strongest sidebands occurring around $(0.33, 1.2)$. A few more features are also present. A weak signature of the phase velocity is evident as a streak from $(0, 0)$ to the plasma wave signal at $(0.35, 1.5)$, labelled on the plot as v_2 . There is a very low frequency signature at $(0.015, 0.4)$ labelled as v_{beat} – this matches with the frequency and wavenumber difference between the SRS plasma wave and the sidebands. Finally, there is a weak beam-like velocity extending from $(0, 0)$ toward $(0.30, 0.8)$, labelled as v_1 . This beam-like velocity, with $\Delta\omega/\Delta k = 0.30/0.8 = 0.38c$, corresponds to the beam-like behavior of the trapped particles streaming between trapped particle buckets, as will be shown shortly. The beam velocity ($\approx 0.38c$) corresponds to an artificial boundary between lower velocities, where the sideband behavior is supported, and higher velocities at which no sideband modes exist.

The bottom two plots of Figure 3.4 show magnified pictures of the frequency and wavenumber shifts surrounding the primary SRS mode. The shifts are relatively small, and as the frequency and wavenumber shifts are intertwined, the shifts show up as streaks. The SRS plasma wave mode streaks away from the linear dispersion curve in several ways (shown as arrows with matching slopes). First, the bulk of the plasma wave packet shifts negatively in frequency and negatively in wavenumber (shift 1). This streak appears to line up closely with the

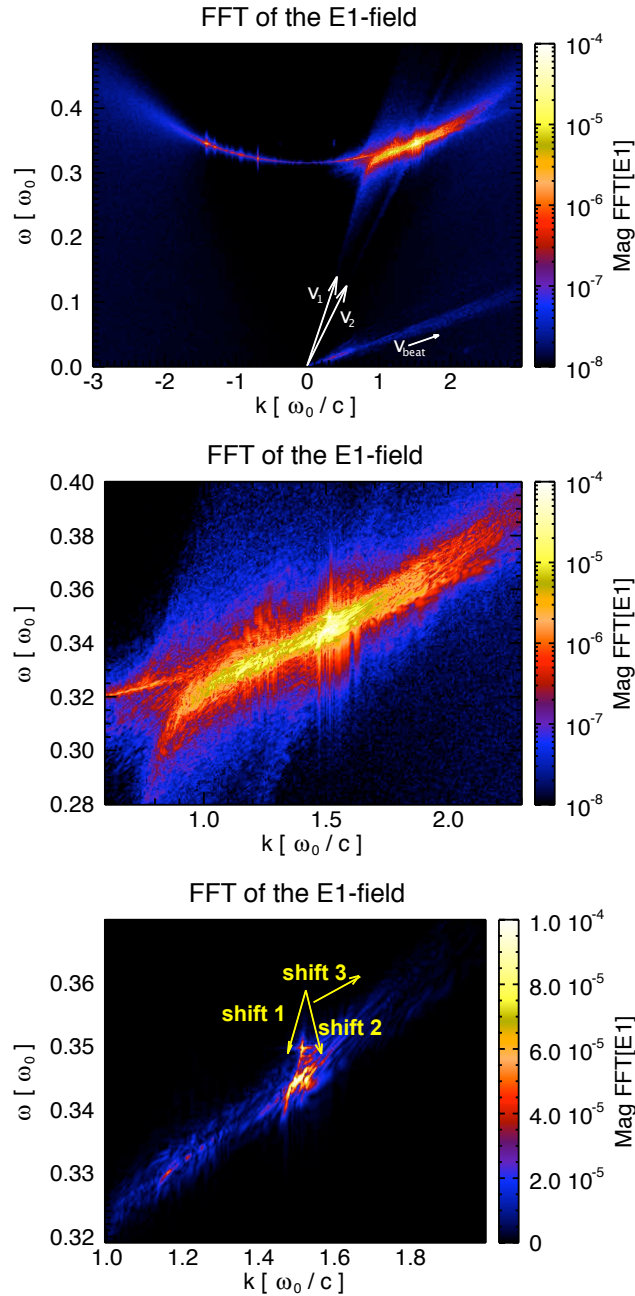


Figure 3.4: Frequency-wavenumber space of the E1-field for Case I. Top and middle plots have logarithmic scales for the magnitude as opposed to the bottom plot which has a linear scale. The ω and k scales are magnified in going from top to bottom.

phase velocity (v_2). Secondly, there is a negative shift in frequency and a slightly positive shift in wavenumber (shift 2). This is due to the continued resonance of the plasma wave with a scattered light wave. If frequency and wavenumber matching are to be maintained in the SRS resonance, a frequency down-shifted plasma wave will resonate with a frequency up-shifted scattered light wave. The scattered light wave can remain on its dispersion curve by also shifting negatively in wavenumber; by wavenumber matching, the plasma wave shifts positively in wavenumber. In Figure 3.4, streaks 1 and 2 are not clearly distinguishable, as the streaks lie so closely together, but this behavior will be clearer in later plots, as well as later simulations with larger shifts. Finally, the tail edge of the plasma packet will be shown to have a negligible frequency shift and a positive wavenumber shift. This corresponds to shift 3, with streaking from $kc/\omega_0 = 1.5$ to 1.7 and frequencies similar to the original plasma wave frequency.

To justify the explanation of the frequency and wavenumber streak labelled “shift 2,” Figure 3.5 shows the light (curve 1) and plasma wave (curve 3) dispersion relations, along with curve 2 that matches the locus of points that frequency match with the beat between the laser (ω_0, k_0) and all other points on the light-wave dispersion relation (ω_1, k_1). With $\omega_2 = \omega_0 - \omega_1$, $k_2 = k_0 - k_1$, and $\omega_{0,1}^2 = \omega_p^2 + c^2 k_{0,1}^2$, we have,

$$\omega_2 = \omega_0 - \sqrt{\omega_p^2 + (k_0 - k_2)^2}. \quad (3.1)$$

Curve 2 is color-coded in correspondence with the matching ω_1 and k_1 along curve 1, and the normal points for backward and forward SRS correspond to the points where curve 2 intersects with the plasma dispersion curve. Backward SRS corresponds to the intersection of curve 2 with the plasma dispersion relation at the point shown by the large black arrow. The other intersection corresponds to forward scatter. “Shift 2” corresponds to those frequency and wavenumber-

Matching modes in frequency and wavenumber

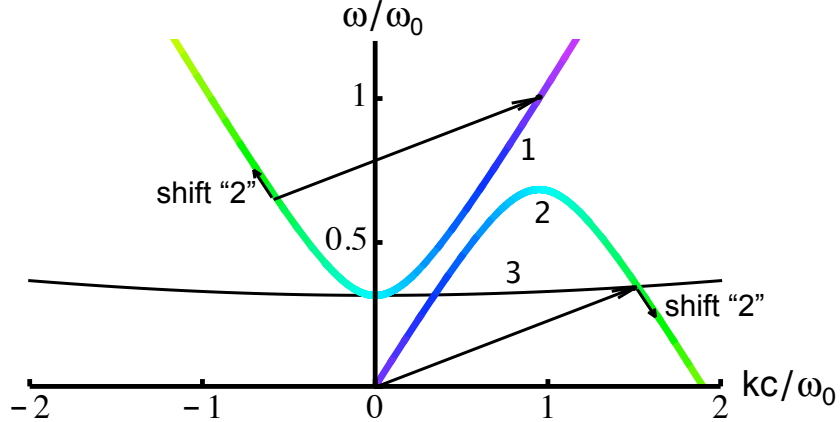


Figure 3.5: The Bohm-Gross plasma wave dispersion curve (3), the light wave dispersion curve (1), and the potential plasma modes that satisfy ω and k matching (2) are shown, color-matched where the matched modes lie.

shifted plasma waves that can satisfy the matching conditions with scattered light waves that lie along curve 1. The “shift 2” of Figure 3.5 is in direct correspondence with the “shift 2” of Figure 3.4.

Figure 3.6 shows both the wavenumber and frequency content of the E1-field as a function of space for three times close to SRS saturation. The frequency (bottom) is obtained as a Fourier transform of the field centered at the time shown, with a temporal window of $2000 \omega_0^{-1}$. The wavenumber (top) is obtained as a Wigner transform of the field, with a Choi filter. The sequence of plots shows the evolution of the wavenumber and frequency shifts in the plasma wave packet. The magnitude of the shifts are very small relative to the primary values. The tail of the packet (toward $x\omega_0/c = 0$) shows the increase in wavenumber and negligible shift in frequency. Further into the packet, the wavenumber shift is negligible while the frequency shifts negatively.

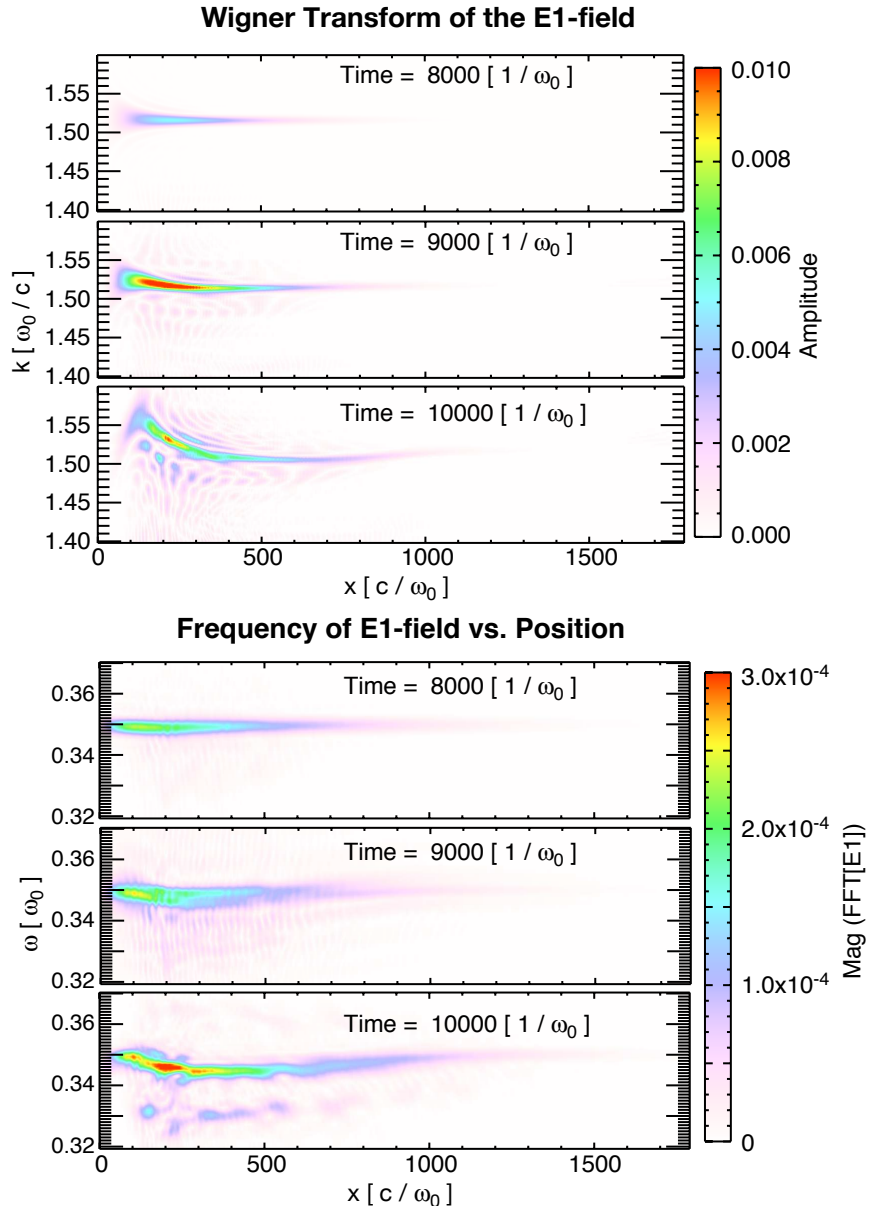


Figure 3.6: Spatial profile of the frequency (bottom) and wavenumber (top) content of the E1-field for Case I.

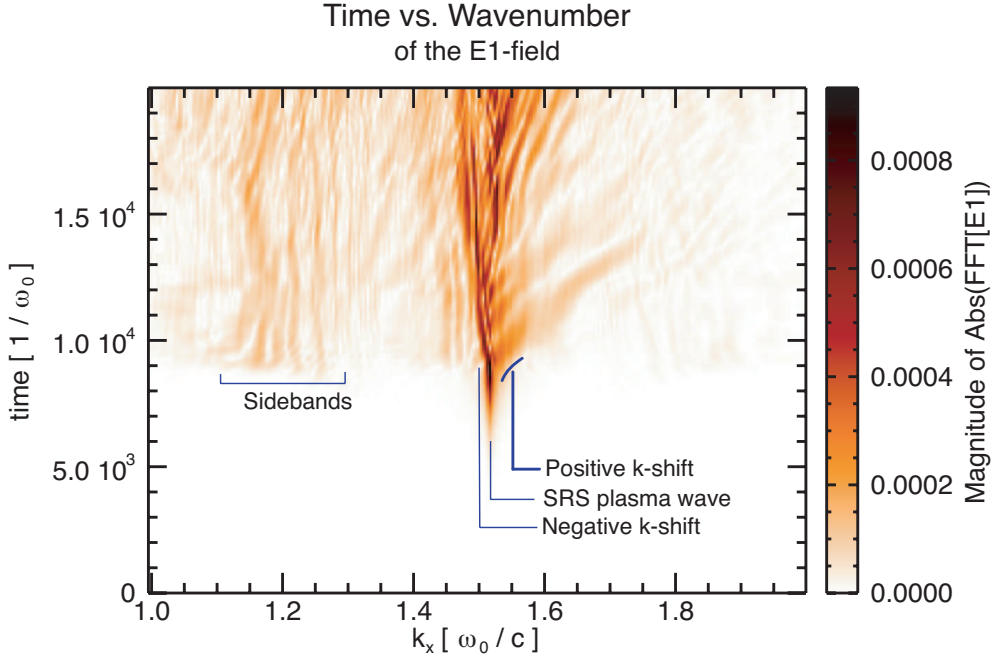


Figure 3.7: Wavenumber vs. time for the E1-field of Case I.

While theoretical analyses such as that of Morales and O’Neil [57] have investigated frequency shifts in the context of an initial value problem, the spatial-temporal growth is more complex here, with shifts in both wavenumber and frequency (shifts in the plasma wave’s wavenumber have not been noted in previous publications analyzing SRS simulations). During the initial growth of SRS, the primary mode of the E1-field is at $kc/\omega_0 = 1.52$. Around the time of saturation, two wavenumber shifts develop. The most evident shift is the positive k -shift at the tail of the plasma wave packet. A weak shift towards lower wavenumber is present in the bulk of the plasma wave packet. While it is difficult to discern in Figure 3.6, the shift is evident in Figure 3.7, where the temporal evolution of the wavenumber of the E1-field is plotted. The primary SRS plasma wave is at 1.52, and the wavenumber shift is now clearer at $\omega_0 t \approx 9000$. The bulk shift corresponds to the negative k -shift, while the tail shifts toward positive k look

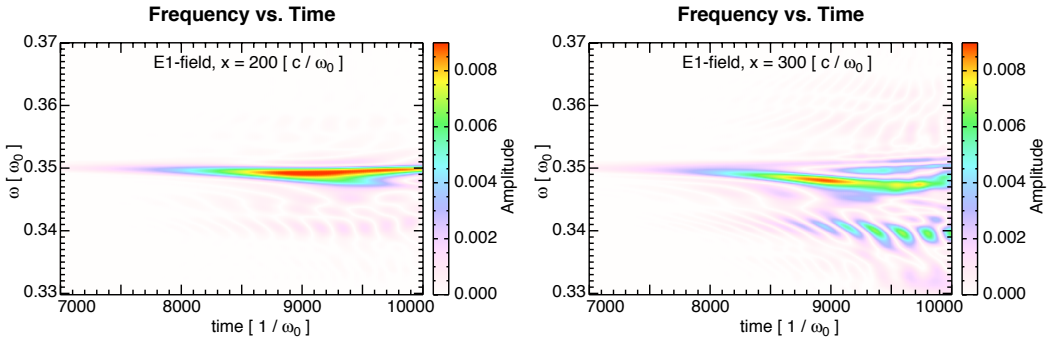


Figure 3.8: Temporal evolution of the frequency content of the E1-field for Case I.

like wisps off the primary wavenumber mode. This figure also shows the sidebands, predominantly at $kc/\omega_0 \approx 1.2$ and 1.8 . The lower wavenumber sidebands are much stronger than the higher wavenumber sidebands. This was explained in Brunner and Valeo as due to the stronger Landau damping of the higher- k sidebands [59]. The sidebands have their peak growth at approximately the same time as the wavenumber shift, when a swath of sideband modes are seen as opposed to just one dominant sideband mode. Rather than growing exponentially as SRS grows, this sudden swath of sideband modes grows sharply as SRS is saturating. In addition, there is a broad spectrum of k 's outside the dominant wavenumbers of the sidebands.

The temporal evolution of the frequency is shown in Figure 3.8, where the Wigner transform of the E1-field is plotted at two spatial points close to the peak of SRS growth, $x\omega_0/c = 200$ and 300 . Frequency shifts have been posited as a cause of SRS saturation, and in these plots, it is seen that the frequency for both points begins to shift after $\omega_0 t = 8500$. If saturation were due to the maximum nonlinear shift ($\Delta\omega/\omega_0 \approx 0.004$), the time to detune would be on the order of $\pi/\Delta\omega \approx 790\omega_0^{-1}$. These numbers will be compared shortly with the time

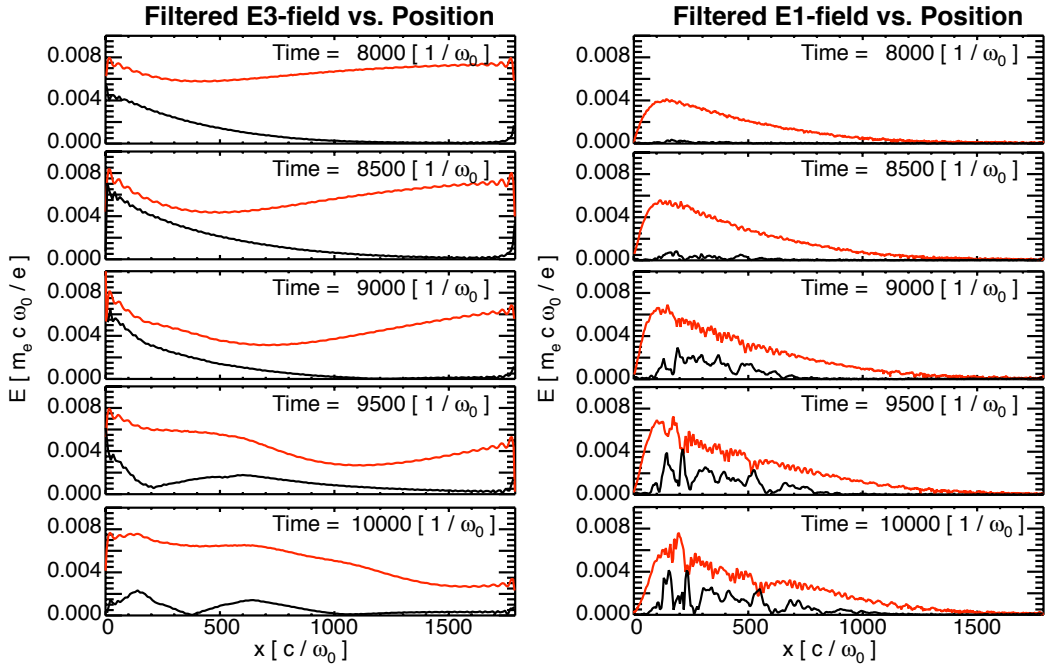


Figure 3.9: High/low-pass filtered E1 and E3 fields during SRS growth for Case I. The incident (red) and backscattered (black) light waves are shown on left; the SRS plasma wave (red) and lower wavenumber sidebands (black) are on the right. The E1-field is filtered at $kc/\omega_0 = 1.4$, while the E3-field is filtered at $kc/\omega_0 = 0.8$.

of saturation.

The saturation of the light and plasma wave amplitudes may be seen in Figure 3.9. Four envelopes are plotted. They are the incident light (left, red), backscattered light (left, black), SRS plasma wave (right, red), and lower wavenumber sidebands (right, black). The envelopes are obtained by applying a high-pass and low-pass filter to the E-fields at a wavenumber intermediate between the primary plasma wave and sideband, and the incident and backscattered light. The higher wavenumber sidebands are small enough that they do not noticeably affect the filtered results. In the first frame ($\omega_0 t = 8000$), the plasma and backscat-

tered light waves are in their growth phase and the incident light is depleted in the region of maximum growth. There is no evidence yet of the sidebands. By the second frame ($\omega_0 t = 8500$), the backscattered light wave is approaching the amplitude of the incident light wave, the incident light has been depleted, and the sidebands are just beginning to grow. This plot shows the backscattered light at its largest amplitude of the time sequence. By the middle frame ($\omega_0 t = 9000$), there is a kink in the light waves (at $x\omega_0/c \approx 200$) where the backscattered light wave has decreased in amplitude and there is a disruption in the smoothly decreasing amplitude of the incident light. This is a sign that SRS (reflectivity) has saturated. SRS saturation will be denoted as the time at which the backscattered light stops growing. The point of maximum depletion of the incident light wave has continued to decrease, however, as the instability continues to occur in regions of the plasma where the instability is still supported. Saturation is not a spatially uniform event; in addition to saturation at a specific time, saturation can be localized in space, with SRS saturation a function of both time and space. The sidebands have now grown noticeably, and they are most significant in that region where the saturation has occurred (the region of the light wave's kink). The fourth and fifth frames ($\omega_0 t = 9500, 10000$) continue to show the evolution of the waves until the point of maximum depletion of the transmitted light reaches the end of the simulation box. The sidebands have grown throughout the packet, but they stop growing once they become of comparable amplitude to the primary plasma wave.

In comparing the evolution of the wave amplitudes with the frequency versus time plots, the frequency does not significantly begin to shift until the time of saturation, similarly to the timing of the sideband growth. At $\omega_0 t = 9000$, the reflected light has reached its maximum and the frequency shift is at most $\Delta\omega/\omega_0 = 0.004$. A frequency shift of this magnitude would cause the resonance

to go from in phase to out of phase in a time $\pi/\Delta\omega \approx 800\omega_0^{-1}$, indicating that the frequency shift should have occurred by $\omega_0 t \approx 8200$ for the saturation to occur by $\omega_0 t = 9000$, whereas Figure 3.8 appears to indicate that the frequency is only beginning to shift by $\omega_0 t = 8200$.

We attempt to make this approximate argument more precise by plotting the resonance diagnostic (see Chapter 2) to determine whether the local three-wave resonance condition is satisfied. This local picture of resonance detuning is shown in Figure 3.10. Following from Chapter 2, SRS that satisfies phase-matching for resonant growth is represented by positive values (red) whereas SRS that is detuned, or equivalently is being stabilized, is represented by negative values (blue). Immediately at $\omega_0 t = 9000$, which has been established as the saturation time, the resonance value is still positive, although shortly after $\omega_0 t = 9000$ it changes from positive to negative. The frequency shift leads to a resonance detuning shortly after $\omega_0 t = 9000$ since the frequency shift continues to affect the interaction of the waves even after the backscattered light has saturated.

Even though the very first saturation may be significantly affected by pump depletion, the resonance detuning will clearly affect the growth of plasma waves and backscattered light as the system continues to evolve. Figure 3.10 illustrates a number of different effects that have been mentioned. First, the complex combination of both frequency and wavenumber shifts of the plasma wave packet can be seen in the area of $(x\omega_0/c, \omega_0 t) = (200, 10000)$. The dark red areas represent that part of the packet that continues resonating with backscattered light, that is, the part of the packet that has shifted down in frequency and up in wavenumber. The blue edge of the convecting packet is evidence of the positive wavenumber shift of the packet's tail; the wavenumber shift detunes the resonance in space as opposed to the temporal oscillation that results from the frequency shift de-

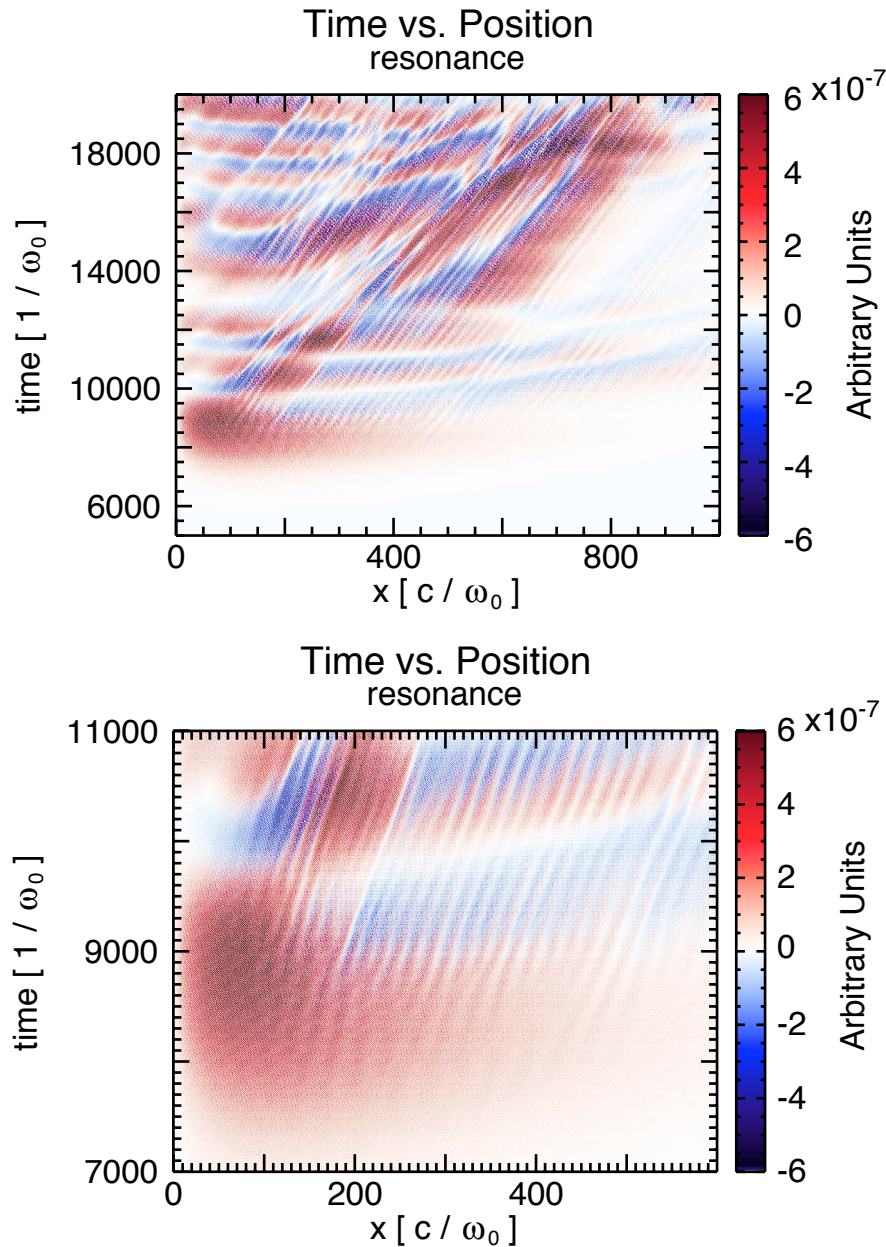


Figure 3.10: SRS resonance diagnostic for the first SRS burst of Case I.

tuning. Finally, the region in $(x\omega_0/c, \omega_0 t) = (200, 18000)$ shows the oscillating pattern of resonance/nonresonance that results from frequency up-shifted light driving the background plasma.

For Case I, pump depletion plays a significant role in the initial saturation of the reflectivity, that is, the incident light wave is sufficiently depleted of energy to disrupt the instability. Detuning eventually causes the plasma wave amplitude to decrease and the reflectivity to decrease further. The sidebands grow as the backscattered light has reached a maximum in amplitude. However, they do not grow exponentially and they do not appear to saturate the instability. It may be noted that the frequency content of the SRS plasma wave packet shifts lower in approximately the same region of space where the saturation occurs, as well as where the sidebands grow. The phase detuning and pump depletion occur at very similar times, and the next chapter will present more simulation results to show that the relative timing between the two effects determines which one plays the dominant role in saturating the instability.

The evolution of the sidebands merits further discussion. The sidebands appear as a modulation of the E1-field. The amplitude of the sidebands relative to the SRS plasma wave can be roughly determined by the strength of the modulation, that is, if the sideband were equal in amplitude to the SRS plasma wave, the enveloped pattern of the waves would have a point of completely destructive interference (zero amplitude). These points of low amplitude were seen as striations in the enveloped E1-field moving at approximately the group velocity in Figure 3.1. They are shown again in Figure 3.11, where a smaller region of space and time is plotted (left), along with a (non-logarithmic) plot of time-sequences of the E1-field (right). As the sidebands grow and move with the plasma wave, the group velocity of the beat pattern will be $v_{beat} = (\omega_1 - \omega_2)/(k_1 - k_2) \approx v_g$.

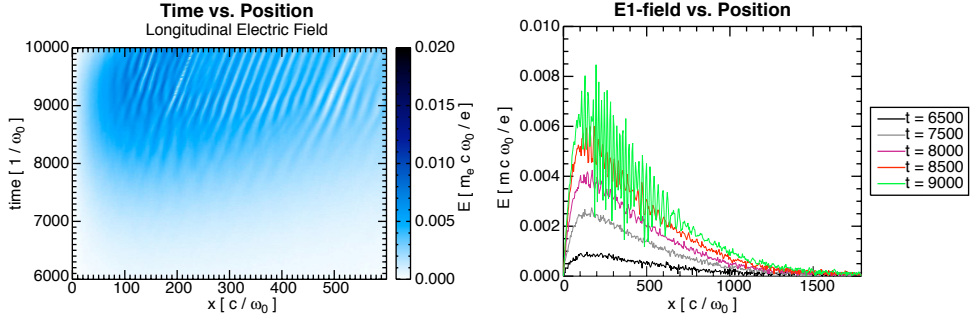


Figure 3.11: Spatial profile of the E1-Field during SRS growth for Case I.

The frequency and wavenumber of the SRS plasma wave during growth are $\omega_2/\omega_0 = 0.35$ and $k_2\omega_0/c = 1.52$, while those of the dominant sideband are $\omega_{sideband}/\omega_0 = 0.33$ and $k_{sideband}\omega_0/c = 1.2$. The phase velocity of the SRS plasma wave ($v_\phi/c = 0.23$) is the fast velocity of the phase fronts, while the modulation of the wave travels at $\Delta\omega/\Delta k \approx 0.02/0.3 = 0.07c$. This v_{beat}/c is close to, but slightly higher than, $v_g/c = 0.05$. This striated pattern of a convecting, modulated packet of plasma waves may be seen throughout the entire temporal span of the simulation in Figure 3.1.

The amplitude modulation in the E1-field has a direct effect on the behavior of trapped particles. Figure 3.12 shows the E1-field versus space, along with plots of electron phasespace over the same spatial region. For plot (a), the instability is still slightly before saturation, the E1-field is only very slightly modulated, and the electrons are uniformly phase-mixed as they bounce in the trapped particle buckets. By the time of plot (b), when the sidebands have grown significantly and the modulation is clear, the electrons begin to stream between different buckets. An electron that bounces in a modulated potential well may be trapped on one side of the well but not on the other, i.e., an electron will bounce on one side of its bucket but escape on the lower-amplitude side and move into the neighboring bucket. This effect may be seen in the amplitude modulations at $x\omega_0/c = 245$

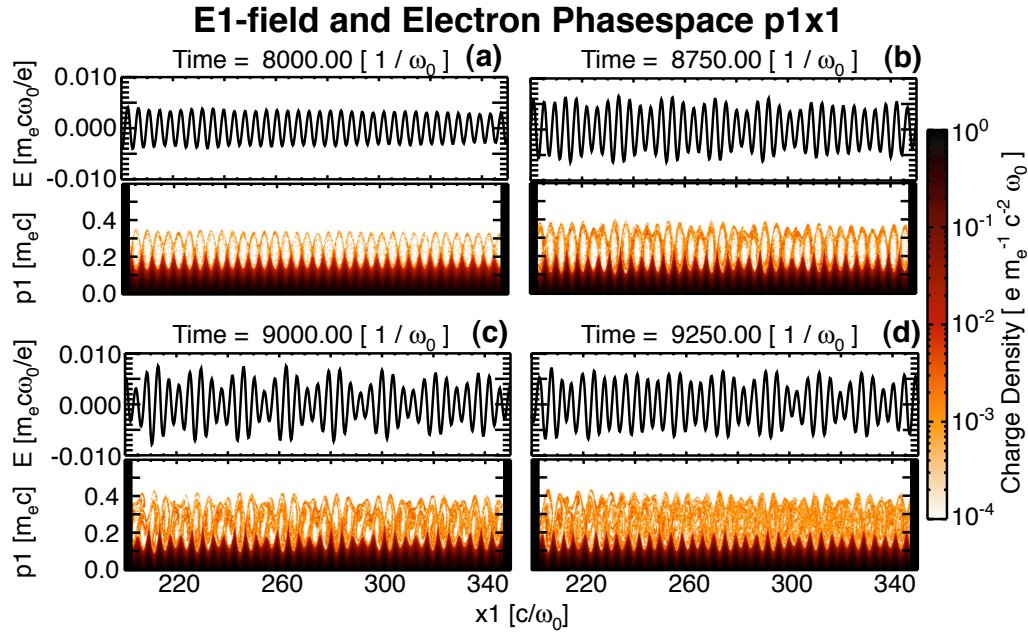


Figure 3.12: Effect of sidebands on the electron phasespace and the E1-field for Case I.

and 280 in plot (b), for example, and the corresponding streaming of trapped electrons at the same spatial points. This streaming occurs at a velocity of approximately $v_\phi + v_{tr}$. As the modulation grows even larger by plot (c), large numbers of trapped particles move between buckets. It can appear as if the buckets are coalescing (the vortex-merging effect noted by Albrecht-Marc [63]). By the time for plot (d), the modulation has weakened and the trapped particle buckets have returned to bucket sizes that are more spatially uniform. The total progression has resulted in the principal effect that trapped particles have been smeared throughout the buckets in phasespace.

The velocities v_1 and v_2 that were noted on the ω versus k plot in Figure 3.4 have corollaries in the electron phasespace. The same ω versus k plot is again shown in Figure 3.13, along with the electron phasespace and the distribution

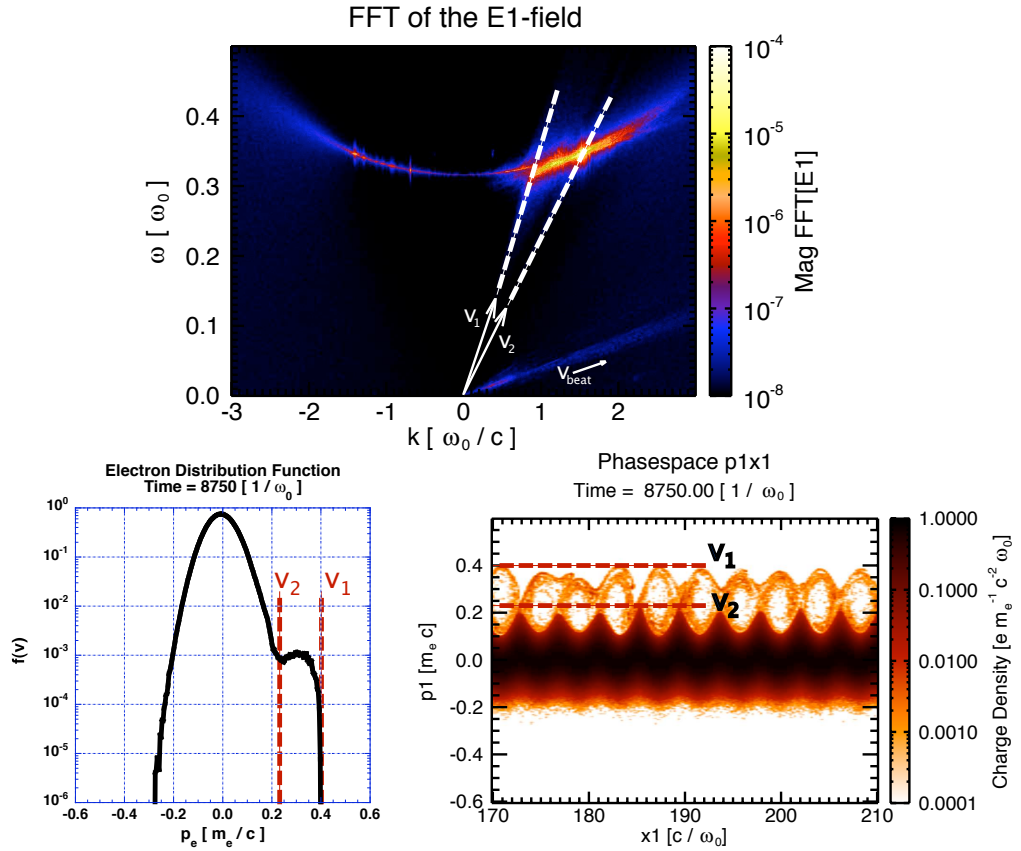


Figure 3.13: The phase velocity (v_2) and velocity at the top of the trapped particle buckets (v_1) are shown on the distribution function, phasespace, and ω versus k plots.

function spatially-averaged over $x\omega_0/c = 170 - 210$, both at $\omega_0 t = 8750$. The phase velocity of the plasma wave is v_2 , whereas v_1 is the maximum velocity of the trapped particle buckets. There are two key features. First, the distribution function is flattened from v_2 to v_1 , that is, from v_ϕ to $v_\phi + v_{tr}$. While trapping may accelerate particles from below v_ϕ to above v_ϕ , the distribution function does not flatten very much for velocities less than v_ϕ due to the large number of particles that can be instantaneously between $v_\phi - v_{tr}$ and v_ϕ but still outside of the trapped particle buckets (the dark regions in phasespace up to v_ϕ). Secondly, v_1 sets an upper bound on the phase velocities of the sidebands. Without the presence of trapped particles above v_1 , there is no sideband signature in the ω versus k plot for phase velocities larger than the dotted line extending v_1 . This feature will again (and more prominently) be evidenced in later simulations.

The temporal progression of electron behavior can be further analyzed in terms of the spatially averaged distribution function. Figure 3.14 shows a temporal sequence of such plots within a spatial window moving at the phase velocity (both time and space move forward in this sequence, so the same buckets are plotted in each frame). The distribution functions at each time are the spatially averaged distribution function over the region of phasespace plotted next to them. The first frame shows the distribution function when SRS is growing and the electron phasespace has phase-mixed but is not uniform throughout each bucket. Despite the appearance of holes in phasespace, the spatially averaged distribution function is not a bump on tail. This flat tail on the distribution function extends from approximately v_ϕ to $v_\phi + v_{tr}$, corresponding to the population of particles that have become trapped. It may again be noted that the flattened region is only flattened down to v_ϕ ($= 0.23$), i.e., the distribution function does not flatten down to $v_\phi - v_{tr}$. The second frame shows a distribution function with a slight bump-on-tail due to the beam-like behavior of the trapped

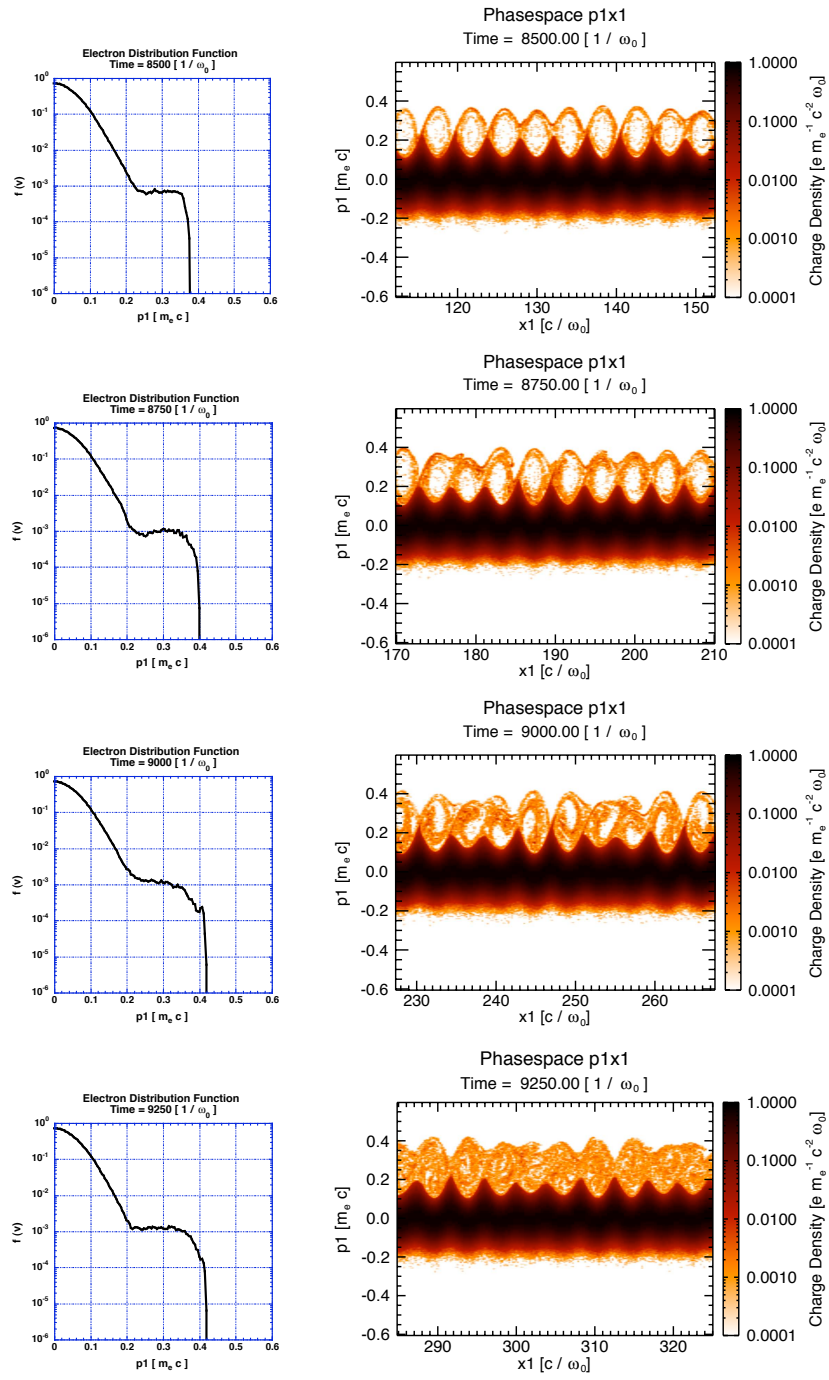


Figure 3.14: Electron phasespace and the corresponding distribution function (spatially averaged over the same region as the plotted phasespace) for Case I.

particles that have begun streaming from one bucket to another. For electrons travelling faster than v_ϕ , the largest portion of them are now travelling at slightly less than $v_\phi + v_{tr}$, with a velocity that is seen in phasespace at the top of the slightly depressed buckets. This bump is negligible in magnitude and is due to the disruption of phasespace buckets, rather than the presence of a clear beam. The third frame shows strong bucket mixing and merging, and the distribution function has relaxed from the slight bump-on-tail of the second frame to a tail with a slightly-negative slope. In the progression of these first three frames, the high-velocity end of the tail extends to increasingly higher velocities, and the total number of particles in the flattened region of velocity space is constantly increasing. Although the primary SRS plasma wave has stopped growing, the E1-field of the plasma wave combined with the sidebands continues to increase at points of constructive interference, resulting in a collectively larger trapping width. Finally, the last frame shows the distribution function corresponding to a phasespace whose buckets have been smeared out. The tail has flattened and stopped extending to higher velocities.

After the saturation, the packet of plasma waves convects through the simulation domain. As was pointed out in Figure 3.1, the rear edge of the packet convects at v_{NL} , a velocity intermediate between the phase and group velocity. The packet itself may be unstable, with several apparent packet-like forms evolving simultaneously. This is also evident in Figure 3.1 at $\omega_0 t = 14000$ and $x\omega_0/c = 400$, where the packet coming from the original region of growth has now died out, and the formation of a new packet (or region of instability) is growing at $x\omega_0/c = 650$. The two packets appear as a unit due to the continued convection of a group of plasma waves at v_{NL} , as well as due to the fact that the second packet grows from plasma waves that grew during the initial burst of SRS. This reveals the complex nature of SRS even after growth and saturation

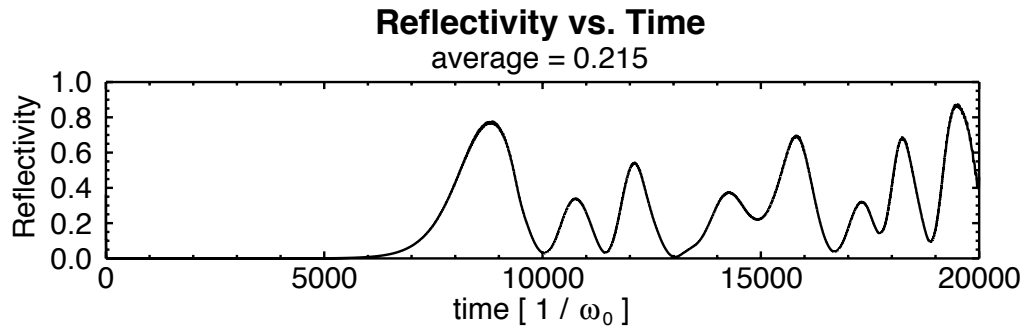


Figure 3.15: Reflectivity versus time for Case I.

has occurred - the system can continually undergo regrowths of SRS. The system is continually driven with new laser energy that enters, and regions of plasma waves that previously were not driven as strongly due to the presence of pump depletion can suddenly be driven again at the original laser intensity and grow anew until they reach the same saturated state. This is seen as the second packet reaches approximately the same amplitude as the first packet.

The reflectivity as a function of time is shown in Figure 3.15, where the reflectivity is measured at the laser-entrance side of the simulation box. It is immediately evident that the initial burst of SRS is only one part of the reflectivity's evolution. Subsequent bursts occur on a roughly periodic basis. This periodicity will be elucidated with more simulations in the next chapter, but a first explanation is offered here as well. The periodicity can be understood in terms of the nonlinear frequency shift of the plasma wave. As the saturated packet of frequency down-shifted plasma waves convects through the box, new laser energy enters and interacts with this packet. An SRS resonance can continue, although the growth is weaker than the original resonance at the linear SRS frequencies. The backscattered light from this new resonance is frequency up-shifted (to maintain frequency matching with the down-shifted plasma waves).

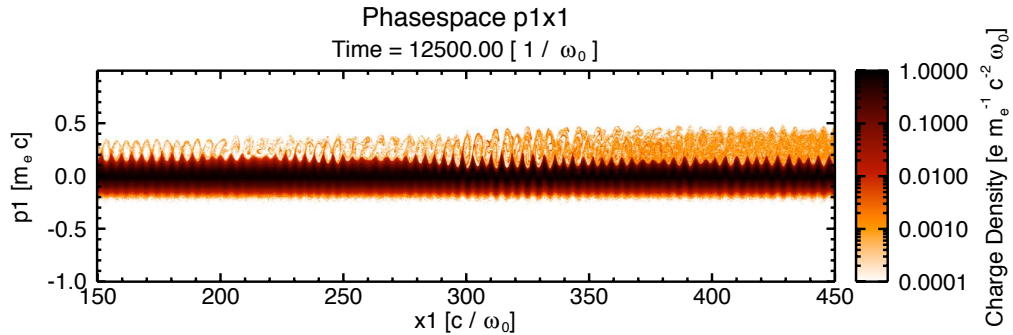


Figure 3.16: Electron phasespace at edge of packet for Case I.

The frequency shifted backscattered light grows in the packet, but outside of the packet it interacts nonresonantly with the background plasma, as linear plasma waves in this region of plasma can not resonate with the beat between the pump and the frequency shifted light. Therefore, in this region of space, the ponderomotive force from the pump and nonlinearly shifted backscattered light drives a plasma wave slightly off resonance. This leads to the growth and then decay of the plasma wave as the drive and plasma wave get out of phase. This growth and decay occurs in a time $2\pi/\Delta\omega$. This same growth and decay occurs in the backscattered light and this is what leads to the short bursts of reflectivity.

The result is a beating pattern of plasma waves, as can be seen in Figure 3.1 in the region of plasma from approximately $x\omega_0/c = 0$ to 500 and $\omega_0 t = 10000$ to 20000. The total effect is a reflectivity pattern that beats with a periodicity dependent on the frequency shift, that is, the time between bursts of reflectivity is $2\pi/\Delta\omega$. For the frequency shift shown before of amplitude $\Delta\omega/\omega_0 = 0.004$, the periodicity is $\omega_0 t \approx 1600$. This corresponds rather well with the periodicity in Figure 3.15. Later in time, the frequency shift becomes slightly bigger and the periodicity correspondingly becomes slightly shorter, dropping to $\omega_0 t \approx 1000$.

In Figure 3.16, the electron phasespace is plotted in a region that surrounds

the edge of the convecting plasma wave packet, showing the simultaneous existence of two regions of plasma waves, one of which has grown, saturated, and smeared the phasespace (right half), while the other is weak and has not strongly affected phasespace (left half). The interaction of these two waves in the center part of the plot shows the dynamics at their intersection.

In summary of Case I, the onset of SRS begins from a noise source in the plasma. SRS grows in time in all regions of space and it grows in time at a fixed position in space near the absolute growth rate, despite the fact that it is below the theoretical absolute threshold. In the first detectable growth of the plasma wave, a small percentage of particles are trapped and bounce in the plasma wave's potential. Even if the growth is at first convective, the subsequent bouncing of trapped particles in the wave will modify the damping of the plasma wave from its linear value and affect its regime of growth. The saturation of SRS involves complex spatio-temporal behavior of the plasma wave, complicated by the presence of sidebands, frequency shifts, and wavenumber shifts. By decomposing the transverse electric field into laser and scattered light components, it is seen that the scattered light approaches similar amplitudes to the incident laser. After the incident laser light becomes appreciably depleted of energy by SRS, the scattered light stops growing and decreases dramatically to zero amplitude. This is denoted as the SRS saturation. This process starts in a region of space and time that precludes any appreciable influence by the sidebands or the frequency and wavenumber shifts. A decomposition of the longitudinal field into the SRS plasma wave and the lower sidebands reveals that the sidebands grow appreciably only after the scattered light has started to decrease in amplitude, while plots of the frequency and wavenumber behavior in time show that they shift primarily during and after the saturation as well.

Ascertaining the evolution of the nonlinear frequency shift of the plasma wave is limited by the ability to simultaneously resolve frequency and time. The phase resonance was explored further by plotting the resonance diagnostic described in Chapter 2, showing that phase detuning occurred between the waves after the saturation of the backscattered light signal. Nevertheless, the resonance detuning occurred close in time to saturation, and it is difficult to conclusively assign the saturation to one effect. For Case I, it appears that pump depletion plays a significant role in the saturation of the reflected light, while the frequency shift causes the reflected light and plasma waves to decrease after saturation.

A picture of the sideband modes as a modulation of the longitudinal electric field envelope has been presented, and the effect of the sidebands on the electron phasespace has been thoroughly illustrated. There is a link between this electric field modulation and the behavior of trapped particles, namely, when particles are trapped in a potential well that has different amplitudes on each side of the well, some of the particles may escape from the bucket on the side that has the lower amplitude. This occurs because the velocity of the modulation is slower (near v_g) than the velocity of the buckets (near v_ϕ). These particles stream from one bucket to the next. As the sidebands grow to a similar amplitude as the SRS plasma wave, the trapped particle buckets are dramatically mixed and the distribution of particles smear throughout the bucket. Equivalently, the number of particles within the flattened tail of the spatially averaged distribution function grows as more and more particles are trapped, with the spatially averaged distribution function oscillating between a slight bump-on-tail and a slightly negatively sloped flattened tail as trapped particles stream between buckets and the buckets mix together. Eventually, it relaxes to a uniformly flat tail after the smearing of particles in the buckets. This oscillation between a slight bump-on-tail and a flat tail is very weak here, but it will be much more evident in later simulations that

are more strongly driven.

For a conceptual picture of why the sidebands do not grow strongly until close to saturation, consider a potential well (moving from left to right) whose left side is at a higher amplitude than the right side. Ordinarily, a particle that traps on the left side may not be reflected by the lower potential on the right. During the growth of SRS, however, the particle may remain trapped as long as the amplitude on the right grows fast enough. In this case, all particles remain in their buckets and sideband growth is minimal. When the SRS saturates, however, and the plasma wave stops growing, trapped particles will effectively move between buckets. As they do so, there is an uneven exchange of energy and momentum between the trapped particles and the SRS plasma wave. Particles that would have taken energy and momentum from a potential well and returned it to the same well as they bounced will now take energy and momentum from one well and deposit it into the neighboring well they stream into, rather than the same well from which they took it. A model of the interaction of the trapped particles and the sidebands has not been formulated, but it may be argued that the beam-like streaming of trapped particles between buckets acts to re-inforce the modulation in the electric field, and thereby the sidebands.

After the saturation, the packet of SRS plasma waves convects through the simulation system. SRS can continue to grow in the region of the convecting plasma packet, in the region left behind by the packet, and even for points farther into the packet which are driven more strongly as the packet is etched away. The evolution of the packets and recurrence will be studied more closely in other cases, but this provides a comprehensive picture of general SRS behavior as a framework from which to work.

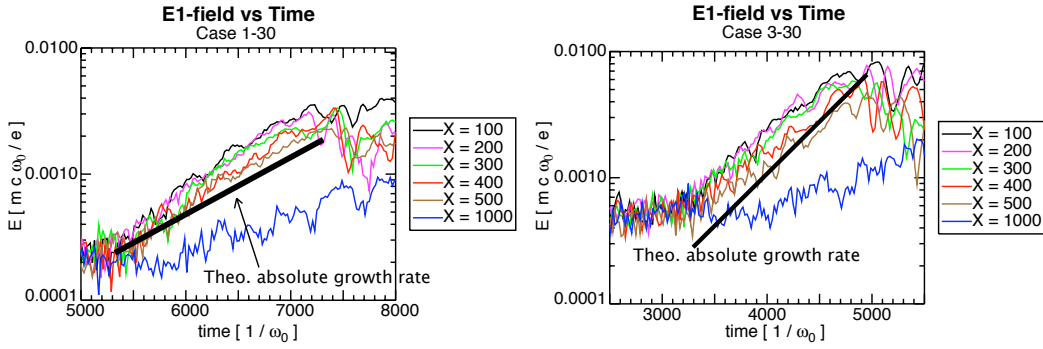


Figure 3.17: Temporal evolution of the E1-field at several positions in space for Cases 1-30 (left) and 3-30 (right).

3.4 Cases 1-30 vs. 3-30

The two simulations shown in this section were chosen as intermediate between the parameters of Case I and Case IV in terms of driving laser intensity and $k\lambda_D$. They are presented side by side to draw comparisons both between them and with the previous analysis. As a reminder, the only differences between these two simulations are the electron temperature and density, but $k\lambda_D = 0.30$ (for the SRS plasma wave) for both cases. They are referenced as 1-30 and 3-30 for their respective electron temperatures of 1 and 3 keV while keeping $k\lambda_D = 0.30$.

Figure 3.17 shows the magnitude of the plasma wave E1-field envelope during the first burst at several spatial points within the growing plasma wave packet, as well as one point outside the packet at $x\omega_0/c = 1000$ (approximately 2/3 of the way into the domain). While both of these cases are below the threshold for an absolute instability ($\beta \approx 5-6$), each spatial point within the growing packet grows at similar rates which are close to the theoretical absolute growth rate with no damping (black line). Similarly to Case I, trapped particle bouncing motion that modifies the damping rate is a possible cause of this “inflationary”

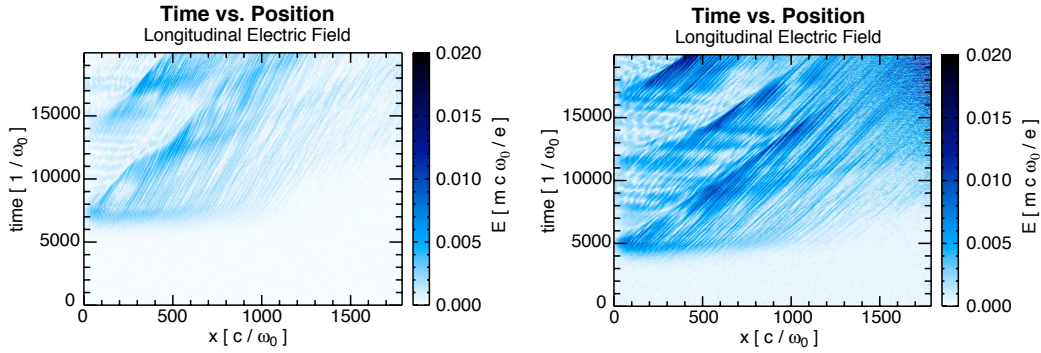


Figure 3.18: Spatio-temporal evolution of the E1-field for Cases 1-30 (left) and 3-30 (right).

transition from the convective regime to the absolute regime. The growth of the far point at $x\omega_0/c = 1000$ shows that there is a region in the plasma where growth occurs at a slower rate. One possible explanation is that the instability first grows convectively and the conditions for absolute growth arise after the plasma wave has reached a sufficient amplitude, that is, after the plasma wave amplitude is large enough to cause several bounces of the trapped particles and modify the damping rate. Hence, the nonlinear damping rate is less on the left side of the box (where the wave is largest), so the absolute growth rate is greater than on the far right side. Another explanation could be that the incident laser intensity is sufficiently depleted by $x\omega_0/c = 1000$ that it drives SRS at a lower growth rate. This second explanation will be ruled out by Case 1-30, where it will be shown that there is negligible pump depletion.

In Figure 3.18, the E1-field envelope is plotted in time and space. In Case 3-30, the plasma wave reaches larger amplitudes and there are more frequent major bursts, with three major packets over the course of the simulation compared to two major packets for Case 1-30. The plotted spatial scale is in terms of laser wavelengths, rather than Debye lengths; while the phase and group velocities of

the two cases are the same in terms of v_{the} , the packets move faster for Case 3-30 in terms of c . There are striations (fine scale) in both plots which are evidence of the amplitude modulation due to sidebands, convecting in both cases at approximately v_g , and there is a nonlinear packet velocity v_{etch} of the rear edge of the packets at a velocity greater than v_g , as was seen in Case I.

As the packets convect across the domain, it is also seen that they can subsequently undergo renewed growth. For example, in Case 3-30, the first burst undergoes regrowth at $(x\omega_0/c, \omega_0 t) = (550, 9000)$ and the second major burst grows in amplitude at $(600, 15000)$. Case 1-30 shows similar nonlinear convective behavior as the first major burst convects forward; at $(600, 12000)$, renewed growth occurs. In addition, for this case, the slope (velocity) of the rear edge of the packet dramatically shifts at $(300, 11000)$, possibly due to an increase in the local Landau damping rate as the packet interacts with nonlinearly heated plasma. In all of the above cases, the renewed growth occurred at a position and time into which previous plasma waves were moving at the group velocity, and as the original packet etched away, there could be renewed SRS growth of plasma waves travelling close to the region of the rear (etched) packet edge. Furthermore, there may be an interaction between packets that are growing and convecting in separate regions of plasma (as will also be shown in Case IV). In the first several hundred $x\omega_0/c$ of both simulations, the periodic bursts of plasma waves due to scattered light from the convecting packets is also evident.

The periodicity of the major bursts, as well as of the smaller bursts from the scattering from packets, can be seen in Figure 3.19, where the temporal evolution of the E1-field envelope at $xc/\omega_0 = 129$ is plotted for both simulations (a point near the packet's peak SRS growth). Case 1-30 has peak amplitudes that are smaller than Case 3-30 (by approximately a factor of two), as well as fewer

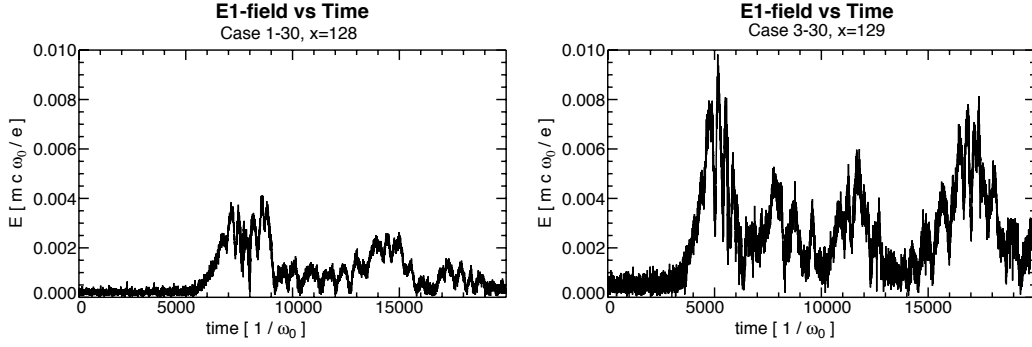


Figure 3.19: Temporal evolution of the E1-field at $x\omega_0/c = 129$ for Cases 1-30 (left) and 3-30 (right).

large peaks. In terms of v_{the} and ω_p , however, the etching velocity (v_{etch}/v_{the}), periodicity of major bursts ($\omega_p t_{burst}$), and the amplitudes ($eE/mv_{the}\omega_p$) are approximately equal between the two cases. The relevant proximity of these values between simulations with different parameters is deferred to the next chapter. The periodicity of the smaller peaks (spaced approximately $\omega_0 t = 800$ apart) is consistent for both cases, and these regular, minor bursts will be shown to correspond to SRS in regions vacated by packets, and seeded from backscatter within the packet, at a rate determined by the frequency shift (as was pointed out in Case I).

The total frequency and wavenumber content is plotted in Figure 3.20, where the FFT of the E1-field sampled over the entire space and time of the simulation is plotted. These plots show the same qualitative features that were illustrated in the discussion for Case I, albeit here the effects are more pronounced. There is a shift of the primary SRS plasma mode from the linear dispersion relation to lower frequencies. This is accompanied by wavenumber shifts, both positive and negative. There is a wide swath of sidebands (very broadband), predominantly to lower wavenumbers. Furthermore, both simulations show weak streaks at

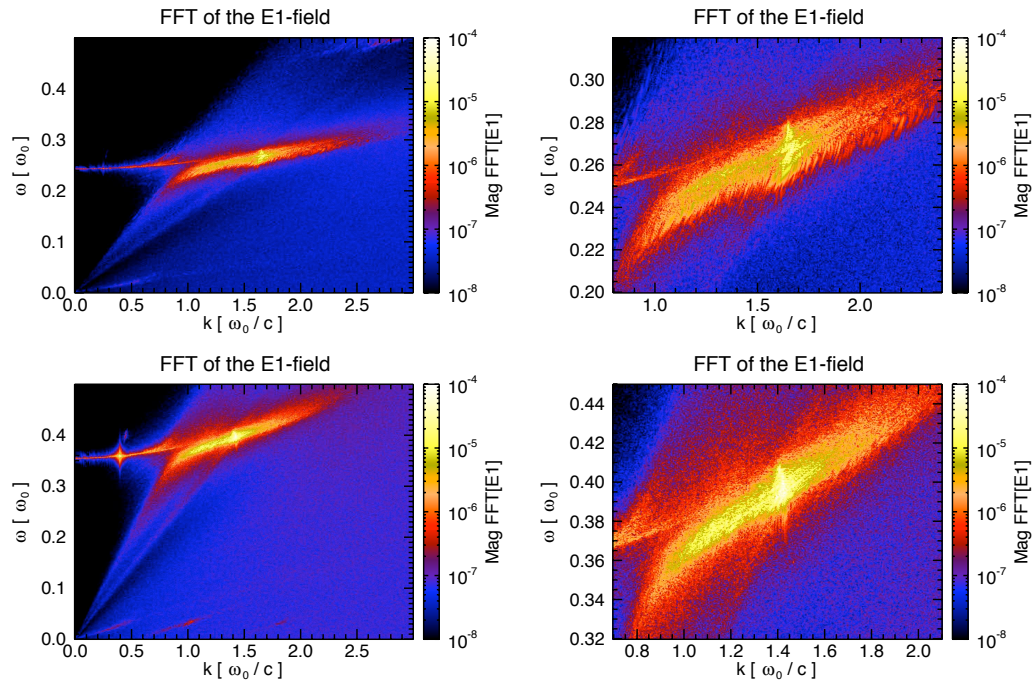


Figure 3.20: Frequency vs. Wavenumber for Cases 1-30 (top) and 3-30 (bottom).
The right column is zoomed-in plots.

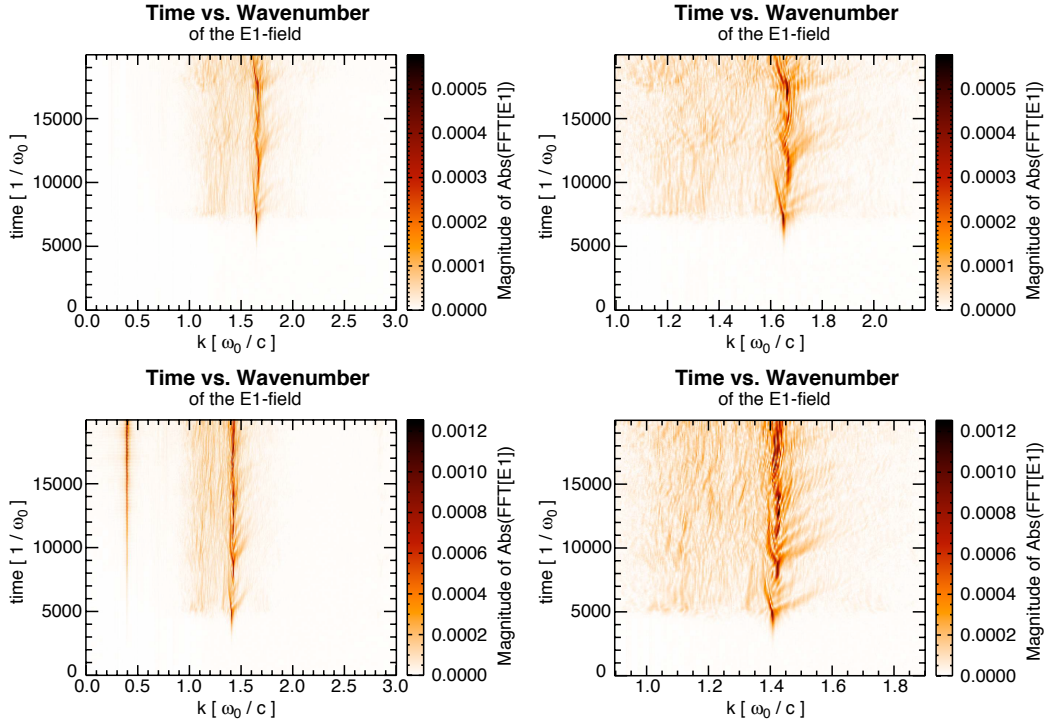


Figure 3.21: Wavenumber evolution for Cases 1-30 (top) and 3-30 (bottom).

velocities corresponding to (1) the phase velocity, (2) the beam-like velocity of trapped particles moving between buckets as the plasma wave is modulated by sidebands (and bounding the region where sidebands are present ($v = \omega/k < v_\phi + v_{tr}$) and where they are not present ($v > v_\phi + v_{tr}$)), and (3) the beat mode streak at low frequencies and wavenumbers that matches the beat between the SRS plasma wave and the sidebands.

The temporal evolution of wavenumbers is shown in Figure 3.21. The sudden swath of sidebands during saturation of the first SRS burst is seen in both plots at lower wavenumbers compared to the primary plasma wave. The primary wave evolves nonlinearly, but with several distinct features. The wave shifts to slightly lower wavenumbers during the saturation of each burst, in line with a general wavenumber shift of the plasma packet. There are wispy lines that streak to

higher wavenumbers, corresponding to the higher wavenumber shifts of the rear edge of the packet. Finally, there is a general trend to slightly higher wavenumbers over the course of the entire simulated time. Given that there is frequency-shifted backscattered light in addition to frequency-shifted plasma waves, the backscattered light is most resonant along the light wave dispersion curve. If both frequency and wavenumber matching conditions are to be met by the bursts of SRS, then as the frequency of the plasma wave shifts down (light wave shifts up), the wavenumber must shift slightly higher to resonate with a light wave along the light wave dispersion curve (see Fig. 3.5 and Eqn. 3.1). This is seen as well in Figure 3.20, where the time-integrated frequency and wavenumber content of the plasma waves over the course of the simulation shows that wavenumbers shift slightly upwards as the frequency shifts down (see the brightest streak in the lower right plot in Figure 3.20), even though each individual burst might contain a streak to slightly lower wavenumbers. Movies of ω vs. k make this clearer.

Before further investigating the nonlinearities, the first SRS burst and its saturation will be studied. Figures 3.22 and 3.23 show the envelopes of the transverse and plasma wave fields, filtered into incident (red) and backscattered (black) light waves for E3 (top), and the primary SRS plasma waves (red) and lower sidebands (black) for E1 (bottom). The larger plasma wave amplitude (in units of $mc\omega_0/e$) for Case 3-30 is again evident. Correspondingly, the magnitude of backscattered light and the amount of pump depletion is larger for this case. The first plotted time for both shows that the sidebands have negligible amplitude. By the second plot, both cases have developed the kink in the backscattered light amplitude which is due to non-uniform spatial growth, and they have entered the saturation phase. It is during this saturation phase (in analogy with Case I) that the sidebands begin to grow significantly and the amplitude of the plasma wave becomes modulated. By the final plotted time, the depleted region of incident

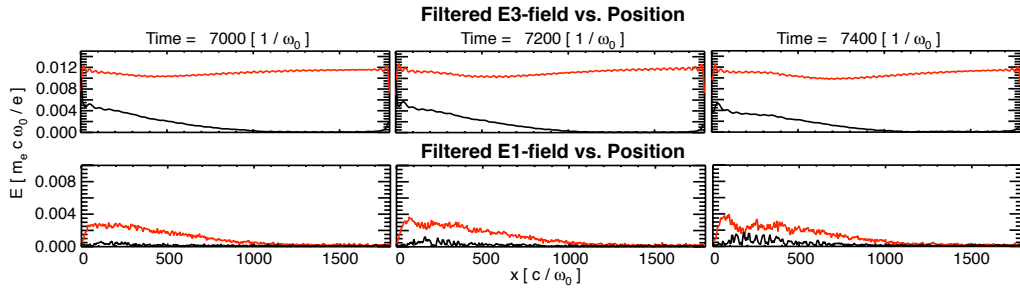


Figure 3.22: Filtered E1 (bottom) and E3 (top) Fields for Case 1-30 at the time of saturation of the first SRS burst.

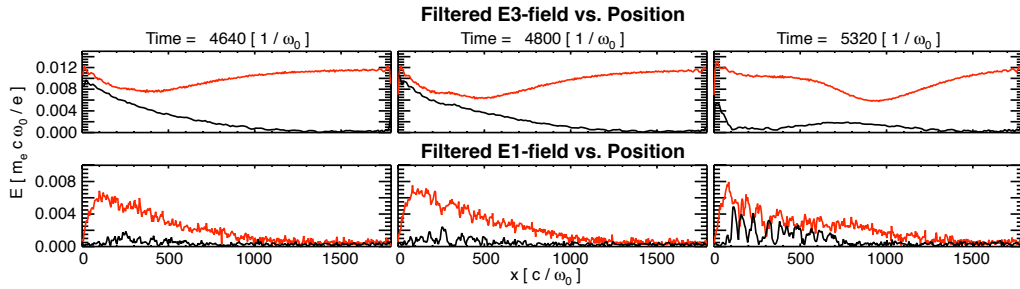


Figure 3.23: Filtered E1 (bottom) and E3 (top) Fields for Case 3-30 at the time of saturation of the first SRS burst.

light has moved further into the box and new laser energy is entering the box behind it. The backscattered light has decreased in amplitude, the sidebands have grown to comparable amplitudes with the SRS plasma wave in parts, and the SRS plasma wave has become strongly modulated.

A more inclusive picture of saturation is shown in Figure 3.24, where the time versus space plots of the E1-field are shown in tandem with the light wave envelopes at the time of saturation, as well as the frequency content of the plasma waves (E1-field) versus time. First, the amplitudes of the backscattered light waves compared against the incident light waves are noticeably different between the two cases, with lower relative amplitudes for Case 1-30. Case 1-30 has a

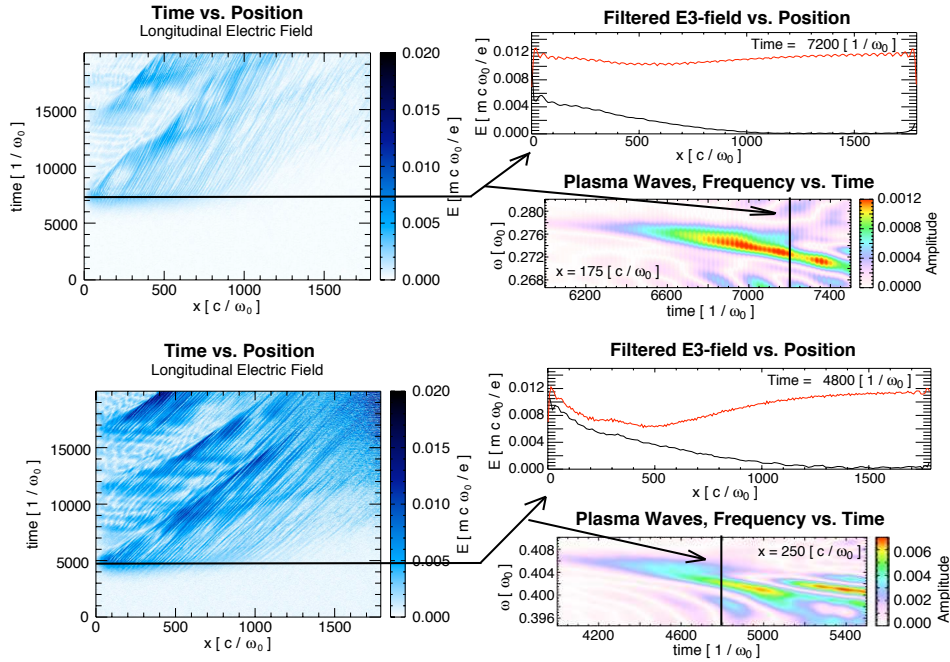


Figure 3.24: Saturation time for Cases 1-30 (top) and 3-30 (bottom).

negligible amount of pump depletion, while Case 3-30 has a significant amount of pump depletion and the backscattered light is no longer growing uniformly in space. Second, the frequency shifts of the plasma waves are different at the time of saturation. Case 1-30 has a frequency shift of $\Delta\omega/\omega_0 = 0.006$, while the frequency shift for Case 3-30 is roughly half of that value (in terms of $\Delta\omega/\omega_p$, the difference in shifts is even larger, and a comparison of shifts with ω_p and the growth rate γ is left for the next chapter). In Case 1-30, SRS saturates due to the frequency shift, while in Case 3-30 the frequency shifts might cause the reflected light to drop in amplitude but pump depletion plays a very important role.

It may further be noted that for Case 3-30, a frequency shift eventually develops that is comparable in magnitude to that of Case 1-30. The plasma wave may stop growing while continuing to shift in frequency, resulting in a final shift by the same amount. Figures 3.25 and 3.26 show the frequency content versus position

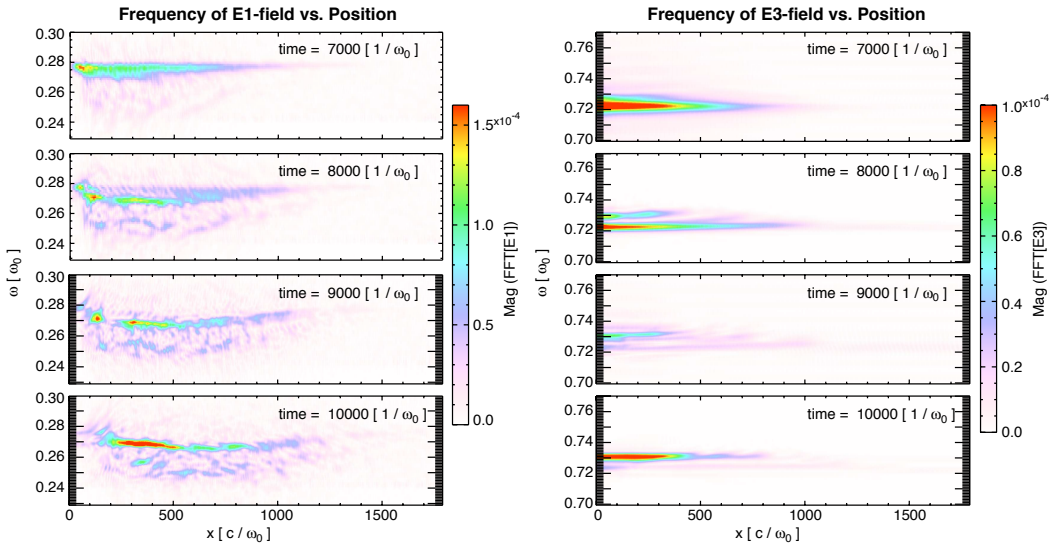


Figure 3.25: Frequency vs. Position of the E1 (left) and E3 (right) Fields for Case 1-30.

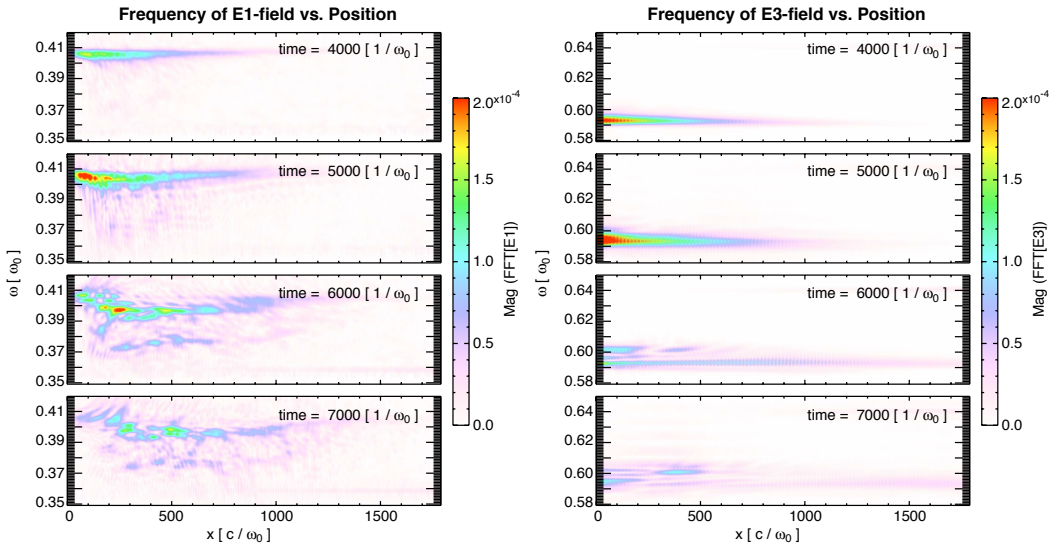


Figure 3.26: Frequency vs. Position of the E1 (left) and E3 (right) Fields for Case 3-30.

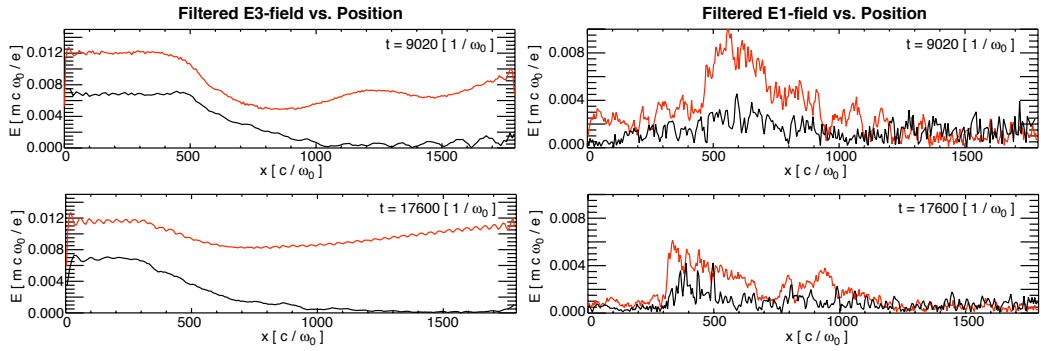


Figure 3.27: Filtered E1 and E3 Fields for Case 1-30 (bottom) and 3-30 (top) showing SRS growth in a convecting plasma packet.

of the primary SRS plasma wave and the backscattered light at four times, during and after SRS saturation. In both, the frequency of the plasma wave packet shifts negatively as expected. The frequency of the backscattered light is also observed to shift, with a positive shift equal in magnitude to the negative shift of the plasma wave. This reveals the continued SRS resonance that can continue from convecting packets of frequency shifted plasma waves, even after the initial saturation has occurred. True resonance also requires that the wavenumber shift also allows the scattered light wave to remain resonant.

While the cause of the initial saturation is important, a complete picture of SRS evolution must include much more. In all these cases, the convection of the packets and the subsequent growth of new scattering bursts are both vitally important to the total and instantaneous reflectivity levels. In Figure 3.27, we show the E1 and E3-field envelopes of the plasma waves and sidebands of convecting packets, as well as the scattered light from these packets. The plasma waves are strongly modulated by the sidebands, but they nevertheless exist as a cohesive packet. Subsequent time slices would show these packets convecting through the simulation domain at relatively constant amplitudes. The incident

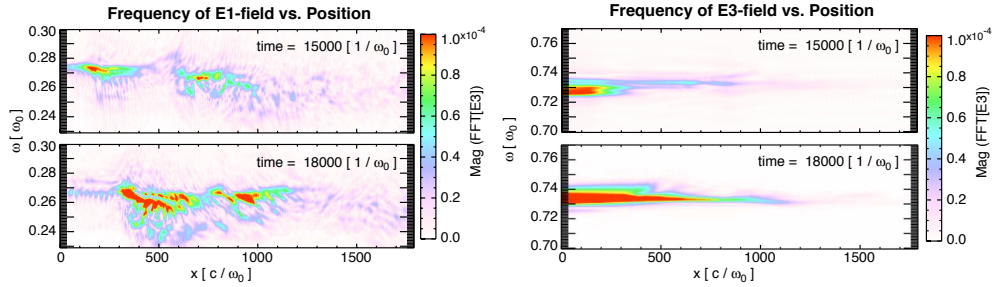


Figure 3.28: Frequency vs. Position of the E1 and E3 Fields for Case 1-30.

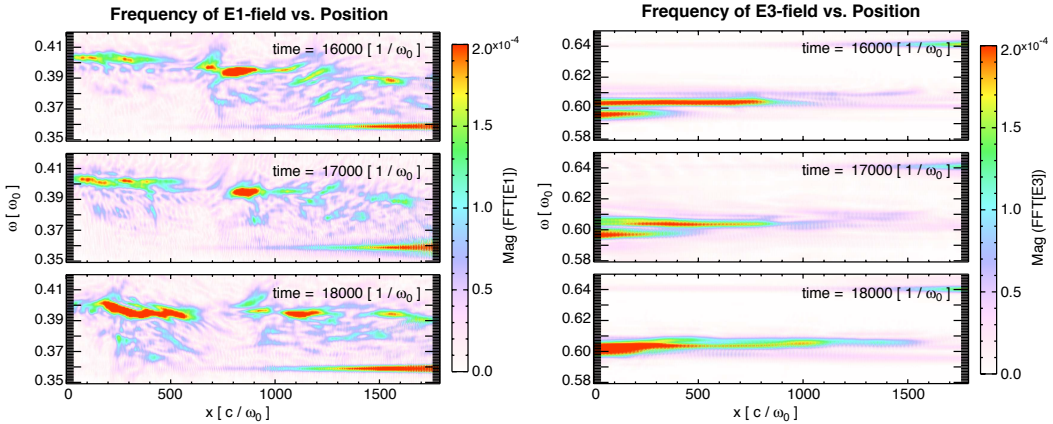


Figure 3.29: Frequency vs. Position of the E1 and E3 Fields for Case 3-30.

light is continually driving the system, and here it is seen that the scattered light grows exponentially in the region of the plasma packets (and depletes the incident laser energy in this region), but once the backscattered light leaves the region of the packet, it stops growing and has a relatively constant amplitude until it exits the edge of the domain.

Figures 3.28 and 3.29 show the frequency content of the convecting packets and of the backscattered light. The frequency of the plasma waves is down-shifted relative to the original resonant SRS frequency. In order to satisfy the necessary frequency-matching conditions for SRS resonance, the frequency of the scattered light is up-shifted relative to the original resonant frequency. These

later times show multiple (clearly separated) frequencies existing simultaneously in the plasma. The separate frequencies of the packets will result in separate backscattered light frequencies (they can beat together, creating modulated reflectivity).

Furthermore, the up-shifted light from a packet that has convected further into the plasma will potentially resonate with a packet that is just growing up in a region closer to the laser-entrance side. The backscattered light travels toward this growing packet. This new packet will shift in frequency similarly to the prior SRS burst, but now (in contrast with the first burst), the frequency shift could potentially result in a resonance with the frequency-shifted backscattered light traveling towards it from the other packet. This can be one cause of the renewed packet growth that was mentioned earlier in reference to Figure 3.18. The separate packets appear to reach a temporary equilibrium frequency due to this effect between packets. As the renewed resonance occurs at the shifted frequency, the new packet (closer to the laser-entrance side) can in fact grow to a larger amplitude than that of the earlier packet. This is further evidenced by a larger frequency shift of the new packet, due to its larger amplitude. This is also seen in Figure 3.28.

In total summary of Case 1-30 and 3-30, we have seen similar nonlinearities with Case I. However, the two cases illustrate how the interplay of these nonlinearities can have different results in slightly different regimes. In both cases, the instability grows at approximately the temporal absolute growth rate. During the saturation of the first burst of SRS, pump depletion plays a very important role in Case 3-30, while in Case 1-30, saturation is completely due to the frequency shift. There is thus a competition between the growth rate of the instability and the rate at which the frequency shift will detune the instability. In

both cases, the sidebands grow immediately after saturation, and as evidenced in the frequency and wavenumber plots, the sidebands give rise to a beam-like velocity indicative of trapped particles streaming between trapped-particle buckets (similarly to Case I). The plasma wave amplitudes at saturation are larger for Case 3-30 than for Case 1-30, but they are relatively similar when normalized to $mv_{the}\omega_p/e$. Both cases show the growth of plasma wave packets. These packets consist of frequency-shifted plasma waves after saturation that convect through the simulation domain (with shifted frequency) at a nonlinear velocity for the rear edge that is intermediate between the group and phase velocities. As the incident light continues to drive the system, further backscattered light grows from these convecting packets at an up-shifted frequency that maintains the frequency-matching conditions for SRS resonance. This backscattered light grows in the packets and stops growing outside of the packets. However, the weak resonance with the background plasma (which has a resonant frequency at the original SRS frequency) results in a periodicity of reflected light shown by the recurrence of minor bursts at $2\pi/\Delta\omega$. In addition to being weakly resonant with the background plasma, these bursts of frequency-shifted light can resonate with new packets of SRS plasma waves that are growing and frequency-shifting. This is a method by which two convecting plasma packets can interact with each other.

3.5 Case IV

The parameters for Case IV are similar to the simulations of L. Yin *et al.* and the experimental parameters of D. Montgomery *et al.* Compared to Cases I, 1-30, and 3-30, the laser intensity is much higher (with $v_{osc}/c = 0.030$ as compared to $v_{osc}/c = 0.007$ and 0.0116) and $k\lambda_D$ is higher (0.34 as opposed to 0.26 and 0.30).

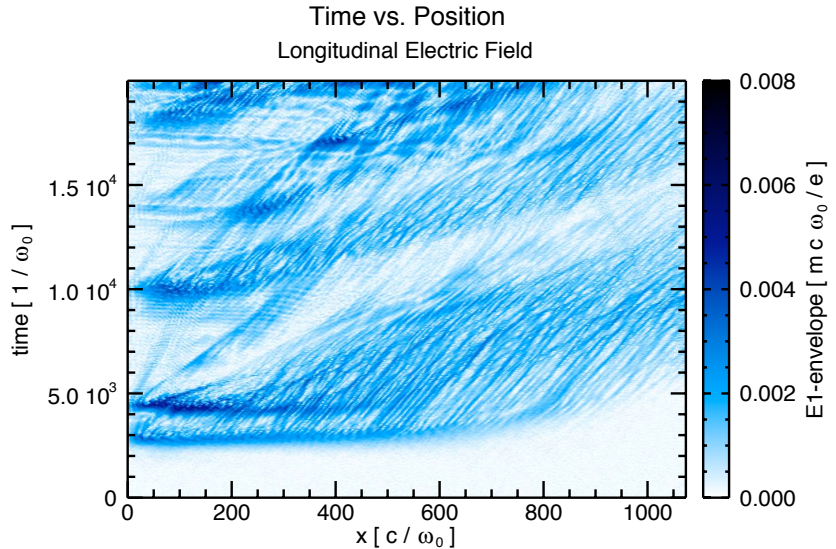


Figure 3.30: Spatio-temporal evolution of the enveloped E1-field for Case IV.

The evolution of the SRS plasma waves is shown in Figure 3.30. The evolution is more complicated for this case as compared to the previous three cases (contrast Figure 3.30 with Figures 3.1 and 3.18). For this case, the length of the plasma in units of c/ω_0 is shorter (the simulations of Yin *et al.* were for a $100\ \mu\text{m}$ length with a 2ω ($\lambda_0 = 0.527\ \mu\text{m}$) rather than 3ω laser), but the length in terms of the convective spatial length in the strong damping regime is greater. Later in Chapter 4 we show how the box length relative to the convective gain length determines the onset of SRS. For this case, the E1-field is smaller in units of $mc\omega_0/e$ when one compares Figure 3.30 with 3.1. However, in terms of $mv_{the}\omega_p/e$, or similarly $mv_\phi\omega_p/e$ for comparable $k\lambda_D$, the peak field is comparable in all cases. This is discussed in the next chapter as well.

There are multiple bursts of SRS plasma waves, compared with just one for Case I. These bursts in plasma waves are correlated with bursts in reflectivity (more detail is also given in the next chapter). The bursts are separated in time

by 4000-5000 ω_0^{-1} . There are two micro-bursts closely spaced together at 3000 ω_0^{-1} and 4500 ω_0^{-1} . This second micro-burst occurs at nonlinearly shifted ω 's and k 's, indicating that SRS occurs within the same packet after a new burst of reflected light grows at the appropriate ω and k . The subsequent bursts (at 10000 ω_0^{-1} , 14000 ω_0^{-1} , and 19000 ω_0^{-1}) appear to occur after the packet from the previous burst has convected a sufficient distance.

The dynamics after saturation are also different for this case. In Figure 3.30, the left edges of the packets appear to have several velocities. For example, the rear edge of the second burst starts at $\omega_0 t = 10000$ and $x\omega_0/c = 0$. The etching speed alluded to earlier corresponds to a line that starts at this point and moves to $\omega_0 t = 20000$ and $x\omega_0/c = 500$. This line can be seen as a boundary for packet activity. However, there are also 3-4 separate streaks of packets seen within this larger packet. This appears to be due to the larger nonlinear frequency shifts. Reflected light coming from deep in the plasma is at a frequency such that its beat with the pump is out of phase with the nonlinearly shifted plasma waves near the edge of the packet. This leads to apparent packet velocities closer to v_ϕ . For example, there is a packet edge that moves from $\omega_0 t = 10000$ and $x\omega_0/c = 0$ to $\omega_0 t = 14000$ and $x\omega_0/c = 500$, giving an apparent velocity of $0.125c$ or $3.4v_{the}$ ($\approx v_\phi$).

The frequency and wavenumber content of the SRS plasma waves is shown in Figure 3.31, where the Fourier transform of the E1-field over the entire length and time of the simulation is plotted. The bottom plot is a zoomed-in plot for the strongest signals. The spectrum of waves is much more nonlinear for this case. The first burst of SRS corresponds to $(\omega/\omega_0, kc/\omega_0)$ of $(0.225, 1.73)$. Similarly to previous cases, there is a frequency and wavenumber shift of this burst that appears as a streak originating from $(0.225, 1.73)$ to a lower frequency and lower

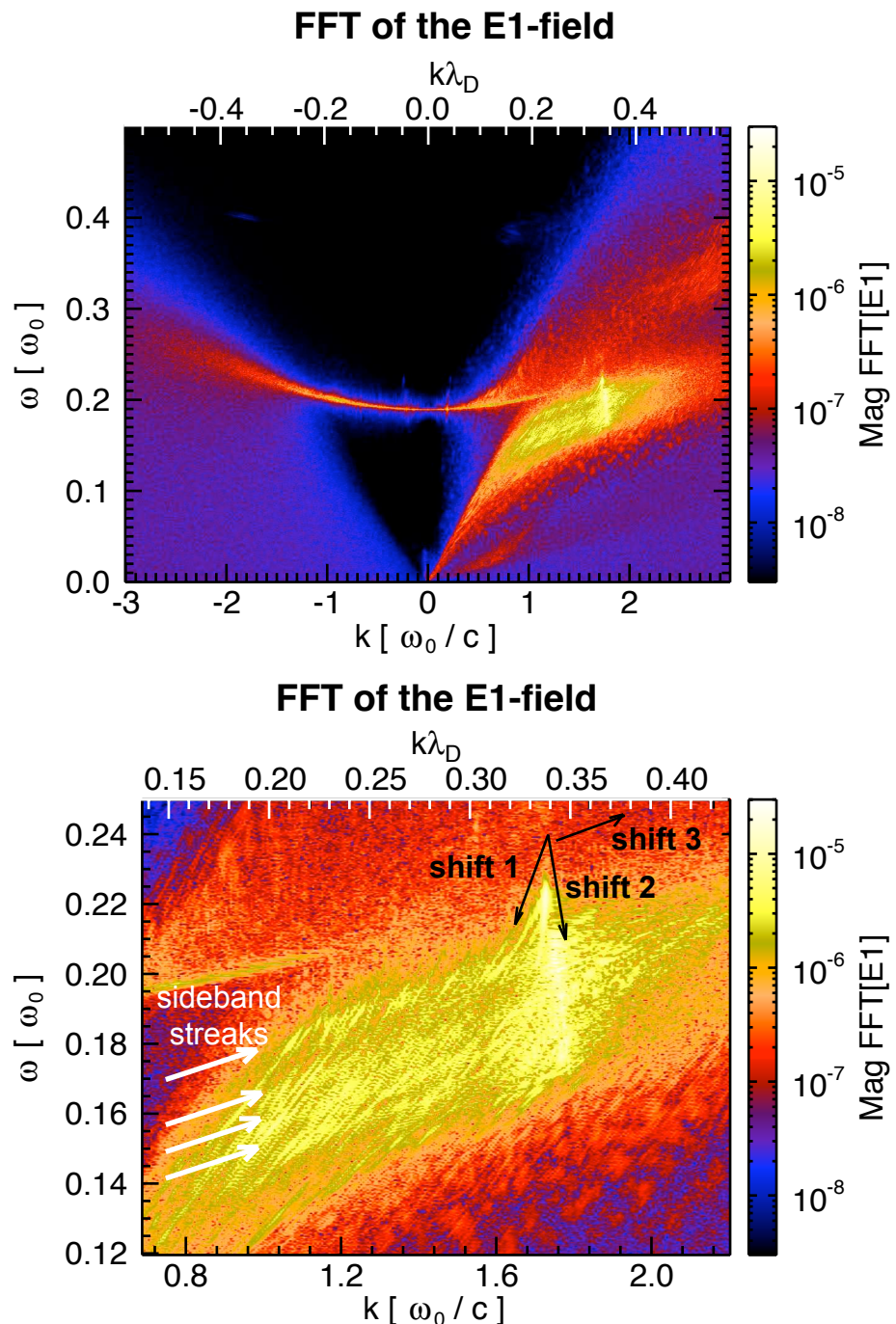


Figure 3.31: Frequency vs. wavenumber of the E1-field for Case IV.

wavenumber of $(0.205, 1.70)$, labelled in the figure as shift 1. Subsequent bursts of SRS appear as points on the line labelled shift 2 at approximately $(0.20, 1.75)$, $(0.19, 1.80)$, and $(0.17, 1.85)$, each of which have their own respective shifts in frequency and wavenumber in time. The sequence of bursts lies along the locus of points that satisfy frequency and wavenumber matching between the incident laser and all possible backscattered light waves that exist along the light wave dispersion curve, as explained previously with Eqn. 3.1. This locus of points falls along the line labelled shift 2; this shift 2 is qualitatively the same shift 2 that was shown in Figure 3.5. Shift 3 shows the shift to higher wavenumbers at constant frequency, but it is less pronounced as compared to Case I.

In addition to the shifts, Figure 3.31 has a low frequency and wavenumber pattern stretching from $(0, 0)$ to $(0.3, 1.0)$; similarly to Case I, this matches the frequency and wavenumber differences between the first SRS burst and the initial sideband modes. The Figure shows sideband modes spread throughout a large range, with several apparent streaks stretching over the frequency and wavenumber range between $(0.14, 0.8)$ and $(0.20, 1.7)$. These sidebands each lie along a streak of modes (labelled sideband streaks) that intersect with the sequence of progressively lower-frequency SRS bursts (described above along the line for shift 2). Yin *et al.* referenced these sideband streaks as beam acoustic modes, with their intersection with SRS modes representing scattering off the beam acoustic modes (as opposed to scattering from linear plasma wave modes). Finally, there is an artificial boundary to these streaks that stretches from $(0, 0)$ to $(0.2, 1.0)$, similarly to Case I (where this boundary corresponded to the velocity of particles streaming at the high-velocity edge of the trapped-particle buckets).

The temporal evolution of the wavenumbers for the E1-field is shown in Figure

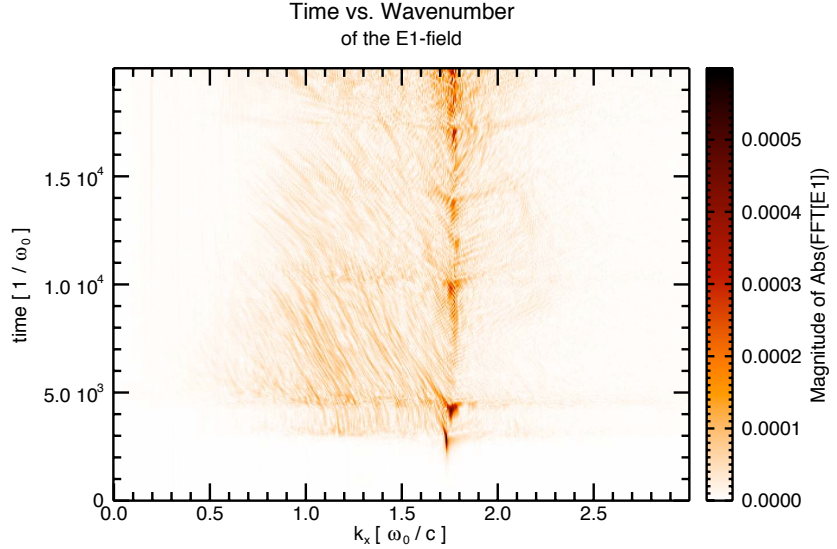


Figure 3.32: Wavenumber vs. time for the E1-field for Case IV.

3.32, where the (very slight) progression of bursts to successively higher wavenumbers is seen. Here the bursts are much more punctuated in time, but similarly with previous cases, there are both positive and negative wavenumber shifts. Each burst ends with a streak to lower wavenumber. The wisp-like behavior to higher wavenumbers here consists of more uniform streaks. As the evolution of a convecting packet does not exist in the same sense for Case IV, the gradual shifts in wavenumber are replaced by abrupt streaks in wavenumber over time at a relatively constant rate. There is a wide swath of modes to lower and higher wavenumbers that occurs during the first burst (and can be seen also in several other bursts). These sideband modes again occur predominantly at lower wavenumbers. Here it is clear that the shifts to lower wavenumber are present in the sidebands as well with the slope (dk/dt).

The temporal evolution of the plasma waves' frequency is shown in Figure 3.33, where the Wigner transform of the E1-field is plotted for $x\omega_0/c = 200$ and

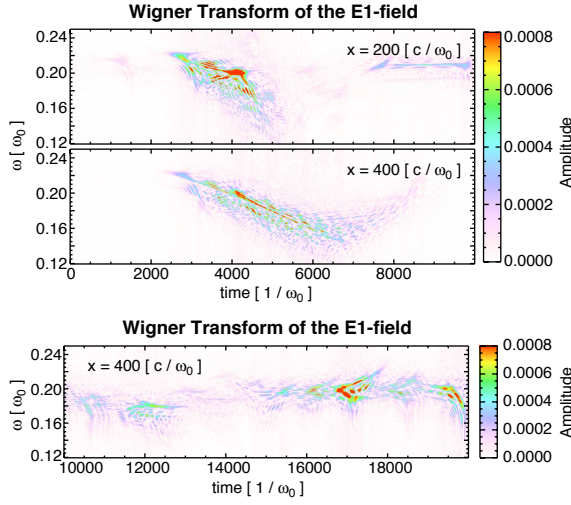


Figure 3.33: Frequency vs. time of the plasma waves (Wigner transform of the E1-field) at $x\omega_0/c = 200$ and 400 for Case IV. Top two plots show first half of simulation from $\omega_0 t = 0 - 10000$, while the bottom plot shows the second half (only for $x\omega_0/c = 400$) from $\omega_0 t = 10000 - 20000$.

400. The first two plots are for a time domain corresponding to the first half of the simulation, while the third also shows later times for $x\omega_0/c = 400$. The unperturbed frequency was $\omega/\omega_0 = 0.23$. The frequency shifts are large, rapid, and nearly continuous during the first two bursts (occurring between $\omega_0 t = 2000$ and 5000). Compared with previous frequency shifts on the order of $\Delta\omega/\omega_0 = 0.006$, here the shifts are much larger, with shifts for individual bursts between $\Delta\omega/\omega_0 = 0.01$ and 0.06 ($\omega_0/\omega_p \approx 5$ so between $\Delta\omega/\omega_p = 0.002$ and 0.012). The duration of the bursts' growth and saturation is very short, with each burst being $\approx 1000\omega_0^{-1}$. Based on studying movies of $\omega(t)$ versus x , we observe that there is a prolonged shift resulting from the first two bursts that persists well after the time of saturation. Even though the second burst saturates at $\omega_0 t \approx 5000$, the plasma waves still continue to shift significantly in frequency after $\omega_0 t \approx 5000$. This is evident in Figure 3.33 and later in Figure 3.39. Eventually, the frequency of the

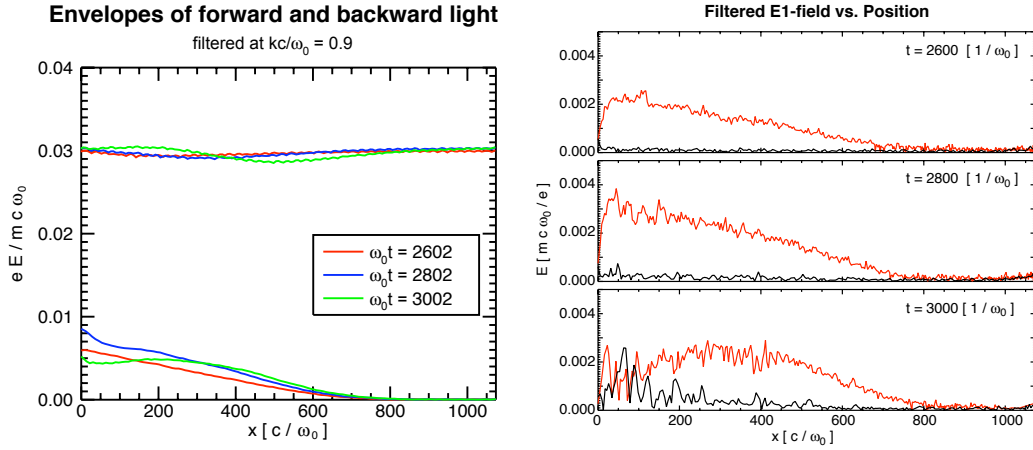


Figure 3.34: Envelopes of filtered E-fields for Case IV. Left: incident (top 3 lines) and backscattered (bottom 3 lines) light waves; right: SRS plasma wave (red) and sidebands (black).

wave at a location in x returns to its linear (unshifted) value. The frequency shifts that result from subsequent bursts are not as negative, but they still occur rapidly.

In Figure 3.34, the filtered E-fields during the first SRS burst are plotted. The filtering process is the same as that described previously. On the right, the SRS plasma waves are again plotted in red and the sidebands are plotted in black, while on the left are shown the light wave envelopes. The backscattered light is near its saturated maximum amplitude at $\omega_0 t = 2600$. Similarly with Case 1-30, this amplitude is not at all close to the incident light wave's amplitude, and pump depletion is ruled out as a saturation mechanism for this case. The sidebands grow significantly only after the second plotted time, that is, only after saturation. The sidebands are also therefore ruled out as a saturation mechanism of the first burst. With regard to frequency shifts, the maximum frequency shift of the first burst is on the order of $\Delta\omega/\omega_0 = 0.01$, with the detuning rate on the

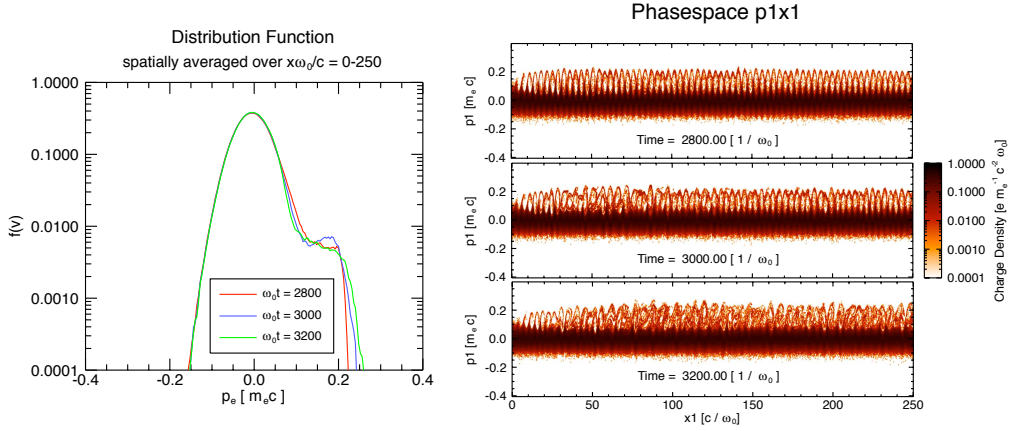


Figure 3.35: Spatially averaged distribution function (left) and electron phasespace plots (right) for Case IV at $\omega_0 t = 2800, 3000$, and 3200 .

order of $\pi/0.01 \approx 300\omega_0^{-1}$. In Figure 3.33, the plasma waves at $x\omega_0/c = 200$ have already shifted by $\omega_0 t = 2800$, so the saturation mechanism here is attributed to the resulting phase detuning.

The electron phasespace during the first burst of SRS shows qualitatively similar behavior to Case I. Figure 3.35 shows the first quarter of the simulation domain where the mixing of trapped-particle buckets can be seen in analogy with the sideband behavior of Case I. These three times are shortly after the saturation point for this burst (note that the first frame here corresponds to the second frame of Figure 3.34). At $\omega_0 t = 2800$, only a few trapped particles are moving between buckets. Saturation occurs at approximately $\omega_0 t = 2800$, at which time the sidebands have just begun to grow, as seen by the modulation of the E1-field. By $\omega_0 t = 3000$, the particles have begun to mix more significantly as the sidebands grow after saturation, and by $\omega_0 t = 3200$, all of the trapped particle buckets in the visible window have significantly phase-mixed. The distribution function (spatially averaged over the same region that is plotted to the right) shows a more dramatic bump-on-tail compared to Case I as the trapped particles begin

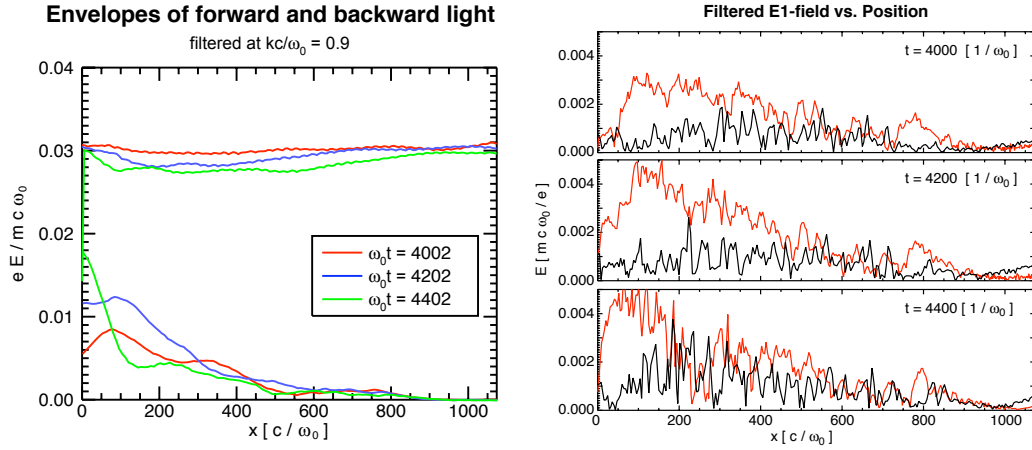


Figure 3.36: Envelopes of filtered E-fields for Case IV. Left: incident (top 3 lines) and backscattered (bottom 3 lines) light waves; right: SRS plasma wave (red) and sidebands (black).

to stream across buckets, but again this is not a coherent beam. When the buckets begin to mix and particles begin streaming from one bucket into a neighboring bucket (or buckets), then the distribution function looks like the bump-on-tail. However, as the mixing evolves and the particles streaming into neighboring buckets are once again trapped, the population of trapped particles begins to mix again and there is no bump-on-tail. This progression can be seen in the tail's behavior between the three times, with a relatively flat tail at $\omega_0 t = 2800$, a slight bump-on-tail at $\omega_0 t = 3000$, and back to flattened at $\omega_0 t = 3200$. More particles are trapped by $\omega_0 t = 3200$, and the tail can be seen to extend to a slightly higher velocity.

SRS is driven strongly enough in Case IV that a second micro-burst quickly grows after the saturation of the first burst. The wave amplitudes of this second burst are shown in Figure 3.36. In comparison with the first burst (Figure 3.34), the plasma wave is driven to a higher amplitude and the backscattered light is

driven to roughly twice the amplitude. The scattered light is driven primarily in the range between $x\omega_0/c = 0 - 200$, a region in which there is a large amplitude plasma wave, negligible sidebands, and backscattered light from regions further into the plasma. The brief resonance that occurs is shortly shut off by another frequency shift, as can be seen again in Figure 3.33, where the frequency evolution at $x\omega_0/c = 200$ versus 400 can be compared.

Contrary to Case I, where the plasma wave packet is a long-lived entity that moves through the system, the character of the whole plasma changes dramatically during the SRS bursts in Case IV. The trapping effects are so strongly driven, and so many particles are trapped, that there is even a slight return drift of the bulk plasma in compensation. The large population of trapped particles can be seen in Figure 3.37 which shows the spatially averaged distribution function at five times close to the second burst ($\omega_0 t = 3400, 4000, 4200, 4400$ and 4800) and the phasespace for the regions over which the distribution function is taken are plotted on the right (from $x\omega_0/c = 100 - 300$). The first frame at $\omega_0 t = 3400$ provides the reference point for the phasespace just after the saturation of the first SRS burst. From $\omega_0 t = 4000$ to 4400 , the wave structure is being driven again as SRS recurs during the second micro-burst and more particles are being trapped. The saturation has already occurred by $\omega_0 t = 4400$, as can be seen in Figure 3.36. Although the sideband amplitudes are roughly 25-50% of the primary SRS plasma wave amplitude throughout the frames of Figure 3.37, the bucket mixing becomes much more chaotic when the sidebands are of equal amplitudes to the SRS plasma wave, which here occurs after $\omega_0 t = 4400$. By $\omega_0 t = 4800$, many particles have been influenced by the wave, and the distribution function has its maximum at a slightly negative velocity (drifting backwards relative to the direction of the SRS plasma waves).

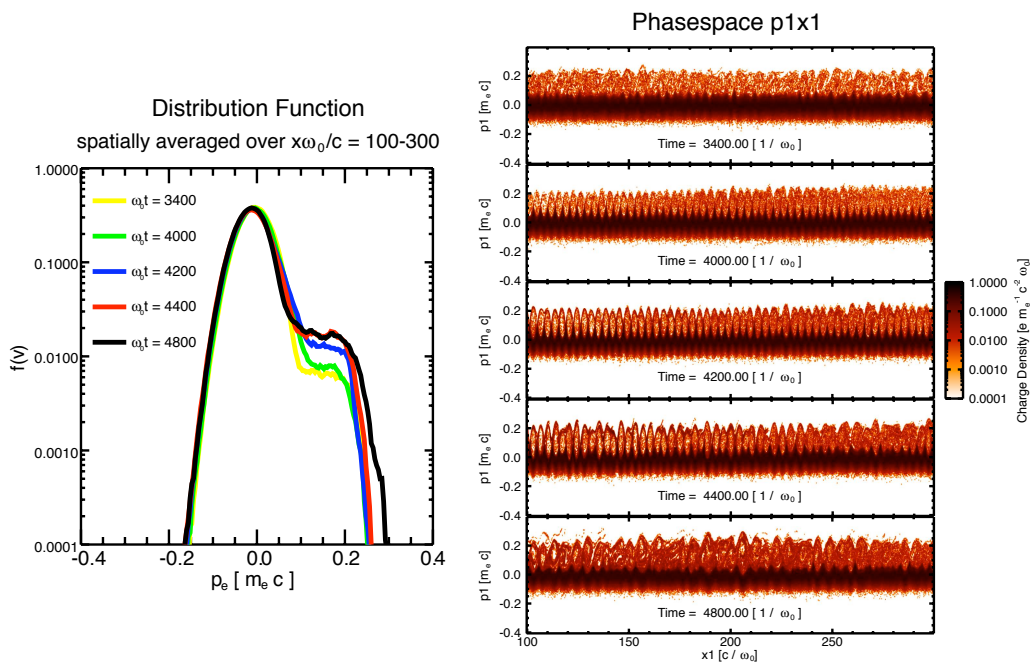


Figure 3.37: Spatially averaged distribution function for Case IV at $\omega_0 t = 0, 2500$, and 5000.

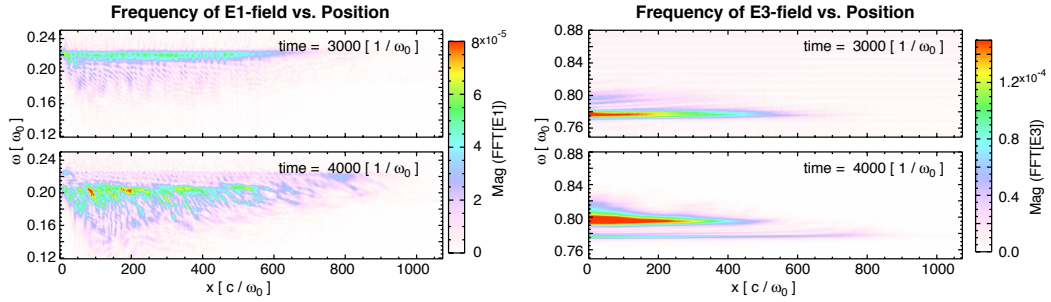


Figure 3.38: Frequency vs. space of the plasma waves (E1-field, left) and scattered light waves (E3-field, right) for Case IV.

The strong trapping leads to large shifts of the real and imaginary parts of the frequency which also affect the scattered light waves. With the second burst of SRS occurring at a lower frequency, the scattered light wave in this burst must occur at a higher frequency. The difference in frequencies between the two bursts can be seen in Figure 3.38, where the Fourier transforms of the E1 and E3-fields are plotted to give frequency versus space for two different times, one during the first burst and one during the second. The plasma waves (left) occur first at $\omega/\omega_0 = 0.22$, followed by 0.20, and the backscattered light waves correspondingly occur at $\omega/\omega_0 = 0.78$ and 0.80. The second frame also shows some scatter at the originally resonant frequency, scattering due to the very front of the first burst (at $x\omega_0/c = 800$) that has not completely decayed.

Subsequent scattering events show similar trends. In Figure 3.39, the frequencies of the third major burst are plotted (at $\omega_0 t = 10000, 11000$, and 12000). There are two bursts of SRS in the simulation box at these times. Early in the box (on the left edge of the plots) is the third burst, while further into the box (on the right edge) is the second burst that is still convecting through the box. The light coming from the second burst is frequency up-shifted relative to the frequency of the third burst. As the third burst grows, saturates, and frequency

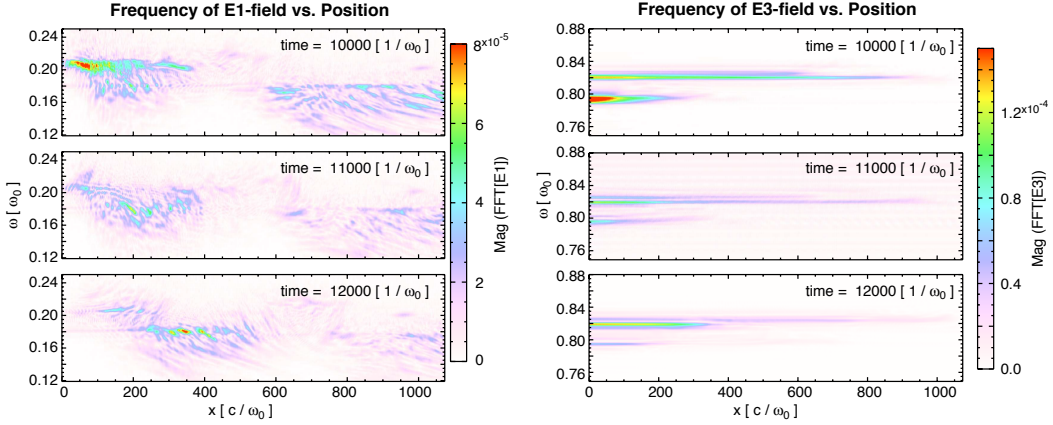


Figure 3.39: Frequency vs. space of the plasma waves (E1-field, left) and scattered light waves (E3-field, right) for Case IV.

shifts, it shifts towards a potentially resonant interaction with the light coming from the second burst. This renewed resonance, even though the third burst has saturated, causes the third burst to grow again slightly at the new down-shifted frequency. As with the previous cases, this is a novel way for convecting plasma packets to interact with each, even if both have saturated and frequency-shifted.

In summary, while qualitatively similar nonlinearities were seen for Case IV as for previous cases, the overall dynamics of the simulation were much more strongly nonlinear. The frequency shifts were very dramatic by comparison, and here they saturated SRS before pump depletion occurred. The sidebands grew after saturation and the phasespace of trapped particle buckets followed a similar nonlinear evolution. Here, however, due to the more nonlinear evolution, a much more significant population of electrons was affected, so many in fact that the bulk of the distribution was also slightly affected. These sidebands could be interpreted as beam acoustic modes, given the altered nature of the distribution function, and the resonance of SRS from frequency down-shifted plasma waves could also be interpreted as scattering from beam acoustic modes, as a frequency down-shifted

plasma wave will match with the plasma mode given by modified distribution functions. The frequency shifts of the plasma waves resulted in backscattered light at correspondingly shifted frequencies such that ω and k matching were satisfied. When two packets exist at different locations, the backscatter from one packet can be further amplified if the frequency shifts of each packet are nearly equal. Overall, Case IV represents the most strongly driven and most strongly kinetic case that will be represented in the trends of the next chapter.

3.6 Conclusions

Four simulations have been presented in this chapter. Case I was the most weakly nonlinear and most weakly driven, Cases 1-30 and 3-30 had an intermediate value of $k\lambda_D$ and driving laser intensity, and Case IV was the most strongly nonlinear and most strongly driven.

SRS appears to grow absolutely in all four cases (growth in time at each location), regardless of initially being below the threshold for absolute instability. The presence of trapped particle motion suggests that the plasma wave's damping rate was modified during growth. As the instability grew, there were nonlinear frequency and wavenumber shifts in all cases. The bulk of the plasma wave packet shifted negatively in frequency and slightly negatively in wavenumber, while the tail end of the packet shifted negligibly in frequency and positively in wavenumber. Subsequent bursts of the plasma wave that either grew at lower frequencies or shifted to lower frequencies had a more positive wavenumber. This positive shift in wavenumber matched the wavenumber-matching condition determined by the driving laser and frequency up-shifted backscattered light.

Saturation was due to two separate effects. For Cases I and 3-30, pump

depletion played a significant role in saturation, while for Cases IV and 1-30, the saturation was due to a detuning of the SRS resonance by a nonlinear frequency shift of the plasma wave. While the pump was significantly depleted in Cases I and 3-30, the plasma waves in these cases also had frequency shifts. These shifts, however, did not affect the resonance until after the backscattered light had grown to significant levels and depleted the pump laser intensity. In all four cases, sidebands to the SRS plasma wave grew immediately after saturation. The resulting modulation of the plasma waves were shown for Cases I and IV, as was the modification of electron phasespace due to the modulation. As SRS was growing, electrons were initially confined to bouncing in single buckets. After SRS saturated, the plasma waves stopped growing, but sidebands now grew and the modulation of the wave increased, resulting in the movement of electrons between buckets. With very strong modulations, entire buckets appeared to coalesce. After the strong mixing of trapped particle buckets, the end result was a smearing of electrons throughout the phasespace region of the buckets. The tail of the spatially-averaged distribution functions progressed in time from an initially flat tail (as the wave grew and more particles were trapped), to a tail that alternated between a slight bump-on-tail and a slightly negatively-sloped tail (as particles moved between buckets and buckets coalesced), and ending with a flat tail again (as the electrons were smeared throughout the bucket). It was also pointed out that the spatial average over phasespace results in a tail that is flattened from approximately $v_\phi < v < v_\phi + v_{tr}$, as the region from $v_\phi - v_{tr} < v < v_\phi$ still contains a large number of untrapped particles.

After the initial saturation, the plasma wave packets convected through the simulation domain. The rear edge of the packet etches away, causing the packet to appear to move faster than the group velocity. SRS scattering continues as the packet convects, since the system is continually driven with new laser en-

ergy. The backscattered light arising from this SRS off convecting packets is frequency up-shifted to match the frequency shift of the plasma waves in the packet. The frequency shifted light grows within the region of the packet and stops growing outside of the packet. The plasma waves in the region behind the convecting packet grow at the linearly resonant frequency, and as they are driven off-resonance with the frequency shifted backscattered light from the packet, there is a periodic growth of weak, nonresonant SRS at a rate determined by the frequency shift. This is evident in both weak plasma wave growth and the periodic recurrence of the reflectivity.

After the plasma packet has convected a sufficient distance for convective growth to recur, a new major burst of SRS can occur. This new burst undergoes similar nonlinear behavior to the initial burst of SRS. However, if the previous convecting packet has not exited the domain yet, the frequency shift of the new plasma waves can also now bring these waves into another resonance with the frequency shifted backscattered light coming off the other packet. As a result, the behavior of SRS after saturation is dependent on the convection of plasma wave packets and the possible interaction of these packets with each other through scattered light that travels from one packet to another.

These four simulations set the stage for a more methodical study of SRS across this range of parameters. The growth, saturation, and recurrence are all affected by nonlinear trapped particle effects, and a determination of the growth rates, the maximum wave amplitudes, the determination of whether pump depletion (large growth) occurs before frequency shifts detune the instability (or vice versa), and the evolution of plasma wave packets are all affected by trapped particles. This is the subject of the next chapter.

CHAPTER 4

Trends in 1D SRS

The previous chapter illustrated the richly nonlinear behavior of SRS in a kinetic regime where $k\lambda_D \gtrsim 0.25$. This regime is relevant for NIF. The growth of SRS was affected by trapped particles, SRS saturation was dominated by either nonlinear frequency shifts or pump depletion, and SRS recurrence was affected by the convection of plasma wave packets. The analysis of SRS is continued in this chapter by quantitatively comparing an array of simulations that covers the parameter space of the previous chapter.

The variable parameters in this array include the electron temperature, electron density, plasma length, and driving laser intensity. Two electron temperatures were chosen - 700 eV and 3 keV, with 3 keV as the NIF-relevant electron temperature and 700 eV chosen for comparison with the lower simulation temperatures of [54, 59, 61, 64] and the laser hot-spot experiments of Montgomery *et al.* [40]. The electron temperature and density both affect $k\lambda_D$ of the scattered plasma wave, a parameter that indicates how strongly the plasma wave will be subject to kinetic effects ($k\lambda_D \approx v_{the}/v_\phi$). The comparison between electron temperatures of 3 keV and 700 eV is extended between $k\lambda_D = 0.26$ (similar to simulations of Vu *et al.* [54] and Case I of the previous chapter), 0.30 (similar to Cases 1-30 and 3-30), and 0.34 (similar to simulations of Yin *et al.* [61] and Case IV).

The parameters are presented first, followed by an exploration of how the

onset and growth of SRS depend on the parameters. The saturation of the first burst of SRS is then shown, with an emphasis on the plasma wave magnitudes and frequency shifts. The recurrence is then studied in terms of the convection of plasma wave packets, particularly in trends that are seen as plasma length is varied. Finally, the total time-averaged SRS reflectivity is analyzed.

4.1 Parameters

For comparison with NIF-relevant parameters, the laser wavelength was taken to be $\lambda_0 = 0.351\mu\text{m}$. Laser intensities ranged from 10^{14} to 10^{16} W/cm^2 . Two electron temperatures were investigated, 3 keV and 700 eV. The electron densities were then chosen so that the $k\lambda_D$ of backward SRS is 0.26, 0.30, or 0.34, resulting in nine densities. Finally, three simulation lengths, 100, 60, and 30 μm , were investigated.

The parameters are tabulated (in normalized units) in Table 4.1. Laser intensities ranged over $v_{osc}/c = 0.003$ to 0.030. The electron temperatures corresponded to $v_{the}/c = 0.0766$ and 0.037. The simulation lengths were $x\omega_0/c = 1790$, 1074, and 537. All of the simulations in this chapter used 512 particles per cell, a cell size on the order of the electron Debye length, fixed ions, and a total simulation time of 20,000 ω_0^{-1} ($\approx 4 \text{ ps}$).

Particular cases will be referenced by a shorthand notation of three numbers. The first number will denote $k\lambda_D$ ($\times 10^2$), followed by electron temperature (3 and 700 for 3 keV and 700 eV) and length (in μm). For example, Case 26-3-100 refers to the simulation in which $k\lambda_D = 0.26$, $T_e = 3 \text{ keV}$, and the plasma length is 100 μm , whereas Case 34-700-30 refers to the simulation in which $k\lambda_D = 0.34$, $T_e = 700 \text{ eV}$, and the plasma length is 30 μm . In both cases, the density is

Table 4.1: Normalized simulation parameters for studying SRS trends.

v_{osc}/c	0.0030, 0.0042, 0.0059 0.0067, 0.0079, 0.0082 0.0097, 0.011, 0.013 0.016, 0.019, 0.021, 0.030
$x\omega_0/c$	1790, 1074, 537
$v_{the}/c = 0.0766$ $(T_e = 3 \text{ keV})$	$n/n_{cr} = 0.153, k\lambda_D = 0.26$ $n/n_{cr} = 0.128, k\lambda_D = 0.30$ $n/n_{cr} = 0.107, k\lambda_D = 0.34$
$v_{the}/c = 0.037$ $(T_e = 700 \text{ eV})$	$n/n_{cr} = 0.056, k\lambda_D = 0.26$ $n/n_{cr} = 0.044, k\lambda_D = 0.30$ $n/n_{cr} = 0.036, k\lambda_D = 0.34$

implied by the particular combination of $k\lambda_D$ and T_e .

4.2 SRS threshold and growth

This section explores the SRS threshold and growth rate. The growth rates of SRS for both the spatial and temporal cases, and in the absolute and convective regimes, was examined analytically by Forslund *et al.* [6]. Recent work by Vu *et al.* [58] has postulated that if particles start bouncing in the plasma wave and decrease the Landau damping rate, SRS can undergo kinetic inflation and grow to larger amplitudes than are predicted by convective growth in the strongly damped regime. Comparisons are made with both convective and absolute instability. We note that, to our knowledge, none of the recent work on kinetic inflation has explicitly discussed if absolute growth occurs.

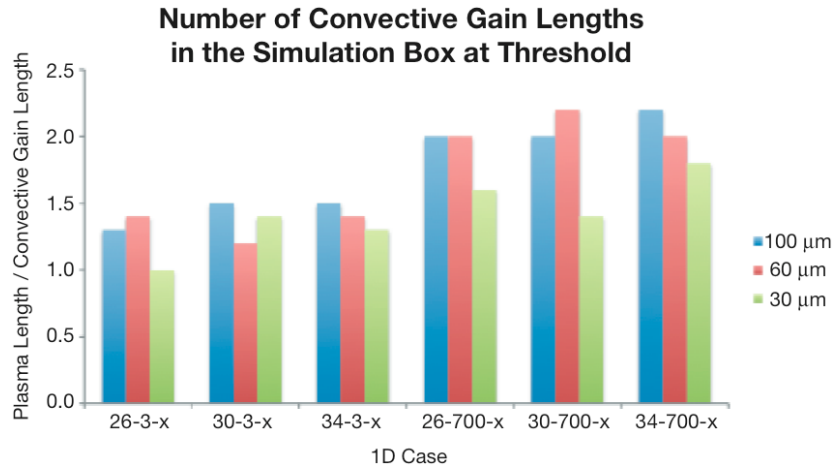


Figure 4.1: The number of convective gain lengths in the simulation box at the onset of SRS.

The onset threshold is shown first, where the SRS threshold for each set of plasma parameters is defined here as the minimum laser intensity for which time-averaged SRS reflectivities are above 0.1%. The simulation thresholds, expressed as a ratio of plasma length to convective gain length (in the strongly damped regime), are shown in Figure 4.1. The onset threshold will be examined in terms of laser intensity at the end of the chapter (see Figure 4.26) when reflectivities are analyzed, but for the purposes of classifying a threshold in terms of absolute versus convective instability, the onset laser intensity is here converted into a convective gain length (defined as $v_{\perp}\gamma_p/\gamma_0^2$, see Chapter 2). In each case, the laser intensity is below the absolute threshold, where the Landau damping rate is used for the plasma wave damping rate.

The onset threshold in all cases lies between ≈ 1 and 2 , meaning that the interaction length at threshold is equal to the length for which 1-2 e-foldings of convective growth can occur. As each set of parameters is below the theoretical threshold for absolute instability at the onset laser intensity, Figure 4.1 implies

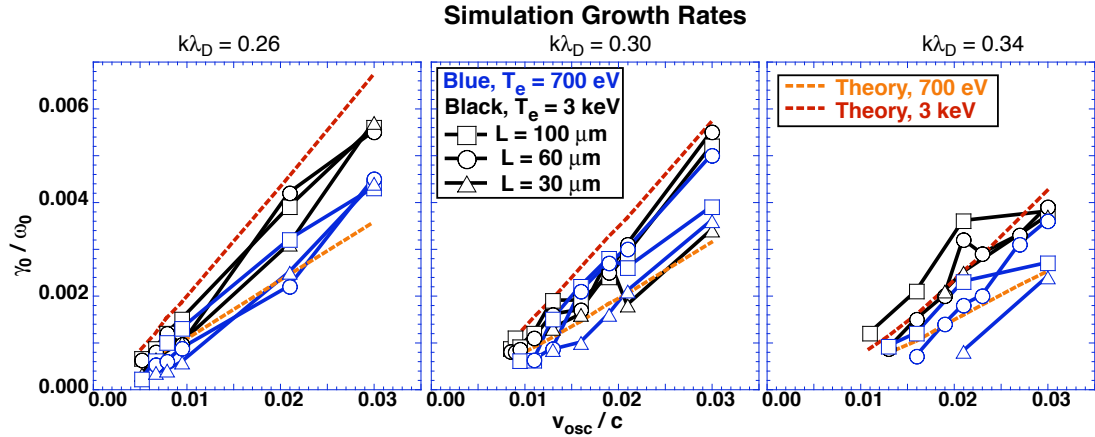


Figure 4.2: Measured simulation growth rates. Theory curves show the absolute growth rate.

that some level of convective growth is necessary before significant SRS occurs, that is, there is a requirement on the interaction length to be longer than one to two convective gain lengths. It is also evident that the lower temperature/density cases (with $T_e = 700$ eV) have a slightly higher ratio. An interpretation of this effect will be presented after discussing the growth rates.

The simulations of the previous chapter showed that the plasma and scattered light waves did not grow as a convective instability, but rather indicated that SRS grows to its first peak as an absolute instability. The temporal growth rate of SRS for the first burst in each simulation is shown in Figure 4.2. The growth rate was measured by fitting an exponential curve to the amplitude of the E1-field at a fixed position where the first peak of SRS grows. Even though the onset laser intensity for each set of parameters matches a convective gain length, each simulation shows an absolute-like growth, where the location in space of the peak amplitude of the plasma wave remains fixed and each point of the plasma wave packet that is stimulated by the scattering process grows uniformly until saturation. If the instability were to grow primarily as a convective instability,

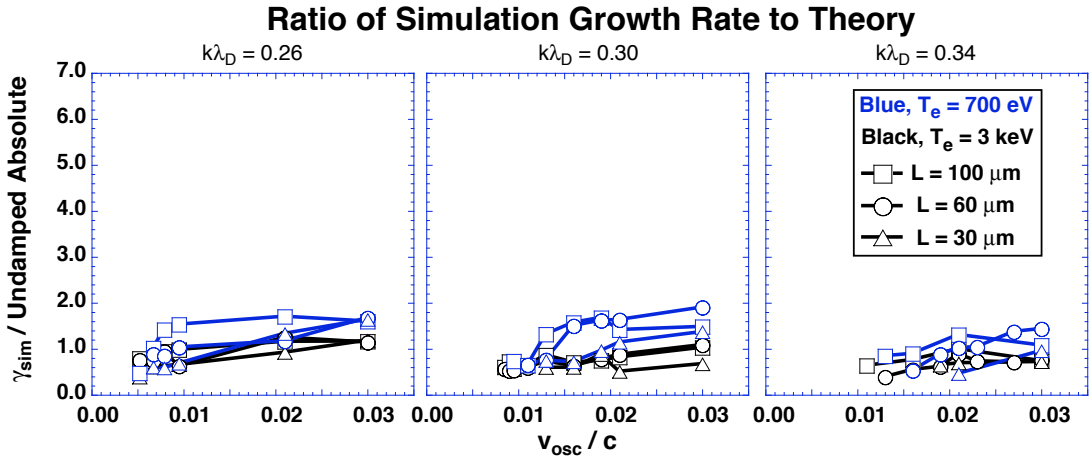


Figure 4.3: Ratio of measured growth rate to the undamped ($\gamma_p = 0$) absolute growth rate.

the point of peak growth would convect backwards at a velocity given by $\partial\omega/\partial k$ of the Raman dispersion relation ($\approx 0.5c$ for the simulations here).

The measured growth rates are compared against each other and against the theoretical absolute growth rate as given by $\gamma_{\text{abs}} = 2\gamma_0\sqrt{v_g/v_-}$, where γ_0 is the undamped temporal growth rate and the damping rate, γ_p , has been neglected. While the fit with theory is not exact, the simulation growth rates do compare well against the theory curves. The growth rates increase linearly with v_{osc}/c , are slightly higher for the higher temperature/density combination ($T_e = 3 \text{ keV}$), and decrease as $k\lambda_D$ increases. These results indicate that kinetic inflation occurs and that this leads to absolute growth after the damping rate approaches zero.

This correspondence with the theoretical growth rate is further illustrated in Figure 4.3, where the ratios of the measured growth rates with the undamped ($\gamma_p = 0$) absolute growth rates are plotted. Even though the simulation growth rate is measured at a fixed point, all points grow at a similar growth rate, as discussed in the previous chapter. For a value of 1.0 in Figure 4.3, the simulation

growth rate equals the theoretical value. Here, the measured growth rates are between 0.5-1.5 times the theoretical value for all of the simulations. For comparison, the purely temporal growth is approximately 1.5-2.5 times larger than the absolute growth rate.

The agreement of the simulation growth rates with the undamped absolute growth rates implies that the damping has become less significant by the time SRS is exponentially growing towards saturation. Even though each set of parameters had an onset intensity below the absolute threshold and appeared to require that the laser intensity must be large enough for convective growth to occur, these growth rates imply that a nonlinear mechanism is at work. The spatio-temporal growth of SRS is complicated by the presence of multiple noise sources and time-dependent trapped particle effects as the waves grow. Kinetic inflation is an obvious explanation, but the plasma wave amplitudes are still small by the time particles begin bouncing; this makes it very difficult to establish whether SRS has entered a kinetically inflated regime in a particle-in-cell simulation.

To illustrate that particles execute several bounces during the initial stage of SRS growth at the onset, Figure 4.4 shows a number of plots for Case 30-3-100 with $v_{osc}/c = 0.008$. For its parameters, SRS is initially considerably below the absolute threshold with $\beta \simeq 16$ ($\beta < 2$ is the absolute threshold). When the laser drives the plasma, SRS first grows as a convective instability.

The upper two plots show the tranverse E3-field, with wavenumbers versus space (left) and a lineout of $kc/\omega_0 = 0.7$ (right). The strong signal at $kc/\omega_0 \approx 0.94$ is the incident laser. While there are edge effects from the transform on the sides of the box, it is still clear that the backscattered light signal at $kc/\omega_0 = 0.7$ is growing exponentially across the box. At this time ($\omega_0 t = 6000$), the spatial growth rate is 0.0007, in good agreement with the theoretical convective growth

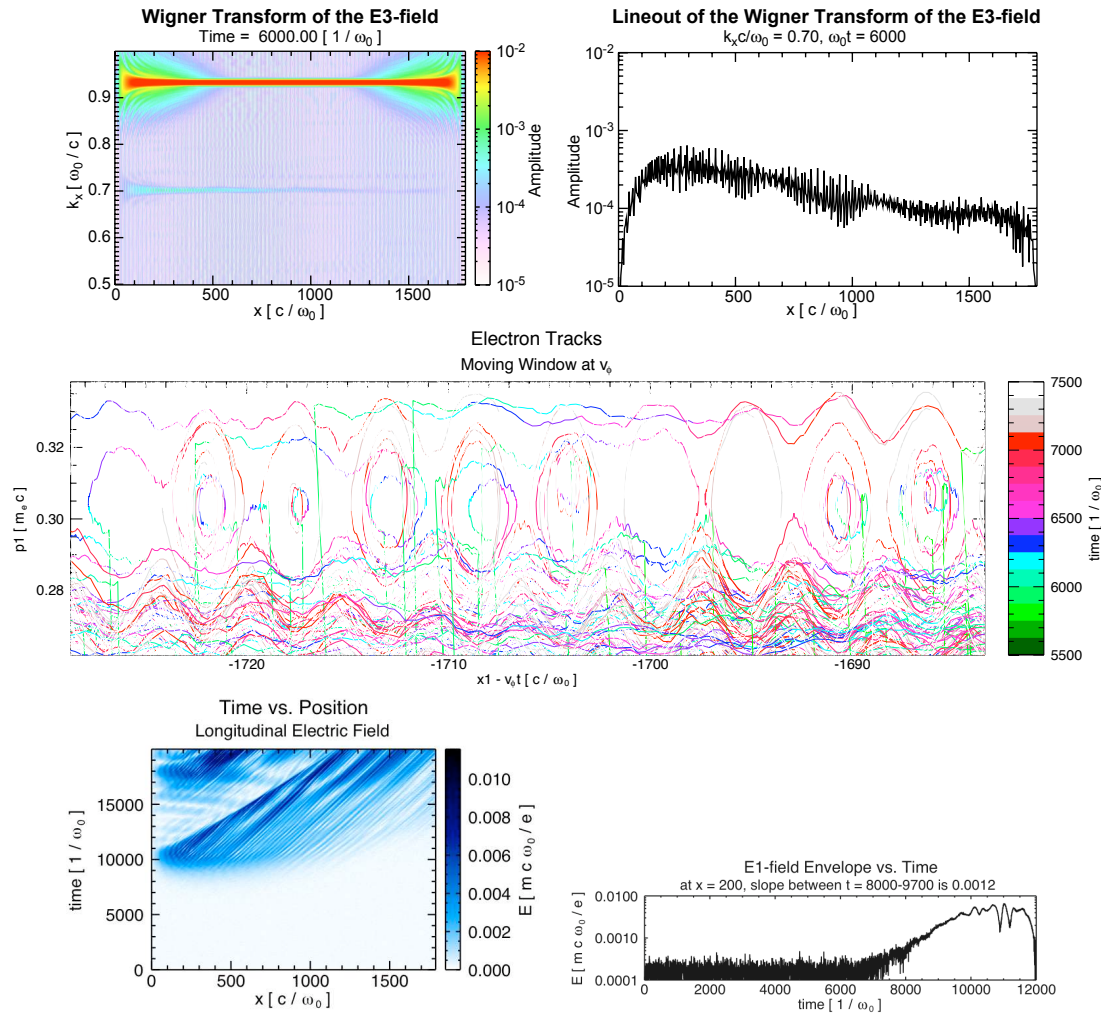


Figure 4.4: Trapped particles in simulation 30-3-100, with $v_{osc}/c = 0.008$.

rate of 0.00068. As shown in the bottom two plots, later in time, starting at $\omega_0 t = 7000$, the growth rate in time is measured to be 0.0012, in good agreement with the theoretical absolute growth rate of 0.0014. To see why this transition from convective to absolute growth occurs, several trapped particles have been tracked in space and time and are plotted in the middle. The window has been altered to reflect a scale that is moving at the phase velocity of the SRS plasma wave. The oval structures show that particles are bouncing, and the time scale has been artificially clamped at $\omega_0 t = 7500$ (any tracks past $\omega_0 t = 7500$ will be colored white and are hence invisible). By comparing the plot of the E1-field to the time when bouncing occurs, the absolute growth clearly occurs after particle bouncing in the middle plot occurs. Taken together, these plots indicate that SRS first grows convectively. If the convective growth is sufficient to create a plasma wave that traps particles, then the damping rate is modified and can transition into an absolute instability.

If the plasma wave's damping is modified substantially through the action of trapped particles, the threshold between convective and absolute instability may shift during growth. Another indication of the transition from convective to absolute growth lies in Figure 4.1, where the SRS threshold was shown to require more convective gain lengths for the lower temperature/density cases than those at higher temperature/density. The condition for absolute instability is $(\gamma_p/\gamma_0) \sqrt{v_-/v_g} < 2$. The lower temperature/density cases require a higher v_{osc}/c (laser intensity) to satisfy the threshold for absolute instability. For similar pump intensities, therefore, their damping rate has to be decreased more than that of the higher temperature/density cases before they fall below the absolute threshold. The onset intensity threshold between the two cases is a similar fraction of the absolute threshold. For example, the onset thresholds (in terms of v_{osc}/c) for both 30-3-100 and 30-700-100 are approximately 30% of the absolute threshold

values. This would seem to imply that the relation to number of convective gain lengths is not as important as the fact that there is sufficient convective growth for particle trapping to occur and modify the damping by an amount sufficient to reduce the absolute threshold by the required fraction. What is important is that there is enough convective growth for the instability to transition into the absolute regime. The onset threshold in terms of convective gain lengths is relatively similar between cases of different lengths, even though the driving intensity differs between different lengths, confirming that the transition relies mainly on plasma temperature and density.

4.3 First Burst of SRS

The amplitudes and frequency shifts of the plasma waves will be explored next. To simplify the analysis, only the first bursts of SRS will be considered in this section. The maximum amplitude of the first bursts of SRS are shown in Figure 4.5, where the maximum amplitudes of the longitudinal E-field are plotted as a function of v_{osc}/c . The plots are grouped by constant $k\lambda_D$, and the amplitudes are normalized to the Coffey wavebreaking limit [78] (E/E_{Coff} , top), the plasma parameters ($eE/mv_{th}\omega_p$, middle), and the laser parameters ($eE/mc\omega_0$, bottom).

For all parameters, the maximum amplitudes linearly increase with v_{osc}/c . If the SRS plasma waves were limited to a maximum amplitude by the Coffey limit, then progressively stronger drive intensities would not drive the plasma waves to higher amplitudes. This figure therefore implies that SRS does not saturate due to wavebreaking (catastrophic particle trapping). In comparison with the Coffey wavebreaking limit, the simulations never surpass the limit (save for one, the most strongly driven of simulations 30-700-100). The most strongly driven simulations approach the wavebreaking limit, but most stay below $0.6E_{Coff}$. Strictly

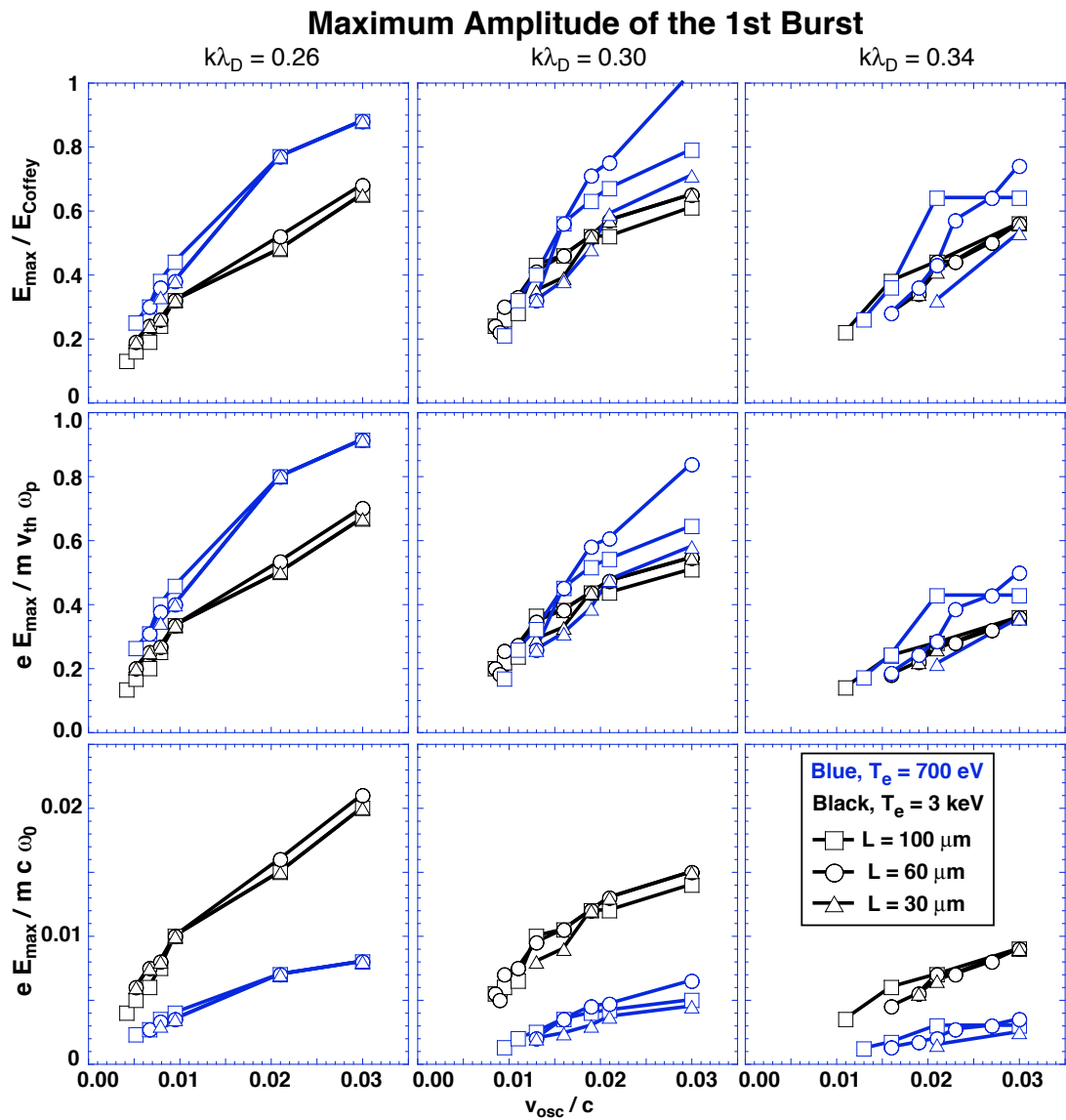


Figure 4.5: Maximum E1-field amplitude during the first burst of SRS.

speaking, the Coffey wavebreaking limit does not account for trapped particle effects.

Relative to the Coffey wavebreaking limit, there is only weak evidence of a dependence on $k\lambda_D$. That trend is amplified in the middle and bottom plots. When normalized to $mv_{th}\omega_p/e$, the maximum amplitudes show a fair similarity for constant $k\lambda_D$ but different temperatures/densities. The group of simulations at $T_e = 700$ eV are generally driven to slightly higher amplitudes than the simulations of $T_e = 3$ keV, but the difference is slight ($\approx 20\% - 30\%$ for $k\lambda_D = 0.26$) and becomes less significant for increasing values of $k\lambda_D$. In contrast to the scaling against the Coffey limit, here the maximum amplitudes decrease for increasing $k\lambda_D$.

For the normalization with $mv_{th}\omega_p/e$, another horizontal axis that could be used is v_{osc}/v_{the} instead of v_{osc}/c . The lower temperature/density cases would be shifted right by a factor of 2 relative to the higher temperature/density cases. The normalization to $mc\omega_0/e$ (Fig. 4.5, bottom row) makes this difference evident. A marked difference can be seen between the two separate temperatures/densities for a given $k\lambda_D$, with the higher temperature/density combination having the higher amplitudes. This scaling is most relevant to the SRS reflectivity, for this amplitude trend indicates that the plasma waves in the higher temperature/density simulations are driven to larger amplitudes relative to the driving laser amplitude, and therefore result in more pump depletion, larger scattered light wave amplitudes, and higher reflectivities.

Finally, the length of the plasma generally does not affect the maximum amplitude (at least for the first SRS burst). With the exception of the $T_e = 700$ eV cases for $k\lambda_D = 0.34$, and to a lesser extent $k\lambda_D = 0.30$, the points for different plasma lengths are approximately equal. This implies that the initial saturation

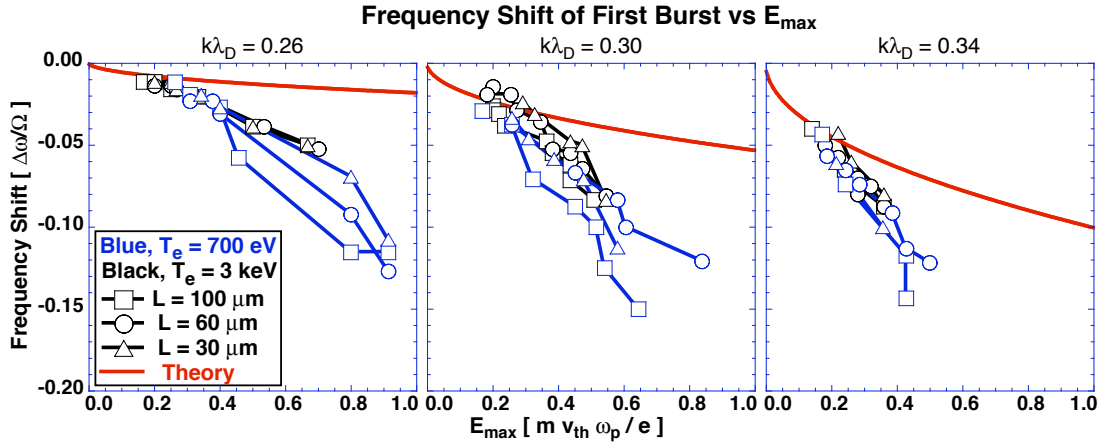


Figure 4.6: Frequency shift versus maximum E1-field amplitude of the first burst of SRS.

of SRS is independent of the available length of plasma. The exceptions occur for those simulations which are driven above the theoretical threshold for absolute instability. Since these cases are not constricted to grow convectively, the spatial extent of the initial SRS burst can cover a larger region, and the interaction of waves across this whole region can drive the plasma waves slightly higher.

Plasma waves that are driven to the amplitudes seen in Figure 4.5 trap electrons and shift in frequency; nonlinear frequency shifts similar to those of the previous chapter are seen across all parameters. In Figure 4.6, the frequency shifts of the first bursts of SRS are plotted as a function of the maximum longitudinal E-field amplitudes (in normalized plasma units of $eE/mv_{th}\omega_p$). These shifts are measured after SRS saturation, representing the final shift of the saturated SRS plasma waves. The theoretical curves are the shifts blindly calculated from the expression in Morales and O’Neil [57], where a Maxwellian distribution has been used in their formula, although all of the amplitudes here are larger than the range of valid amplitudes in their theory.

The frequency shifts are independent of electron temperature, as is expected from theory. As is also expected, for a given amplitude, the frequency shifts become more negative as $k\lambda_D$ increases. Within each group of constant $k\lambda_D$, the rate of change of the frequency shifts with respect to E_{max} decreases approximately linearly, as opposed to the theoretical square-root dependence. A further investigation of frequency shifts for strongly nonlinear plasma waves is needed to properly account for the frequency shifts seen here. While the exact frequency shift of a nonlinear plasma wave in SRS has been the subject of recent study [91, 92, 93, 83], finding a more exact theoretical fit to the frequency shifts seen in these simulations is left for future work.

While the SRS resonance can be detuned due to the nonlinear frequency shift of the plasma wave, the previous chapter showed that pump depletion must also be considered. For weakly coupled SRS, the temporal Manley-Rowe relations can be used to show that the backscattered light wave (with field E_1 and frequency ω_1) will grow at the expense of the pump wave (E_0 and ω_0) until $E_1^2/\omega_1 = E_0^2/\omega_0$ [6]. The simulations here are not of the purely temporal instability, so the backscattered light wave can continue growing past this amplitude, but this condition on the maximum amplitude of the backscattered light wave amplitude can be used to roughly visualize whether a pump-depleted state has been reached.

Figure 4.7 presents a clearer example of saturation by pump depletion than was shown in Chapter 3. Here we plot the spatial-temporal evolution of the plasma (top-left) and backscattered light (top-right) waves, where the backscattered light is obtained by applying a low-pass filter to the transverse E3-field; the bottom plots show the spatial-temporal evolution of the resonance diagnostic (bottom-left) and the condition on the maximum backscattered light wave amplitude, $\omega_1 E_0^2 - \omega_0 E_1^2$ (bottom-right), that is, the plot will show negative (non-white)

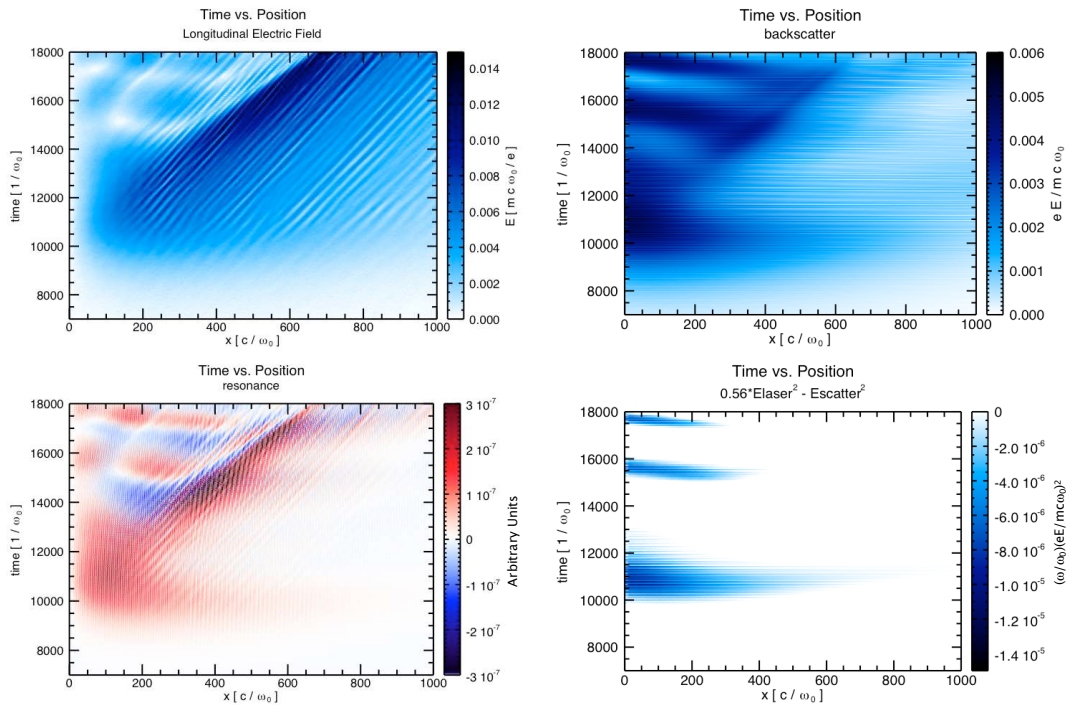


Figure 4.7: Saturation of the first SRS burst due to pump depletion for Case 26-3-100, $v_{osc}/c = 0.0052$. Space versus time of the longitudinal E1-field (top-left) and backscattered light (top-right), resonance diagnostic (bottom-left), and Manley-Rowe (bottom-right).

values when the backscattered light wave has exceeded the maximum set by this condition. In contrast with the resonance plot that was shown earlier, here the resonance plot does not show negative (blue) values when the saturation occurs ($x\omega_0/c \approx 300$ and $\omega_0 t \approx 11000$ as evidenced in the plot of backscattered light), but rather simply goes from positive to zero (red to white). The bottom-right plot shows that the backscattered light wave is reaching its maximum amplitude and that $E_1^2 > (\omega_1/\omega_0)E_0^2$. Therefore the saturation is clearly by pump depletion. As a side-note, the continued scattering of backscattered light from the resulting packet of plasma waves as they convect can also be seen, along with the oscillation of the resonance condition (red to blue and back) in the area that is left behind by the convecting packet.

If saturation by pump depletion is to occur, the growth rate must be fast enough for the pump to be depleted to levels below which further growth can occur ($\beta > 2$) and this process must occur before a frequency shift can detune the instability, that is, the time to pump deplete must be shorter than the time to detune. The figures so far have indicated saturation mechanisms, but they have not indicated the conditions for which the frequency shift dominates pump depletion as the saturation mechanism. If saturation by detuning is to occur, the frequency shift must detune the instability more quickly than the instability can grow and deplete the drive's energy. Frequency shifts and pump depletion always occur, but their role in SRS saturation depends on which one occurs first. For further analysis, the growth rate is compared against the frequency shift by examining the ratio of the growth rate to the detuning rate. This ratio is plotted in Figure 4.8, where the detuning rate is taken to be $\Delta\omega/\pi$ with $\Delta\omega$ the measured frequency shift, and the growth rate used for these data points is the measured growth rate rather than a theoretical value, that is, the growth rate comes from the fit to the longitudinal E-field growth in the simulation (as plotted earlier).

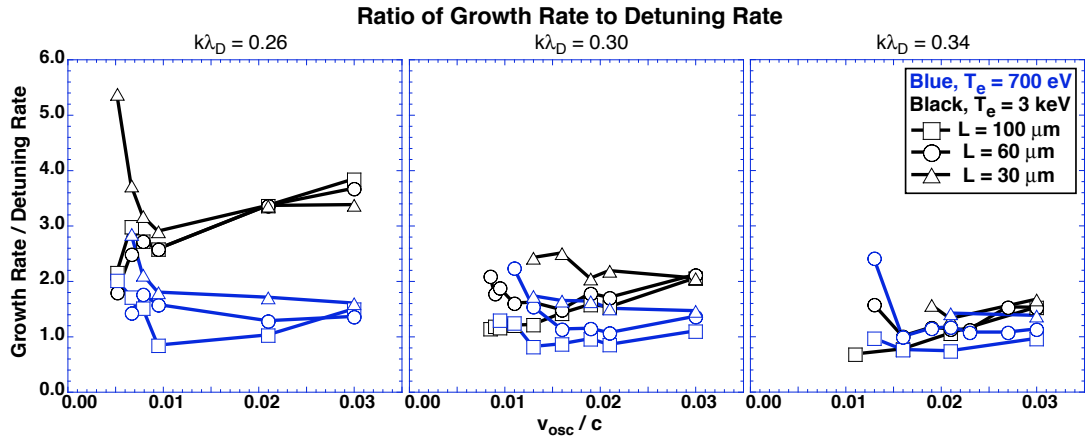


Figure 4.8: Ratio of the measured growth rate to the detuning rate as given by $\Delta\omega/\pi$ from the frequency shift of the first burst.

While there is strictly no information in this figure about the time it takes for SRS to grow and reach a pump-depleted state, nor any information about when the frequency shift occurs or how quickly it develops (the frequency shift could happen before or after saturation), there are indicative trends. Given that the maximum frequency shifts are used for the plot, the detuning rate is an upper bound. This implies, for example, that the 26-3-30 simulations have at least three e-foldings of growth before the frequency shift (the maximum frequency shift of the plasma wave at saturation) could detune the instability. With a resulting factor of ≈ 20 in growth, it is likely that SRS will significantly deplete the pump before a frequency shift has any effect in these cases. As $k\lambda_D$ increases from 0.26 to 0.34, all of the simulations approach the value of 1.0, meaning that the detuning rate is equal to the growth rate. For $k\lambda_D = 0.26$, there will be several e-foldings of SRS growth before detuning can affect the instability, whereas for $k\lambda_D = 0.34$, there will be only one e-folding before detuning affects the growth. This trend indicates that a frequency shift will have a more dramatic affect for higher $k\lambda_D$.

Furthermore, Figure 4.8 shows that there is a difference between the two temperatures/densities for constant $k\lambda_D$. For $k\lambda_D = 0.26$, the ratio is higher for the $T_e = 3$ keV simulations than for 700 eV. As $k\lambda_D$ increases, the ratios converge to similar values. This trend implies that the $T_e = 3$ keV simulations will have more e-foldings of growth before detuning can affect the instability, as compared to the $T_e = 700$ eV simulations that will be more immediately affected by detuning. As was indicated previously in Figure 4.2, the cases with the higher temperature (and therefore higher density for constant $k\lambda_D$) have the higher theoretical growth rate. For simulations at a lower $k\lambda_D$ that have approximately equal frequency shifts, the higher temperature/density case could grow more before detuning affects SRS, thereby reaching a pump-depleted state and saturating by that mechanism before detuning takes effect. This is a possible explanation of the difference between Case 1-30 and 3-30 of the previous chapter, where it was seen that the lower temperature case was saturated by detuning and the higher temperature case was saturated by pump depletion. With frequency shifts that were approximately equal between the two cases, the higher temperature/density case could grow faster and reach a pump-depleted state before detuning affected SRS. Regardless of the exact saturation mechanism, it is likely that the higher temperature/density cases in general will grow to higher amplitudes and result in higher reflectivities than the lower temperature/density cases before saturating.

4.4 Recurrence

The initial growth and saturation of SRS, while important, are only part of the SRS process that determines the total time-averaged reflectivity. The behavior of the plasma waves after saturation, and the conditions that determine the recurrence of SRS, are also important and are discussed in this section. The

conclusions of the previous chapter are first summarized, as they will be evidenced here as well. This section seeks in addition to explore how these effects alter the specific behavior of SRS reflectivity.

SRS initially grows in a localized region of the plasma, with the resulting plasma waves forming a nonlinear plasma wave packet. Following SRS growth and saturation, the resulting plasma wave packets convect through the plasma. Even though the initial saturation has occurred, the frequency-shifted packet continues to reflect the incident laser. This nonlinearly shifted light interacts with the pump and relatively unperturbed plasma to cause a reflectivity with a recurrence rate that depends on the nonlinear frequency shift of the packet. This continued scattering locally depletes the incoming laser energy, but as the packet is etched and the effects of pump depletion decrease, there can be renewed packet growth. After the packet has moved a sufficient distance into the plasma, a new burst of SRS will grow, creating a new packet in the region left behind. Thus, the recurrence rate also depends on the packet speed. Finally, new bursts of SRS can interact with scattered light coming from packets that are farther into the plasma, provided the interaction length is long enough to permit several packets to coexist.

Figure 4.9(a) shows the enveloped temporal evolution of the reflected light at the incident boundary (left) and the spatio-temporal evolution of the backscattered light (middle) and plasma waves (right) for Case 30-3-30. Three packets of SRS-generated plasma waves grow and convect over the total simulation, but the reflectivity shows many more than three bursts due to continued reflection from frequency-shifted plasma wave packets. During SRS growth and saturation, a plasma packet grows in amplitude and traps particles, resulting in a negative frequency shift as shown previously. The peak amplitude is a factor of two less

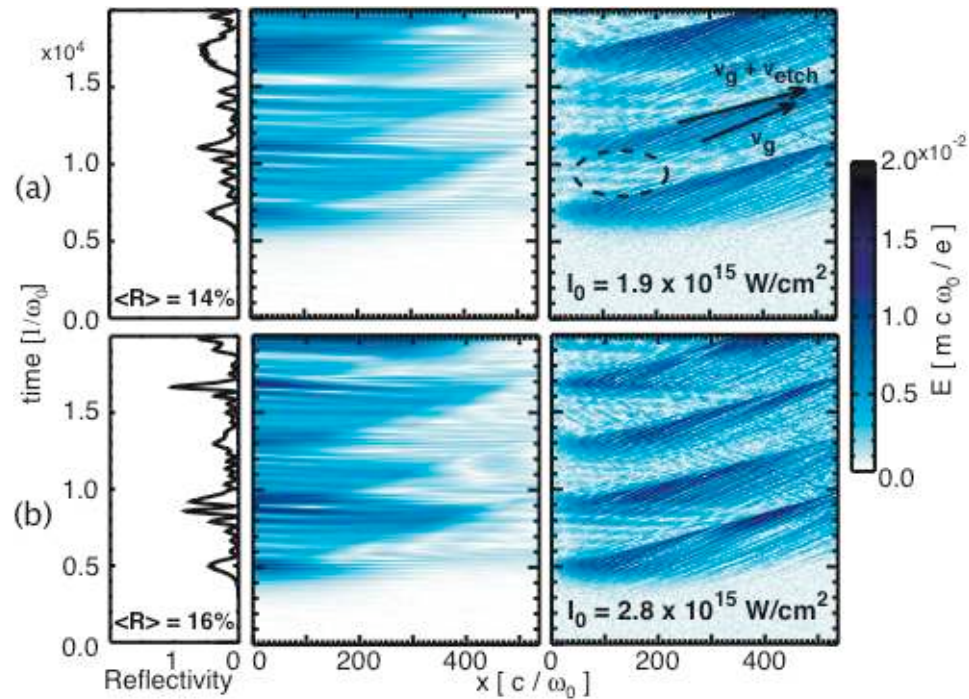


Figure 4.9: Time vs. reflectivity (left) and time vs. space of the backward-propagating light (middle) and E_x -field (right). The simulation parameters are equivalent with the exception of driving laser intensity I_0 as noted.

than the Coffey limit [78] and saturation is due to detuning from the nonlinear frequency shift. After saturation, these packets of frequency down-shifted plasma waves convect forward. As they convect, new laser energy enters the system. The frequency matching condition for SRS growth, $\omega_0 = \omega_1 + \omega_2$, where $\omega_{0,1,2}$ are the laser, scattered, and plasma wave frequencies, respectively, can be maintained if ω_1 shifts positively for the negative shift in ω_2 . The frequency-matching condition is then satisfied by $\omega_0 = (\omega_1 + \Delta\omega) + (\omega_2 - \Delta\omega)$.

As the frequency up-shifted light moves outside the packet, however, the frequency-matching condition can no longer be satisfied. The beat of the scattered light wave with the incident laser nonresonantly drives SRS in the background plasma left behind the packet with $\omega_0 = (\omega_1 + \Delta\omega) + \omega_{NR}$, where the dielectric $\epsilon(k, \omega_{NR}) \neq 0$. Like a simple harmonic oscillator driven off-resonance, the nonresonant drive produces a low frequency beat pattern in the plasma waves with maxima separated in time at $\tau = 2\pi/\Delta\omega$. This beat pattern can be seen in areas behind the packets, for example in Fig. 4.9(a) in the circled region. This beat pattern is additionally seen in the reflected light. The plasma wave initially grows secularly as pump energy is transferred to the reflected light and plasma waves, but the detuning causes the growth to saturate and energy to be transferred from the reflected light and plasma waves back to the pump. This effect manifests itself as the high frequency recurrence in the reflected and transmitted light. We measure $\Delta\omega/\omega_0 \simeq 0.008$, giving $\tau \simeq 800\omega_0^{-1}$ in good correspondence with the burst times of the reflectivity in Fig. 4.9(a), left.

For proof, a modified simulation was performed. The simulation had exactly similar parameters as Case 3-30 of Chapter 3 with the exception that now a second laser with half the intensity was also launched from the opposite side (and traveling in the opposite direction) with a frequency that matched the shifted

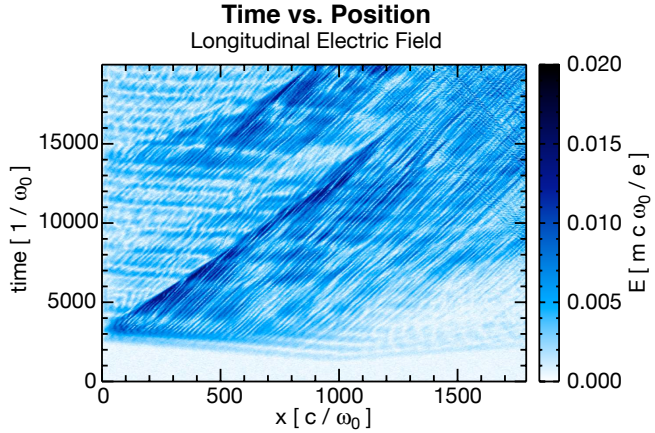


Figure 4.10: Spatial-temporal content of the longitudinal E-field with laser of half-intensity launched from the left.

backscattered frequency. The plasma wave behavior in space and time can be seen in Figure 4.10. For $\omega_0 t \approx 2000$, before the first burst of main SRS grows, a beat pattern of plasma waves grows in the center of the box, corresponding to off-resonant SRS that is stimulated when the two lasers from opposite sides meet at $x\omega_0/c \approx 900$. The temporal periodicity of this initial beat pattern matches the beat pattern that is seen in Figure 4.9, and the beat pattern continues with the same periodicity in the left half of the box even after growth and saturation of a plasma wave packet.

Additional numerical experiments similar to Case 3-30 were performed with lasers that were launched from the same side as the initial laser. The initial laser was cut off at $\omega_0 t = 7000$ after the first burst of SRS had grown and saturated, and a laser of equal intensity and frequency was sent in afterwards. The plasma wave behavior for two of these simulations can be seen in Figure 4.11. The top plot shows the simulation in which there was no second laser. The plasma packet convects through the box without a laser driving further SRS in it. The bottom plot shows the simulation in which a second laser is turned on at $\omega_0 t = 9000$.

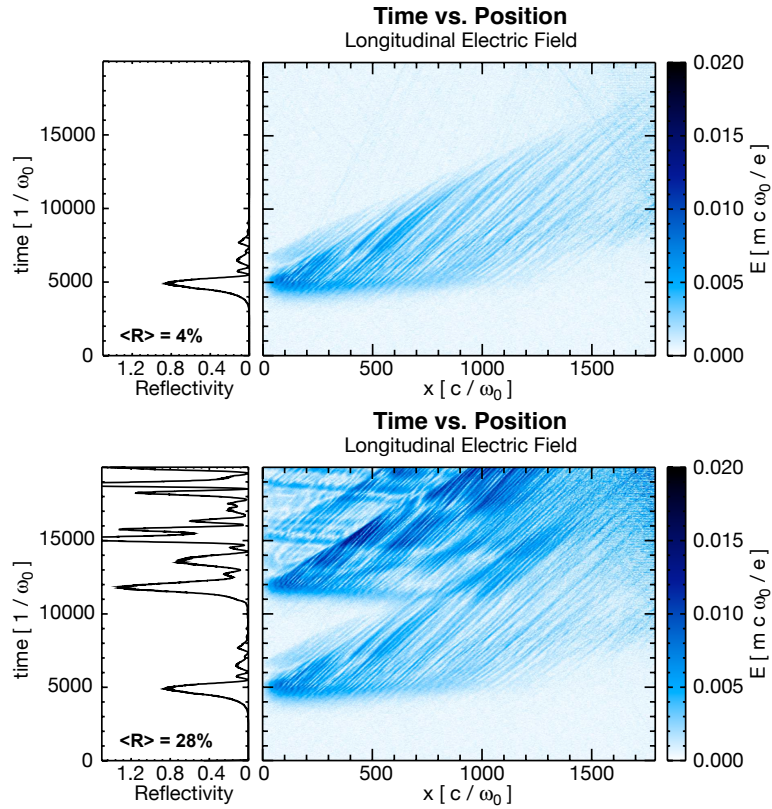


Figure 4.11: Reflectivity (left) and spatial-temporal content of the longitudinal E-field (right) when the initial laser stops at $\omega_0 t = 7000$ and a second laser is sent in at $\omega_0 t = 9000$ (bottom) or not at all (top).

This second laser takes a time $\omega_0 t \approx 1000$ to propagate to the packet, after which time it undergoes SRS as it interacts with the packet and drives a new burst of SRS in the left-most part of the box.

Several more points can be made about this figure. First, now that a laser is not driving the plasma packet during the time from $\omega_0 t = 7000 - 9000$, there is not a beat pattern of plasma waves in this time interval in the area of $x\omega_0/c = 0 - 400$, nor is there a periodic train of reflectivity bursts. This is further evidence that the beat pattern is driven by laser energy that interacts with the convecting plasma

packet. There are a few reflectivity bursts after the first major burst of SRS up until the laser turns off, as well as one burst during the time it would take reflected light to propagate from the packet at $\omega_0 t = 7000$ to the incident edge, but the reflectivity is then zero until the second laser drives SRS again. Second, the edge of the first plasma packet does not decay as strongly in the bottom plot when the second laser is present. The packet edge in the region of $\omega_0 t = 12000$ and $x\omega_0/c = 1200$ shows renewed packet growth as the second laser comes into the packet region and provides new energy for continued SRS.

Reflectivity bursts also come from new SRS growth. These stronger bursts occur less frequently and can be seen in Fig. 4.9(a) (left and middle) as the three large peaks at $\omega_0 t \simeq 7000$, 11500, and 17000. As packets convect forward, new SRS bursts grow in the region of plasma left behind once there is a sufficiently large region for gain. Their recurrence therefore depends on how quickly packets leave, which is determined by the speed of the rear side of the packet. As was shown by Fahlen *et al.* [90], the packet convection speed is faster than the group velocity, v_g , of the SRS plasma wave because packets are continually etched by resonant particles traveling at the phase velocity, $v_\phi > v_g$. As shown by the arrows in Fig. 4.9(a), the rear side of the packet has a speed $v_{packet} = v_g + v_{etch}$, where v_{etch} is the packet's etching speed. Here we measure $v_{packet} = 1.4v_{th}$, slightly lower than that predicted by [90]. However, strict agreement is not expected as the plasma waves here are continuously driven outside the packet by recurring SRS in the convecting packets, a process affecting trapped particle motion behind the packet and thereby the etching rate. This recurrence rate would roughly scale as $\Delta t \simeq L/v_{packet}$ where Δt is the time between bursts and L is the convective gain length.

The modeled etching rate in [90] is reproduced in Figure 4.12, where it is

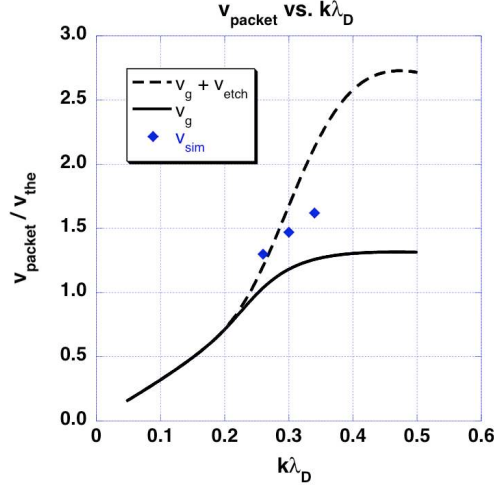


Figure 4.12: Packet velocity versus $k\lambda_D$.

compared against the packet speed in the simulations of this chapter. Each point represents an average of the packet speeds seen in all simulations for the particular $k\lambda_D$. The velocity that is seen here is close to the theoretical model for $k\lambda_D = 0.26$ and 0.30 , but lower for 0.34 . In contrast with the single electrostatic packet simulations of [90], the plasma packets here are continually being driven and SRS continues to recur from convecting packets. Plasma waves exist outside of the packet, continually affecting the motion of trapped particles at the packet edge and thereby the etching rate. For the higher $k\lambda_D$ simulations, the motion of trapped particles in the transition from outside-the-packet to inside-the-packet might be affected by plasma waves of different frequency, where a large frequency shift will be present inside the packet but not necessarily outside the packet.

To show that v_{packet} affects the recurrence rate, Fig. 4.9(b) shows a simulation with the same plasma parameters as Fig. 4.9(a) but a higher driving laser intensity (2.8 vs. $1.9 \times 10^{15} \text{ W/cm}^2$). Since the convective gain length is shorter,

the packets do not have to travel as far before a sufficient length is available for convective growth of a new burst. The packet speeds in Fig. 4.9(a) and 4.9(b) are nearly the same, despite the larger plasma wave amplitudes, since the etching rate is only weakly dependent on the amplitude for these conditions. With a similar packet speed but a shorter distance to travel, the time for new bursts is shorter and consequently the recurrence rate of new bursts is faster. Furthermore, the recurrence rate of high-frequency bursts from continuous scattering off convecting packets is slightly faster as well, since the higher amplitude plasma waves have a slightly larger frequency shift ($\Delta\omega/\omega_0 \simeq 0.01$ and $\tau \simeq 600$). The effect of v_{packet} can also be clearly seen in backscattered light for both cases. Figure 4.9 makes clear that the backscattered light originates deeper in the plasma for the low intensity case. It also shows that the packet's rear edge, moving at v_{packet} , acts like a barrier, continually reflecting and locally pump-depleting the incoming laser. The time-averaged reflectivity is 14% and 16%, respectively, indicating that 50% higher intensity increases the reflectivity only slightly.

Since each packet leaves the interaction length before the next packet is well established, the recurrence of new bursts in both simulations is fairly periodic. When the interaction length is long enough for packets to stay in the system during the growth of new bursts, SRS behavior becomes more complex. Figure 4.13 shows the SRS activity for a simulation with identical parameters as Fig. 4.9(a) except for a doubled interaction length (60 vs. 30 μm). With a longer length, the total time-averaged reflectivity is larger (34%) for several reasons. First, the reflectivity bursts from each packet's growth are higher, even for the first burst. Even though the saturated plasma waves have comparable amplitude for both lengths at approximately half the Coffey limit, they are excited over a larger region in the longer simulation, leading to more backscattered light and a larger burst of reflectivity at the edge. Pump depletion plays a role in the

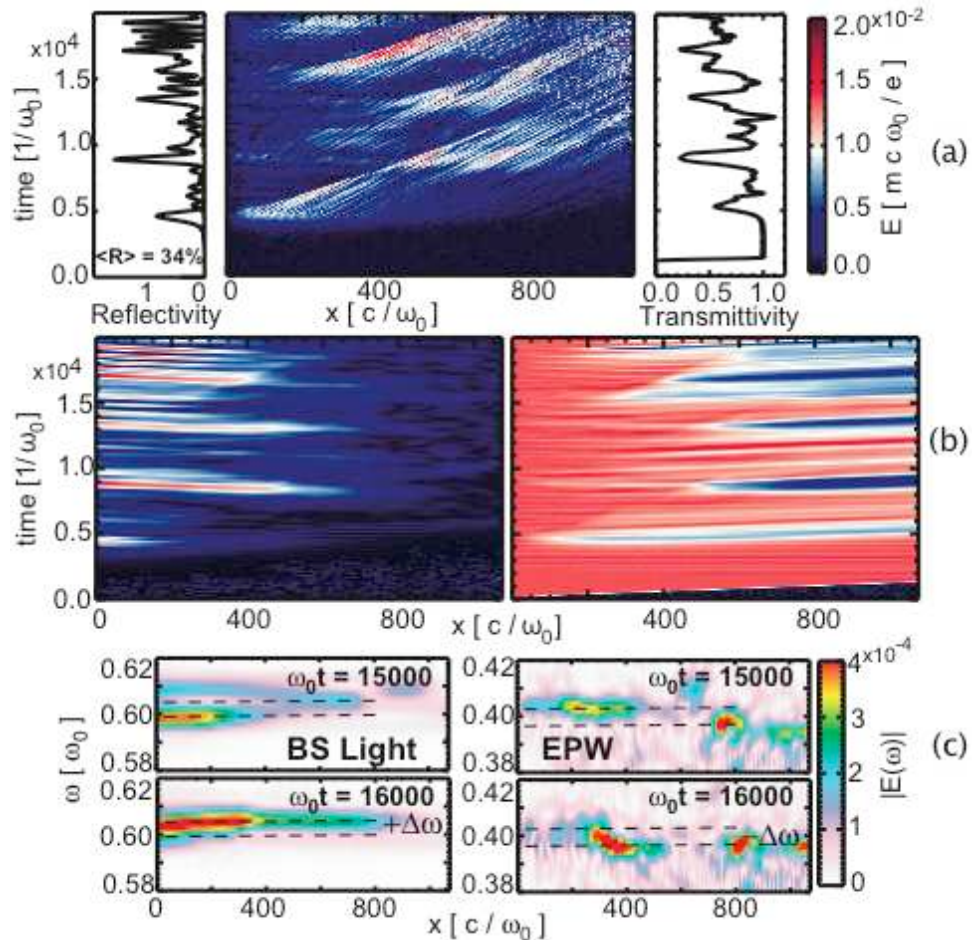


Figure 4.13: (a) Reflectivity vs. time (left), transmittivity vs. time (right), and time versus space of the E_x -field (middle) for $L = 60 \mu\text{m}$ and $I_0 = 1.9 \times 10^{15} \text{ W/cm}^2$. (b) Spatio-temporal evolution of backward (left) and forward (right) propagating light for the same simulation. (c) Spatial-frequency content of the transverse (left) and longitudinal (right) E -fields at two times during packet convection, obtained by a windowed FFT.

saturation for this case. The bursts of reflectivity from the first convecting packet have the same periodicity for both simulations as well, since the frequency shifts are comparable.

Second, new packet growth does not occur solely in the region left behind by packets. For the longer plasma of Fig. 4.13(a), the packet can nearly etch away before it propagates across the system, allowing the pump to reach further into the plasma. The second plasma “packet” grows at ($x\omega_0/c \simeq 600$, $\omega_0 t \simeq 8000$), giving the second major reflectivity burst at $\omega_0 t \simeq 9000$. Whereas the second burst of new SRS for the shorter length in Fig. 4.9(a) came from the region left behind by the first packet, here the second burst comes from renewed SRS growth in the region into which the first packet travels, as seen in Fig. 4.13(a) and (b), left, where the second major burst in reflected light is generated deep into the plasma at $x\omega_0/c \simeq 800$. As predicted for backscatter, the rear of the packet has the highest amplitude and furthermore continuously scatters light, thereby locally depleting the laser intensity. The whiter regions of Fig. 4.13(b), right, show how the depleted pump drives the plasma at a lower intensity than its incident intensity. As the initial packet’s energy is etched away and the packet shrinks, it depletes less and less of the pump, as seen in the transmittivity. By $\omega_0 t = 7500$, the full laser intensity passes the packet’s rear edge, allowing it to penetrate deeper into the plasma and excite the packet more strongly. The process results in renewed packet growth and the large burst of reflectivity at $\omega_0 t = 9000$.

Finally, the scattered light in the longer length plasma can come from SRS interactions between multiple packets, in contrast to the short systems in which only one packet is present at a time. These multi-packet interactions steadily increase the amplitude of the reflectivity bursts in time. For instance, scattered

light generated from the packet at $(x\omega_0/c, \omega_0 t) = (800, 16000)$ can also interact with the packet at $(400, 16000)$ on its path to the rear edge. To illustrate, Fig. 4.13(c) shows the frequency content of the plasma and backscattered light waves late in time ($\omega_0 t = 15000$ and 16000) when there are two distinct packets in the simulation domain. The frequency plots are obtained by an FFT of the longitudinal and transverse E-fields, with a Gaussian-shaped window with FWHM $= 832\omega_0^{-1}$ and size $\omega_0 t = 2000$ centered about the time shown. At $\omega_0 t = 15000$, the linear SRS frequencies of the backscattered light and plasma waves can be seen in the newly growing burst (packet 1 at $x\omega_0/c \simeq 400$). In addition, the convecting packet (packet 2 at $x\omega_0/c \simeq 800$) and its backscattered light can be seen at shifted frequencies. At $\omega_0 t = 16000$, packet 1 has shifted down to a frequency which is resonant with the frequency up-shifted light traveling toward it from packet 2. Packet 1's magnitude now increases, having shifted into a new resonance. As can be seen in Fig. 4.13(b), left, the scattered light from packet 2 also increases in amplitude as it passes through packet 1. The reflected and nonlinearly shifted light from packet 1 is then larger, which leads to larger bursts due to the nonresonant excitation of plasma waves described earlier. Specifically, the reflectivity bursts between $\omega_0 t = 17000$ and 20000 are larger than the bursts between 14000 and 16000 , which are in turn larger than the bursts between 10000 and 12500 .

In summary, the nonlinear packet speed and the nonlinear frequency shift of plasma waves in the packet both determine a recurrence rate. In addition, packets locally deplete energy from the pump; as the packets are etched away and deplete less energy, the pump can then more fully penetrate the packet to drive renewed SRS growth. Finally, scattered light can travel between and interact with multiple packets, increasing the SRS reflectivity.

4.5 Reflectivity

The total time-averaged reflectivities will be discussed at the end of this section. First, in order to draw together the previous analyses of this chapter, the temporal evolution of the reflectivities for many of the simulations in this chapter are presented next, along with the corresponding plots of the spatio-temporal behavior of the plasma waves (as seen in the longitudinal E-field). Figures 4.14 through 4.25 show these plots for the six electron temperatures and densities, all three lengths, and a representative sample of driving laser intensities. While the scales on the E1-field plots are intentionally kept the same for comparison, care must be taken in interpreting the reflectivity plots, as the scales between different $k\lambda_D - T_e$ combinations are not kept the same.

Several overarching insights can be drawn from this collection of data. First, plasma wave activity and reflectivity begins at lower laser intensities for the longer lengths as compared to the shorter lengths, in accord with the requirement that the driving laser intensity must be high enough for 1-2 convective gain lengths to be in the simulation domain, that is, the onset intensity is lower for the longer lengths because the total convective gain across the simulation domain is greater. Second, SRS starts progressively earlier in time as the laser intensities increase. The start times are in rough agreement with the total time necessary for 1) the laser to propagate into the box, followed by 2) convective growth that propagates backwards (towards the laser-entrance side) at a velocity given by $\partial\omega/\partial k$ of the Raman dispersion relation ($\approx 0.5c$), followed in turn by 3) absolute growth at the absolute growth rate until saturation. This is also evidenced by the fact that the start times for different length boxes all converge to similar times as the laser intensity increases and the spatial gain length that is required drops below the length of the shortest box. Third, as a consequence of this method of growth,

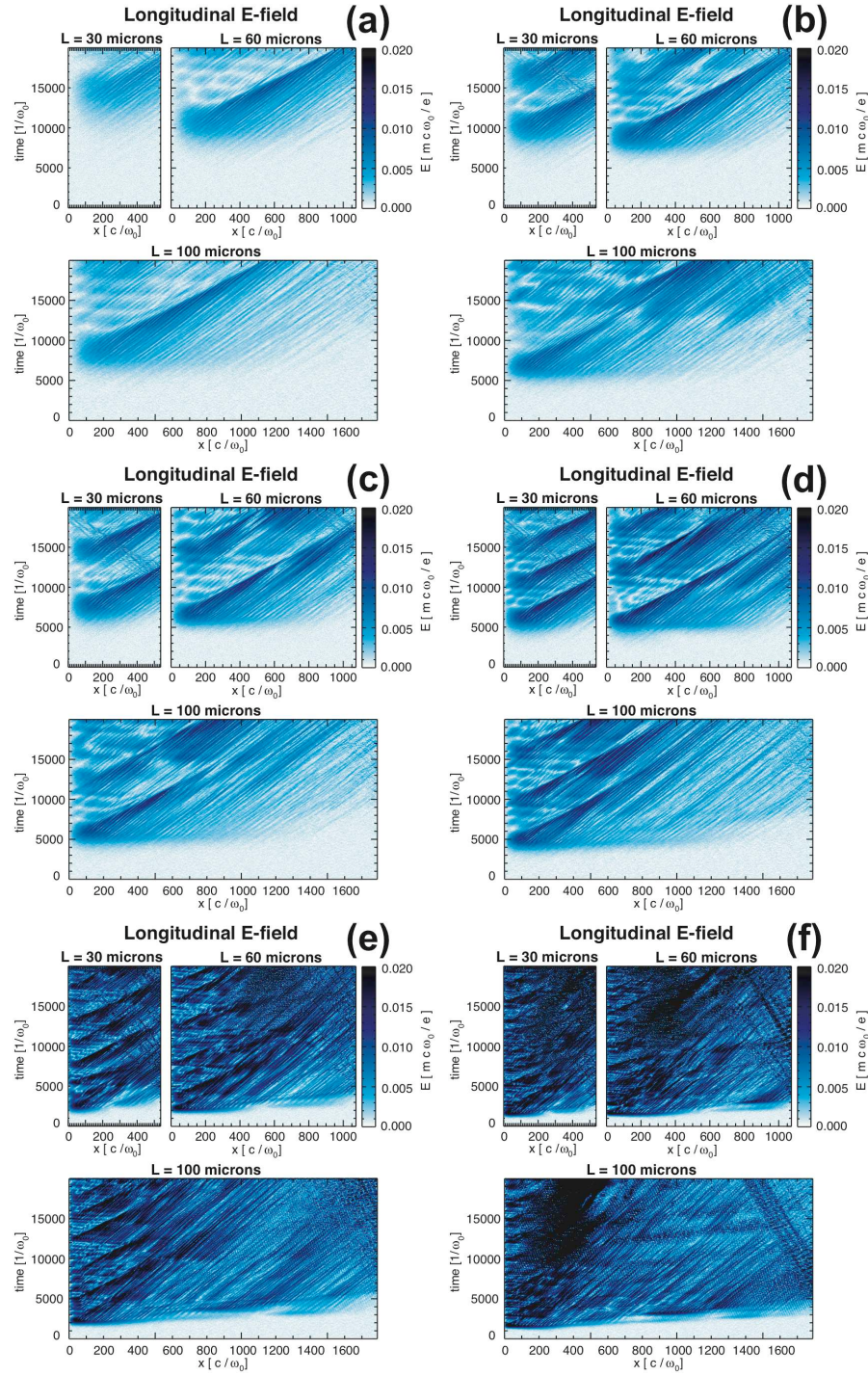


Figure 4.14: Evolution of the plasma wave for Case 26-3, with v_{osc}/c of (a) 0.0052, (b) 0.0067, (c) 0.0079, (d) 0.0095, (e) 0.021, and (f) 0.030.

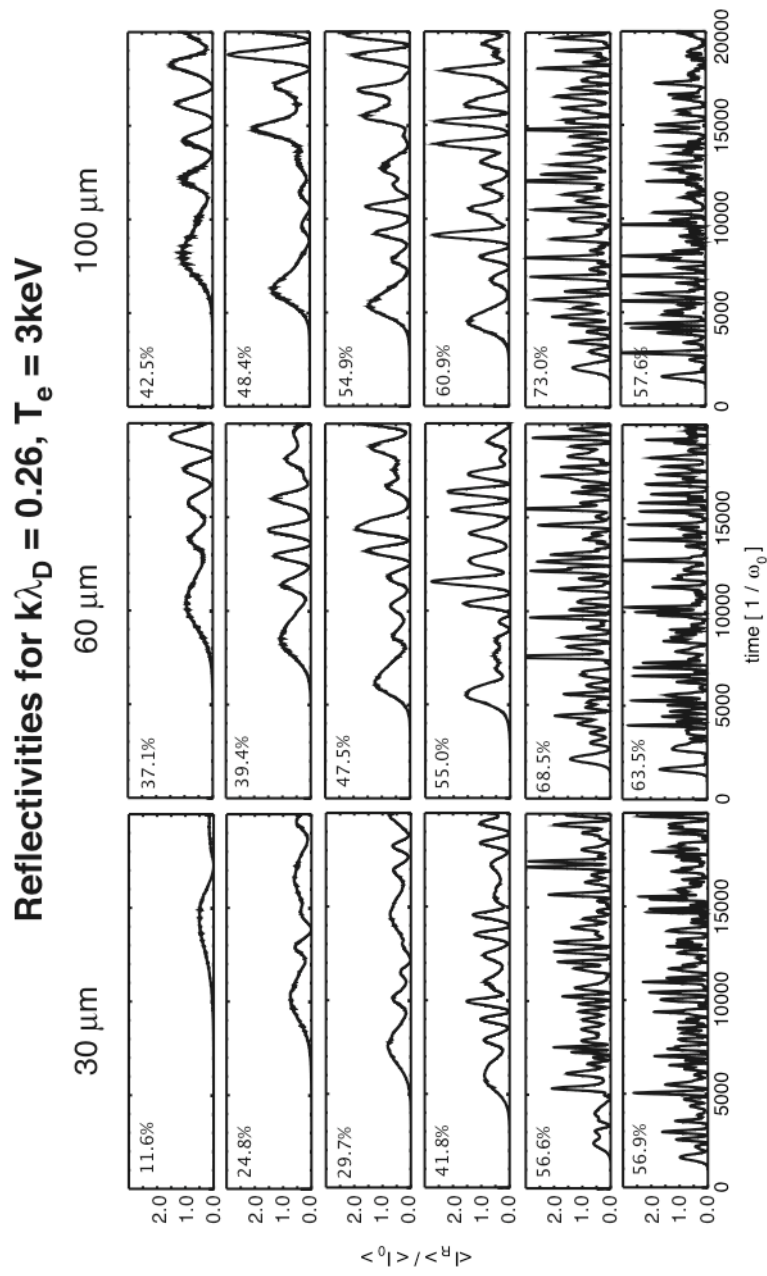


Figure 4.15: Reflectivities vs. time for Case 26-3.

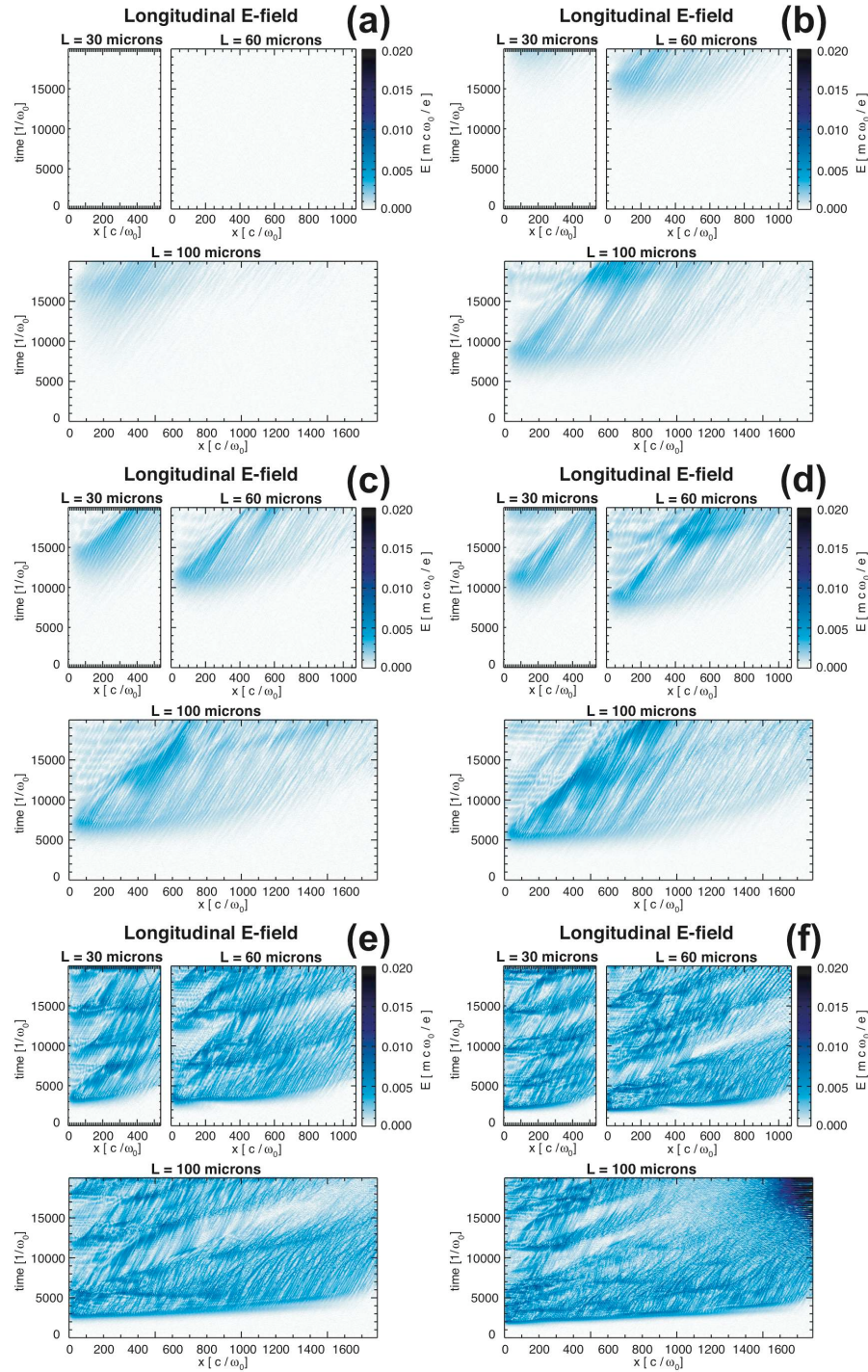


Figure 4.16: Evolution of the plasma wave for Case 26-700, with v_{osc}/c of (a) 0.0052, (b) 0.0067, (c) 0.0079, (d) 0.0095, (e) 0.021, and (f) 0.030.

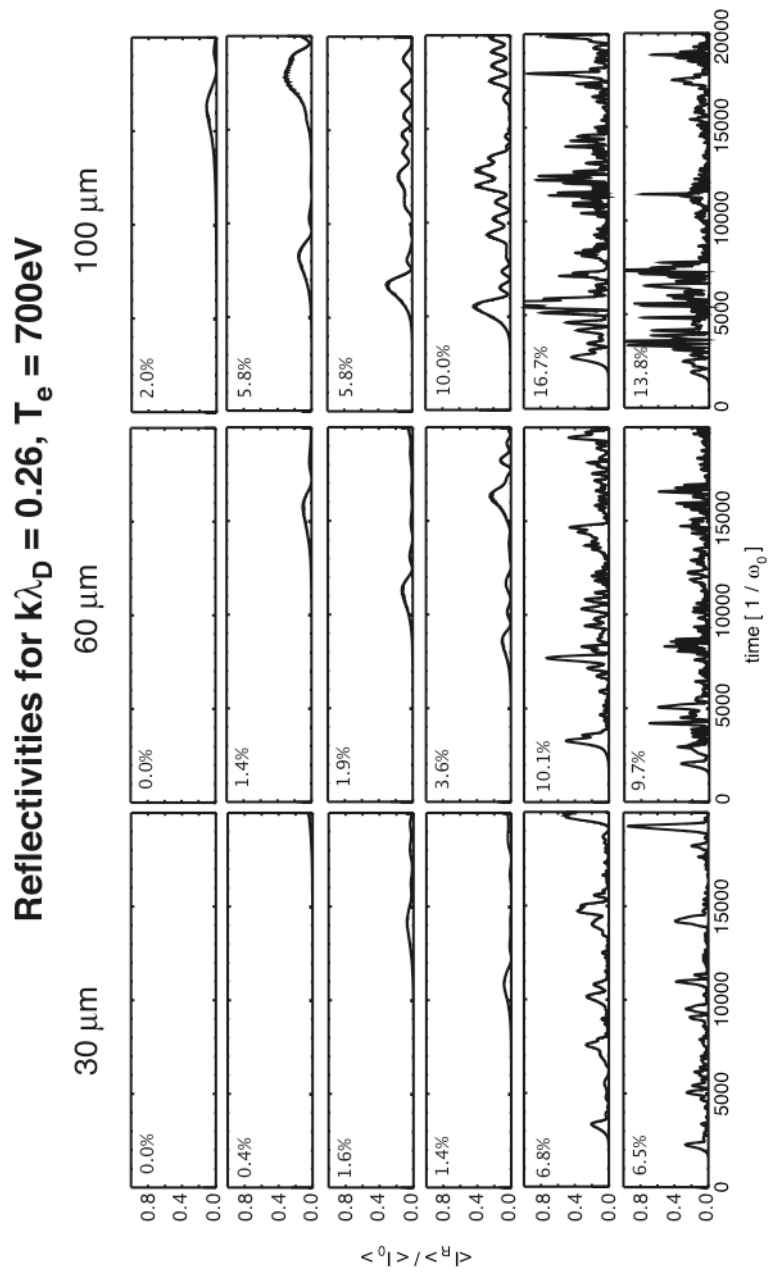


Figure 4.17: Reflectivities vs. time for Case 26-700.

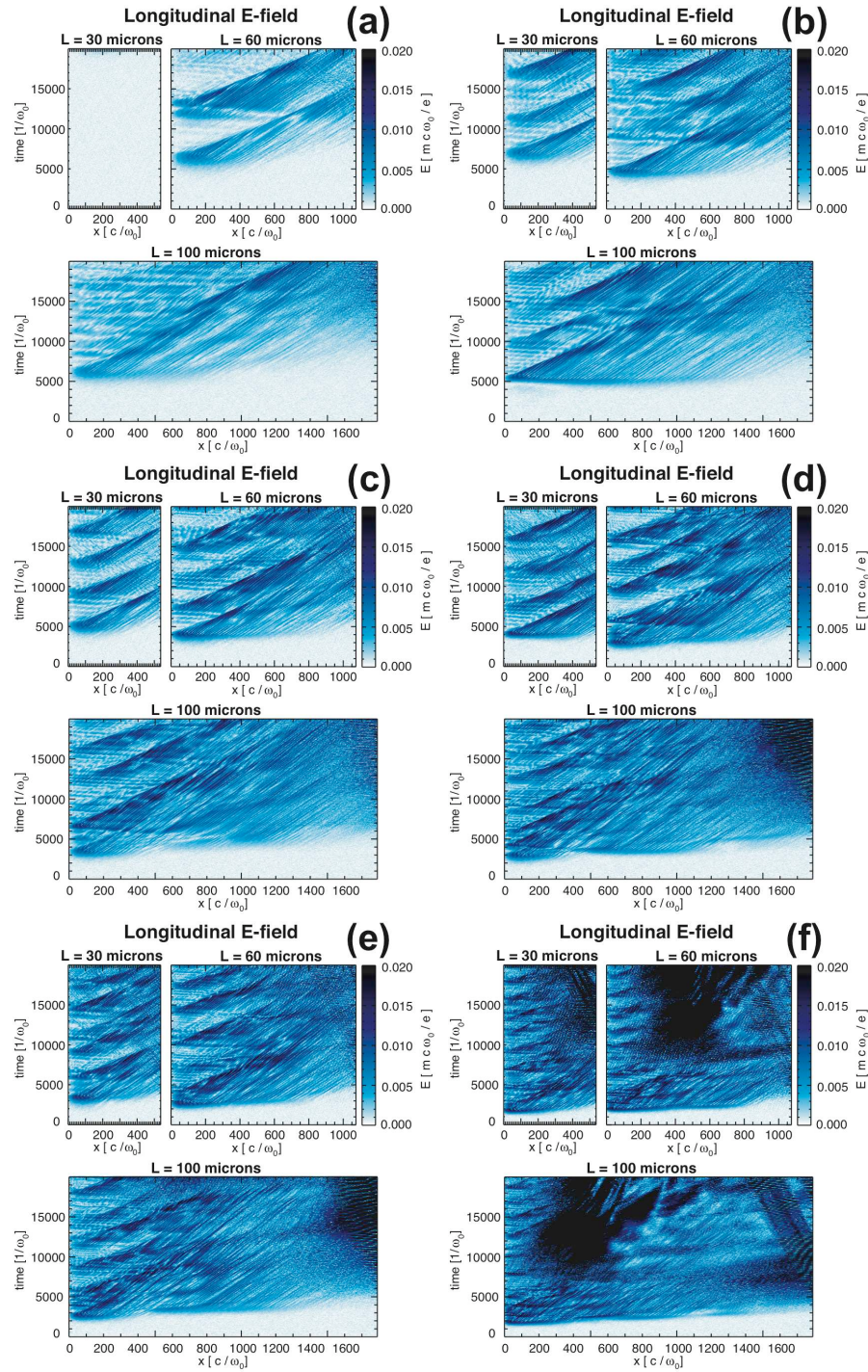


Figure 4.18: Evolution of the plasma wave for Case 30-3, with v_{osc}/c of (a) 0.011, (b) 0.013, (c) 0.016, (d) 0.019, (e) 0.021, and (f) 0.030.

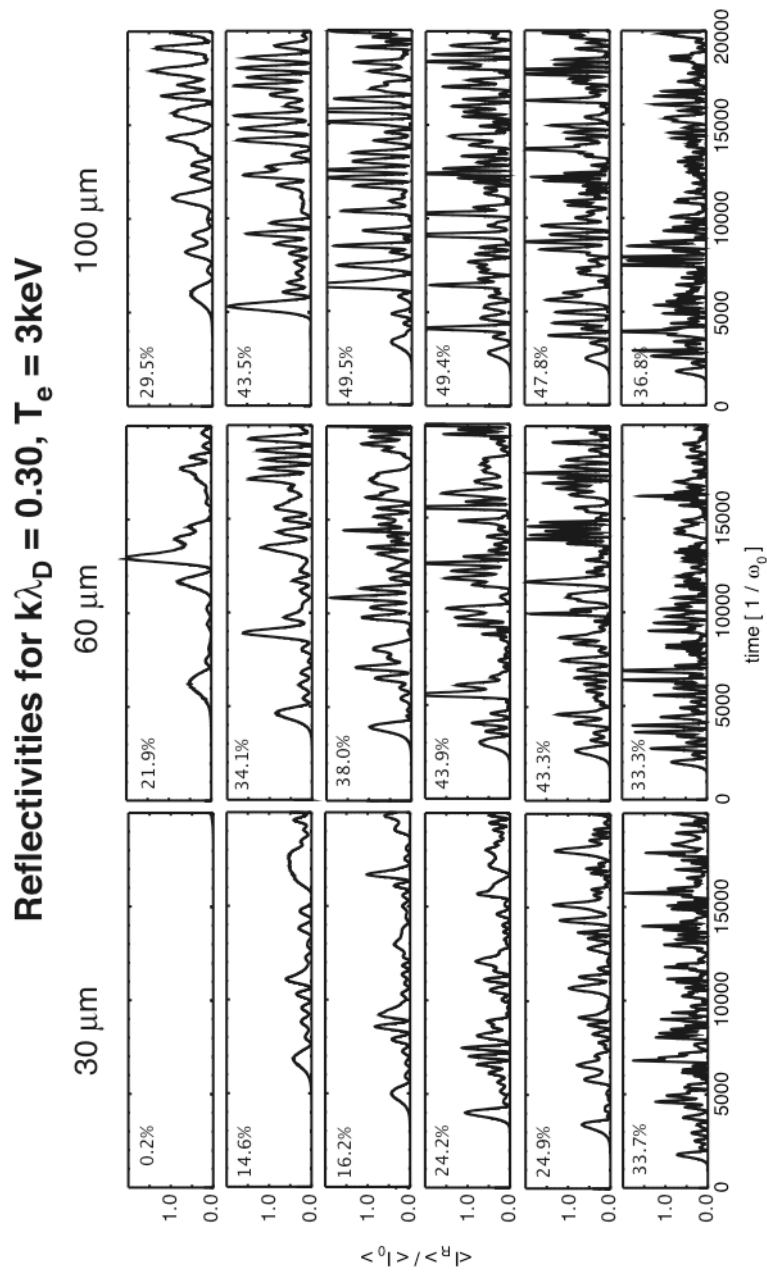


Figure 4.19: Reflectivities vs. time for Case 30-3.

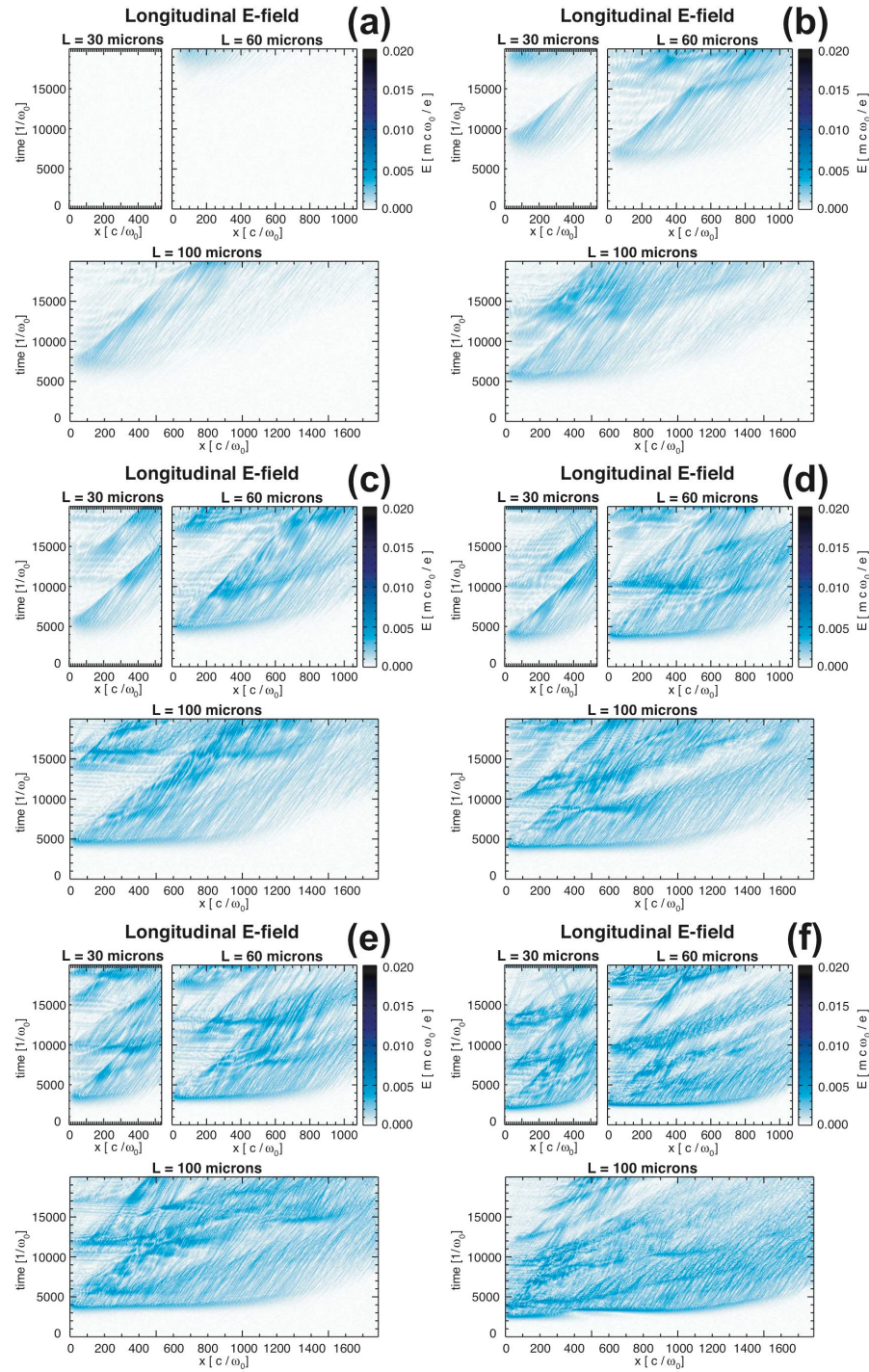


Figure 4.20: Evolution of the plasma wave for Case 30-700, with v_{osc}/c of (a) 0.011, (b) 0.013, (c) 0.016, (d) 0.019, (e) 0.021, and (f) 0.030.

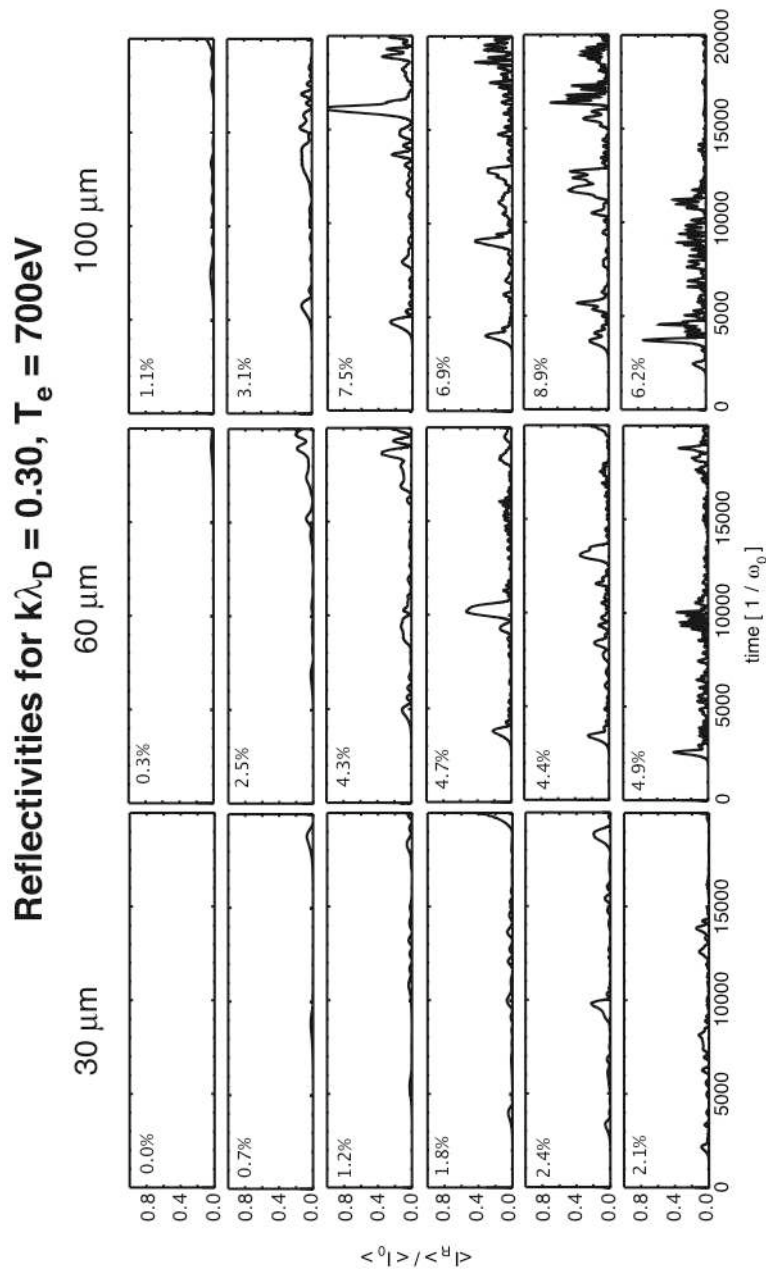


Figure 4.21: Reflectivities vs. time for Case 30-700.

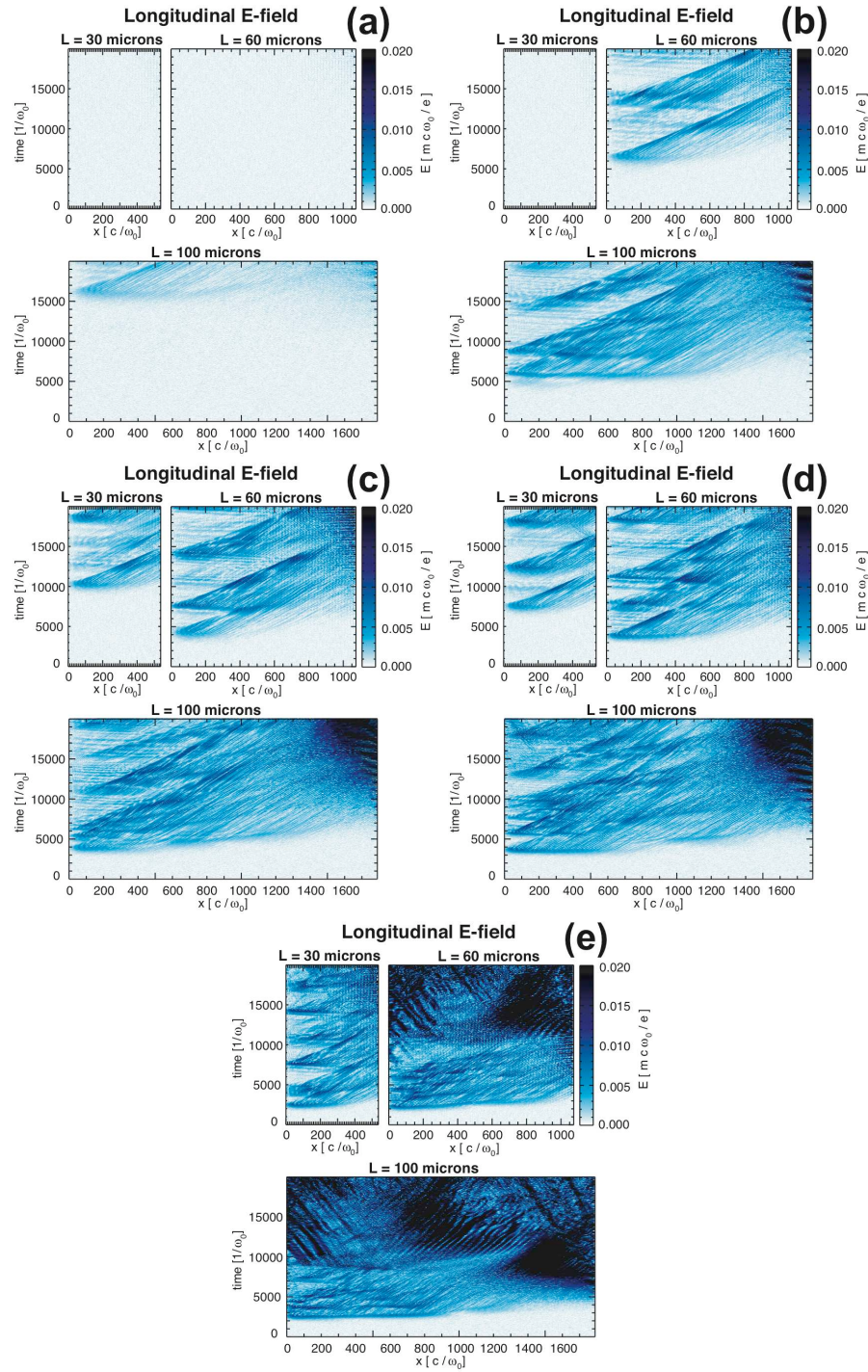


Figure 4.22: Evolution of the plasma wave for Case 34-3, with v_{osc}/c of (a) 0.011, (b) 0.016, (c) 0.019, (d) 0.021, and (e) 0.030.

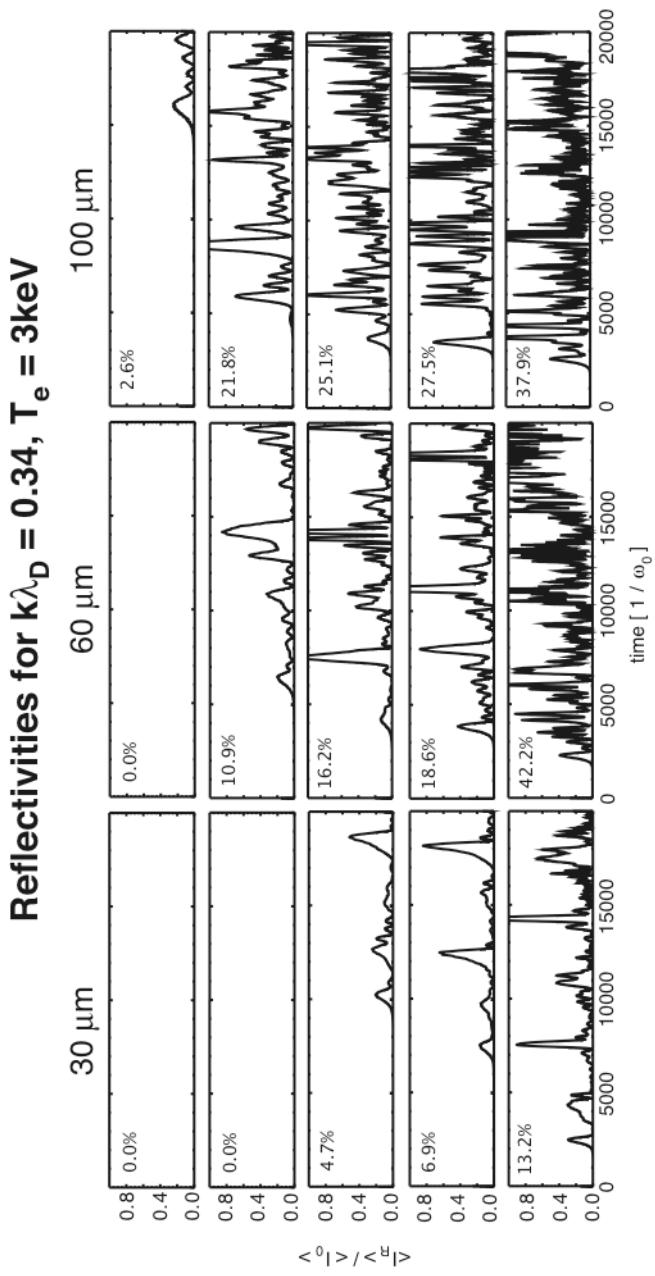


Figure 4.23: Reflectivities vs. time for Case 34-3.

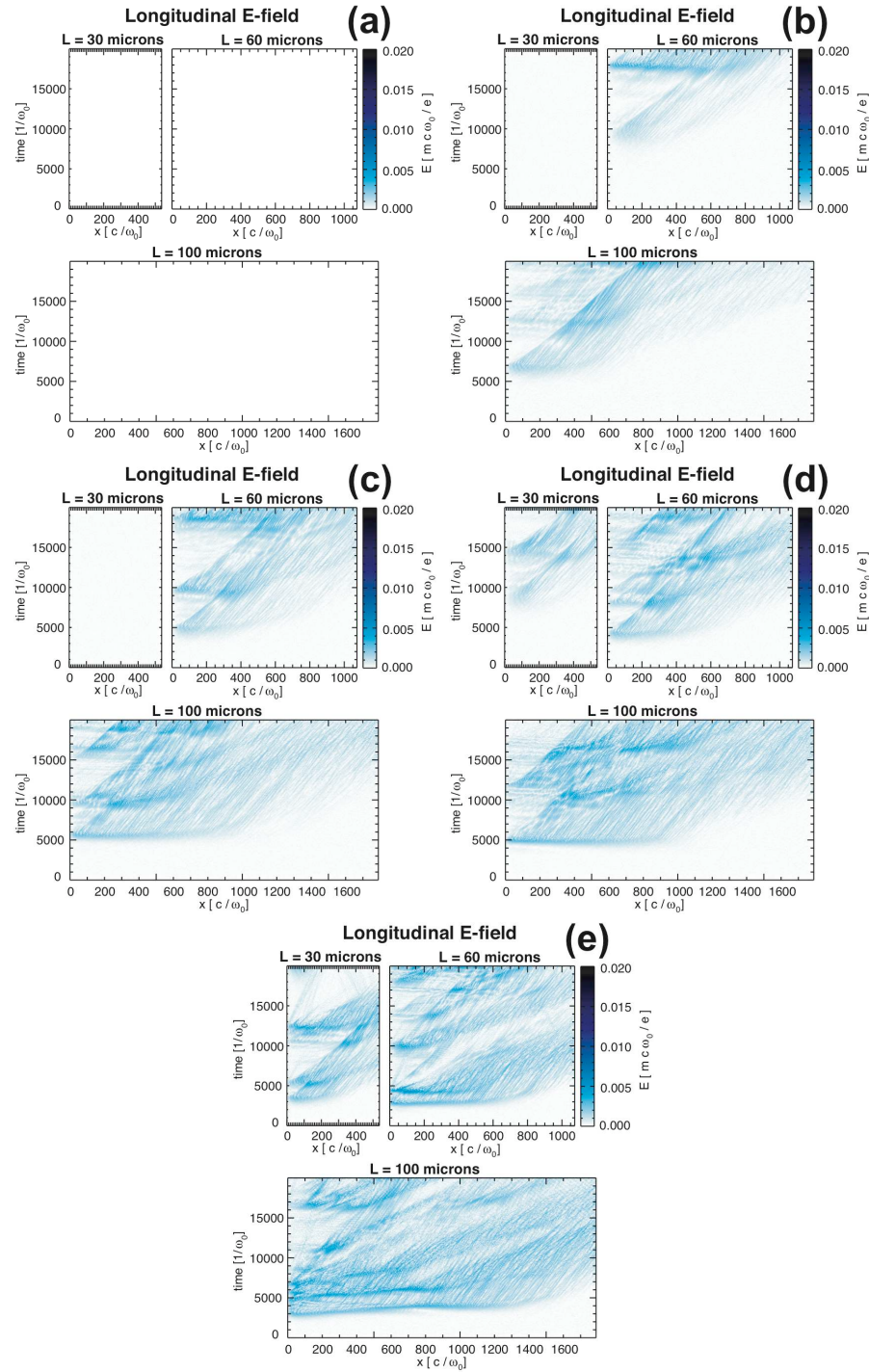


Figure 4.24: Evolution of the plasma wave for Case 34-700, with v_{osc}/c of (a) 0.011, (b) 0.016, (c) 0.019, (d) 0.021, and (e) 0.030.

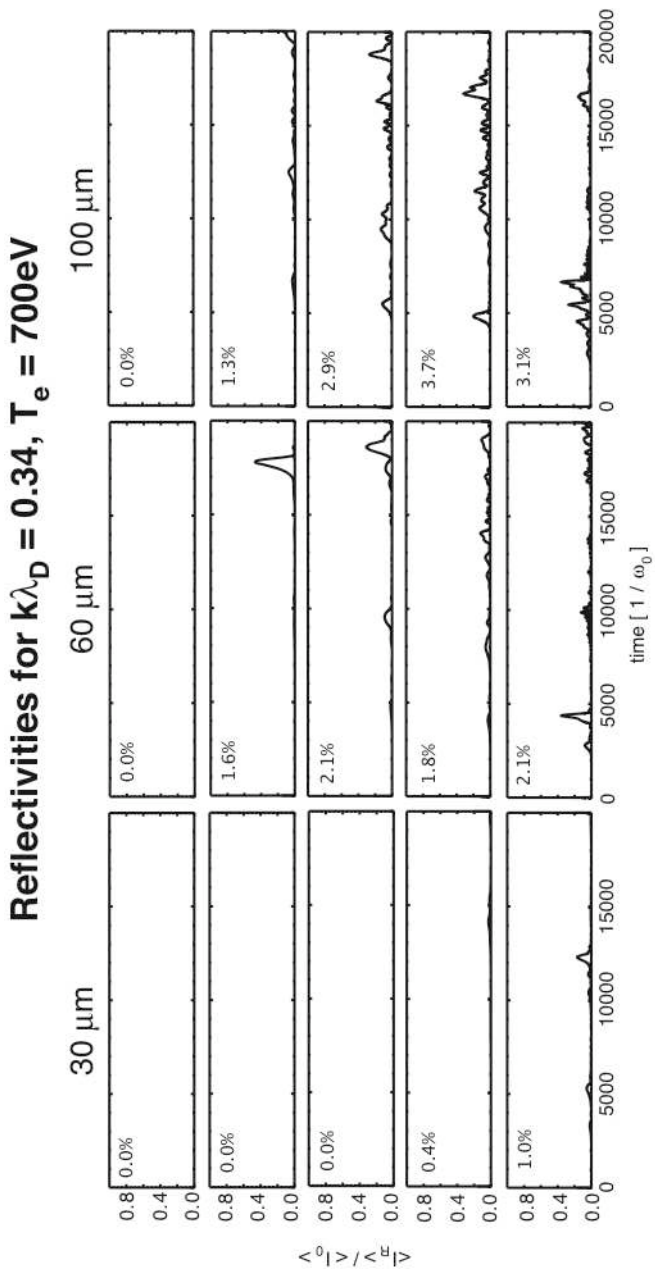


Figure 4.25: Reflectivities vs. time for Case 34-700.

the plasma packets that are initially excited by SRS have a longer spatial extent for higher laser intensities. As the laser intensity increases, the convective gain increases, resulting in a longer region of plasma wave activity that is driven to amplitudes that are sufficient for transitioning into the absolute regime. For the cases of $k\lambda_D = 0.26$ and 0.30 , the laser intensities do increase to the point at which they are above the absolute threshold, even when Landau damping for the unperturbed distribution function is considered, but this transition point is not obvious in the figures due to the absolute-like growth even for intensities below the absolute threshold.

Following the initial burst, SRS is seen to be temporally bursty, with the frequency of major bursts of SRS and the number of plasma wave packets within the simulated time increasing as laser intensity increases, in line with the conclusions drawn in the section on recurrence. The speed with which the plasma wave packets move is uniform as the laser intensity increases, as well as within simulations of constant intensity but different length. However, as the laser intensity increases, the distance that the packets move into the box before another SRS burst occurs steadily decreases, since the distance needed for growth of another packet shrinks as laser intensity increases. In the reflectivity plots, the temporal burst rate increases as the laser intensity increases, in accord with an increase in the nonlinear frequency shift as the plasma waves are driven to higher amplitudes. The amplitude and frequency of the reflectivity bursts are also seen to increase with time within each given plot, in accord with the conclusions that were previously drawn from the interaction of plasma wave packets in the section on recurrence.

Finally, the differences between the simulations at constant $k\lambda_D$ but different temperatures/densities is clearly evident. Since the higher temperature/density

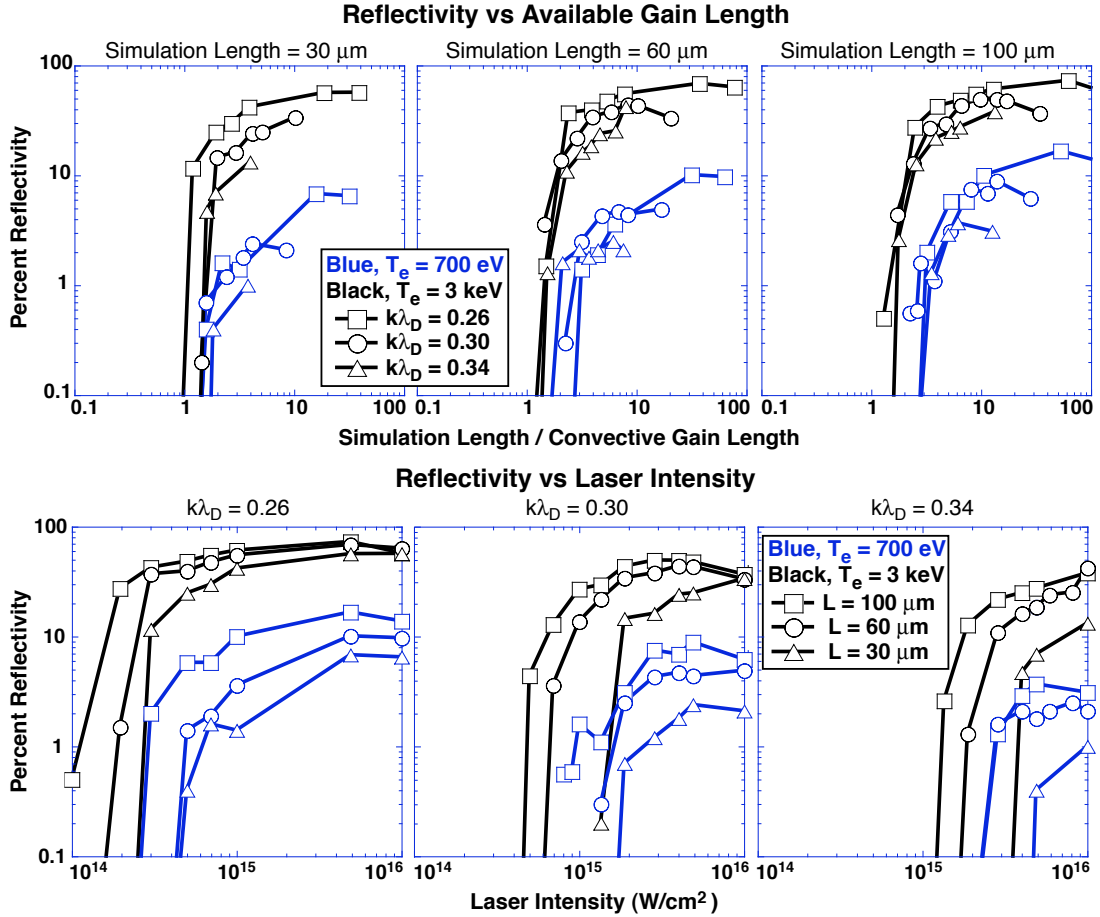


Figure 4.26: Reflectivity versus the number of convective gain lengths in the simulation box (top) and incident laser intensity for 3ω light (bottom).

simulations have the higher growth rates, SRS is driven more strongly in them before saturation occurs. As a result, they have larger plasma wave amplitudes (in units of $eE/mc\omega_0$) and larger reflectivities.

The total time-averaged reflectivity of SRS can be described in terms of the nonlinear behaviors that have been examined. Figure 4.26 plots reflectivity as a function of driving laser intensity (grouped according to $k\lambda_D$) and reflectivity as a function of the number of convective gain lengths in the simulation box

(grouped by simulation length). Even in the plots that are graphed as a function of the number of convective gain lengths, the driving laser intensity is still the independent variable.

First, the onset of SRS to significant levels ($> 1\%$ reflectivity) occurs when the intensity is high enough for there to be $\approx 1\text{-}2$ convective gain lengths in the simulation box. Therefore, there is a higher onset intensity threshold for (a) the lower temperature/density (e.g., 26-700-100 vs. 26-3-100), (b) the shorter length box, and (c) higher $k\lambda_D$. For (a), the lower temperature/density cases have the lower growth rates, and therefore need to be driven at higher intensities before sufficient convective growth occurs. For (b), the shorter boxes need to be driven at higher intensities before they have the same amount of convective gain as the longer boxes and can enter a similar nonlinear growth stage that is absolute-like. For (c), the cases with higher $k\lambda_D$ have the lower growth rates (due primarily to their lower densities compared to lower $k\lambda_D$) and therefore, similarly to (a), need to be driven at higher intensities for sufficient convective growth.

Between cases of constant $k\lambda_D$, the higher temperature/density combinations always have the higher reflectivity levels. They have the larger growth rates and the SRS daughter waves will be driven to larger amplitudes before the nonlinear frequency shift detunes the instability. The growth may even out-strip the detuning, in which case the saturation occurs by pump depletion. The amplitudes of the plasma waves between the two temperature/density combinations for a given $k\lambda_D$ are fairly similar in terms of the Coffey limit or in units of ω_p and v_{th} , and they have similar nonlinear frequency shifts. However, on the scale of laser units (c and ω_0), the amplitudes and frequency-shifts (time-scales) between the two are very different, resulting in the different reflectivity levels.

Finally, within each subcase of constant $k\lambda_D$, temperature, and density, the

simulations with the longer length have the larger reflectivity. There is a longer available region of space in the longer boxes for the instability to convectively grow. In addition, continued scattering from packets influences the long-time behavior of SRS if packets are able to coexist with new bursts of SRS before exiting the box. This interaction contributes to larger reflectivities.

4.6 Conclusions

SRS in regimes of relevance to IFE and currently for NIF continues to present a theoretical challenge. Trends in the highly kinetic, nonlinear behavior of SRS for moderate values of $k\lambda_D$ ($= 0.26 - 0.34$) have been presented. The initial onset of the instability scales approximately with the convective gain length, with the interaction length between the plasma and laser satisfying at least 1-2 convective gain lengths. The growth rate to saturation, nevertheless, is close to the absolute growth rate since SRS transitions from the convective to the absolute regime as trapped particles bounce in the plasma wave and decrease its damping rate. The maximum amplitude and frequency shift of the plasma waves at saturation are very similar in terms of ω_p and v_{the} , but the scaling against normalized units of c and ω_0 is more accurately indicative of the trends seen in total reflectivity, where the higher temperature/density combinations (for a given $k\lambda_D$) have the higher reflectivity. The saturation can be due to either pump depletion or phase detuning due to the nonlinear frequency shift, with the particular mechanism dictated by the particular plasma parameters. The plasma packets convect as a group after saturation (with an etching velocity that agrees with the model of [90]), with SRS recurrence determined by both the rate at which these packets evacuate the previously unstable region and the frequency shift of the plasma waves in the packet. SRS continues to occur from

packets as they convect, as was demonstrated in several simulation-experiments. In addition, packets locally deplete energy from the pump; as the packets are etched away and deplete less energy, the pump can then more fully penetrate the packet to drive renewed SRS growth. Finally, scattered light can travel between and interact with multiple packets, increasing the SRS reflectivity. The scalings of all these nonlinearities serve to inform conclusions about the total time-averaged reflectivity and its increase with 1) increasing laser intensity, 2) decreasing $k\lambda_D$, 3) increasing temperature/density for constant $k\lambda_D$, and 4) increasing plasma length.

CHAPTER 5

Mobile Ions and Multi-dimensional Behavior of SRS

One-dimensional, fixed-ion simulations are useful for isolating SRS and simplifying its nonlinear behavior, but they lack any information about the potential effects of mobile ions or multi-dimensional behavior. In this chapter, results are shown from several simulations that extend Cases 1-30 and 3-30 of Chapter 3 to include mobile ions in 1D simulations, as well as their extension with fixed ions to 2D simulations. The results indicate that the general picture presented in the previous two chapters still holds true.

It has been argued that LDI saturates SRS for $k\lambda_D < 0.30$, while kinetic effects dominate for $k\lambda_D > 0.30$ (for example, [58, 42]). The lower $k\lambda_D$ simulations of 0.26 are compared against those at 0.30 to investigate the extent to which this is true in one dimension.

5.1 Parameters

The first group of mobile ion simulations are exactly similar to Cases 1-30 and 3-30 with the exception of ions. The second ion species in each case was taken to be singly ionized hydrogen, with $Z = 1$ and a mass ratio of $M_i/m_e = 1836$. For each case, three separate ion temperatures were simulated, $ZT_e/T_i = 10, 5$ and

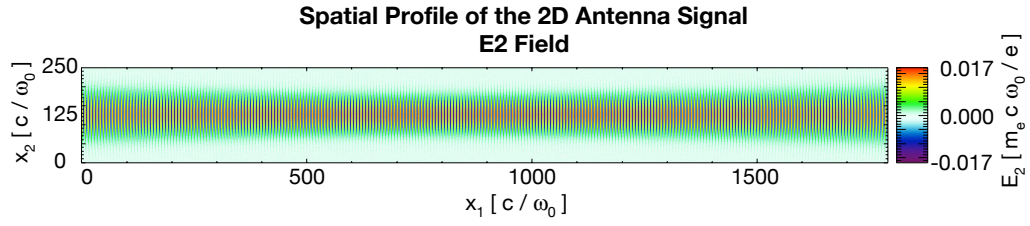


Figure 5.1: Transverse Field (E2-field) showing the incident laser profile.

3. A few cases with $ZT_e/T_i = 1$ were done, with little difference from the $ZT_e/T_i = 3$ case. For Case 3-30, these result in ion temperatures of 300, 600, and 1000 eV, while for Case 1-30 these are 100, 200, and 333 eV. 512 ions were simulated per cell.

In addition to this comparison, the three ion temperature ratios were also examined for $k\lambda_D = 0.26$. The simulations had the same two electron temperatures as the previous chapter (3 keV and 700 eV) with electron densities chosen appropriately to give $k\lambda_D = 0.26$ of the SRS plasma wave ($n/n_{cr} = 0.153$ and 0.056, respectively). Similarly to above, three separate ion temperatures were simulated, $ZT_e/T_i = 10, 5$ and 3 , giving the same temperatures as above for the simulations of $T_e = 3$ keV, while for $T_e = 700$ eV we have $T_i = 70, 140$, and 233 eV. In each of the simulations for $k\lambda_D = 0.26$, $I_{laser} = 1.0 \times 10^{15}$ W/cm² ($v_{osc}/c = 0.0095$), $L = 100\mu\text{m}$, and 512 ions were simulated per cell.

For the extension of Cases 1-30 and 3-30 to 2D (labelled 1-30-2D and 3-30-2D respectively), the parameters are as follows. Both simulations have a length of 1790 c/ω_0 (285 λ_0). The driving laser enters from the left side of the simulation with a spatial profile as shown in Figure 5.1. The laser focuses to the center of the simulated domain with a spot size $w_0 = 48.6 c/\omega_0$ (7.7 λ_0) and an intensity that increases from $v_{osc}/c = 0.012$ at the simulation edge to a focus of $v_{osc}/c = 0.015$.

In unnormalized parameters for a 3ω laser, the spot size is $2.7 \mu\text{m}$, the simulation length is $100 \mu\text{m}$, and the laser intensity is $2.5 \times 10^{15} \text{ W/cm}^2$ at focus. For the backscattered plasma wave, $k\lambda_D = 0.30$. The electron (T_e [keV], n/n_{cr}) is (1.0, 0.059) and (3.0, 0.128) for Case (1-30-2D, 3-30-2D), while the ions are fixed. Both simulations had 8192×512 cells, with 256 particles per cell. The number of particles per cell was reduced from that of the 1D simulations to accommodate the simulations' increase in total computational size. However, the number of particles per cell needed in 2D is less than in 1D for a desired noise level and finite size particle collision frequency.

5.2 Mobile Ions

The effect of mobile ions for Cases 1-30 and 3-30 is small. Figures 5.2 and 5.3 show the spatio-temporal evolution of the longitudinal E-field and the reflectivity, respectively, for the six cases corresponding to Cases 1-30 and 3-30 (compare to Fig. 3.18). The primary effect of mobile ions can be seen in the plasma waves that travel backwards (towards the left in the space-time plots). This is a signature from LDI, where the forward traveling SRS plasma wave decays into a plasma wave traveling backwards and an ion acoustic wave. The presence of LDI was verified by matching the modes in frequency and wavenumber space. The backward-traveling plasma waves, that is, LDI, become more pronounced for the increasing temperature ratio because the ion acoustic wave damping rate correspondingly decreases and the LDI threshold is therefore decreased.

Even though the amount of LDI increases as ZT_e/T_i increases, the reflectivity actually increases (although only slightly). While LDI is a process through which the SRS plasma wave decays, more LDI in these cases does not result in a decrease in the plasma wave amplitudes nor, correspondingly, in their reflectivities. The

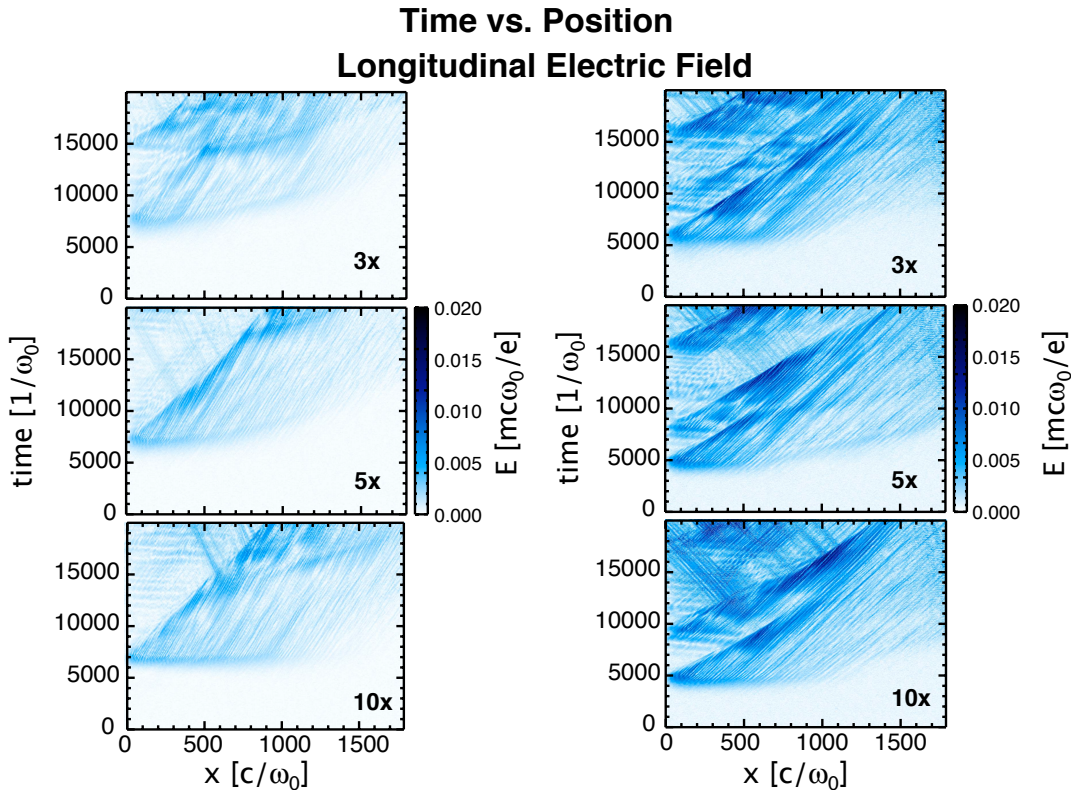


Figure 5.2: For $k\lambda_D = 0.30$, time vs. space plots of the longitudinal E-field for $T_e = 1$ (left) and 3 keV (right), with $ZT_e/T_i = 3$ (top), 5 (middle), and 10 (bottom).

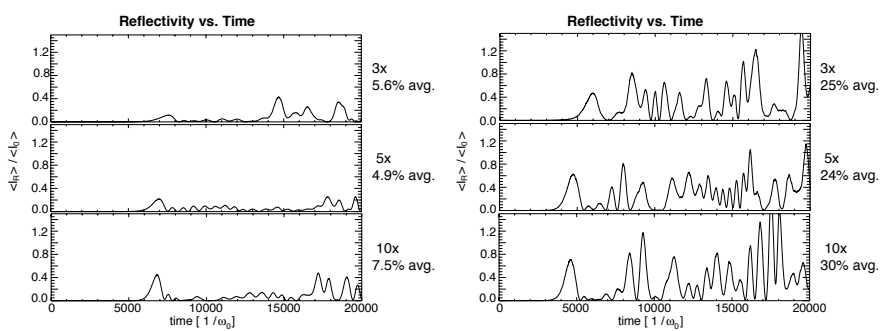


Figure 5.3: For $k\lambda_D = 0.30$, reflectivity vs. time for $T_e = 1$ (left) and 3 keV (right), with $ZT_e/T_i = 3$ (top), 5 (middle), and 10 (bottom).

difference in reflectivities is slight, with a 25% increase in reflectivity for $T_e = 1$ keV and 17% for $T_e = 3$ keV.

For $T_e = 1$ keV, the number of SRS packets in the simulated time does decrease as LDI grows to larger levels, but the plasma wave amplitudes and activity in the first convecting packet increase. The presence of LDI appears to stabilize the plasma wave packet's convection after saturation, with the packets undergoing stronger SRS later in time as a result. The slight increase in reflectivity comes from continued scattering from convecting packets, whereas the recurrence of new bursts of SRS are slightly diminished as the ratio of ZT_e/T_i increases.

While the number of packets does not change as clearly for the $T_e = 3$ keV cases, the increasing presence of LDI has a stabilizing effect for these simulations as well. For example, in simulation 3-30-10x, the plasma packet has a higher amplitude at $x\omega_0/c = 1000$ and $\omega_0 t = 15000$ than it does at most points in simulation 3-30-3x. Continued scattering from this strong plasma packet results in the bursts of reflectivity seen in the corresponding reflectivity plot at $\omega_0 t = 16000 - 17000$.

The effect of mobile ions is more noticeable in the simulations for $k\lambda_D = 0.26$, specifically for $T_e = 700$ eV. As has been postulated theoretically and experimentally, LDI has a more pronounced affect on SRS at lower $k\lambda_D$. The simulations for $k\lambda_D = 0.26$ are shown in Figures 5.4 and 5.5, where again the spatio-temporal evolution of the longitudinal E-field and the reflectivity are shown.

For these simulations at $k\lambda_D = 0.26$, the cases with $T_e = 3$ keV show the most dramatic LDI activity, as evidenced in the backward traveling plasma waves, but the reflectivity is negligibly different from the fixed ion simulation for the same laser intensity (with differences of only a few percent), and the reflectivities only slightly vary for differing ratios of ZT_e/T_i . By contrast, the simulations for

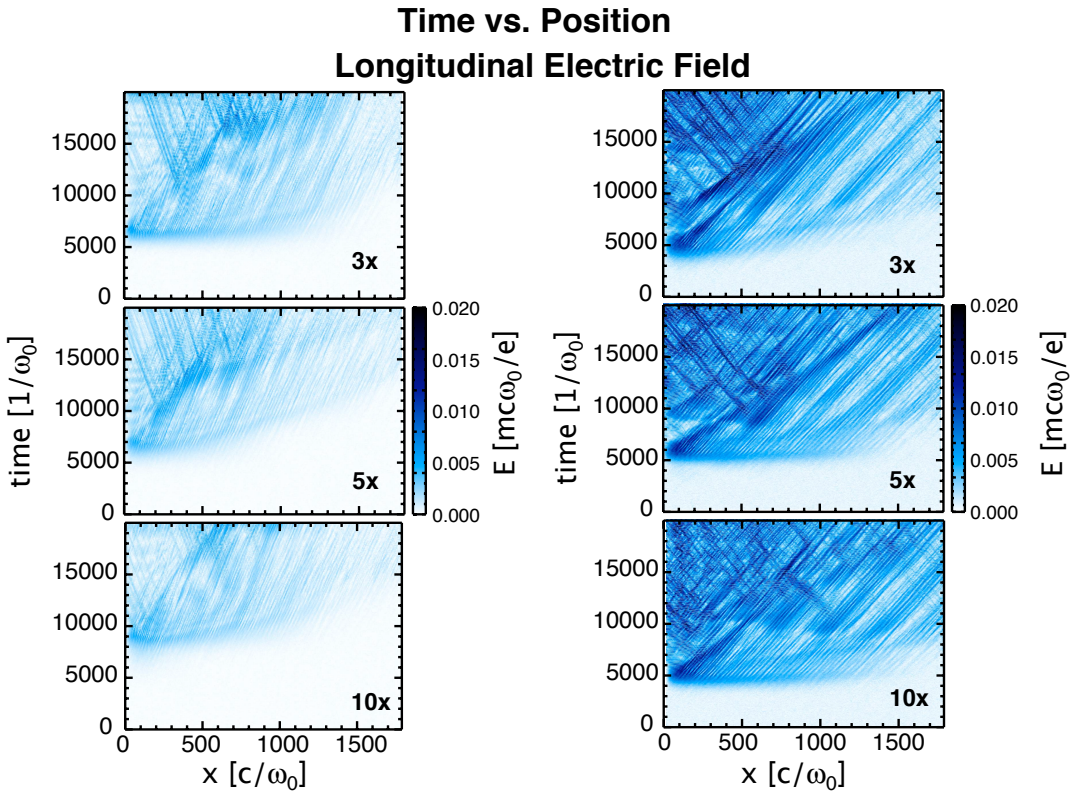


Figure 5.4: For $k\lambda_D = 0.26$, time vs. space plots of the longitudinal E-field for $T_e = 700$ eV (left) and 3 keV (right), with $ZT_e/T_i = 3$ (top), 5 (middle), and 10 (bottom).

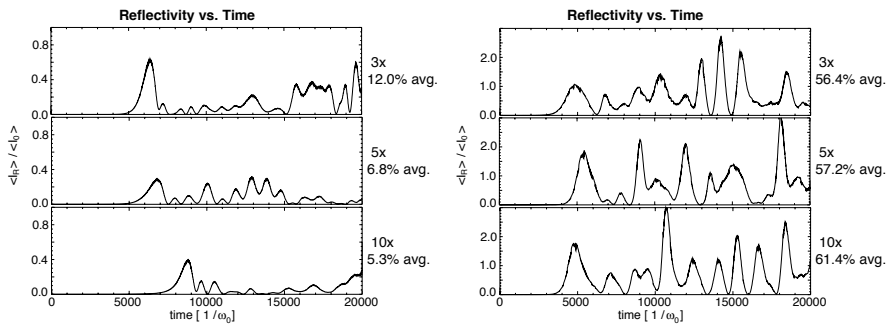


Figure 5.5: For $k\lambda_D = 0.26$, reflectivity vs. time for $T_e = 700$ eV (left) and 3 keV (right), with $ZT_e/T_i = 3$ (top), 5 (middle), and 10 (bottom).

$T_e = 700$ eV are affected by mobile ions. Case 26-700-100 with the same laser intensity but fixed ions showed a reflectivity of 10%. Here, as the damping rate of the ion acoustic waves decreases, the reflectivity decreases from 12% to 5%, dropping to half the reflectivity level of the fixed ion simulation. Even though the most dramatic LDI activity appears to occur for 26-700-3x (with the largest amplitude LDI daughter waves), this is because the plasma waves reach higher amplitudes in this case before saturation occurs. With LDI acting as a possible saturation mechanism as ZT_e/T_i increases, the plasma waves only grow to as high an amplitude as necessary to undergo LDI and then stop. With LDI occurring in the 26-700-10x and clamping the SRS plasma wave amplitude, the daughter LDI modes do not grow as strongly.

In all of the ion simulations shown here, the reflectivities show a periodicity similar to that found in the fixed ion simulations. Once again, this corresponds to continued scattering from convecting packets that recurs with a periodicity dependent on the nonlinear frequency shift of the electron plasma wave. This periodicity, and correspondingly the frequency shift, varies little as the ion temperature is varied. The periodicity between new bursts of SRS as packets convect away from a region of plasma is more affected by the presence of ions, as now the plasma daughter waves from LDI travel back into the region. Regardless of how mobile ions affect the saturation of the initial burst of SRS, in all cases the stronger growth of LDI for increasing ZT_e/T_i disrupts the periodicity of later bursts.

The results of this section support the conclusion that LDI has a more dramatic effect on SRS for the lower $k\lambda_D$ of 0.26 versus that of 0.30. This section is far from comprehensive, and leaves the door open for further investigation, but the results with mobile ions continue to support the results of the previous

chapter on the nonlinear evolution of SRS: the evolution of SRS is still affected by convecting plasma wave packets, with continued scattering that is dependent on the nonlinear frequency shift. The magnitude of the plasma waves and the average reflectivity levels are largely unchanged for $k\lambda_D > 0.26$, and even for the higher T_e case at $k\lambda_D = 0.26$.

5.3 2D

The 2D simulations (with fixed ions) introduce a number of new effects. The first 2D result is that the reflectivities are lower than the corresponding 1D cases. The reflectivities for Cases 1-30-2D and 3-30-2D are shown in Figure 5.6. On the left is shown the temporal evolution of the backscattered light along the transverse direction at the incident edge. The driving antenna signal has been subtracted out of the transverse field, with the remaining E2-field due solely to scattered light. The square of this signal is summed across the transverse extent of the box and divided by the total squared laser field that is driving the plasma. The envelope of this reflectivity ratio is plotted versus time on the right.

There is only weak SRS for Case 1-30-2D (with $v_{osc}/c = 0.012$ at the laser entrance), with a total time-averaged reflectivity of 1.0% in 2D versus 6.1% in 1D, while for Case 3-30-2D (with $v_{osc}/c = 0.012$ at the laser entrance) the total time-averaged reflectivity is 12% in 2D versus 33% for 1D. Given the small amount of SRS for Case 1-30-2D, the description of two-dimensional SRS evolution in this section will focus on Case 3-30-2D. The initial burst of SRS will be studied first, followed by an analysis of the subsequent evolution.

Similarly to 1D, the growth rate of SRS is close to the undamped absolute growth rate. Even though it is in the strongly damped regime, the temporal

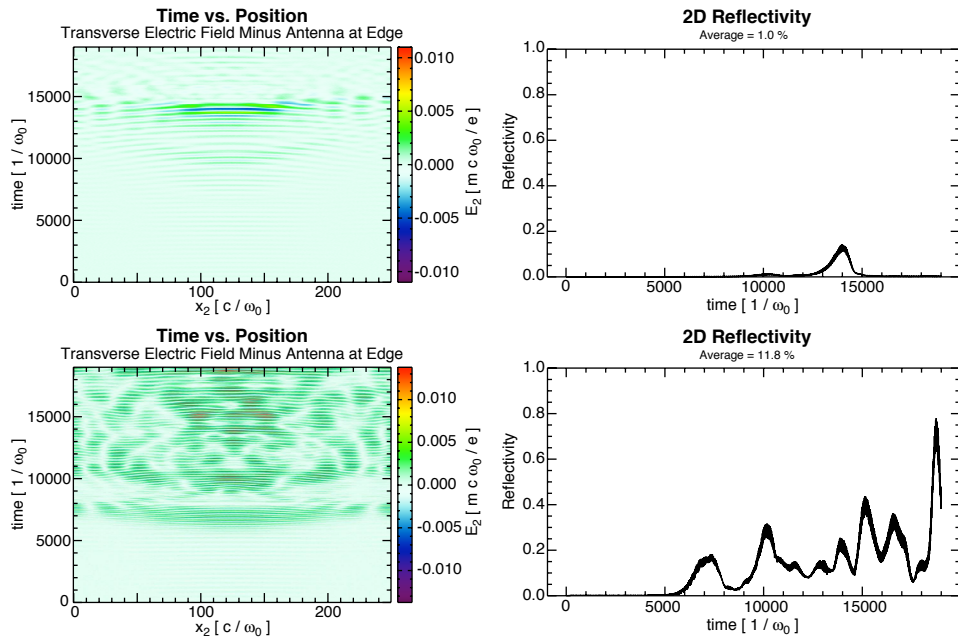


Figure 5.6: Reflectivities for Cases 1-30-2D (top) and 3-30-2D (bottom). Reflected light shown as time vs. x_2 (left) and the temporal evolution of the total reflected intensity divided by incident intensity (right).

growth rate is $\gamma/\omega_0 \approx 0.0014$ in comparison with $\gamma_{abs}/\omega_0 \approx 0.0017$ (both growth rates are measured/calculated at the same point $x\omega_0/c = 150$).

The 2D behavior of the plasma wave's E1-field is shown in Figure 5.7 at three times during the first SRS burst. The plasma waves only grow to the left of the focus. This first burst of SRS demonstrates several multi-dimensional nonlinearities. First, the wave fronts of the plasma waves are bending. As the plasma waves grow, the amplitude grows larger along the center ($x_2\omega_0/c = 125$) than along the top or bottom of the plasma wave packet ($x_2\omega_0/c = 100$, for example). The nonlinear frequency shift of the plasma wave is therefore larger in the center. Translating this to a nonlinear shift in the phase velocity is not straight-forward since the k of the plasma wave (and of the reflected light) is also adjusting. Both a transverse difference in the phase velocity of an undriven wave and the nonlinear response to a driver can lead to bowing.

This wave-bowing was first noted by Yin *et al.* [94], where it was postulated that the SRS saturation in 2D was due to plasma wave self-focusing and filamentation due to wave-front bowing. Such instabilities depend on amplitude dependent phase velocities. This filamentary effect, which is starting to occur by the third plotted time of Figure 5.7, has also been studied by Fahlen *et al.* [95] who has shown that the localization is due instead to nonuniform trapped-particle damping on the edges of a plasma wave packet. In addition, the 2D analog of the sidebands can be seen as “holes” (modulations) in the packet's wave structure. Similarly to 1D, the sidebands are present as an amplitude modulation of the plasma wave, but here they form hole-like patches as they modulate the amplitude both longitudinally and transversely.

To analyze the reflected light, Figure 5.8 shows the transverse E2-field along the centerline, filtered and enveloped to show the incident and backscattered light

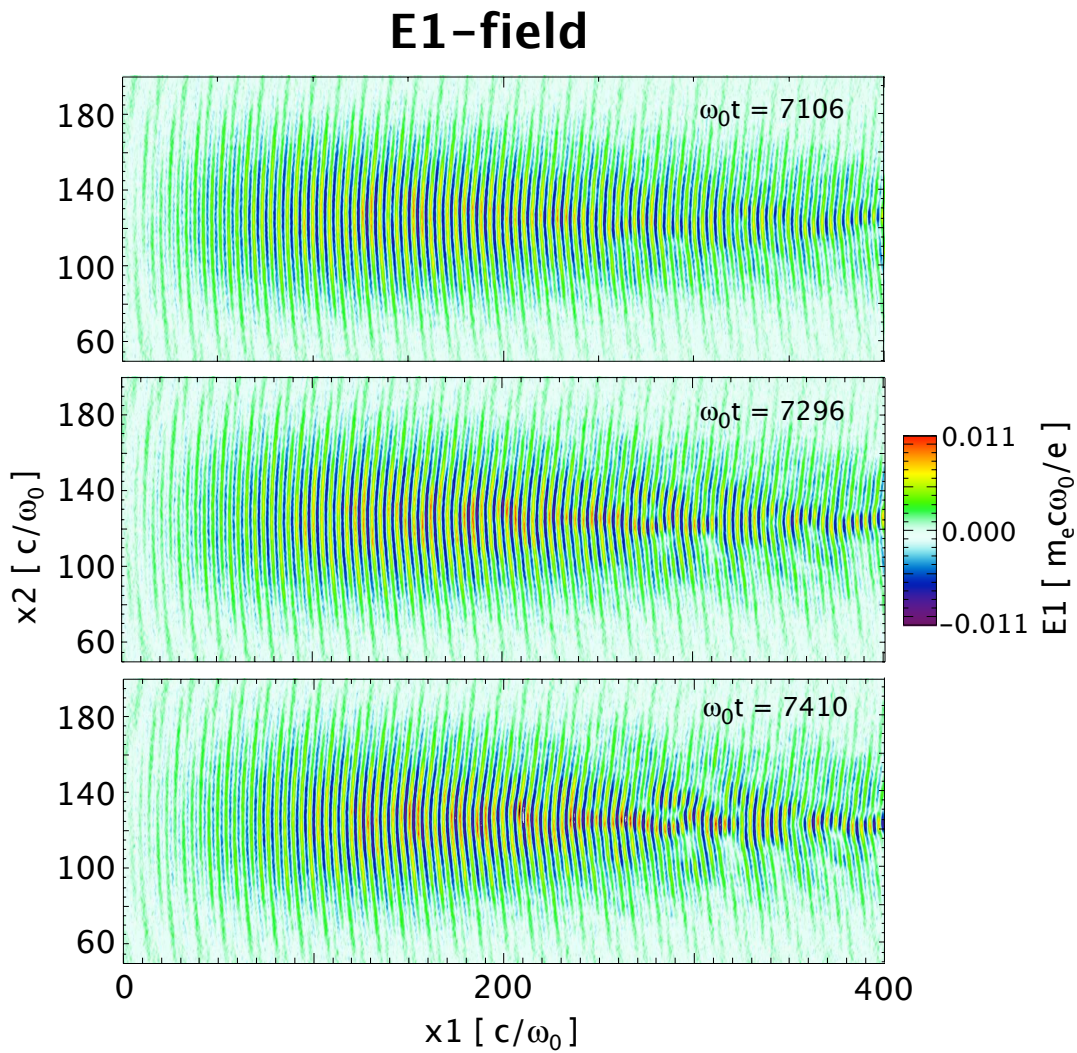


Figure 5.7: E1-field during saturation of the first burst of SRS.

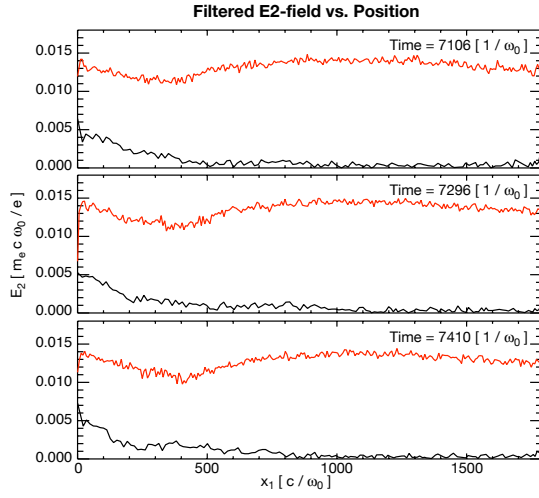


Figure 5.8: Incident and backscattered laser light at three times during saturation of the first burst of SRS.

waves. The same three time frames as in Figure 5.7 are shown. The temporal progression from $\omega_0 t = 7106 - 7410$ shows a slight decrease in the backscattered light and a slight movement of the depleted incident light signal into the box. The SRS is saturated at the earliest time frame and, when combined with Figure 5.7, indicates that the relative timings of the nonlinearities are intertwined as before in 1D. The frequency shift, as evidenced in the bowing of the plasma wave phase-fronts, has already begun by $\omega_0 t = 7106$. The sidebands grow up next along with the “filamentation,” that is, the localization along the axis of the plasma packet structure.

Given that the backscattered light in Figure 5.8 already appears to be saturated in the first frame, and furthermore is negligibly pump-depleted, it appears that the frequency shifts are the cause of saturation for this case. The sidebands, as evidenced by the modulation of the plasma wave’s amplitude, grow after the instability has saturated, and the central filament structure does not form until

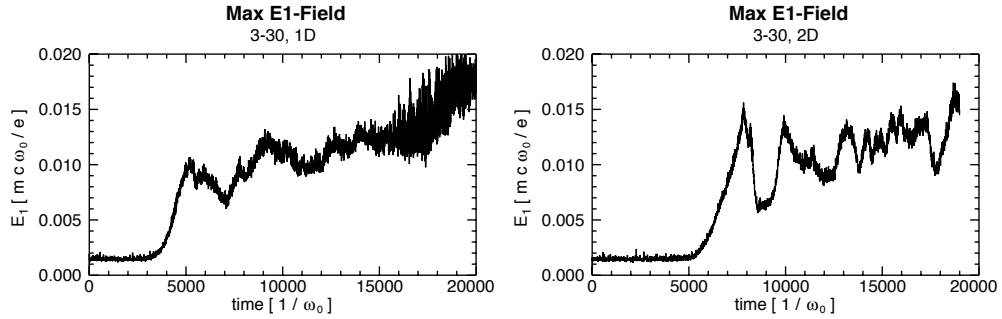


Figure 5.9: Maximum E1-field amplitude versus time for 1D (left) and 2D (right). The 2D plot represents the E1-field maximum on a lineout through the center of the simulation domain.

after the sidebands have grown and after the saturation has occurred. The saturation is therefore not attributable to the formation of this central filament, nor to the sidebands.

The previous chapter focussed on several trends, among which were the maximum amplitude and the nonlinear frequency shift of the plasma wave. Figures 5.9 and 5.10 show representative plots for the 2D case in comparison with the 1D simulation, where the maximum amplitudes and frequency-wavenumber modes are for the E1-field only along the central axis. As mentioned, the amplitudes in 2D are comparable to those in 1D. Early in time, the amplitudes are actually larger. The frequency shift may be slightly less in the 2D case, but it does match fairly closely as well. Similar frequency shifts, despite the larger amplitudes, may be due to transverse side-loss of trapped particles in 2D. The sidebands are seen in similar (ω, k) -streaks around the primary SRS plasma wave mode, and a faint point at approximately $(0.36, 0.4)$ is evidence of slight forward scatter. The acoustic-like streaks at constant velocity are not as prevalent in 2D, presumably due to the fact that any such mode will have a certain range of transverse velocities as well, with any purely on-axis acoustic modes having a smaller amplitude

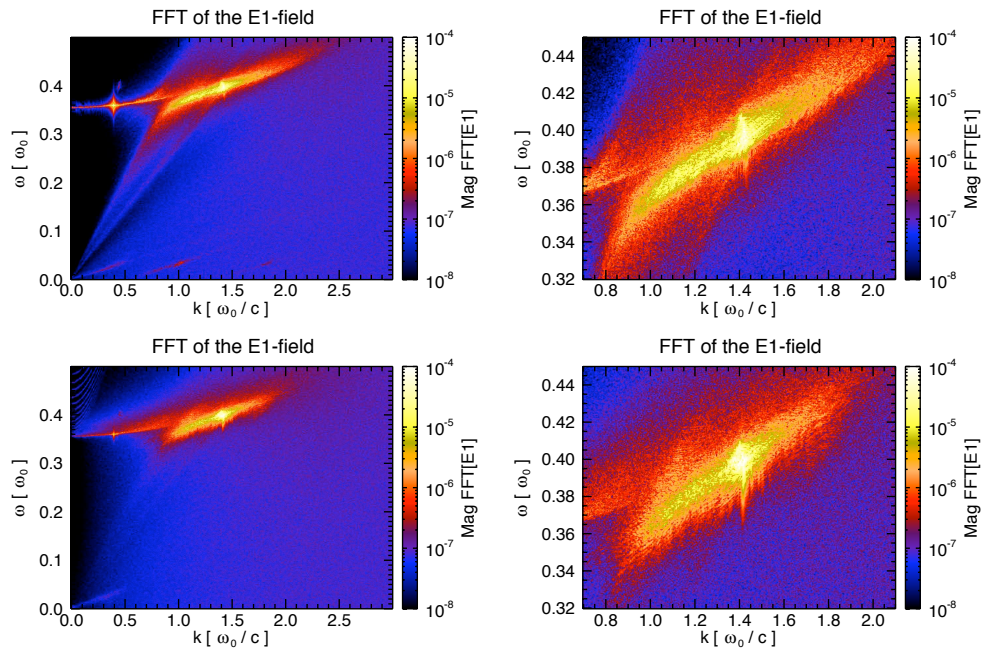


Figure 5.10: Frequency versus wavenumber of the E1-field for 1D (top) and 2D (bottom), where the 2D E1-field is taken along the central axis.

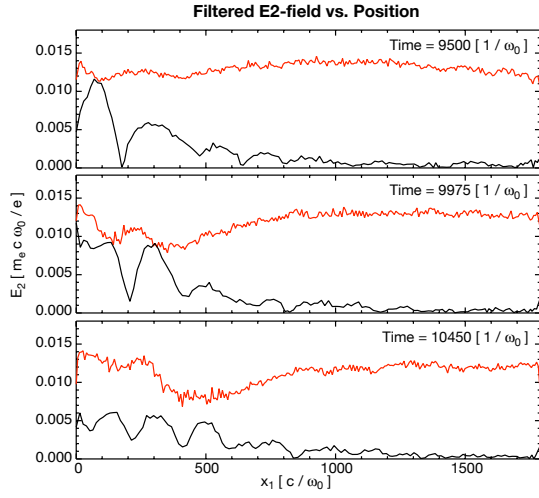


Figure 5.11: Incident and backscattered laser light at three times during saturation of the second burst of SRS.

as a result. Overall, Figures 5.9 and 5.10 show that on-axis, the plasma wave behavior is not very different in 2D versus 1D.

As for comparing reflected wave amplitudes, the second burst of SRS is much more like the 1D case than the first burst, with saturation occurring only after the backscattered light has reached an amplitude that looks similar to the 1D pump-depleted case. Figure 5.11 shows the filtered transverse field for three times during the saturation of the second SRS burst, with the second time frame showing that the backscattered light reaches an amplitude that is comparable to the incident laser over a range of space. The third frame shows the decrease in reflected light amplitude after saturation, and a strongly pump-depleted laser signal that is due to the strong scattering that has occurred. This progression of events is similar to the SRS activity that was shown in 1D. The modulation in space is due to the nonlinear frequency shift.

Regardless of the reflected light amplitude on axis, however, the total reflec-

tivity summed over the transverse direction is not similar to the 1D reflectivity levels. A comparison of results between Cases 3-30 (1D) and 3-30-2D is shown in Fig. 5.12. Figure 5.12 (top) shows 1D simulation results, while Fig. 5.12 (bottom) shows 2D results. In the 1D case, the plasma waves and reflectivity evolve similarly to what has been shown in previous chapters, with packets that move at v_{packet} and scatter light at a rate determined by the frequency shift. The first packet locally depletes the incident laser energy, but as trapped particles progressively etch it, the pump is more weakly depleted by $\omega_0 t = 8000$ and there is renewed packet growth, resulting in the larger reflectivity bursts at $\omega_0 t = 8000$. The reflectivity continues to grow in amplitude as time evolves. Plasma wave packets interact with each other via scattered light traveling between them, a process that ultimately leads to higher reflectivity.

The total time-averaged reflectivity is lower for the 2D case (12%) versus the 1D case (33%). A focused Gaussian profile was used in the 2D case, so geometric effects related to varying laser intensity across the spot, the finite width of the plasma wave, and the finite spread in incoming angles all lead to a decrease in overall reflectivity. Furthermore, nonlinear finite spot-size effects such as transverse localization of 2D plasma packets further reduce the SRS activity to the central axis after saturation.

Although localization occurs, it does not completely destroy the packets, as may be seen in Fig. 5.13 (top); the arrows show how far a point moving at the group velocity would travel. The filamentary structures consist of saturated, transversely-localized plasma wave packets that convect through the simulation domain. SRS is still 1D-like along axis, but the localization limits SRS activity off-axis and reduces reflectivity levels from 1D. The recurrence of SRS with frequency-shifted backscattered light is also evident in Figure 5.13 (bottom),

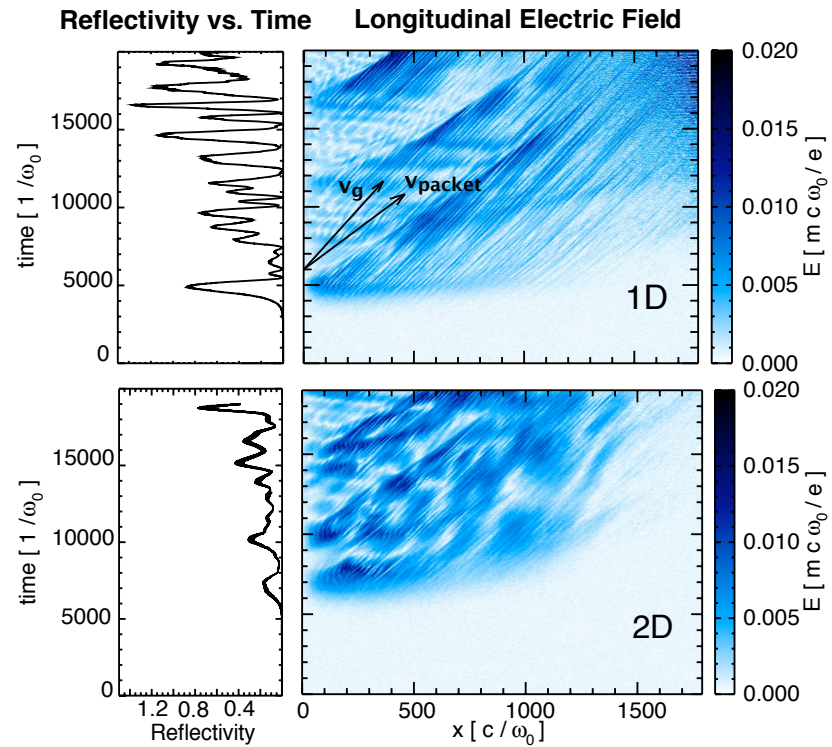


Figure 5.12: Reflectivity vs. Time (left) and Time vs. Space plots of the E1-field (right). The 2D plot represents the E1-field on a lineout through the center of the simulation domain.

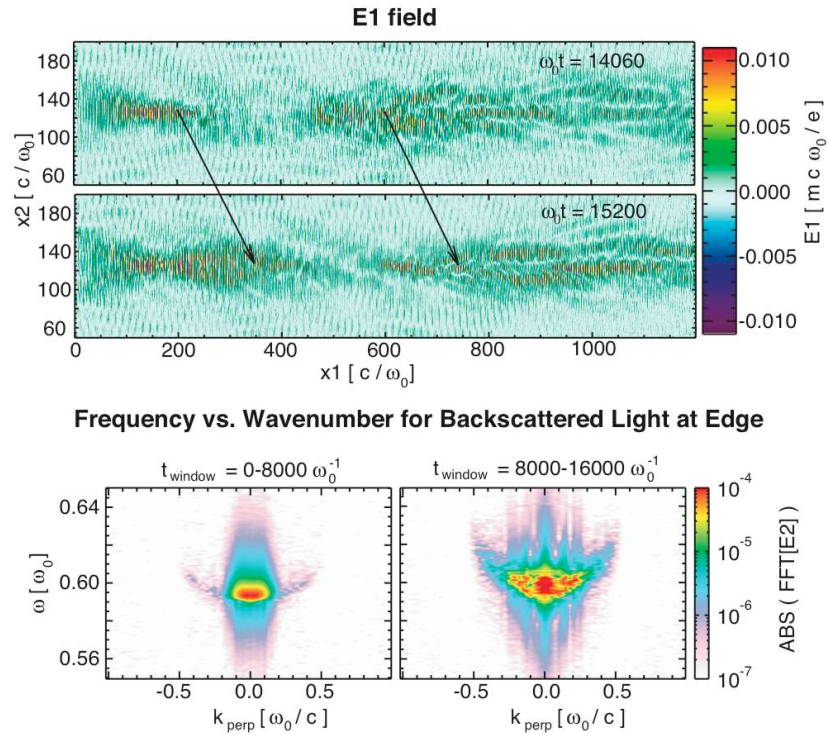


Figure 5.13: Top: E1-field in space at two neighboring times for 2D case. Bottom: Frequency versus Perpendicular Wavenumber for the backscattered light is shown for early (left) and late (right) times.

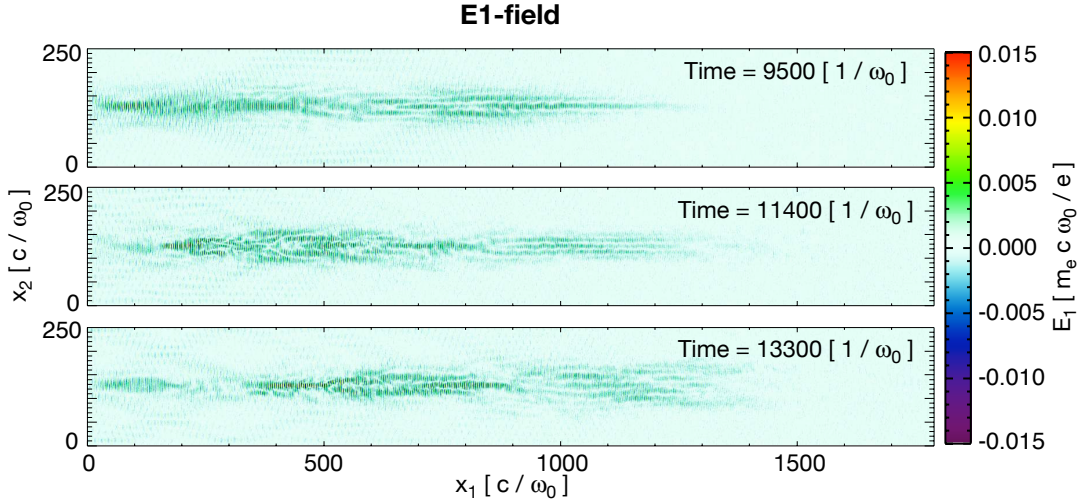


Figure 5.14: E1-field during and after the second burst of SRS.

where the perpendicular wavenumber of the backscattered light at the incident edge is plotted. The frequencies of the backscattered light consist of both the linear frequency (bottom-left) and up-shifted frequency (bottom-right), as light continues to backscatter at a shifted frequency from convecting packets. Figure 5.12 (bottom-right) shows the beating pattern in reflectivity and plasma wave activity behind the convecting packets as frequency up-shifted light drives the background plasma nonresonantly, similar to 1D. There is also a slight spread in perpendicular wavenumber in Figure 5.13 (bottom), due to slight side-scattering in addition to purely 1D-like backward SRS.

The evolution of plasma wave packets off-axis is more difficult to visualize without presenting a large number of 2D plots, but the essential characteristics can be gleaned from a few snapshots. The evolution of plasma waves subsequent to the second major SRS burst (at $\omega_0 t \approx 10000$) is shown in Figure 5.14, where the E1-field is plotted in space. After the growth of plasma waves with a transverse spread and subsequent plasma packet localization, the packet stops localizing at a finite width and convects through the plasma similarly to the 1D packets. The

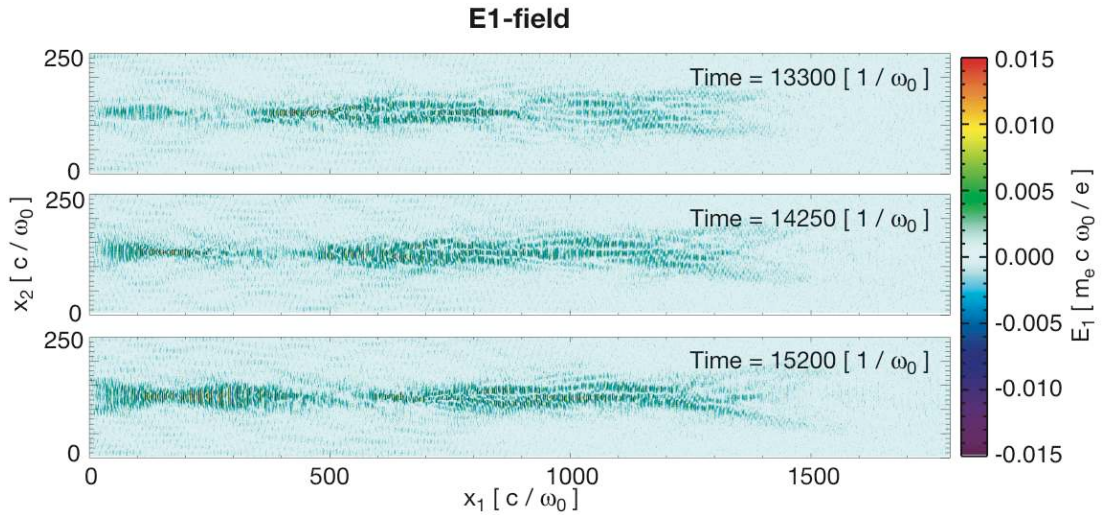


Figure 5.15: E1-field during continued convection of the central filament and subsequent regrowth of a third burst of SRS.

sideband behavior and the decay of the plasma wave structure into a central filament may not cause the saturation of SRS, but they do have consequences for the continued recurrence of SRS in 2D. Whereas in 1D there was a well-defined wave packet that convected through the system after saturation, here the plasma waves have decayed into the filament and the continued scattering of SRS from a convecting plasma packet is limited to this filament. The reflectivity off-center is therefore reduced as compared to 1D results, and while similar nonlinearities are affecting SRS on-axis, the total result is that the total 2D reflectivity is reduced.

The convective behavior of the filament continues in Figure 5.15. Here the continued resonance of SRS off the convecting packet is seen as (in the second frame) a new burst of SRS grows behind the convecting filament. Even if the continued scattering is limited in two-dimensional extent, the frequency content of the scattered light in Figure 5.13 showed that a resonance is occurring between a frequency down-shifted plasma wave and a corresponding frequency up-shifted

backscattered light wave. In fact, the plasma wave localization appears to be slightly reversed by the packet interaction, as was seen in Figure 5.13 (top) in the region of the left-most arrow. A newly saturated and localizing burst of plasma waves (on left) undergoes new growth and widens as it interacts with the backscattered light coming from the packet in front of it.

In summary, the behavior of SRS in 2D is affected by several multi-dimensional effects, notably the transverse localization of plasma wave packets. While the localization does not contribute as a new saturation mechanism, it limits SRS activity to the central laser axis. The total reflectivity is therefore reduced, but the key conclusions from 1D simulations of the previous chapters still carry over into higher dimensions. First, the reflectivity has a periodicity that is determined by the recurrence of new bursts and a finer-scale recurrence from continued scattering off convecting packets that is determined by the nonlinear frequency shift. Second, the nonlinear packet velocity is approximately equal in both 1D and 2D simulations, implying that the etching rate that was theorized in Fahlen *et al.* [90] can be extended to higher dimensions. Finally, the reflectivity increases as a function of time, implying that scattered light interacts with multiple packets.

CHAPTER 6

Conclusions and Directions for Future Work

6.1 Summary

The growth, saturation, and recurrence of SRS for moderate $k\lambda_D$ have been studied in 1- and 2D particle-in-cell simulations using the code OSIRIS. The laser and plasma parameters were chosen to be relevant to NIF, IFE, and related experiments. SRS was simulated across a range of laser intensities ($10^{14} - 10^{16}$ W/cm² for 3ω light), electron temperatures ($T_e = 0.7 - 3.0$ keV), electron densities ($n/n_{cr} = 0.036 - 0.16$), and plasma lengths ($30 - 100$ μ m), with $k\lambda_D$ of the SRS plasma wave ranging from 0.26 – 0.34.

The initial onset of the instability scaled approximately with the convective gain length, with the interaction length between the plasma and laser satisfying at least 1-2 convective gain lengths at threshold (> 1% reflectivity). The growth rate, nevertheless, was approximately equal to the absolute growth rate. This occurs because SRS transitions from the strongly damped convective to the weakly damped convective to the absolute regime as trapped particles bounce in the plasma wave and decrease its damping rate to nearly zero.

Several nonlinear trapped-particle effects are shown to affect the plasma wave. The frequency shifted negatively, while the wavenumber shifted positively at the plasma packet tail to maintain resonance with scattered light and the bulk of the plasma packet shifted slightly negatively in wavenumber to maintain the initial

phase velocity. Sidebands grow after SRS saturation, causing a modulation of the E-field of the plasma waves and contributing to a mixing of the trapped particle buckets. The tail of the distribution function at the phase velocity of the plasma wave initially flattens, as particles are initially trapped in the wave. After the sidebands grow and modulate the wave amplitude, the trapped particles move between buckets and the tail of the distribution develops a slight bump. As the sidebands grow to comparable amplitudes with the primary SRS plasma wave, entire buckets of trapped particles combine and the tail of the distribution relaxes back to a negatively sloped curve. Finally, the buckets return to their periodic waveform but with particles uniformly phase-mixed throughout the entire buckets. At this point in time, the distribution function is purely flat.

The maximum amplitude and frequency shift of the plasma waves at saturation are very similar in terms of ω_p and v_{the} across a wide range of parameters, but the scaling against normalized units of c and ω_0 is more accurately indicative of the trends seen in total reflectivity, where the higher temperature/density combinations (for a given $k\lambda_D$) have the higher reflectivity. The saturation can be dominated by either pump depletion or phase detuning due to the nonlinear frequency shift, with the particular mechanism dictated by the particular plasma parameters. Saturation by pump depletion has been shown for $k\lambda_D < 0.30$, while saturation by phase detuning has been shown for $k\lambda_D > 0.30$. Even for constant $k\lambda_D$, however, the saturation mechanism can be different for different temperatures and densities. A rough estimate of the saturation mechanism was shown to be the ratio of the growth rate to the detuning rate, as the frequency shift detuning will only be the cause of saturation if it can saturate the instability before the backscattered light depletes the pump to saturation.

After saturation, the resulting plasma wave packet convects through the sim-

ulated plasma with an etching velocity that agrees with the model of [90]. SRS recurrence is determined by both the rate at which these packets evacuate the previously unstable region and the frequency shift of the plasma waves in the packet. SRS continues to occur from packets as they convect at a rate of $2\pi/\Delta\omega$, where $\Delta\omega$ is the nonlinear frequency shift of the plasma waves. In addition, packets locally deplete energy from the pump; as the packets are etched away and deplete less energy, the pump can then more fully penetrate the packet to drive renewed SRS growth within the packet. Finally, scattered light can travel between and interact with multiple packets, increasing the SRS reflectivity. The scalings of all these nonlinearities serve to inform conclusions about the instantaneous reflectivity as well as the total time-averaged reflectivity and its increase with 1) increasing laser intensity, 2) decreasing $k\lambda_D$, 3) increasing temperature/density for constant $k\lambda_D$, and 4) increasing plasma length.

The 1D, fixed ion simulations were extended to include mobile ions and 2D effects. The mobile ions had little effect on the reflectivities with the exception of the low temperature/density, $k\lambda_D = 0.26$ simulations, where the reflectivity was decreased due to LDI. Evidence of LDI was seen for other simulations, but the effect on reflectivity was negligible. As for the 2D simulations, the reflectivities were shown to decrease, primarily due to the localization of the plasma wave activity along the center of the laser. Nevertheless, the wave amplitudes, frequency shifts, and nonlinear packet behavior were shown to be similar to the 1D results, with periodic scattering at a rate dependent on the frequency shift and an increase in reflectivity over time as multiple packets interacted.

6.2 Extending Simulations to Density Gradients and Higher Temperatures and Laser Intensities

This section provides indications of the richly nonlinear SRS behavior that has been seen but not fully explored, that is, indications for possible new directions. The previous chapters focussed on plasmas and laser intensities relevant to NIF. Simulations have also been performed for higher electron temperatures (5–20 keV) and higher laser intensities ($10^{16} – 10^{17}$ W/cm²). These are more relevant to high-energy-density physics that is found, for example, in high-temperature hohlraums, fast ignition, and shock ignition. The array of SRS physics becomes even more complicated in these regimes. In addition to backscattering, there can be significant forward scattering, rescattering (where the backscattered light itself undergoes scattering), and strong electron acceleration due to trapping by these higher phase velocity waves. Results are also presented on SRS in density gradients which, while relevant to NIF, have not been extensively analyzed.

6.2.1 Density Gradients

Inhomogenous plasmas are relevant to NIF. Two cases will be shown here. Case I-grad is similar to Case I from Chapter 3 with the exception that n/n_{cr} ranges from 0.10 to 0.11 over the 100 μm length, while Case 3-30-grad is similar to Case 3-30 with the exception that n/n_{cr} ranges from 0.128 to 0.138. In each case, the density scale length $n/(dn/dx) \approx 1000$ μm. As a result of traveling up a gradient, the laser excites plasma waves with decreasing $k\lambda_D$. For backward SRS in Case 3-30-grad, $k\lambda_D \approx 0.30 – 0.28$, while for Case I-grad, $k\lambda_D \approx 0.26 – 0.24$.

The evolution of the plasma waves can be seen in Figure 6.1, along with the temporal evolution of the wavenumbers and ω versus k . In contrast with

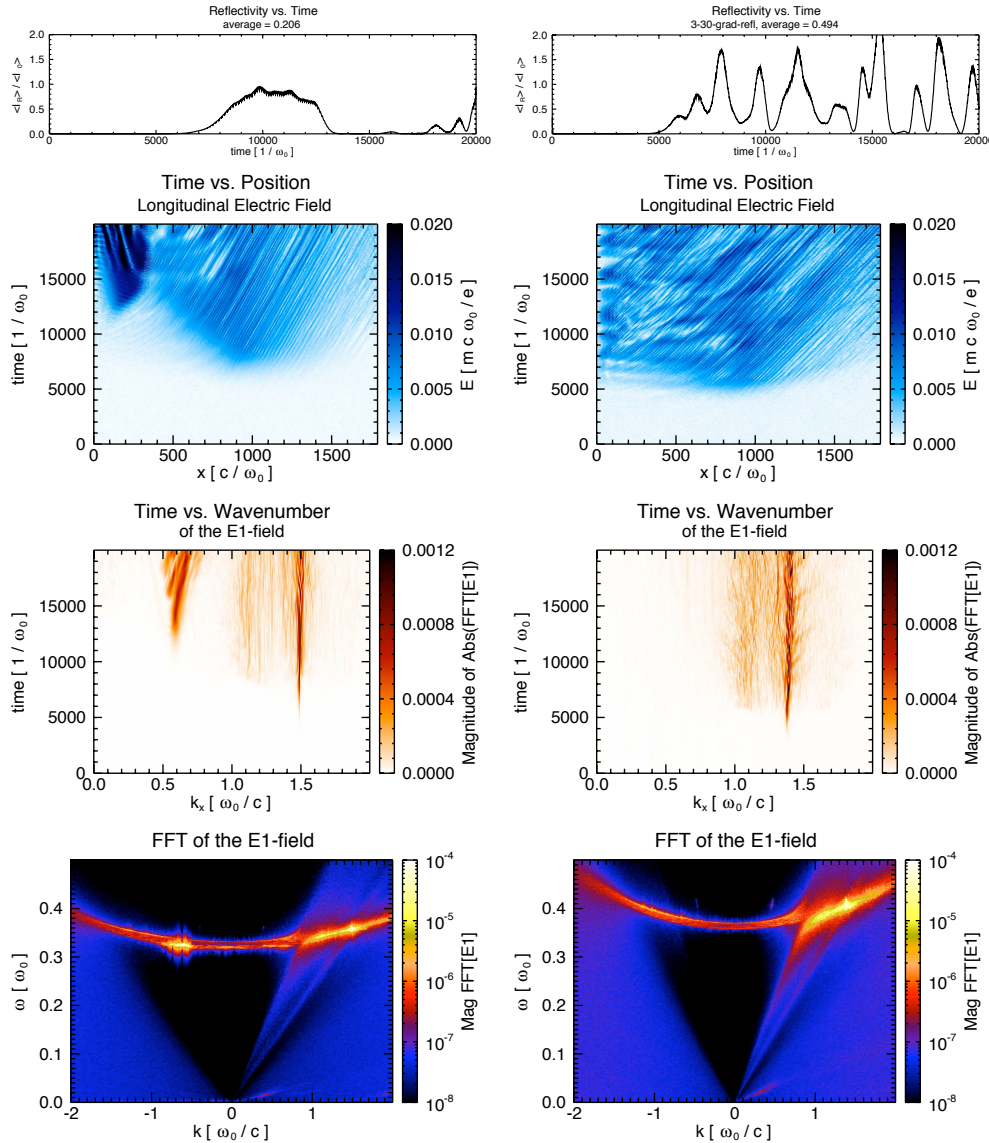


Figure 6.1: Temporal evolution of reflectivity (top), longitudinal E1-fields (2nd from top), and wavenumbers (3rd from top), and frequency versus wavenumber of the E1-fields (bottom) for Cases I-grad (left) and 3-30-grad (right).

the homogenous densities where the SRS grew across the entire box to the left side of the box (toward the laser's entrance side), here the SRS starts near the middle of the simulated region. With decreasing $k\lambda_D$ as the laser travels up the gradient, SRS is more unstable on the far side of the box, as well as having a lower threshold.

Notably, SRS still grows at a growth rate close to the undamped absolute growth rate. Case 3-30-grad grows at $\gamma_0/\omega_0 \approx 0.0013$ in comparison with $\gamma_{abs}/\omega_0 = 0.0016$, and Case I-grad grows at $\gamma_0/\omega_0 \approx 0.0008$ in comparison with $\gamma_{abs}/\omega_0 = 0.0007$, where the growth rates have been measured in the center of the simulation ($x\omega_0/c = 895$) and the theoretical growth rates have been calculated with the density at that point.

As plasma waves travel up or down the gradient, their frequencies remain constant but their wavenumbers can shift. The resonant SRS wavenumbers at the low/high end of the gradients are $kc/\omega_0 = 1.51/1.49$ for Case I-grad and $1.40/1.37$ for Case 3-30-grad. Furthermore, the wavenumbers should decrease as the plasma waves travel up the gradient. This behavior is not evident for the original SRS waves in each case. If there is a slight modification of the wavenumbers in time, it is a slight trend toward larger wavenumbers. In combination with the frequency versus wavenumber plots, it can be seen that the SRS plasma waves still shift negatively in frequency, and this shift, along with continued resonance with the backscattered light, is a larger contributor to wavenumber shifts than the density gradient.

The reflectivities in uniform plasmas and density gradients due to backward SRS are qualitatively similar for Case 3-30-grad but different for Case I-grad. The existence and convection of plasma packets is very different with the gradient, and for Case I-grad the packet behavior is absent in favor of continuous SRS.

The instability grows backwards in space, presumably due to backward-travelling scattered light that seeds further scattered light along the gradient, and the reflectivity is a continuous burst until it is clamped by rescatter (backscattering of the backscattered light).

This rescatter grows late in time for Case I-grad. It grows much more strongly than the original SRS since it is driven by the longer wavelength backscattered light. The wavenumber shifts are much more evident for the plasma wave due to rescatter. Since these plasma waves travel down the gradient, their wavenumber shifts to larger wavenumbers. The rescatter causes a dramatic decrease in the instantaneous reflectivity levels.

The behavior of SRS in gradients opens up new avenues of exploration. The frequencies and wavenumbers that were shown to affect homogenous simulations will be now also be affected by gradients with their varying plasma frequency. The convection of packets in gradients will also presumably be affected, and the frequency up-shifted light that is scattered from packets may result in different behaviors as it encounters background plasma of varying plasma frequency in a gradient. Finally, the onset and growth of SRS, shown here to be absolute-like, is an interesting topic for future study.

6.2.2 Forward SRS and Rescatter

Rescatter has also been seen in several homogenous density simulations. Here we will present one case that is a reproduction of a simulation from Hinkel *et al.* [53] for a hohlraum with a radiation temperature of 300 eV. The ions are fixed, $T_e = 5$ keV, $n/n_{cr} = 0.09$, $L\omega_0/c = 200$ μm , and $I_0 = 1 \times 10^{16}$ W/cm² with 3ω light.

This run shows several different scatterings, namely backward SRS, forward

SRS, and backward SRS of the forward SRS scattered light. Figure 6.2 shows the full spectrum of modes. The relevant wavenumbers of the drive, scattered, and plasma waves are (1) backward SRS with $(k_{\text{driver}}, k_{\text{plasma}}, k_{\text{scatter}}) = (0.95, 1.50, 0.55)$, (2) forward SRS with $(0.95, 0.30, 0.65/1.30)$, and (3) backward SRS (rescatter) of forward SRS scattered light with $(0.65, 0.85, 0.20)$. The plots show more than the three modes listed. These other modes are separated from the listed plasma waves by multiples of the plasma frequency. Several of them are harmonics. Others, such as the modes at $(\omega, k) \approx (0.6, 1.2)$ and $(0.02, 0.5)$, appear to match the beat between other plasma modes, in this case the beat between the plasma modes for (2) and (3). It is possible that there are higher-order processes occurring, such as four-wave coupling.

With the presence of so many modes, it is possible to get nonlinear interactions between them that affect the electron distribution. For example, Figure 6.3 shows the plasma wave evolution in space and the electron phasespace at $\omega_0 t = 18800$ over a zoomed-in region of space, along with the transmittivity (where forward scattered light has been included). Forward SRS is the predominant signal in the space-time plot, with all of the other scattering mechanisms smaller by roughly an order of magnitude.

Late in time, plasma waves in the region of $x\omega_0/c = 1500 - 2000$ become very localized, slow-moving wave packets. The phasespace plot also shows that these localized structures (here at $x\omega_0/c \approx 1700, 1800, 1900$, and 2000) are only a couple wavelengths long. These structures accelerate electrons to very high energies, as can be seen in the accompanying plot of the distribution function where electrons have been accelerated up to approximately 3 MeV ($p_e/m_e c \approx 6$). The flattening that occurs at $p_e/m_e c \approx 0.4$ is due to backscatter of the forward SRS.

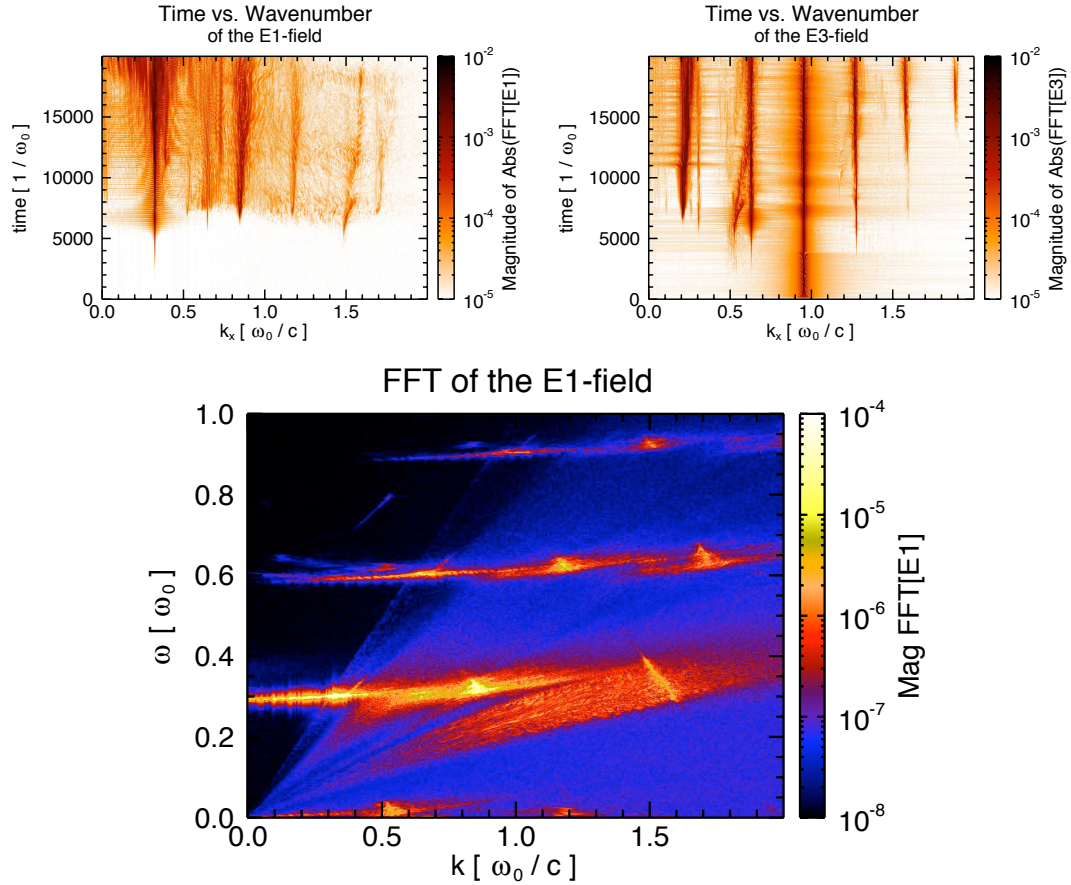


Figure 6.2: Wavenumber evolution of plasma waves (left) and light waves (right), and frequency versus wavenumber for the plasma waves (bottom), for $T_e = 5.0$ keV, $n/n_{cr} = 0.09$, and $I_0 = 1 \times 10^{16}$ W/cm² for 3 ω light.

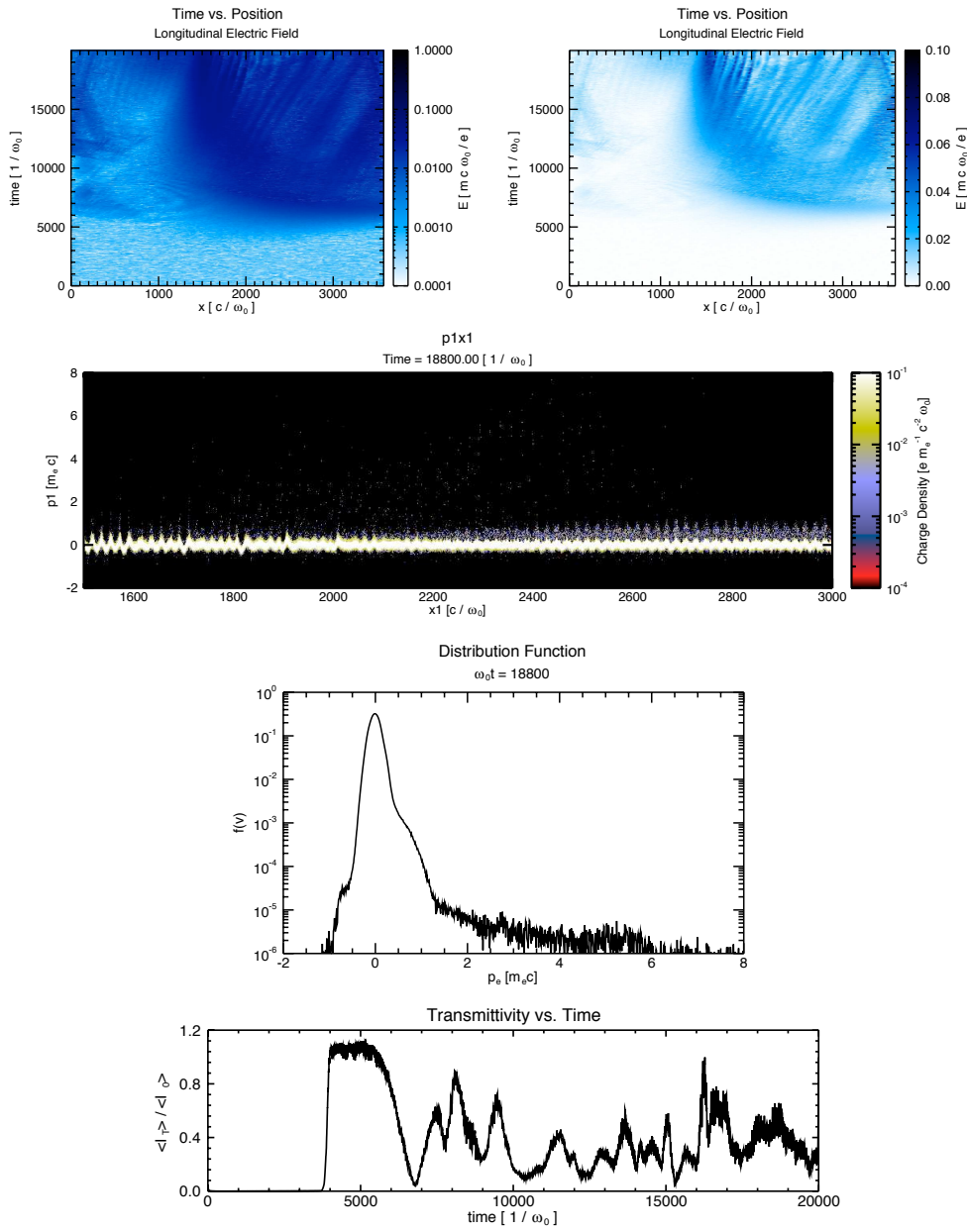


Figure 6.3: Space versus time of the E1-field with log (top-left) and non-log (top-right) scales; electron phasespace (2nd down) and spatially averaged distribution function (3rd down) at $\omega_0 t = 18800$; and transmittivity versus time (bottom). $T_e = 5.0$ keV, $n/n_{cr} = 0.09$, and $I_0 = 1 \times 10^{16}$ W/cm² for 3ω light.

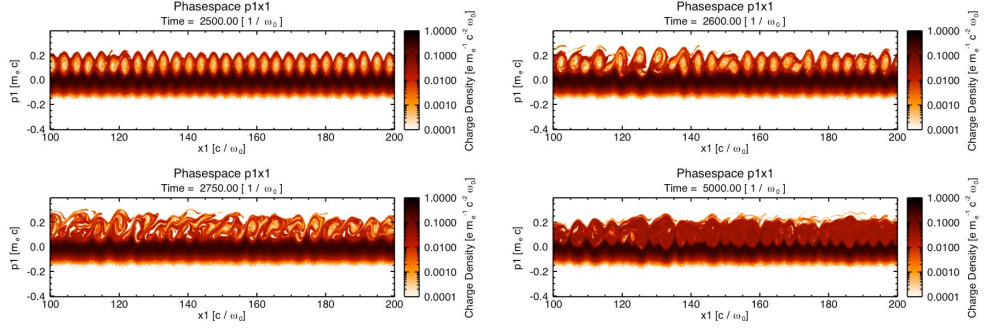


Figure 6.4: Electron phasespace for Case IV with $v_{osc}/c = 0.045$.

The transmitted light shows that a significant amount of energy is not making it through the plasma. SRS backscatter is negligible, but backscatter of the forward scatter will effectively reflect the laser (the resulting light travels in the opposite direction to the incident laser). As shown in the phasespace and distribution function, where the electrons get accelerated to very high energies, lots of energy may be getting absorbed by the plasma too.

Rescatter and the interaction between multiple different plasma modes may play a vital role in the region of the laser entrance hole on NIF, where multiple incoming and outgoing, scattered, light waves can interact. There are many interesting aspects of this simulation such as mode competition, wave interactions, and hot electron production that could be explored.

6.2.3 Stationary Structures

It is also possible to get fairly stable and slow moving phasespace vortices with purely backward SRS. These have been seen in the simulations that are most like the Montgomery experiments and the simulations of Yin *et al.*. They are exactly similar to the parameters of Case IV of Chapter 3, with the exception that the laser intensity is $1 \times 10^{16} \text{ W/cm}^2$ for a 2ω laser, with $v_{osc}/c = 0.045$.

The electron phasespace that arises after strong SRS in this simulation is shown in Figure 6.4. The dramatic flattening of the distribution that results from these strongly driven SRS plasma waves is sufficient to create modes that move at a speed intermediate between the phase velocity of the plasma wave and the thermal speed of the electrons. Their frequencies can range all the way down to $\omega/\omega_0 \approx 0.11$, that is, approximately half the linear SRS frequency and significantly below $\omega_p/\omega_0 = 0.19$.

This simulation represents a boundary case between the simulations of this dissertation and the simulations of the previous section, that is, high-intensity lasers and hot plasmas that may be of interest to high-energy-density physics. Such simulations could be used to extend the conclusions of this dissertation into different regimes.

6.2.4 Exciting Nonresonant Modes

Finally, it is possible to scatter off modes that are not on the normal dispersion curve. This is seen for a more strongly driven Case 3-30. Figure 6.5 shows frequencies and wavenumbers of the driven plasma waves for Case 3-30 with incident laser intensities of 1×10^{16} and $1 \times 10^{17} \text{ W/cm}^2$ for a 3ω laser.

The hyperbolic curve matches the locus of points that frequency match with the beat between the laser and all other points on the light-wave dispersion relation. As described previously in Chapter 3, with $\omega_2 = \omega_0 - \omega_1$, $k_2 = k_0 - k_1$, and $\omega_{0,1}^2 = \omega_p^2 + c^2 k_{0,1}^2$, we have,

$$\omega_2 = \omega_0 - \sqrt{\omega_p^2 + (k_0 - k_2)^2}. \quad (6.1)$$

The maximum frequency occurs when the incident laser and plasma wavenumbers are equal, that is, when $k_0 = k_2$ and where $\omega_2 = \omega_0 - \omega_p$, matching appropriately

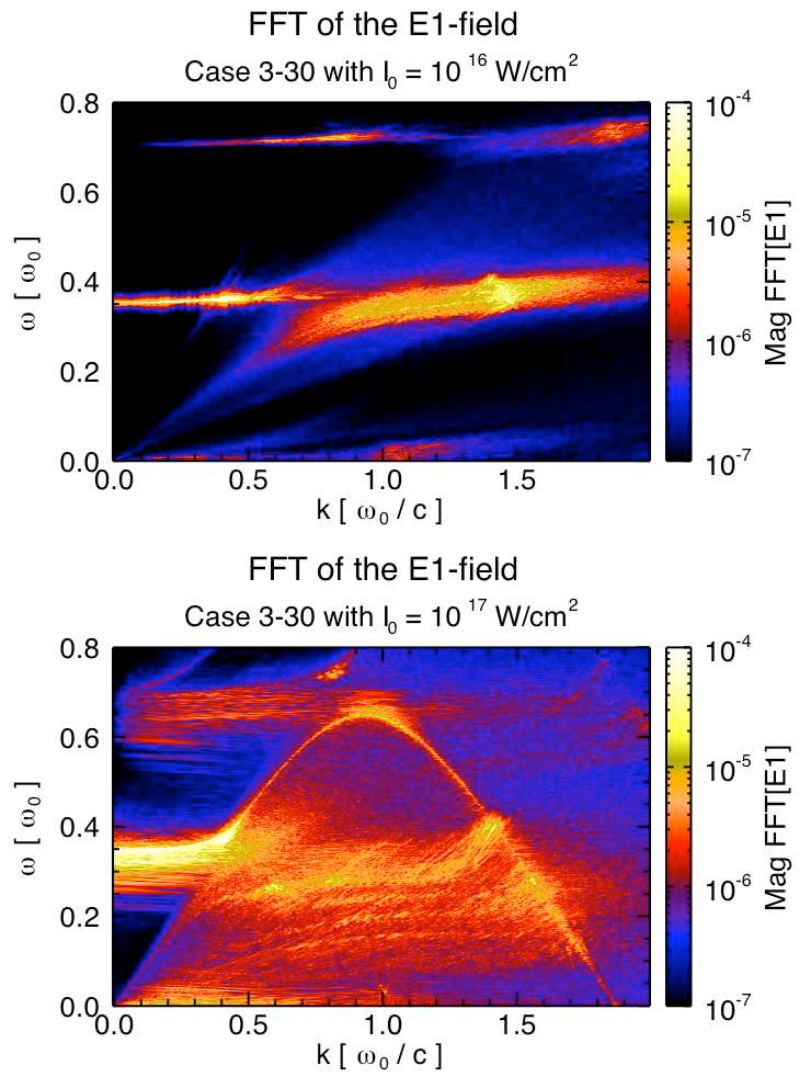


Figure 6.5: Frequency versus wavenumber for $T_e = 3.0 \text{ keV}$, $n/n_{cr} = 0.129$, and $I_0 = 1 \times 10^{16}$ (top) and 10^{17} (bottom) W/cm^2 for 3ω light.

with the figure and the maximum at $(\omega, k) \approx (0.65, 0.95)$. The normal points for backward and forward SRS correspond to the points on this curve where it intersects with the plasma dispersion curve.

The spectral features that have been referred to previously are represented dramatically in this figure. The wavenumber shifts of the backward SRS plasma waves are quite large and can be seen as the streaks to lower wavenumber (and frequency) at $(\omega, k) \approx (0.2 - 0.4, 1.5)$. Four distinct beam modes can be seen as the swath of points at $\omega = 0.27, 0.24, 0.20, 0.16$ and covering a wide range of wavenumbers from 0.5 to 1.5. The renewed scattering as a result of the intersection of these beam modes with possible scattered light waves can be seen in the bright point at $(\omega, k) = (0.27, 1.56)$, corresponding to the point of intersection between the strongest beam mode and the locus of points described by Eqn. 6.1.

These simulations again show that there is a range of highly nonlinear plasma physics that remains to be explored in strongly-driven high-energy-density science, including nonresonant plasma waves driven off the normal dispersion curve and the resulting beam modes that result from driving such nonlinear plasma waves.

6.3 Seeding SRS

As a final note of future work that could be done, we should mention that seeded runs of SRS would be very beneficial. It has been shown in this dissertation that SRS can transition from the strongly-damped, convective regime into the absolute regime when particles are trapped, bounce, and reduce the damping rate of the plasma wave.

Seeded runs would allow one to investigate the convective growth of a con-

trolled noise source for SRS. By varying the seed's amplitude, frequency, and duration, a better picture of the convective regime might emerge. In addition, one could probe those seed parameters that appear to result in a transition from the convective regime to the absolute regime. If one could determine how one seed alters the plasma left behind it, then one could also send in a subsequent seed to study the interaction of seeds with non-Maxwellian distributions or localized regions of SRS plasma wave growth.

6.4 Concluding Remarks

SRS in regimes of relevance to NIF continues to present a theoretical challenge. This highly nonlinear, kinetic instability continues to present challenges for future work. The simulations here only begin to touch on extensions to mobile ions and multi-dimensional effects, and much work remains to be done to obtain a predictive model of SRS reflectivity that might be used to inform future experiments with relation to NIF. Nevertheless, the range of simulations presented here gives a more comprehensive picture of SRS than has previously been presented in the simulation literature pertaining to SRS. It is our hope that it will lead the way to more comprehensive models as well.

APPENDIX A

The Fluid Frequency Shift of an Electron Plasma Wave

In this Appendix, we investigate the frequency shift due to fluid nonlinearities in the absence of kinetic effects. Reprinted with permission from B. J. Winjum, J. Fahlen, and W. B. Mori. Phys. Plasmas **14**, 102104 (2007). Copyright 2007, American Institute of Physics.

We use the Eulerian fluid description and let the wave number shift as well – in a driven wave, the phase velocity of the wave can remain fixed as the frequency shifts, so there will be shifts in the wave number as well. In the limit of no shift in the wavenumber, our results agree with those of Dewar and Lindl [76] and Coffey [78]. We then estimate the total shift as the sum of the fluid and kinetic shifts. A rigorous derivation of the total shift is an area for future work. Here we show that for parameters of relevance to Raman Backscatter in ICF, the shift due to harmonics can be important even when it is smaller than the kinetic shift.

A.1 Derivation of the Fluid Frequency Shift

In order to calculate the frequency shifts due to fluid nonlinearities, we use Euler's equation with an adiabatic equation of state, i.e., the pressure is given by $p = (kT_0/m)(n^3/n_0^2)$ where m is the electron mass, k is Boltzmann's constant, n

is the plasma density, n_0 is the background ion density, and T_0 is the electron temperature. It is well known that these equations follow from the use of a waterbag distribution function, where the edge of the unperturbed distribution function $v_0 = \sqrt{3kT_0/m}$ is chosen such that $\int dv v^2 f$ is the same as for a Maxwellian.

Our starting equations are Euler's equation, Ampere's Law, and Gauss' Law:

$$(\partial_t + V\partial_x)V = -\frac{e}{m}E - \frac{v_0^2}{2n_0^2}\partial_x n^2, \quad (\text{A.1})$$

$$\partial_t E - 4\pi e n V = 0, \quad (\text{A.2})$$

$$\partial_x E + 4\pi e(n - n_0) = 0. \quad (\text{A.3})$$

where V is the fluid velocity. Following the perturbation theory of Bogoliubov and Mitropolsky [96], we express E , n , and V as expansions in the smallness parameter ϵ (which is set equal to 1 later),

$$n = n_0 + \epsilon n_1 + \epsilon^2 n_2 + \epsilon^3 n_3, \quad (\text{A.4})$$

$$E = \epsilon E_1 + \epsilon^2 E_2 + \epsilon^3 E_3, \quad (\text{A.5})$$

$$V = \epsilon v_1 + \epsilon^2 v_2 + \epsilon^3 v_3. \quad (\text{A.6})$$

We equate similarly ordered terms and use the resulting wave equations to deduce the form of the variables at each order. Furthermore, we assume all waves go as $\cos(\int dx k - \int dt \omega)$ or $\sin(\int dx k - \int dt \omega)$ and normalize time and space as $\bar{t} = -\int^t dt' \omega(t')$ and $\bar{x} = \int^x dx' k(x')$;

$$\partial_t = -\omega \partial_{\bar{t}} = -(\omega_0 + \epsilon \omega_1 + \epsilon^2 \omega_2) \partial_{\bar{t}}, \quad (\text{A.7})$$

$$\partial_x = k \partial_{\bar{x}} = (k_0 + \epsilon k_1 + \epsilon^2 k_2) \partial_{\bar{x}}. \quad (\text{A.8})$$

At first order we have the following equations:

$$-\omega_0 \partial_{\bar{t}} v_1 = -\frac{e}{m} E_1 - \frac{v_0^2}{n_0} k_0 \partial_{\bar{x}}(n_1), \quad (\text{A.9})$$

$$-\omega_0 \partial_{\bar{t}} E_1 - 4\pi e n_0 v_1 = 0, \quad (\text{A.10})$$

$$k_0 \partial_{\bar{x}} E_1 + 4\pi e n_1 = 0. \quad (\text{A.11})$$

These equations may be combined to form

$$(\omega_0^2 \partial_{\bar{t}}^2 - v_0^2 k_0^2 \partial_{\bar{x}}^2 + \omega_p^2) E_1 = 0, \quad (\text{A.12})$$

from which we say (normalizing E)

$$\frac{eE_1}{m\omega_0 v_\phi} = \frac{v_{osc}}{v_\phi} \cos(\bar{x} - \bar{t}) \quad (\text{A.13})$$

where we introduce v_{osc} as a first-order amplitude. This gives the expected

$$\omega_0^2 = \omega_p^2 + v_0^2 k_0^2. \quad (\text{A.14})$$

We obtain equations for v_1 and n_1 similarly, and after normalizing v_0 as $\alpha = v_0^2/v_\phi^2$, we obtain,

$$\frac{v_1}{v_\phi} = \frac{v_{osc}}{v_\phi(1-\alpha)} \sin(\bar{x} - \bar{t}), \quad (\text{A.15})$$

$$\frac{n_1}{n_0} = \frac{v_{osc}}{v_\phi(1-\alpha)} \sin(\bar{x} - \bar{t}). \quad (\text{A.16})$$

At second order, the resulting wave equations have driving terms. For E_2 , we have

$$\begin{aligned} (\omega_0^2 \partial_{\bar{t}}^2 - v_0^2 k_0^2 \partial_{\bar{x}}^2 + \omega_p^2) \frac{eE_2}{m\omega_0 v_\phi} &- 2\omega_0^2 \frac{v_{osc}}{v_\phi} \left(\frac{\omega_1}{\omega_0} - \alpha \frac{k_1}{k_0} \right) \cos(\bar{x} - \bar{t}) \\ &= \omega_0^2 \frac{v_{osc}^2}{v_\phi^2} \left(\frac{3+\alpha}{1-\alpha} \right) \sin[2(\bar{x} - \bar{t})]. \end{aligned} \quad (\text{A.17})$$

There is no secular growth because there are no driving terms on the right-hand side for the $\cos(\bar{x} - \bar{t})$ term. Similar cos terms also arise in the equations for v_2 and n_2 , from which we conclude that $k_1 = \omega_1 = 0$. Thus, there is no first order frequency or wavenumber shift.

At second order we obtain

$$\frac{eE_2}{m\omega_0 v_\phi} = \frac{v_{osc}^2}{v_\phi^2} \frac{3+\alpha}{6(1-\alpha)^2} \sin[2(\bar{x} - \bar{t})], \quad (\text{A.18})$$

$$\frac{v_2}{v_\phi} = -\frac{v_{osc}^2}{v_\phi^2} \frac{1}{6(1-\alpha)^2} \left(3 + \frac{3+5\alpha}{1-\alpha} \cos[2(\bar{x} - \bar{t})] \right), \quad (\text{A.19})$$

$$\frac{n_2}{n_0} = -\frac{v_{osc}^2}{v_\phi^2} \frac{3+\alpha}{3(1-\alpha)^3} \cos[2(\bar{x} - \bar{t})]. \quad (\text{A.20})$$

Our ordering can now be inferred as

$$\epsilon = \frac{v_{osc}}{v_\phi} \propto \left| \frac{v_1}{v_\phi} \right|, \left| \frac{n_1}{n_0} \right| \quad (\text{A.21})$$

This reveals the intuitive idea that our ordering is related to the density perturbation associated with the plasma wave ($\epsilon \sim O(n_1/n_0)$). In addition, factors of $1/(1 - \alpha)$ are also present, in line with the fluid approximation. As the phase velocity of the plasma wave becomes comparable to the electron thermal velocity, i.e., as α approaches 1, there are large numbers of trapped particles and fluid theory breaks down. Viewed another way, for a wave with v_ϕ near its linear value, $\alpha = (3k^2\lambda_D^2)/(1 + 3k^2\lambda_D^2)$, so in order for α to approach unity $k\lambda_D$ must be large.

We can also now determine the amplitudes of the harmonics,

$$\left| \frac{n_2}{n_1} \right| = \frac{1}{3} \frac{v_{osc}}{v_\phi} \frac{3 + \alpha}{(1 - \alpha)^2}, \quad (\text{A.22})$$

$$\left| \frac{E_2}{E_1} \right| = \frac{1}{6} \frac{v_{osc}}{v_\phi} \frac{3 + \alpha}{(1 - \alpha)^2}. \quad (\text{A.23})$$

For the amplitudes of relevance in this paper, the harmonic ratios are significantly larger than those found in Rose and Russell [81].

At third order, we get the following equation for E_3

$$\begin{aligned} (\omega_0^2 \partial_t^2 - v_0^2 k_0^2 \partial_{\bar{x}}^2 + \omega_p^2) \frac{eE_3}{m\omega_0 v_\phi} &- 2\omega_0^2 \frac{v_{osc}}{v_\phi} \left(\frac{\omega_2}{\omega_0} - \alpha \frac{k_2}{k_0} \right) \cos(\bar{x} - \bar{t}) = \\ &- \frac{\omega_0^2}{6} \frac{v_{osc}^3}{v_\phi^3} \frac{(15\alpha + \alpha^2)}{(1 - \alpha)^3} \cos(\bar{x} - \bar{t}) \\ &+ \frac{\omega_0^2}{2} \frac{v_{osc}^3}{v_\phi^3} \left(\frac{(6 + 9\alpha + \alpha^2)}{(1 - \alpha)^3} \right) \cos[3(\bar{x} - \bar{t})]. \end{aligned} \quad (\text{A.24})$$

Eliminating secularity here does give a frequency and wavenumber shift, given by

$$\frac{\omega_2}{\omega_0} - \alpha \frac{k_2}{k_0} = \frac{1}{12} \frac{v_{osc}^2}{v_\phi^2} \frac{(15\alpha + \alpha^2)}{(1 - \alpha)^3}. \quad (\text{A.25})$$

If the plasma is cold ($\alpha = 0$), then there is no frequency shift, as expected [97]. However, the pressure term is not the only nonlinearity that contributes to the frequency shift. The current term from Ampere's Law (nV) and the convective term in Euler's Equation ($V\partial_x V$) also contribute. These nonlinear terms may both be tracked through the derivation by adding subscripts, which we label c (convective) and j (current). The contributing factors are

$$\frac{v_{osc}^2}{12v_\phi^2(1-\alpha)^3} \left(\frac{1}{2}\right) (-4_c - 1_j + 5_{cj} + (10_c + 17_j + 3_{cj})\alpha), \quad (\text{A.26})$$

and it may be seen that both of these nonlinearities contribute to the final form of the shift. The only contribution which comes purely from the pressure term is

$$\frac{v_{osc}^2}{12v_\phi^2(1-\alpha)^3} (\alpha^2). \quad (\text{A.27})$$

Note that the current and convective contributions in equation (A.26) that are not proportional to α cancel. Therefore, there is no frequency shift for $\alpha \rightarrow 0$. In addition, there are terms proportional to α from the current and convective terms, so each type of nonlinearity contributes to the frequency shift.

A.2 Comparison of the Fluid and Kinetic Frequency Shifts

We now consider two cases: (I) $k_2 = 0$ and (II) $\omega_0/k_0 = v_\phi$, where v_ϕ , the wave phase velocity, is held constant. Case I is an analysis of the initial value problem in which k is fixed. Taking $\omega = \omega_0 + \omega_2$ and setting $W^2 = v_{osc}^2/(v_\phi^2(1-\alpha)^2)$ yields a nonlinear modification to the dispersion relation. To second order in v_{osc} ,

$$\omega^2 = \omega_p^2 + v_0^2 k^2 \left(1 + \frac{5}{2} W^2\right). \quad (\text{A.28})$$

This is in agreement with Dewar and Lindl [76] and Coffey [78].

Morales and O'Neil also studied the temporal problem, but they considered nonlinearities due only to trapped particle effects. Their frequency shift is given

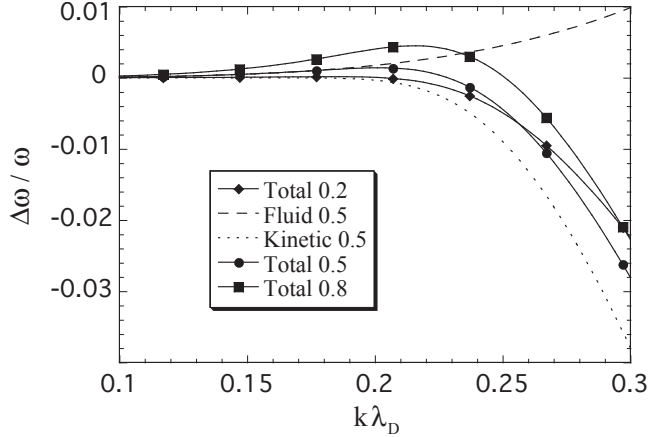


Figure A.1: Frequency shifts. Solid lines represent the sum of fluid plus kinetic shifts for three amplitudes, $eE/m\omega_p v_{the} = 0.2, 0.5, 0.8$. The dashed lines are the fluid or kinetic shift only for $eE/m\omega_p v_{the} = 0.5$.

by

$$\frac{\delta\omega}{\omega_0} = -1.63 \sqrt{\frac{eE}{mk}} \left(\frac{\omega_p}{k}\right)^2 \left(\frac{\partial^2 f_0}{\partial v^2}\right)_{v_\phi} \left(\frac{\partial \epsilon}{\partial \omega}\right)_{\omega_0}^{-1},$$

with the amplitude restricted to be $(eE/mk)^{1/2} \ll v_{th}^2/v_\phi$, or equivalently $v_{osc}/v_{th} \ll (v_{th}/v_\phi)^3$.

Figure A.1 shows a comparison between kinetic and fluid shifts as a function of $k\lambda_D$, as well as the sum of the fluid and kinetic shifts for several amplitudes. The most obvious difference is that the shifts are opposite in sign. The fluid shift (positive) initially dominates, but as $k\lambda_D$ increases, the kinetic shift (negative) dominates.

Figure A.2 shows the total shift (fluid plus kinetic) as a function of wave amplitude for various values of $k\lambda_D$. Here, the amplitude is normalized to Coffey's wavebreaking limit, which is the wave amplitude where particles at the edge of the waterbag become trapped. For such a wave amplitude, both the fluid theory and the weakly nonlinear theory of Morales and O'Neil break down. For small

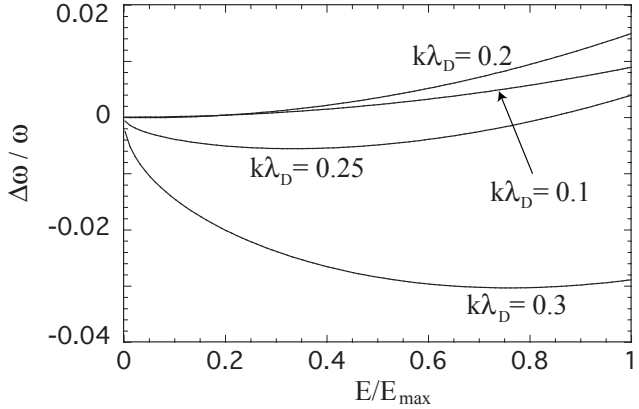


Figure A.2: Fluid plus kinetic frequency shift as a function of amplitude relative to the Coffey wavebreaking limit, E_{max} .

$k\lambda_D$, the frequency shift is exclusively positive — the fluid effects dominate. As $k\lambda_D$ is increased, the frequency shift first increases in amplitude, but then it begins to show the effects of a predominantly kinetic shift. Even for large values of $k\lambda_D$ where the negative kinetic frequency shift dominates, the fluid shift is not negligible.

We next consider Case II. We constrain the plasma wave to have a fixed phase velocity,

$$v_\phi = \frac{\omega_0 + \omega_2}{k_0 + k_2}, \quad (\text{A.29})$$

which is the most relevant case for a driven wave, as in Raman backscatter. If $\omega_2, k_2 \ll \omega_0, k_0$, respectively, then the phase velocity $v_\phi \simeq \omega_0/k_0$ and

$$\frac{\omega_2}{\omega_0} \simeq \frac{k_2}{k_0} \simeq \frac{1}{12} \frac{v_{osc}^2}{v_\phi^2} \frac{(15\alpha + \alpha^2)}{(1 - \alpha)^4}. \quad (\text{A.30})$$

Therefore, the only change from the frequency shift of Case I is an increase in magnitude by $1/(1 - \alpha)$, which can be relatively large for $k\lambda_D > \approx 0.3$. The normalized shift for the wavenumber is equal in magnitude and has the same

sign to that for the frequency. Because no kinetic theory exists for the constant phase velocity case, we have only plotted the frequency shift for the initial value problem. As a result, these plots represent a lower bound for the fluid contribution to the frequency shift in a driven wave case relevant to Raman scattering. A kinetic theory for the constant phase velocity case is an area for future work.

A.3 Summary

In summary, we have calculated the nonlinear frequency shift of a plasma wave (for arbitrary wavenumber) using the fluid model. The shift is due to harmonics and is proportional to the wave amplitude squared. At zero temperature, we find no frequency shift, and for finite temperature in the limit where the wavenumber does not shift, we find agreement with previous work [76, 78]. For fixed wavenumber (the initial value problem), a comparison between the fluid frequency shift and the kinetic shift due to trapped particles illustrates that both must be taken into account. The shifts are of opposite sign and have different dependences on the wave amplitude. For small wave amplitudes, the positive fluid shift dominates, while for higher amplitudes the negative kinetic shift dominates. Likewise, as $k\lambda_D$ increases, the frequency shift changes from predominantly fluid to predominantly kinetic. It should also be pointed out that even for higher amplitudes or $k\lambda_D$, the fluid shift still makes a positive contribution to the total shift. Therefore, theories which use a nonlinear frequency shift to explain the behavior of Raman Scattering in laser driven ICF should include both the fluid and kinetic shifts, for if the frequency and wavenumber both change such that the phase velocity of the wave remains relatively constant, as for a driven wave, then the fluid frequency shift can be larger. A theory for nonlinear frequency shifts which combines harmonics and trapped particles remains an item for future work.

APPENDIX B

Number of Particles Per Cell

For the parameters of this dissertation, SRS is predominantly in the strongly damped regime, with the damping rate exceeding the growth rate. PIC simulations of such weakly driven SRS require that the background noise level (which depends on the number of particles per cell) is low enough that convectively amplified waves are not washed out by the fluctuations. It is also important to have a sufficient number of particles for wave-particle interactions to be accurately simulated.

In order to verify that we used an appropriate number of particles per cell, we did several simulations with varying numbers of particles per cell to test for convergence. First, the reflectivity levels as a function of driving laser intensity were tested. Figure B.1 shows the reflectivity for plasma parameters $T_e = 3$ keV, $n/n_{cr} = 0.128$, and $L = 100 \mu\text{m}$ (the same as Case 3-30 of Chapter 3). The reflectivity curves as a function of intensity all increase with increasing intensity, but the reflectivity for a given intensity increases with the number of particles per cell until 512 particles per cell. The simulations with 512 and 1024 particles per cell show good agreement, with overlapping curves and similarly low levels of reflectivity at $4 \times 10^{16} \text{ W/cm}^2$. 512 particles per cell was chosen as the appropriate number of particles per cell to use in our 1D simulations. We emphasize that we also use higher order particle shapes and current smoothing.

We also show here two simulations with a very large number of particles per

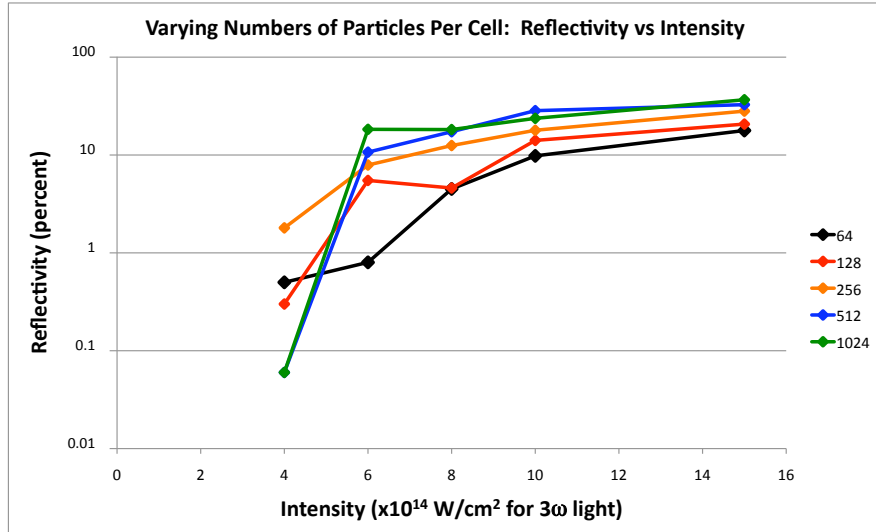


Figure B.1: Reflectivity for simulations with varying numbers of particles per cell. $T_e = 3 \text{ keV}$, $n/n_{cr} = 0.128$, $L = 100 \mu\text{m}$.

cell, 8192, in comparison with 512. The plasma parameters are $T_e = 3 \text{ keV}$, $n/n_{cr} = 0.128$, and $L = 100 \mu\text{m}$ (Case 3-30 of Chapter 3) for one simulation and $T_e = 1 \text{ keV}$, $n/n_{cr} = 0.059$, and $L = 100 \mu\text{m}$ (Case 1-30 of Chapter 3) for the other. Both have $k\lambda_D = 0.30$ for the backscattered SRS plasma wave.

Figures B.2 and B.3 show very similar behaviors between the simulations with different number of particles per cell. Each set of simulations shows similar growth of plasma packets that etch away as they convect (with similar etching rates), the periodic recurrence of plasma waves and reflectivity due to continued scattering from convecting packets (with similar periodicity rates that imply similar frequency shifts), and the increase in reflectivity as a function of time.

The time-averaged reflectivity is within several percent for the high temperature set, while the reflectivities differ by a factor of 2 for the lower temperature set. However, all of the simulations are dependent on SRS growth from random noise, and a key difference in reflectivities in the lower temperature set is due to

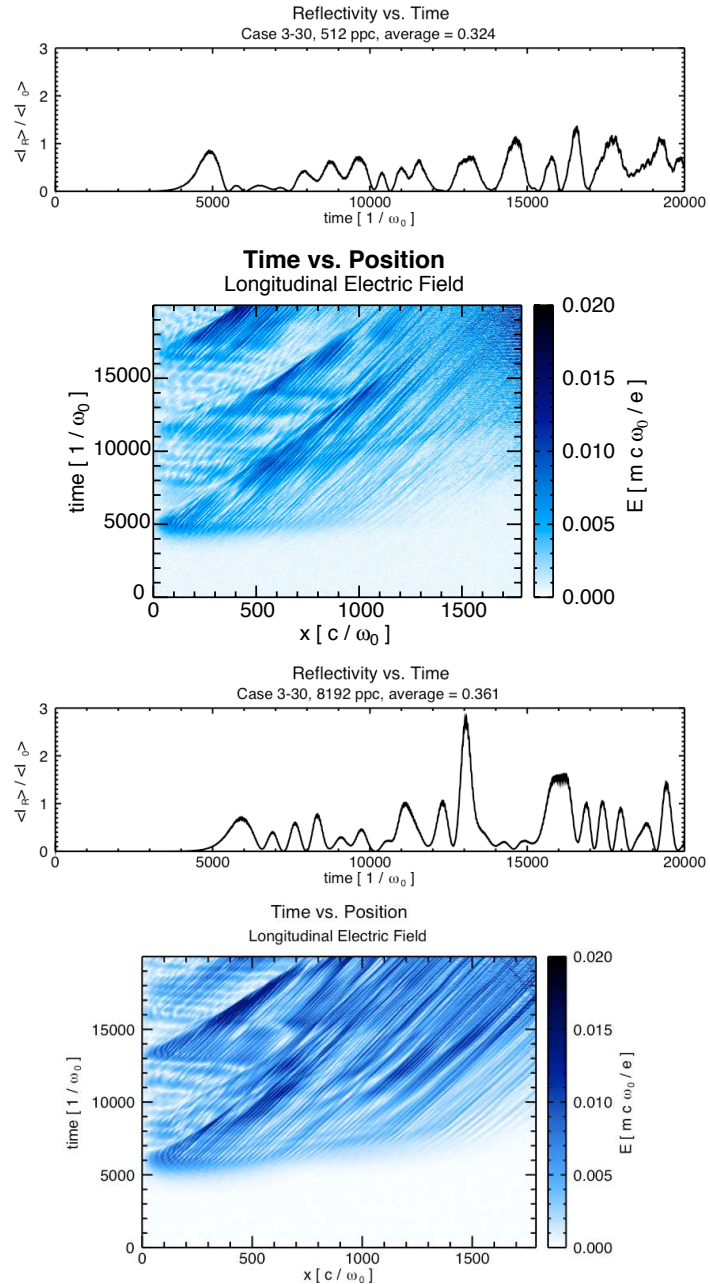


Figure B.2: Reflectivity and enveloped longitudinal E-field for simulations with 8192 (bottom) versus 512 (top) particles per cell. $T_e = 3$ keV, $n/n_{cr} = 0.128$, $L = 100 \mu\text{m}$.

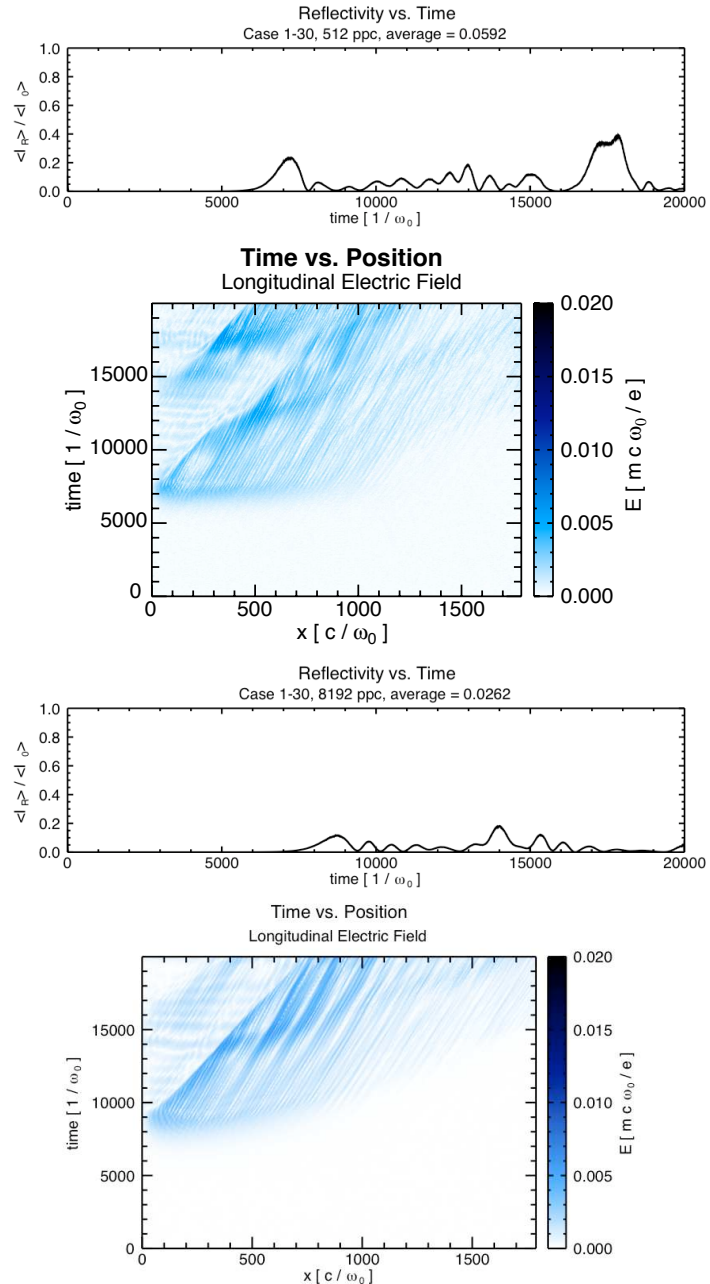


Figure B.3: Reflectivity and enveloped longitudinal E-field for simulations with 8192 (bottom) versus 512 (top) particles per cell. $T_e = 1$ keV, $n/n_{cr} = 0.059$, $L = 100 \mu\text{m}$.

the earlier growth of the initial SRS and subsequent growth of a second packet that can interact with light coming from the initial packet. Essentially, the simulations with 8192 particles per cell only reinforce the conclusions that were made with simulations with 512 particles per cell. We do not expect the behavior to be exactly identical, but we do believe that the basic processes remain the same.

REFERENCES

- [1] J. D. Lindl, P. Amendt, R. L. Berger, S. G. Glendinning, S. H. Glenzer, S. W. Haan, R. L. Kauffman, O. L. Landen, and L. J. Suter. *Phys. Plasmas*, 11:339, 2004.
- [2] John Nuckolls, Lowell Wood, Albert Thiessen, and George Zimmerman. *Nature*, 239:139, 1972.
- [3] J. S. Clarke, H. N. Fisher, and R. J. Mason. *Phys. Rev. Lett.*, 30:89, 1973.
- [4] G. S. Fraley, E. J. Linnebur, R. J. Mason, and R. L. Morse. *Phys. Fluids*, 17:474, 1974.
- [5] John Lindl. *Phys. Plasmas*, 2:3933, 1995.
- [6] D. W. Forslund, J. M. Kindel, and E. L. Lindman. *Phys. Fluids*, 18:1002, 1975.
- [7] D. W. Forslund, J. M. Kindel, and E. L. Lindman. *Phys. Fluids*, 18:1017, 1975.
- [8] J. F. Drake, P. K. Kaw, Y. C. Lee, G. Schmidt, C. S. Liu, and M. N. Rosenbluth. *Phys. Fluids*, 17:778, 1974.
- [9] J. L. Bobin, M. Decroisette, B. Meyer, and Y. Vitel. *Phys. Rev. Lett.*, 30:594, 1973.
- [10] R. G. Watt, R. D. Brooks, and Z. A. Pietrzyk. *Phys. Rev. Lett.*, 41:170, 1978.
- [11] C. Joshi, T. Tajima, J. M. Dawson, H. A. Baldis, and N. A. Ebrahim. *Phys. Rev. Lett.*, 47:1285, 1981.
- [12] D. W. Phillion, E. M. Campbell, K. G. Estabrook, G. E. Phillips, and F. Ze. *Phys. Rev. Lett.*, 49:1405, 1982.
- [13] D. W. Phillion, D. L. Banner, E. M. Campbell, R. E. Turner, and K. G. Estabrook. *Phys. Fluids*, 25:1434, 1982.
- [14] R. E. Turner, D. W. Phillion, E. M. Campbell, and K. G. Estabrook. *Phys. Fluids*, 26:579, 1983.
- [15] R. P. Drake, R. E. Turner, B. F. Lasinski, K. G. Estabrook, E. M. Campbell, C. L. Wang, D. W. Phillion, E. A. Williams, and W. L. Kruer. *Phys. Rev. Lett.*, 53:1739, 1984.

- [16] R. E. Turner, Kent Estabrook, R. L. Kauffman, D. R. Bach, R. P. Drake, D. W. Phillion, B. F. Lasinski, E. M. Campbell, W. L. Kruer, and E. A. Williams. *Phys. Rev. Lett.*, 54:189, 1985.
- [17] H. Figueroa, C. Joshi, H. Azechi, N. A. Ebrahim, and Kent Estabrook. *Phys. Fluids*, 27:1887, 1984.
- [18] R. E. Turner, Kent Estabrook, R. P. Drake, E. A. Williams, H. N. Kornblum, W. L. Kruer, and E. M. Campbell. *Phys. Rev. Lett.*, 57:1725, 1986.
- [19] R. P. Drake, E. A. Williams, P. E. Young, Kent Estabrook, W. L. Kruer, H. A. Baldis, and T. W. Johnston. *Phys. Rev. Lett.*, 60:1018, 1988.
- [20] H. A. Baldis, P. E. Young, R. P. Drake, W. L. Kruer, Kent Estabrook, E. A. Williams, and T. W. Johnston. *Phys. Rev. Lett.*, 62:2829, 1989.
- [21] Y. Kato, K. Mima, N. Miyanaga, S. Arinaga, Y. Kitagawa, M. Nakatsuka, and C. Yamanaka. *Phys. Rev. Lett.*, 53:1057, 1984.
- [22] S. N. Dixit, J. K. Lawson, K. R. Manes, H. T. Powell, and K. A. Nugent. *Opt. Lett.*, 19:417, 1994.
- [23] S. Skupsky, R. W. Short, T. Kessler, R. S. Craxton, S. Letzring, and J. M. Soures. *J. Appl. Phys.*, 66:3456, 1989.
- [24] S. Pau, S. N. Dixit, and D. Eimerl. *J. Opt. Soc. Am. B*, 11:1498, 1994.
- [25] T. R. Boehly, V. A. Smalyuk, D. D. Meyerhofer, J. P. Knauer, D. K. Bradley, R. S. Craxton, M. J. Guardalben, S. Skupsky, and T. J. Kessler. *J. Appl. Phys.*, 85:3444, 1999.
- [26] J. D. Moody, B. J. MacGowan, J. E. Rothenberg, R. L. Berger, L. Divol, S. H. Glenzer, R. K. Kirkwood, E. A. Williams, and P. E. Young. *Phys. Rev. Lett.*, 86:2810, 2001.
- [27] D. S. Montgomery, B. B. Afeyan, J. A. Cobble, J. C. Fernández, M. D. Wilke, S. H. Glenzer, R. K. Kirkwood, B. J. MacGowan, J. D. Moody, E. L. Lindman, D. H. Munro, B. H. Wilde, H. A. Rose, D. F. Dubois, B. Bezzerides, and H. X. Vu. *Phys. Plasmas*, 5:1973, 1998.
- [28] D. S. Montgomery, R. P. Johnson, J. A. Cobble, J. C. Fernandez, E. L. Lindman, H. A. Rose, and K. G. Estabrook. *Laser and Particle Beams*, 17(3):349, 1999.

- [29] H. A. Baldis, D. M. Villeneuve, B. La Fontaine, G. D. Enright, C. Labaune, S. Baton, Ph. Mounaix, D. Pesme, M. Casanova, and W. Rozmus. *Phys. Fluids B*, 5:3319, 1993.
- [30] J. A. Cobble, J. C. Fernandez, N. A. Kurnit, D. S. Montgomery, R. P. Johnson, N. Renard-Le Galloudec, and M. R. Lopez. *Phys. Plasmas*, 7:323, 2000.
- [31] R. K. Kirkwood, B. J. MacGowan, D. S. Montgomery, B. B. Afeyan, W. L. Kruer, J. D. Moody, K. G. Estabrook, C. A. Back, S. H. Glenzer, M. A. Blain, E. A. Williams, R. L. Berger, and B. F. Lasinski. *Phys. Rev. Lett.*, 77:2706, 1996.
- [32] J. C. Fernandez, J. A. Cobble, B. H. Failor, D. F. DuBois, D. S. Montgomery, H. A. Rose, H. X. Vu, B. H. Wilde, M. D. Wilke, and R. E. Chrien. *Phys. Rev. Lett.*, 77:2702, 1996.
- [33] J. C. Fernandez, B. S. Bauer, J. A. Cobble, D. F. DuBois, G. A. Kyrala, D. S. Montgomery, H. A. Rose, H. X. Vu, R. G. Watt, B. H. Wilde, M. D. Wilke, W. M. Wood, B. H. Failor, R. Kirkwood, and B. J. MacGowan. *Phys. Plasmas*, 4:1849, 1997.
- [34] D. F. DuBois and M. V. Goldman. *Phys. Rev. Lett.*, 14:544, 1965.
- [35] D. F. DuBois and M. V. Goldman. *Phys. Rev.*, 164:207, 1967.
- [36] J. D. Moody, E. A. Williams, L. Lours, J. J. Sanchez, R. L. Berger, G. A. Collins, C. B. Decker, L. Divol, S. H. Glenzer, B. A. Hammel, R. Jones, R. K. Kirkwood, W. L. Kruer, B. J. MacGowan, J. Pipes, L. J. Suter, R. Thoe, W. Unites, , and P. E. Young. *Phys. Plasmas*, 11:2060, 2004.
- [37] J. C. Fernandez, J. A. Cobble, D. S. Montgomery, M. D. Wilke, and B. B. Afeyan. *Phys. Plasmas*, 7:3743, 2000.
- [38] Harvey A. Rose and D. F. DuBois. *Phys. Rev. Lett.*, 72:2883, 1994.
- [39] D. S. Montgomery, R. J. Focia, H. A. Rose, D. A. Russell, J. A. Cobble, J. C. Fernandez, and R. P. Johnson. *Phys. Rev. Lett.*, 87:155001, 2001.
- [40] D. S. Montgomery, J. A. Cobble, J. C. Fernandez, R. J. Focia, R. P. Johnson, N. Renard-LeGalloudec, H. A. Rose, and D. A. Russell. *Phys. Plasmas*, 9:2311, 2002.
- [41] J. L. Kline, D. S. Montgomery, B. Bezzerides, J. A. Cobble, D. F. DuBois, R. P. Johnson, H. A. Rose, L. Yin, and H. X. Vu. *Phys. Rev. Lett.*, 94:175003, 2005.

- [42] J. L. Kline, D. S. Montgomery, L. Yin, D. F. DuBois, B. J. Albright, B. Bezzerides, J. A. Cobble, E. S. Dodd, J. C. Fernandez, R. P. Johnson, J. M. Kindel, H. A. Rose, H. X. Vu, and W. Daughton. *Phys. Plasmas*, 13:55906, 2006.
- [43] N. B. Meezan, L. Divol, M. M. Marinak, G. D. Kerbel, and L. J. Suter. *Phys. Plasmas*, 11:5573, 2004.
- [44] L. J. Suter, S. Glenzer, S. Haan, B. Hammel, K. Manes, N. Meezan, J. Moody, M. Spaeth, L. Divol, K. Oades, and M. Stevenson. *Phys. Plasmas*, 11:2738, 2004.
- [45] C. Niemann, R. L. Berger, L. Divol, D. H. Froula, O. Jones, R. K. Kirkwood, N. B. Meezan, J. D. Moody, J. Ross, C. Sorce, L. J. Suter, and S. H. Glenzer. *Phys. Rev. Lett.*, 100:45002, 2008.
- [46] Juan C. Fernandez, S. R. Goldman, J. L. Kline, E. S. Dodd, C. Gautier, G. P. Grim, B. M. Hegelich, D. S. Montgomery, N. E. Lanier, H. Rose, D. W. Schmidt, , J. B. Workman, D. G. Braun, E. L. Dewald, O. L. Landen, K. M. Campbell, J. P. Holder, A. J. MacKinnon, C. Niemann, J. Schein, B. K. Young, J. R. Celeste, S. N. Dixit, D. C. Eder, S. H. Glenzer, C. A. Haynam, D. Hinkel, D. Kalantar, J. Kamperschroer, R. L. Kauffman, R. Kirkwood, A. E. Koniges, F. D. Lee, B. J. MacGowan, K. R. Manes, J. W. McDonald, M. B. Schneider, M. J. Shaw, L. J. Suter, R. J. Wallace, , F. A. Weber, and J. L. Kaae. *Phys. Plasmas*, 13:56319, 2006.
- [47] Bruce I. Cohen and Allan N. Kaufman. *Phys. Fluids*, 20:1113, 1977.
- [48] Bruce I. Cohen and Allan N. Kaufman. *Phys. Fluids*, 21:404, 1978.
- [49] K. Estabrook, W. L. Kruer, and B. F. Lasinski. *Phys. Rev. Lett.*, 45:1399, 1980.
- [50] K. Estabrook and W. L Kruer. *Phys. Fluids*, 26:1892, 1983.
- [51] K. Estabrook, W. L. Kruer, and M. G. Haines. *Phys. Fluids B*, 1:1282, 1989.
- [52] A. B. Langdon and D. E. Hinkel. *Phys. Rev. Lett.*, 89:15003, 2002.
- [53] D. E. Hinkel, S. W. Haan, A. B. Langdon, T. R. Dittrich, C. H. Still, and M. M. Marinak. *Phys. Plasmas*, 11:1128, 2004.
- [54] H. X. Vu, D. F. DuBois, and B. Bezzerides. *Phys. Rev. Lett.*, 86(19):4306, 2001.

- [55] H. X. Vu, D. F. DuBois, and B. Bezzerides. *Phys. Plasmas*, 9:1745, 2002.
- [56] T. O'Neil. *Phys. Fluids*, 8:2255, 1965.
- [57] G. J. Morales and T. M. O'Neil. *Phys. Rev. Lett.*, 28:417, 1972.
- [58] H. X. Vu, D. F. DuBois, and B. Bezzerides. *Phys. Plasmas*, 14:12702, 2007.
- [59] S. Brunner and E. J. Valeo. *Phys. Rev. Lett.*, 93:145003, 2004.
- [60] W. L. Kruer, J. M. Dawson, and R. N. Sudan. *Phys. Rev. Lett.*, 23:838, 1969.
- [61] L. Yin, W. Daughton, B. J. Albright, B. Bezzerides, D. F. DuBois, J. M Kindel, and H. X. Vu. *Phys. Rev. E*, 73:25401, 2006.
- [62] L. Yin, W. Daughton, B. J. Albright, K. J. Bowers, D. S. Montgomery, J. L. Kline, J. C. Fernandez, and Q. Roper. *Phys. Plasmas*, 13:72701, 2006.
- [63] M. Albrecht-Marc, A. Ghizzo, T. W. Johnston, R. Réveillé, D. Del Sarto, and P. Bertrand. *Phys. Plasmas*, 14:72704, 2007.
- [64] D. J. Strozzi, E. A. Williams, A. B. Langdon, and A. Bers. *Phys. Plasmas*, 14:13104, 2007.
- [65] Roy Gerrit Hemker. *Particle in cell modeling of plasma based accelerators in two-dimensions and three-dimensions*. PhD thesis, 2000. UMI-99-57820.
- [66] R. A. Fonseca, L. O. Silva, F. S. Tsung, V. K. Decyk, W. Lu, C. Ren, W. B. Mori, S. Deng, S. Lee, T. Katsouleas, and J. C. Adam. *Lecture Notes in Computer Science*, 2331/2002:342, 2002.
- [67] R. A. Fonseca, S. F. Martins, L. O. Silva, J. W. Tonge, F. S. Tsung, and W. B. Mori. *Plasma Physics and Controlled Fusion*, 50(12):124034 (9pp), 2008.
- [68] J. D. Huba. *NRL Plasma Formulary*. Naval Research Laboratory, 2009.
- [69] A. B. Langdon. *Phys. Rev. Lett.*, 44:575, 1980.
- [70] A.I. Akhiezer and R.V. Polovin. *Sov JETP*, 3:696, 1956.
- [71] J. M. Dawson. *Phys. Rev.*, 113:383, 1959.
- [72] J. M. Dawson. *Phys. Fluids*, 5:445, 1962.
- [73] P. Bertrand and M.R. Feix. *Phys. Letters*, 28A:68, 1968.

- [74] P. Bertrand, G. Baumann, and M.R. Feix. *Phys. Letters*, 29A:489, 1969.
- [75] D.A. Tidman and H.M. Stainer. *Phys. Fluids*, 8:349, 1965.
- [76] R.L. Dewar and J. Lindl. *Phys. Fluids*, 15:820, 1972.
- [77] T. Kakutani and N. Sugimoto. *Phys. Fluids*, 17:1617, 1974.
- [78] T. P. Coffey. *Phys. Fluids*, 14:1402, 1971.
- [79] I. B. Bernstein, J. M. Greene, and M. D. Kruskal. *Phys. Review*, 108:546, 1957.
- [80] J. P. Holloway and J. J. Dorning. *Phys. Lett. A*, 44:3856, 1989.
- [81] H. A. Rose and D. A. Russell. *Phys. Plasmas*, 8:4784, 2001.
- [82] E. A. Williams, B. I. Cohen, L. Divol, M. R. Dorr, J. A. Hittinger, D. E. Hinkel, A. B. Langdon, R. K. Kirkwood, D. H. Froula, and S. H. Glenzer. *Phys. Plasmas*, 11:231, 2004.
- [83] B. J. Winjum, J. Fahlen, and W. B. Mori. *Phys. Plasmas*, 14:102104, 2007.
- [84] C. B. Wharton, J. H. Malmberg, and T. M. O'Neil. *Phys. Fluids*, 11:1761, 1968.
- [85] S. I. Tsunoda and J. H. Malmberg. *Phys. Fluids B*, 1:1958, 1989.
- [86] P. DeNeef. *Phys. Rev. Lett.*, 31:446, 1973.
- [87] E. L. Lindman. *J. Computational Phys.*, 18:66–78, 1975.
- [88] D. E. Hinkel. private communication. 2009.
- [89] S. Mallat. *A Wavelet Tour of Signal Processing*. Academic Press, 1998.
- [90] J. E. Fahlen, B. J. Winjum, T. Grismayer, and W. B. Mori. *Phys. Rev. Lett.*, 102:245002, 2009.
- [91] D. Benisti and L. Gremillet. *Phys. Plasmas*, 14:0423304, 2007.
- [92] D. Benisti, D.J. Strozzi, and L. Gremillet. *Phys. Plasmas*, 15:030701, 2008.
- [93] R.R. Lindberg, A.E. Charman, and J.S. Wurtele. *Phys. Plasmas*, 14:122103, 2007.
- [94] L. Yin, B. J. Albright, K. J. Bowers, W. Daughton, and H. A. Rose. *Phys. Rev. Lett.*, 99:265004, 2007.

- [95] J. E. Fahlen, B. J. Winjum, T. Grismayer, and W. B. Mori. Transverse plasma wave localization in multiple dimensions. In preparation.
- [96] N. Bogoliubov and Y. A. Mitropolskii. *Asymptotic Methods in the Theory of Nonlinear Oscillations*. Gordon and Breach Science Publishers, New York, 1961.
- [97] E. A. Jackson. *Phys. Fluids*, 5:831, 1960.